Beyond Fixed Instruments: Harnessing UAS Technology for Enhanced Wind Measurements in Meteorology and Wind-Energy Science

Dissertation
der Mathematisch-Naturwissenschaftlichen Fakultät
der Eberhard Karls Universität Tübingen
zur Erlangung des Grades eines
Doktors der Naturwissenschaften
(Dr. rer. nat.)

vorgelegt von
Matteo Bramati
aus *Monza, Italien*

Tübingen
2024

Gedruckt mit Genehmigung der Mathematisch-Naturwissenschaftlichen Fakultät der Eberhard Karls Universität Tübingen.

Tag der mündlichen Qualifikation:	24.03.2025
Dekan:	Prof. Dr. Thilo Stehle
1. Berichterstatter/-in:	Prof. Dr. habil. Jens Bange
2. Berichterstatter/-in:	Prof. Dr Ulrich Löhnert

Aknowledgements

I would like to thank my two supervisors Dr. habil. Andreas Platis and Prof. Dr. habil. Jens Bange for giving me the opportunity to grow as a person and as an engineer over the past four years. I would like to thank Prof. Dr. Professor Ulrich Löhnert for agreeing to read this thesis with interest and for his unbiased assessment. Special thanks to Dr. Frank Beyrich of the DWD for his professionalism and constant support during the second part of my PhD.

I would like to thank all my colleagues, many of whom I can call friends, and without whom this work would not have been possible, both technically and on a human and psychological level.

Abstract

The accurate measurement of wind patterns and profiles in the atmospheric boundary layer (ABL) is of great importance for a number of meteorological applications, including weather forecasting, climate studies and environmental monitoring. Conventional techniques frequently encounter difficulties, including the necessity to rely on fixed instruments and the assumption of homogeneity in diverse topographical settings. In light of these challenges, this research project investigates the potential applications of the emerging technology of uncrewed aircraft system (UAS) to atmospheric measurements and meteorology.

UAS systems are known to be versatile instruments with flexible automatic mission planning capabilities, allowing rapid deployment to collect data in remote locations or in close proximity to sensitive structures. This study focuses on the measurement of the atmospheric wind vector through the use of both fixed- and rotary-wing UAS, addressing several aspects of these two inherently different flight systems.

A low-cost technique for using any rotary-wing UAS as a sensor capable of measuring the horizontal wind vector is presented and analysed from several aspects. The experimental results are presented and demonstrate the practicality and effectiveness of this method. This procedure, which is independent of the specific rotary-wing system, has been applied to numerous UASs subsequently used for different research purposes.

At the same time, the capabilities of the small fixed-wing UAS, the Multipurpose Airborne Sensor Carrier-3 (MASC-3), for the validation of remote sensing instruments are analysed in detail using data from three different experimental campaigns. Both mean wind and turbulent component vectors are analysed to highlight the strengths and weaknesses of this approach for the validation of other stationary instruments. On a 10-minute time average, the UAS proved to be a good reference for stationary sensors even when flying over long horizontal distances, while the accuracy of turbulence measurements was found to be influenced by the heterogeneity of the terrain around the test site, with optimal results obtained where the terrain is flat and homogeneous and greater discrepancies where it is covered by forest patches. This finding emphasises the challenges and limitations associated with the use of UAS for atmospheric turbulence studies in heterogeneous landscapes.

Overall, this thesis illustrates the potential of UAS technology as a versatile tool for atmospheric wind measurement, offering enhanced mobility and precision in various environmental contexts.

Zussammenfassung

Die genaue Messung von Windmustern und -profilen in der atmospheric boundary layer (ABL) ist für eine Reihe von meteorologischen Anwendungen wie Wettervorhersage, Klimastudien und Umweltüberwachung von großer Bedeutung. Herkömmliche Verfahren stoßen häufig auf Schwierigkeiten, u. a. auf die Notwendigkeit, sich auf ortsfeste Instrumente zu verlassen und auf die Annahme der Homogenität in unterschiedlichen topografischen Umgebungen. Angesichts dieser Herausforderungen untersucht dieses Forschungsprojekt die potenziellen Anwendungsmöglichkeiten der neuen Technologie der uncrewed aircraft system (UAS) für atmosphärische Messungen und Meteorologie.

UAS-Systeme sind als vielseitige Instrumente mit flexiblen automatischen Missionsplanungsfähigkeiten bekannt, die einen schnellen Einsatz zur Datenerfassung an abgelegenen Orten oder in unmittelbarer Nähe empfindlicher Strukturen ermöglichen. Diese Studie konzentriert sich auf die Messung des atmosphärischen Windvektors durch den Einsatz von UAS mit festen und rotierenden Flügeln und befasst sich mit verschiedenen Aspekten dieser beiden von Natur aus unterschiedlichen Flugsysteme.

Es wird eine kostengünstige Technik zur Verwendung eines beliebigen Drehflüglers als Sensor zur Messung des horizontalen Windvektors vorgestellt und unter verschiedenen Aspekten analysiert. Die experimentellen Ergebnisse werden vorgestellt und zeigen die Praktikabilität und Wirksamkeit dieser Methode. Dieses Verfahren, das unabhängig vom spezifischen Drehflüglersystem ist, wurde auf zahlreiche UASs angewendet, die anschließend für verschiedene Forschungszwecke eingesetzt wurden.

Gleichzeitig werden die Fähigkeiten des kleinen fixed-wing UAS, des Multipurpose Airborne Sensor Carrier-3 (MASC-3), für die Validierung von Fernerkundungsinstrumenten anhand von Daten aus drei verschiedenen Versuchskampagnen eingehend analysiert. Sowohl der mittlere Wind als auch die Vektoren der turbulenten Komponenten werden analysiert, um die Stärken und Schwächen dieses Ansatzes für die Validierung anderer stationärer Instrumente aufzuzeigen. Im 10-Minuten-Mittel erwies sich der UAS als gute Referenz für stationäre Sensoren, selbst wenn sie über große horizontale Entfernungen fliegen. Hierbei wurde die Genauigkeit der Turbulenzmessungen von der Heterogenität des Geländes um das Testgelände herum beeinflusst, wobei optimale Ergebnisse dort erzielt wurden, wo das Gelände flach und homogen ist, und größere Diskrepanzen dort, wo es von Waldstücken bedeckt ist. Dieses Ergebnis verdeutlicht die Herausforderungen und Grenzen, die mit der Verwendung von UAS für atmosphärische Turbulenzstudien in heterogenen Landschaften verbunden sind.

Insgesamt veranschaulicht diese Arbeit das Potenzial der UAS-Technologie als

vielseitiges Instrument für die Messung des atmosphärischen Windes, das in verschiedenen Umgebungen mehr Mobilität und Präzision bietet.

Contents

List of Figures **xi**

List of Tables **xiii**

1 List of Publications **1**
- 1.1 Peer-reviewed publications as first or corresponding author 1
- 1.2 Peer-reviewed publications as co-author 1
- 1.3 Conference participations 2

2 Introduction **3**
- 2.1 Wind in meteorology 3
- 2.2 Wind in wind-energy research 4
- 2.3 Uncrewed aircraft systems 6
- 2.4 Dissertation structure 7

3 Basic Concepts **9**
- 3.1 Why do we have wind? 9
- 3.2 Turbulence 10
- 3.3 Mean wind profile 11
  - 3.3.1 Geostrophic wind 11
  - 3.3.2 Atmospheric boundary layer 12
  - 3.3.3 Thermal stratification 13
  - 3.3.4 ABL diurnal cicle 14
  - 3.3.5 Heterogeneous terrain 15
- 3.4 How do we measure wind? 15
- 3.5 UASs at Umweltphysik group 17
  - 3.5.1 Fixed-wing UASs 17
  - 3.5.2 Rotary-wings UASs 18
- 3.6 Scientific questions 20

4 Results **23**
- 4.1 Optimizing rotary-wing UASs for wind measurement 23
  - 4.1.1 Calibration strategy 25
  - 4.1.2 Calibration model 26
  - 4.1.3 Directional independence and sensitivity enhancement 26
- 4.2 Fixed-wing UASs for remote-sensing instruments validation 29
  - 4.2.1 Mean wind 29

4.2.2 Turbulence 33

5 Discussion 37

5.1 Validating remote sensing devices with fixed-wing UASs 37
5.2 Further insights on rotary-wings UASs wind measurements 38
5.2.1 Drag coefficient 38
5.2.2 Turbulence 39
5.2.3 Case studies 40

6 Outlook 47

A First/corresponding author peer-reviewed publications 49

Bibliography 109

List of Figures

3.1 The MASC-3 UAS positioned on the catapult and ready to take-off. The sensorhood with the 5HP and the fine-wire thermometer is visible in the front, while on the wings is mounted an optical particle counter pod[74] (right wing) and an atmospheric charge sensor pod[73] (left wing). From BRAMATI et al. [15] 17

3.2 The S900 (left) and X500 (right) UAS. The two systems have been modified through the incorporation of a spherical dome around the central frame. The bigger system has six rotors with the landing gears extending from the frame while the smaller has four rotors and the landing gears are positioned directly below the electric motors. . 18

3.3 The FW-XL10 UASs shortly after take-off. Due to the performance-oriented design, on this system was not possible to incorporate a spherical dome. In the picture it is visible, on top of the main battery, a safety parachute, used to reduce the ground risk during aerial operations. 20

4.1 **a)** Representation of the forces acting on a multi-rotor while hovering. Γ is the tilt angle. **b)** Example of UAS mission (collection of waypoints), for the calibration flights. From BRAMATI et al. [14]. . 24

4.2 The two different calibration models proposed in the publication. TAS stands for the true air speed of the copter during the calibration flights. This represents the atmospheric wind speed when the copter is hovering. From BRAMATI et al. [14]. 26

4.3 Comparison of tilt angle values obtained with two multi-copters of the same type flying simultaneously, one with the styrofoam sphere and one without. From BRAMATI et al. [14]. 27

4.4 Representation of all the flight legs used for the mean wind vector analysis of the VALUAS project. The red column represents the Falkenberg meteorological tower. A consistent amount of legs are located around 99 m altitude which corresponds to the top of the tower itself. The height of the remaining legs has been chosen to match the scanning heights of the two DWLs systems. From BOVENTER et al. [13]. 30

4.5 Flowchart of data processing. Only the legs at 98 m altitude have been grouped into three different time averages in order to study accuracy and precision of the MASC-3. For the UAS vs DWL comparison only 10-minutes averages have been used from all the available legs at different altitudes. From Boventer et al. [13]. 31
4.6 Comparison between TKE measured by the sonic anemometer and the MASC-3. Each of the scatter points corresponds to one leg. a) comparison performed with the correct amount of air for the sonic anemometer, b) comparison performed by simply considering the sonic and UAS time series cut with the start and end time of each leg. From Bramati et al. [15]. 34
4.7 Map including all the legs and the two main wind direction sectors. The purple sector spans from 140° to 220° and includes the E (6 legs) and S (24 legs) wind direction groups: it is characterized by flat cultivated land and a lower elevation than the Falkenberg tower. The red sector spans from 240° to 360° and includes the WNW (47 legs) and the NNW (25 legs) groups: it is characterized by forest patches and a higher elevation than the Falkenberg tower. From Bramati et al. [15]. 36

5.1 Comparison of the C_{A} coefficient obtained experimentally for the two copters of different size. The values of this parameter are particularly similar for both systems especially for tilt angles (and therefore wind speeds) exceeding 9-10°. 39
5.2 Comparison of the power spectral densities of the two copters of different size and weight, plotted together with a sonic anemometer spectrum and the Kolmogorov -5/3 decay law. 40
5.3 **a)** Wind turbine in Schopfloch, Baden Württemberg. **b)** Horizontal mapping of the Schopfloch wind turbine wake obtained during a S900 UAS mission. 41
5.4 The X500 UAS shortly after take off from the maintenance vessel inside the Rødsand II wind farm. For this specific missions the UAS has been equipped with floating bags inside the spherical dome and on the four arms, in order to grant buoyancy in case of landing on water. 42
5.5 Vertical profiles of the wind deficit behind the K07 turbine in the Rødsand II wind park. 43
5.6 Quicklook of the thermodynamic variables collected the morning of May 9, 2024 by profiling the first 900 m of the lower ABL in Lindenberg, Tauche with the FW-XL10 UAS. Timestamp are in UTC. 45

List of Tables

4.1 Statistical measures describing the quality of the MASC-3 UAS as horizontal wind vector sensor. RMSD represents the root mean squared deviation, MBD the mean bias deviation while R the Pearson correlation coefficient. The subscript v refers to the wind speed while ϕ to the wind direction. From BOVENTER et al. [13] 32
4.2 MBD and RMSD between UAS measurements and sonic anemometer measurements for the different wind directions. From BRAMATI et al. [15]. 35

Chapter 1

List of Publications

1.1 Peer-reviewed publications as first or corresponding author

I Bramati, M., M. Schön, D. Schulz, V. Savvakis, Y. Wang, J. Bange, and A. Platis, 2024: A Versatile Calibration Method for Rotary-Wing UAS as Wind Measurement Systems. J. Atmos. Oceanic Technol., 41, 25–43

II Boventer, J., M. Bramati, V. Savvakis, F. Beyrich, M. Kayser, A. Platis, and J. Bange, 2024: Validation of Doppler Wind Lidar Measurements with an Uncrewed Aircraft System (UAS) in the Daytime Atmospheric Boundary Layer. J. Atmos. Oceanic Technol., 41, 705–723[1]

III Bramati, M., V. Savvakis, F. Beyrich, J. Bange, and A. Platis, 2024: In-situ uncrewed aircraft measurements of turbulent kinetic energy over heterogeneous terrain. J. Atmos. Oceanic Technol. 42, 319–338

1.2 Peer-reviewed publications as co-author

I Büchau Y.G., H. Mashni, M. Bramati, V. Savvakis, I. Schäfer, S. Jung, G. Miranda-Garcia, D. Hardt, J. Bange, (2024). PARMESAN: Meteorological Timeseries and Turbulence Analysis Backed by Symbolic Mathematics. Journal of Open Source Software, 9(94), 6127

II Savvakis V., M. Schön, M. Bramati, J, Bange, A. Platis, (2024): Small-scale diffusion dryer on an optical particle counter for high humidity measurements with an uncrewed aerial system, J. Atmos. Oceanic Technol., 41, 205-219

III Savvakis V., M. Schön, M. Bramati, J. Bange, A. Platis, (2024): Calculation of aerosol particle hygroscopic properties from OPC derived PM2.5 data, Meteorologische Zeitschrift. Advances in Atmospheric Sciences., 33, 145-157

---

[1] corresponding author

1.3 Conference participations

- 2023, *Oral Presentation*, ISARRA conference 2023, Bergen - Analyzing horizontal and vertical wind speed using multi-copter UAS aircraft: calibration, environmental factors, and accuracy assessment.
- 2023, *Oral Presentation*, WESC conference 2023, Glasgow - In-situ measurement inside an offshore wind farm using multi-copter UAS.
- 2021, *Oral Presentation*, EAWE PhD Wind Energy Conference, Porto
    - Calibration procedure for horizontal wind estimation using a hovering multi-copter.
    - Development and validation of a fast response dew-point mirror mounted on a UAS.

Chapter 2

Introduction

2.1 Wind in meteorology

In ancient times,the study of meteorology and the ability to predict weather patterns were frequently associated with divination, as it was thought that atmospheric phenomena resulted from the influence of various localised supernatural deities[32]. However, with the advent of the first comprehensive treatise on meteorology, traditionally attributed to Aristotle around 350 B.C., this perspective gradually shifted away from its religious connotations, evolving into a distinct branch within the atmospheric sciences[31].

During the period spanning the Renaissance to the Age of Enlightenment, significant advancements were made by the intellects of the era, leading to the invention of several instruments that remain integral to meteorological studies in the present day[40]. These innovations included the swinging plate anemometer, the barometer, rain gauges, and the thermometer[30]. These inventions facilitated the systematic collection of weather data, although adherence to scientific standards was primarily limited to local levels. It was not until the latter half of the nineteenth century, particularly with the advent of the telegraph, that the establishment of a widespread network for measuring, forecasting, and issuing weather warnings over long distances became feasible[12].

The advent of predictive numerical models in the early 1900s constituted a significant milestone in the evolution of weather forecasting, bringing it closer to the form that is recognisable today[75]. The ability to comprehend meteorological phenomena with greater accuracy has become not only a necessity for modern living but also a significant factor in historical developments. Indeed, it is probable that such knowledge altered the course of entire continents, as evidenced by its pivotal role in the Second World War. As an example, the Allies made use of meteorological predictions in order to plan the Normandy landing on the 6th June 1944. The operation, originally scheduled for the 5th June, was postponed due to inclement weather conditions. The rescheduling of the D-Day operation and its subsequent success, guided by meteorological insights, demonstrated the critical importance of accurate weather forecasting in the execution of large-scale military operations and the shaping of historical outcomes.

Modern meteorology is structured into a number of distinct subcategories, each of which is based on the length scale of the phenomena being studied. These range from the microscale, which is the smallest unit of measurement, to the global scale, which is the largest[41]. In any case, beginning with data collected at specific times and locations, this field of study aims to provide forecasts regarding the atmospheric conditions at those same locations at some future point in time. To accomplish this, meteorologists rely on weather prediction models, which are built upon the principles of fluid dynamics and thermodynamics[51]. At the present time, these models primarily involve solving partial differential equations, which, due to their inherent complexity, cannot typically be solved analytically. Consequently, numerical methods are employed, enabling approximation-based solutions. Although these approximations are essential for obtaining numerical solutions, at the same time they introduce uncertainties and errors, particularly as the forecast time horizon extends into the future[76]. It is therefore essential to continually reinitiate numerical models, which can be achieved through the incorporation of standardised in-situ data obtained from specialised instruments[92]. Common variables of interest include temperature, pressure, humidity, wind speed, and wind direction. The most commonly investigated variables are temperature, pressure, humidity, wind speed and wind direction. While these data can be readily obtained on the ground thanks to an extensive network of weather stations, it is more challenging to obtain vertical profiles covering the lower part of the atmosphere (100 m - 6 km) with a high degree of reliability, as this requires the use of remote sensing techniques[46].

Among the variables predicted by models, the wind speed vector is of particular significance across numerous spheres of human activity. Airports regularly modify their take-off and landing procedures in accordance with prevailing wind patterns. Strong gusts can cause discomfort for passengers and, in extreme cases, impede aircraft from safely navigating certain locations[58],[89]. Moreover, in the context of fire prevention, the atmospheric wind assumes a pivotal role. In order to ensure the protection of communities at risk of wildfires, it is essential to consider wind dynamics in order to optimise the safeguarding of vulnerable areas and individuals[61]. Furthermore, atmospheric winds act as a vector for a multitude of particles, including pollutants, pollen, and dust, dispersing them over vast distances. This dispersion can have a significant impact on human health and safety in daily life, as these particles traverse thousands of kilometres, affecting air quality and allergen exposure levels in diverse regions[18]. It is therefore essential to gain an understanding of and to be able to forecast wind behaviour if risks are to be mitigated and various aspects of human existence optimised.

2.2 Wind in wind-energy research

The utilisation of wind power has been a fundamental aspect of human history, with its potential being harnessed for a multitude of purposes. From the earliest civilisations, sailing vessels have played a pivotal role in facilitating trade, asserting maritime dominance and embarking on exploratory voyages. On land, wind energy was employed to power heavy machinery for tasks such as grain milling and water pumping. However, it was not until the late 1800s, when advancements were made in electricity generation and storage technologies, that the concept of the wind turbine was first conceived[43].

Pioneering researchers conceived the idea of coupling a dynamo to a windmill to charge batteries, effectively laying the groundwork for modern wind energy systems. Initially deployed to provide electricity to remote areas beyond the reach of urban power grids, the potential of wind power remained largely unexplored until the latter part of the 20th century[36]. The growing interest in renewable energy sources during the 1970s and 1980s led to a notable increase in research and development activities within the field of wind energy. This newfound enthusiasm boosted innovations in wind turbine design, efficiency, and deployment strategies, which ultimately established wind power as a prominent player in the global quest for sustainable energy solutions[37].

Modern wind turbines typically consist of a tower that supports a hub, upon which a rotor is mounted. The rotor typically features three aerodynamically designed blades that rotate around a horizontal axis[63]. The interaction between the wind and these blades allows the conversion of a portion of the wind's kinetic energy into electrical energy through the rotational motion of the rotor[8]. Since the very first constructions, wind turbine technology has undergone a significant and remarkable evolution. Early prototypes featured relatively modest tower heights and power generation capacities. However, technological advancements have driven the industry towards increasingly ambitious goals in terms of both size and power generation capabilities[2]. Today, the pinnacle of this progress is represented by wind turbines boasting staggering dimensions, with the largest installations featuring rotor diameters reaching 252 meters, towering at heights of 146 meters, and capable of generating 16 megawatts. Nevertheless, despite these impressive achievements, Europe's pursuit of ambitious targets for reducing greenhouse gas emissions and achieving carbon neutrality by 2030 demands further advancements in renewable energy[91]. It is therefore imperative that the wind energy sector continues to innovate and expand its capabilities in order to play a pivotal role in meeting these sustainability objectives.

The use of land-based wind turbines has become commonplace, yet it continues to confront several challenges[22]. The most critical challenges include technical issues such as the preservation of natural ecosystems, the management of complex terrain, the mitigation of turbine-generated noise, and the integration of wind resources with fluctuating availability. Furthermore, a substantial challenge remains in obtaining social acceptance for this technology. The construction of wind farms frequently results in alterations to the local landscape, which often leads to scepticism and resistance from those residing in the vicinity. Among the communities affected by wind farms, concerns regarding visual impacts and potential disruptions to local wildlife are particularly prevalent.

Although offshore wind turbine clusters are already a reality, ongoing research in this field is vibrant and indicative of a clear trajectory for the future of this renewable energy source[21]. There is a growing interest among companies and investors in offshore installations, which are seen as a crucial step in achieving renewable energy objectives. Despite persistent concerns regarding marine ecosystems, offshore wind turbines offer a number of distinct advantages. These include access to more consistent and powerful wind resources, along with the potential for deploying larger rotors with minimal impact on social acceptance[33]. Moreover, the emergence of innovative technologies, such as floating wind turbines, is expanding the range of potential projects. Previously constrained by a maximum depth limit of 60 meters, floating turbines are now unlocking new possibilities and locations, enabling installations in deeper waters that were previously inaccessible[7].

Whether for onshore or offshore projects, it is evident that significant investments, ranging from tens to hundreds of thousands of euros, are at stake[77]. Consequently, thorough wind resource studies are imperative to pinpoint the most viable locations for wind turbine installations. Simultaneously, it is crucial to conduct measurements and gather data from existing operational installations, whether they are wind farms or individual turbines. This approach allows for a comprehensive understanding of the impact of these facilities on their surrounding airflow dynamics, thereby facilitating the refinement and optimisation of future projects.

2.3 Uncrewed aircraft systems

Over the past 20 years, uncrewed aircraft systems (UASs) have emerged as a cost-effective and innovative technology with diverse applications spanning various industries[39]. These applications range from healthcare[70], search and rescue operations[54],[42], and agriculture[69], to parcel delivery[20] and even sports[71].

UASs offer a more economical operational alternative to crewed aircraft and grant increased flexibility in accessing remote or hard-to-reach locations where interesting data may be lacking. This versatility, coupled with the ability to perform repetitive and scalable missions, has garnered significant interest and enthusiasm from both the scientific community and industry stakeholders, driving further advancements in UAS technology[57].

The earliest known use of UAS for meteorological purposes can be traced back to the early 1970s, when Konrad et al. [45] conducted pioneering research to explore the potential of this new technology in enhancing the understanding of convective processes in the lower atmosphere. Nevertheless, the extensive adoption of UAS by the scientific community only occurred in recent years, coinciding with a decline in the cost of electronic components, which made them more accessible to small research teams.

UASs are remotely controlled aircraft weighing up to 25 kg, equipped with pre-programmable and autonomous flight capabilities. The ongoing trend of sensor miniaturization has facilitated the seamless integration of various meteorological payloads onto these systems, leading to their classification as weather-sensing or weather-research UAS.

These weather-research UASs possess remarkable versatility, enabling vertical profiling up to altitudes of approximately 5-6 km and conducting ad-hoc measurements such as investigating airflow behind wind turbines or within wind parks. The specific quantities measured by a meteorological UAS depend on the payload, but typically include wind speed and direction, pressure, temperature, and humidity. Data collection frequencies vary among systems, ranging from as low as 10 to 100 Hz in some cases.

Nowadays, with UAS technology firmly established and further reductions in component costs at the horizon, a growing number of researchers are exploring the potential of implementing a network of automated UASs to enhance weather forecast models. Addressing gaps in the measurement of thermodynamic and kinematic properties within the lowest part of the Earth's atmosphere is pivotal for advancing weather forecasting capabilities[60].

A study conducted by LEUENBERGER et al. [50] demonstrate how drone observations can effectively bridge spatial and temporal data gaps in temperature and humidity, particularly in regions with limited access to remote sensing technologies or in sparsely covered areas such as polar regions. This research underscores the potential contribution of weather-sensing UAS technology in enhancing our understanding and prediction of meteorological phenomena across diverse geographic and climatic contexts.

2.4 Dissertation structure

For over a decade, the Umweltphysik working group at the University of Tübingen has been at the forefront of successfully operating weather-research UASs. Leveraging insights and expertise gained from the use of precursor technologies, such as the Helipod[5], this research group has made considerable progress in the development of its own remotely operated fixed-wing aircraft, equipped with sensors capable of measuring essential atmospheric parameters: the Multi-purpose Airborne Sensor Carrier-3 (MASC-3)[67]. At the same time, a small fleet of multi-rotor aircraft has been progressively developed in order to expand the possibilities with regard to measurement strategies[14].

The work of the candidate of this thesis is positioned in both areas, having actively participated in the creation of the multi-rotor fleet, but at the same time having used a substantial part of his time for the analysis of data collected in recent experimental campaigns using the fixed-wing aircraft.

The thesis is structured as follows:

- Chapter 3 provides a concise overview of fundamental concepts concerning atmospheric wind, particularly its behavior in the lower part of the atmosphere. Rather than an exhaustive exploration of scientific concepts, these pages aim to offer a foundational understanding necessary for the comprehension of the subsequent three scientific publications that form the core of the work of the candidate. For readers seeking more extensive explanations and further readings, references cited within the text are provided for additional study. The chapter will conclude with an introduction to the UASs employed by the Tübingen Umweltphysik research group, with a focus on their similarities and differences, as well as an overview of the primary scientific questions.

- In Chapter 4, each scientific question is addressed by linking it to the main findings of the three scientific papers that form the core of this thesis. Detailed descriptions of the UASs employed in the respective studies are provided, and the most significant results are highlighted and contextualized within existing literature gaps and initial hypotheses.

- Chapter 5 provides a more detailed examination of the findings presented in the previous section, establishing a clear connection to the central theme of measuring wind with weather-sensing UASs. Furthermore, research activities not covered in the aforementioned publications are described and analysed.
- In conclusion, Chapter 6 turns its attention to prospective future developments weather-research UAS technology, with particular focus on the evolution of the Umweltphysik group's fleet.

Chapter 3

Basic Concepts

3.1 Why do we have wind?[25],[82]

Wind on Earth is a direct result of the uneven distribution of solar radiation hitting the surface of the planet. This non-uniform radiation creates areas of high and low pressure, leading to the generation of wind that moves from regions of high pressure to those of low pressure. Broadly speaking, there are three primary global wind-circulation cells: Hadley Cells, Polar Cells, and Ferrel Cells.

Hadley cells span from the equator to approximately 30 degrees latitude in both hemispheres. The intense solar radiation at the equator causes the air to become heated and rise towards the tropopause, forming a low-pressure zone at the surface. As a result, winds develop at ground level in order to counterbalance this pressure differential, resulting in an airflow directed towards the equator. Conversely, at higher altitudes, the warm air moves away from the equator, condenses, and precipitates frequently in tropical regions. It then cools gradually and descends back to the surface around 30 degrees latitude.

Polar cells, which are situated around the poles up to approximately 60 degrees of latitude, are driven by the temperature contrast between the polar regions and mid-latitudes. At the poles, the descent of cold air is facilitated by the presence of minimal solar radiation and frozen surfaces, which collectively contribute to the formation of a high-pressure zone. Subsequently, this cold air flows towards the mid-latitudes, where the pressure is relatively lower. At approximately 60 degrees of latitude, the temperature of the air has increased sufficiently for it to rise and circulate back towards the poles.

Between the polar and Hadley cells lie the Ferrel cells, characterized by air movement contrary to the preceding two circulation cells and less influenced by temperature differences. Instead, their movement is primarily governed by the rotational direction of the polar and Hadley cells. Consequently, surface winds in Ferrel cells tend to blow towards the poles, transporting warm air.

These three distinct circulation cells broadly determine climatic macro-zones: regions where air ascends in the troposphere tend to exhibit predominantly low-pressure systems accompanied by heavy rainfall, while areas where air descends are characterized by high-pressure zones with minimal precipitation. Additionally, the Coriolis effect further influences atmospheric dynamics by deflecting air movement from its original north-south trajectory, ultimately giving rise to the prevailing winds observed across the Earth's surface.

A variety of circulation phenomena are observed at smaller spatial scales as a consequence of the heterogeneous nature of the Earth's surface. Such phenomena include, but are not limited to, hurricanes, monsoons, and cyclones. At an even smaller scale, local topography gives rise to a variety of phenomena, including land and sea breezes, valley and mountain winds, and atmospheric disturbances such as thunderstorms and tornadoes.

Wind exhibits variability not only over space scales but also on temporal scales which can be classified based on their duration. Changes spanning over a decade to three decades fall under the category of climate changes, while annual fluctuations are typically attributed to the seasonal cycle. Additionally, variations associated with the diurnal cycle occur as a result of direct solar radiation influencing the movement of air masses. Furthermore, variability occurring within the span of 1 to 10 minutes is primarily attributed to the inherently chaotic nature of fluid movement, such as that of air.

3.2 Turbulence[19],[34],[62],[85]

There is no single, universally accepted definition of turbulence. Turbulence is typically described as a state of a flow characterised by chaotic, irregular, and unpredictable motion. Turbulence frequently gives rise to the formation of vortices, swirls, and eddies of varying sizes and intensities, which emerge and dissipate within the flow itself. Since turbulence is characterised by the continuous variability of the properties of the flow (velocity, temperature, pressure, humidity, etc.) it is commonly analysed by separating average values from fluctuations across these variables. This analytical approach, known as the Reynolds average, is widely used to describe turbulence:

$$\boldsymbol{X} = \overline{\boldsymbol{X}} + \boldsymbol{x} \tag{3.1}$$

Where $\boldsymbol{X}$ represents any of the previously mentioned variable, function of space or time while $\overline{\boldsymbol{X}}$ is its average value computed over well defined boundaries in space or time and $\boldsymbol{x}$ is the random fluctuation.

Several factors contribute to the onset of turbulence in the atmosphere. Differential heating of the Earth's surface can lead to density variations, which in turn can give rise to the chaotic motion of air masses and the formation of turbulent eddies. Additionally, the interface between air and surface serves as a source of turbulence, driven by the roughness of the surface itself. Physical obstacles such as buildings, houses, bridges, and wind turbines, which stand out prominently compared to the surrounding environment, can generate large eddies. Furthermore, shear between two air masses moving at different speeds creates turbulence in the interface zone. The phenomenon of atmospheric turbulence is observed across a vast range of spatial scales, from the formation of small eddies generated by ground-level shrubs to the development of large vortices induced by towering skyscrapers.

Turbulent fluctuations lead to increased mixing, diffusion, and transport of momentum, energy, and scalar quantities compared to non-turbulent (or laminar) flow. This characteristic is beneficial in efficiently distributing heat, moisture, and regulating temperature. However, turbulent phenomena can also rapidly disperse pollen or pollutants, and pose significant risks to civil aviation and the structural integrity of buildings exposed to strong winds, such as bridges or skyscrapers.

Although turbulent phenomena are inherently chaotic, it is possible to identify statistical properties that allow for analytical modelling to a certain extent.

3.3 Mean wind profile[78]

To mathematically describe the motion of an air particle in the atmosphere, it's common to start from the Navier-Stokes equations and apply the Reynolds averaging. With few steps it is possible to derive a modified set of equations known as the Eulerian equations of motion:

$$\frac{\partial \overline{\boldsymbol{U}}_i}{\partial t} + \overline{\boldsymbol{U}}_j \frac{\partial \overline{\boldsymbol{U}}_i}{\partial \boldsymbol{x}_j} = -\boldsymbol{\delta}_{j3} g + f_c \epsilon_{ij3} \overline{\boldsymbol{U}}_j - \frac{1}{\rho}\frac{\partial p}{\partial \boldsymbol{x}_i} + \nu \frac{\partial^2 \overline{\boldsymbol{U}}_i}{\partial \boldsymbol{x}_j^2} - \frac{\partial \, \overline{\boldsymbol{u}_i \boldsymbol{u}_j}}{\partial \boldsymbol{x}_j} \tag{3.2}$$

with the $\overline{\boldsymbol{U}}$ being the mean wind speed vector while $\boldsymbol{u}$ the fluctuating part, g the local gravitational field of the Earth, f_c the Coriolis parameter[1], ρ the air density, p the pressure field and ν the kinematic viscosity of the air. The terms on the left side of the equal sign represents the total derivative of the particle velocity (change in time and due to advection), while on the right side we have the forcing terms: gravity, Coriolis effect, pressure gradient and two terms usually addressed as stresses. One is proportional to the kinematic viscosity of the air while the other is a mere consequence of turbulence itself and it is called Reynolds stress.

3.3.1 Geostrophic wind[25],[80]

The most straightforward simplification of the Eulerian equations of motion is applicable to a scenario of purely horizontal wind conditions, in which the dominant forces are the Coriolis force and the pressure gradient.

$$\frac{\partial \overline{\boldsymbol{U}}_i}{\partial t} + \overline{\boldsymbol{U}}_j \frac{\partial \overline{\boldsymbol{U}}_i}{\partial \boldsymbol{x}_j} = f_c \epsilon_{ij3} \overline{\boldsymbol{U}}_j - \frac{1}{\rho}\frac{\partial p}{\partial \boldsymbol{x}_i} \tag{3.3}$$

In the case of steady-state motion, a solution is obtained that describes a straight and uniform wind flow parallel to the isobar contours, with its intensity determined by the Coriolis parameter and the local pressure gradient.

$$f_c \epsilon_{ij3} \overline{\boldsymbol{U}}_j = \frac{1}{\rho}\frac{\partial p}{\partial \boldsymbol{x}_i} \tag{3.4}$$

These equations yield a solution for a type of wind commonly referred to as geostrophic wind, whose magnitude is determined by the Coriolis parameter and the local pressure gradient.

The development of this type of wind occurs under specific conditions, notably minimal frictional forces, which are typically observed at high altitudes where the influence of the Earth's surface can be disregarded. This region is commonly referred to as the free atmosphere.

---

[1] The Coriolis parameter depends on the latitude ϕ and the angular velocity of the Earth $\omega = 2\pi/24\text{h}$ as $f_c = 2\omega \sin\phi$

3.3.2 Atmospheric Boundary Layer[19],[24],[62],[79],[83],[84],[87]

The vertical layer near the Earth's surface where the presence of the surface significantly influences atmospheric dynamics is commonly referred to as the atmospheric boundary layer (ABL). According to STULL [83], the ABL is defined as:

"that part of the troposphere that is directly influenced by the presence of Earth's surface, and responds to surface forcings with a timescale of about an hour or less."

Turbulence characterizes the airflow within the ABL, stemming from interactions between the surface and the overlying air mass. Given the chaotic and unpredictable nature of air movement, defining an average velocity profile is inherently affected. Even in an idealized scenario of uniform rectilinear motion, the Eulerian equations must incorporate terms related to frictional forces.

$$f_c \epsilon_{ij3} \overline{\boldsymbol{U}}_j - \frac{1}{\rho}\frac{\partial p}{\partial \boldsymbol{x}_i} + \frac{1}{\rho}\frac{\partial \boldsymbol{\tau}_{ij}}{\partial \boldsymbol{x}_j} = 0 \tag{3.5}$$

where $\boldsymbol{\tau}_{ij}$ is defined as the stress tensor including viscous and turbulent stresses defined previously.

Close to the Earth's surface, friction forces exert a significant influence compared to Coriolis forces. Consequently, near the ground, the wind direction will be perpendicular to the isobar lines. As one moves away from the surface, frictional effects diminish while Coriolis forces become increasingly dominant. In this part of the ABL, the wind vector gradually rotates until, at the height of the ABL, it aligns with the geostrophic wind, completing a 90-degree rotation.

The analytical description of the mean wind profile within the ABL can be determined through various methods, all of which rely on similarity theory. This theory postulates that for each turbulent boundary layer, there exists a dimensionless velocity profile as a function of dimensionless distance from the surface, exhibiting a universal trend.

$$\frac{\overline{\boldsymbol{U}}}{u_\star} = \frac{1}{\kappa}\ln\left(\frac{z}{z_\star}\right) \tag{3.6}$$

with $u_\star$ being the roughness speed, $z_\star$ the roughness length and κ a constant called Von Kármán constant. This relationship, derived through dimensional analysis, lacks a theoretical proof but has been validated by numerous experiments. The Von Kármán constant κ is typically determined experimentally as well (0.4). Dimensionless variables are normalized using quantities characteristic of the flow under analysis. Determining variables such as roughness length or roughness speed analytically or through models can be challenging, so experimental results are commonly utilized to obtain these parameters.

In ABL meteorology, it is common to categorize the ABL into three distinct zones:

- The roughness sublayer, located directly above the Earth's surface and only a few millimeters thick. In this layer, flow is primarily influenced by viscous frictional stresses, and turbulence remains predominantly laminar.

- The Prandtl layer, also known as the surface layer, is defined as the portion of the ABL where turbulent flows deviate less than 10% from their value immediately at the Earth's surface. Here, wind speed increases rapidly with altitude, and turbulent interaction forces are predominant.

- The Ekman layer, covering the majority of the ABL (about 90%), is where pressure, turbulent friction, and Coriolis effects coexist on a similar magnitude. In certain cases, it is possible to derive an analytical solution for wind speed as a function of height, assuming well-defined trends for turbulent friction forces. This solution describes an exponential approach to the geostrophic wind as altitude nears the upper limit of the ABL. Additionally, within the Ekman layer, the mean wind direction tends to rotate until aligning with the direction of the geostrophic wind.

3.3.3 Thermal stratification[25],[79],[87]

Thermal stratification within the ABL is a crucial aspect in the study of mean profiles and atmospheric turbulence. The primary factors contributing to thermal stratification include solar heating of the Earth's surface and the heat capacity of the surface itself.

The high heat capacity of marine and lacustrine surfaces makes them less susceptible to solar heating, maintaining a relatively consistent temperature regardless of external conditions. In contrast, on terrestrial surfaces, a substantial proportion of incident solar radiation is transformed into heat, which is subsequently transferred to the lower portion of the surface layer (or vice versa if the surface is cooler than the surrounding air).

Thermal stratification is typically classified in three main conditions: stable, unstable, and neutral. Stable stratification occurs when colder air flows beneath layers of warmer air, while unstable conditions are characterized by the opposite scenario. The names of these conditions reflect their defining characteristics; under unstable conditions, vertical air movements are accentuated, leading to increased turbulence.

In order to mathematically distinguish these three cases, we employ a variable known as virtual potential temperature. This parameter is derived from virtual temperature, accounting for the influence of humidity:

$$\Theta_v = T\left(\frac{p_0}{p}\right)^{\frac{R}{c_p}} \cdot (1 + 0.609 \cdot q) \tag{3.7}$$

In a neutrally stratified ABL, this variable remains constant with altitude. However, it decreases in unstable conditions and increases in stable conditions. In unstable scenarios, an upwardly displaced air parcel exhibits a higher virtual potential temperature (Θ_v) compared to its surrounding environment, resulting in further ascent. Conversely, in stable stratification, the parcel returns to its original position due to lower Θ_v.

The important quantity is not solely the virtual potential temperature itself but rather its gradient at a specific point within the ABL. Consequently, it is common to define a dimensionless number characterizing the stability condition. This parameter, known as the Bulk Richardson number, is expressed as:

$$\mathrm{Ri_B} = \frac{g \Delta \Theta_v \Delta z}{\overline{T}_v \left(\Delta u\right)^2} \tag{3.8}$$

Positive values of the Bulk Richardson number denote stable atmospheric conditions, while negative values indicate instability. A value of 0 signifies a neutrally stratified ABL. Given that the mean wind profile, particularly within the lower ABL layer where turbulent fluxes are most pronounced, is determined using similarity theory, it becomes evident that thermal stratification directly influences the generation or suppression of turbulence, thereby impacting the profiles themselves.

In practice, correction functions are often applied to logarithmic wind profiles. In unstable stratification, turbulent mixing is intensified, resulting in reduced wind shear and consequently lower wind speeds at equivalent altitudes compared to neutral stratification. Conversely, in a stable ABL, wind shear is more pronounced, leading to higher wind speeds at the same altitudes compared to neutral stratification.

3.3.4 ABL diurnal cicle[79],[81],[83],[86]

All three stability conditions mentioned earlier can manifest in the same location within a span of 24 hours or even less. Since solar radiation predominantly influences the heating or cooling of the Earth's surface, the ABL over homogeneous terrain typically exhibits diurnal variations.

Shortly after sunrise, a convective boundary layer (CBL) begins to form due to turbulent convective motions. This layer reaches its maximum height typically in the late afternoon. Within the CBL, the wind profile still exhibits a logarithmic pattern in the surface layer. However, due to the presence of significant instability and turbulence, this profile gradually increases with altitude but generally does not reach wind speeds observed above the CBL itself. The growth process occurs through the gradual entrainment of less turbulent air situated above this layer. This entrainment is driven by both convective turbulence and mechanical turbulence arising from wind shear at the interface between the CBL and the air above.

Shortly before sunset, solar radiation ceases to heat the Earth's surface, while the CBL occupies the entire ABL. This layer is often addressed as the residual layer (RL), as it essentially comprises what remains of the earlier CBL. Simultaneously, the Earth's surface transitions into a heat sink, resulting in the gradual formation of a stable boundary layer (SBL) in the lower portion of the ABL during nighttime. Within this layer, turbulent motions are suppressed. However, the growth of the SBL is slower compared to the CBL due to the lack of key factors such as convective motions. Consequently, in most cases, the nighttime ABL remains divided into the SBL and the RL.

The mean wind profile during nocturnal hours may exhibit distinctive features, including the occurrence of low-level jets, characterised by wind speeds exceeding the geostrophic wind. These phenomena contribute to the complex dynamics of the nocturnal atmospheric boundary layer.

3.3.5 Heterogeneous terrain[19],[24],[26],[62]

So far, our discussions have revolved around horizontally homogeneous terrain. However, in reality, such conditions are rarely encountered, and the Earth's surface typically comprises diverse zones with varying physical characteristics. As outlined in the preceding section, similarity theory provides a solution for the profile of mean velocity as a function of dimensionless variables, achieved by utilizing characteristic dimensions pertinent to the flow under examination.

Among these variables, the roughness length stands out as one of the most significant. Defined as the vertical height at which the mean wind speed reduces to zero in the logarithmic velocity profile, this length scale lacks a direct physical interpretation and does not correspond to the vertical extent of surface obstacles. Nevertheless, it serves as a widely adopted parameter for categorizing different surface types. Surfaces with different roughness lengths give rise to varying turbulent stresses, consequently altering the profiles of mean wind velocity.

Similarly, different surfaces such as asphalt, grass, and water surfaces exhibit distinct behaviors in absorbing and emitting heat into the atmosphere due to variations in their thermal capacities and heat conductivities[4]. While this difference doesn't directly impact the logarithmic velocity profile, it does give rise to localized phenomena such as plumes, thermals, or downdrafts.

The presence of vegetation, particularly forested areas, significantly alters wind behavior[6]. Primarily, the forest acts as an obstacle impeding the normal flow of wind. If the foliage is dense enough, the logarithmic wind profile doesn't form from the Earth's surface but instead begins from a certain altitude known as the displacement height, which varies depending on the characteristics of the forest and the height of the trees[47].

Prior to reaching the forested area, there is typically a blocking phenomenon as the wind encounters the physical presence of trees. Upon traversing the forest, the flow often experiences acceleration, while beyond the forest, a wind shear zone emerges, intensifying mechanical turbulence within the ABL[16].

All the aforementioned factors, along with numerous others beyond the scope of this text, contribute to the formation of what are known as internal boundary layers (IBLs). These zones within the ABL arise precisely due to the evolving characteristics of the interface between the Earth and the atmosphere, as the flow gradually adjusts to them. While the vertical profile of mean wind is indeed modified within the IBL, it still adheres to the logarithmic trend. However, there may be more discontinuities in the vertical direction depending on the number of distinct IBLs that have developed and remain discernible at a given location.

3.4 How do we measure wind?[46]

Historically, wind data was recorded using ground weather stations or instruments mounted on meteorological towers, such as cup anemometers and wind vanes[44]. The main limitation of these instruments is that they must be positioned at most a few tens of meters above the ground and remain in a fixed location[88].

Nowadays, other instruments are typically used to measure wind speed profiles.

radar wind profilers (RWPs) represent a mature and integrated technology in meteorological data acquisition[48]. These instruments exploit the Doppler shift of a continuous radio frequency to obtain measurements of atmospheric wind speed and direction. RWPs have the significant advantage of providing wind speed data independent of meteorological conditions up to a height of 10-20 km, with a resolution typically ranging between 100 and 600 meters. RWPs provide measurements at sampling times on the order of minutes but require careful calibration and frequent maintenance. They can be subject to interference from other systems, large objects or atmospheric clutter, and the wind measurement relies on sophisticated post-processing algorithms of the recorded radio signal.

Additionally, sonic detection and ranging (SODAR) technology is employed for the purpose of obtaining a velocity profile. These instruments emit pulses of sound waves and measure the amplitude of the return signal, which is indicative of turbulent structures within the atmosphere[9]. These instruments are capable of measuring already at an altitude of a few tens of metres from the instrument, although they are commonly limited to approximately 1 km due to the strong absorption of sound waves by the air. The precision and accuracy of the measurements are susceptible to alteration by atmospheric conditions, with precipitation events having a detrimental impact on the quality of the acquired data.

A similar technology is doppler wind lidar (DWL). Instead of using radio frequency or sound waves, these instruments emit laser pulses and record the frequency shift of the scattered signal to calculate wind speed[68]. DWLs generally provide higher vertical resolution but are highly dependent on the presence of aerosol particles or dust that can scatter the laser beam back[59]. Consequently, good measurement accuracy is often limited to the height of the atmospheric boundary layer and is significantly reduced in completely clean air. DWLs are frequently used not only to perform vertical profiles but also to study the airflow behind wind turbines or within wind farms[94].

As a complement to these three remote sensing techniques, radiosondes are regularly used to profile the wind and other atmospheric variables up to the troposphere[28]. Radiosondes consist of a weather balloon filled with hydrogen or helium that, when released from the ground, travels several kilometers upward, carrying a set of specialized sensors that directly measure the variables of interest. The great advantage of radiosondes is that they provide direct measurements without the need for complex data processing algorithms. However, their deployment is weather-dependent, they can experience unexpected errors, especially at low altitudes, and it is impossible to control the trajectory of the probe, which is simply carried by the wind[29]. Additionally, there are environmental concerns, as it is not always possible to recover the payload of the radiosonde once it falls to the ground.

In this array of sensors and complex systems, the technology of weather-sensing UAS has emerged over the past decade as a cost-effective alternative to piloted aircraft for targeted measurements and, more recently, as automated tools for vertical profiling.

Figure 3.1: The MASC-3 UAS positioned on the catapult and ready to take-off. The sensorhood with the 5HP and the fine-wire thermometer is visible in the front, while on the wings is mounted an optical particle counter pod[74] (right wing) and an atmospheric charge sensor pod[73] (left wing). From Bramati et al. [15]

3.5 UASs at Umweltphysik group

3.5.1 Fixed-wing UASs

The first truly complete weather-research UAS platform built by the Umweltphysik group of the University of Tübingen is the MASC-3[67]. Built on the foundation of previous fixed-wing aircraft designed by the team, this system is considered the final version, featuring significant improvements in terms of design and efficiency (Figure 3.1).

The aircraft is 2.1 meters long with a wingspan of 4 meters and has a maximum take-off weight of about 8 kg. It features a V-tail configuration with a pusher engine located at the end of the fuselage. Powered by a 4S lithium-polymers battery, it has an average flight endurance of about 1.5 hours under normal flying conditions.

The autopilot system is a Pixhawk Cube Orange, running a stable version of the open-source Arduplane software. This software, together with third-party tools like Mission Planner, provides easy access to the main parameters defining the aircraft's behavior during flight operations. It also enables the programming of missions that the system will execute once the automatic mode is engaged. The autopilot is configured to maintain a true air speed (TAS) of approximately 19.5 m s^{-1}.

The scientific payload is positioned at the very front of the aircraft and includes a 5 holes probe (5HP), a fine wire thermometer, a temperature, pressure, and relative humidity sensor, and optionally a chilled mirror hygrometer. The sensorhood is the minimum payload required to obtain a reliable wind speed measurement with a temporal resolution of 100 Hz, which at the UAS cruise speed corresponds to a spatial resolution of approximately 20 cm. Additionally, various sensor pods can be mounted on both sides of the wings[73],[74]. The sensorhood's position at the foremost part of the UAS ensures minimal disturbance in the measurements from system components such as airfoils and the propulsion system.

Figure 3.2: The S900 (left) and X500 (right) UAS. The two systems have been modified through the incorporation of a spherical dome around the central frame. The bigger system has six rotors with the landing gears extending from the frame while the smaller has four rotors and the landing gears are positioned directly below the electric motors.

For the correct functioning of the 5HP, only uniform straight flight sections are relevant[66]. Sections where the UASs makes turns are useless for retrieving the wind vector. Consequently, there are two main data acquisition strategies. The first is called *racetrack*, consisting of a rectangular pattern with two longer sides called *legs*. The second is called *kite*, which involves flying the same straight line in opposite directions, making a U-bend at the end of each *leg*.

The calibration of the 5HP is performed at the cruising speed that the autopilot is programmed to maintain. This procedure is conducted in a wind tunnel, mapping 442 possible combinations of angles of attack and sideslip angles[65].

The estimation of the wind vector occurs during the data post-processing stage. This is because the system directly acquires the pressure data recorded by the 5HP and the respective high-frequency transducers without performing any conversion in real time. The precise calculation of the wind vector is achieved by merging data from all sensors used in the sensorhood, including an inertial navigation system that records the position, speed, and attitude of the aircraft in flight. A subsequent correction is also necessary to account for potential misalignment errors in the position of the 5HP. This correction is only possible after obtaining an initial estimate of the wind vector and selecting consecutive legs for analysis.

The MASC-3 platform was initially validated in Rautenberg et al. [67] and used in several other studies including a comparison with computational fluid dynamics models[23], a first identification of tip vortices behind a wind turbine[52], the development of new sensors [53],[74], for wind and turbulence studies in the ABL and in complex terrains[96],[97], for ABL research in arctic regions[72] and more recently for atmospheric electric charge measurements[73]

3.5.2 Rotary-wings UASs

S900

The S900 multi-copter was developed based on the DJI S900 hexacopter model. From the original model supplied by the manufacturer, the carbon fibre main frame, the six motors and the 14 inch propellers have been retained. A 500 mm diameter styrofoam sphere was added to protect the central part of the frame, attached to the six arms with velcro straps (Figure 3.2). The system is powered by two 12Ah batteries connected in parallel, it has a characteristic dimension (rotor-to-rotor distance) of 900 mm and a maximum take-off weight of approximately 8 kg. With this configuration, this UAS provides a flight autonomy of approximately 25 min.

The autopilot used in this system is a Pixhawk Cube Orange, running a stable version of the Arducopter software. This open-source autopilot is particularly crucial for this platform, as the wind vector analysis algorithm relies on the attitude data logged by the flight controller (as explained in Bramati et al. [14]). The autopilot logs the flight data at 10 Hz.

An array of six I2C protocol sensors was installed on the S900, with one sensor placed on each arm beneath the propeller disk to ensure proper ventilation. These sensors are housed within a special shield to protect them from solar radiation during flight. The sensor array is designed to operate with various sensor types, currently accommodating temperature, pressure, and relative humidity sensors (SHT31 by Sensirion and BME280 by Bosch), as well as CO_2 sensors. Data acquisition is managed by an ESP32 microcontroller, an SD card reader, and a multiplexer, which allows up to six sensors of the same type to be mounted and read simultaneously. These sensors are logged at a frequency of 2 Hz.

X500

This multi-copter, based on the commercially available frame of the Holybro X500, was designed and built to be a smaller and more compact version of the S900 (Figure 3.2). Its characteristic dimension is 500 mm with 10-inch propellers.

The basic configuration provided by the manufacturer has been significantly modified by designing new landing gear and a new battery compartment (4S, 7Ah). A spherical structure was also installed around the central part of the frame. This sphere was 3D printed with ultra-light material and held in place by magnets. In this configuration, the maximum take-off weight is 2 kg, providing a flight autonomy of approximately 20 minutes.

The choice of autopilot remained consistent with the use of a Pixhawk Cube Orange, ensuring continuity and reliability in the system's control and data logging. Wind vector estimation is carried out in a similar manner to the S900 system, leveraging the precise attitude data provided by the autopilot.

The sensor array philosophy has been similarly adopted for this smaller drone, with four sensors positioned on the four arms, each equipped with a solar radiation shield. Data acquisition is managed by an Adafruit Feather M0 Adalogger, which includes an integrated SD card reader. Due to space and weight constraints, a multiplexer was not utilized in this design, limiting the system to mounting only two sensors of the same model simultaneously. The default sensors equipped are two SHT31 and two BME280, providing essential atmospheric measurements with high precision.

Figure 3.3: The FW-XL10 UASs shortly after take-off. Due to the performance-oriented design, on this system was not possible to incorporate a spherical dome. In the picture it is visible, on top of the main battery, a safety parachute, used to reduce the ground risk during aerial operations.

FW-XL10

The most recent system designed and manufactured is called the FW-XL10 (Figure 3.3). This system uses a carbon fiber frame supplied by IFlight FW-XL10-V5, which has been slightly shortened in the middle part. While it has a similar size to the X500 with a characteristic size of 500 mm and 10-inch propellers, the FW-XL10 is a more powerful and efficient system due to careful optimization of the components.

The autopilot for the FW-XL10 is an mRobotics PixRacer Pro, on which a stable version of the Ardupilot software is installed. The aircraft is powered by a 6S lithium-ion battery with a capacity of 8 Ah, allowing for a maximum take-off weight of 2 kg. To ensure safety, the FW-XL10 is equipped with a parachute designed to slow the descent in case of a malfunction, granting a descent speed of 5.5 m s^{-1}. In this configuration, the system has demonstrated a flight endurance of 40 minutes.

The scientific payload consists of four sensors (two SHT31 and two BME280), similar to the X500 multi-copter. However, the payload system in the FW-XL10 is completely independent and powered by an 800 mAh battery, which can be activated via a switch. The wind vector estimation follows the strategy used in the spherical copters, with adjustments to account for the lack of symmetry of the FW-XL10 frame.

3.6 Scientific questions

The candidate's work in this thesis is centred on the topic of wind measurement using weather-research UAS. In particular, two macro-level topics can be identified:

- **Optimizing a rotary-wings UAS for wind measurements and meteorological applications**: In light of the practical operability and low cost of multi-copter systems, it is imperative that such systems undergo accurate calibration in order to ensure the precision of the wind measurements they produce, which must adhere to established standards. How might this feature of practicality and low cost be maintained for this calibration? What factors may potentially impact the quality of the wind retrieval? What are the performance limits of such systems in wind measurement? What are the operational limitations associated with the environment, and what potential applications may this emerging technology be applied for?

- **Using fixed-wing UAS for the validation of remote-sensing devices**: A comprehensive dataset acquired during multiple experimental campaigns is employed to assess the potential of fixed-wing UAS systems as reference sensors. This assessment is conducted through a systematic analysis and contextualisation of the system's capabilities, with the objective of validating remote sensing instruments for measuring wind (mean and fluctuating components). What are the advantages and disadvantages of comparing data from a moving sensor to a stationary one? Are there any factors that would preclude such a comparison? Are there any technological or environmental factors that could potentially influence the quality of the comparison?

The scientific issues are different depending on the system used, particularly given that the rotary-wing fleet was developed and expanded during the applicant's period of activity, whereas the MASC-3 technology was already well established. Consequently, the subjects addressed and the experiments conducted with multi-copters are of a more technical nature than those concerning the strictly scientific analysis of the MASC-3 data. The three scientific papers forming the core of this thesis seek to address these questions. With regard to the multi-copter, a significant proportion of the scientific questions have been addressed by a substantial body of experimental data that has been collected but not yet published. These latest results and examples are discussed in detail in chapter 4.

Chapter 4

Results

This chapter offers a brief summary of the principal findings presented in this dissertation, which are discussed in greater detail in the attached peer-reviewed publication.

4.1 Optimizing rotary-wing UASs for wind measurement

Multi-rotor UAS systems are increasingly popular today, largely due to their versatility in planning automated missions and the ease of deployment in a short timeframe. The acquisition of measurements of thermodynamic variables, including pressure, temperature, and humidity, is a relatively straightforward process when using rotary-wings UAS, due to the availability of integrated sensors that can be easily located on board. Conversely, the accurate estimation of wind speed and direction represents a significant challenge for these systems[1].

The significant advantage of UASs of this type lies in their ability to maintain a fixed position during flight – a condition commonly known as hovering – making them ideal for conducting vertical profiles and/or acquisitions near sensitive structures. However, it is precisely this characteristic that complicates the task of acquiring wind speed and direction. The multi-rotor itself substantially alters the wind field around it[27], so that traditional sensors such as Pitot probes, 5HPs[64], or sonic anemometers[90] become ineffective if they are not positioned at a sufficient distance from the rotors[35].

This is why a commonly employed strategy for estimating horizontal wind is the tilt angle method[56],[93]. This method relies on fundamental aerodynamic principles, specifically the concept that an object located in a fluid with a certain speed generates a force parallel to the fluid's velocity, known as drag[3]. In the scenario where a multi-copter is hovering, the atmospheric wind will induce a drag force on the system that the UAS has to balance. The only means by which a multi-rotor system can generate this force is by adjusting its orientation. In doing so, a portion of the force produced by the rotors (thrust), typically oriented vertically in calm conditions, is redirected onto the horizontal plane to balance the drag. In this scenario, with data from the autopilot regarding the attitude of the UAS, we can calculate the tilt angle (refer to Figure 4.1a), which increases with higher wind

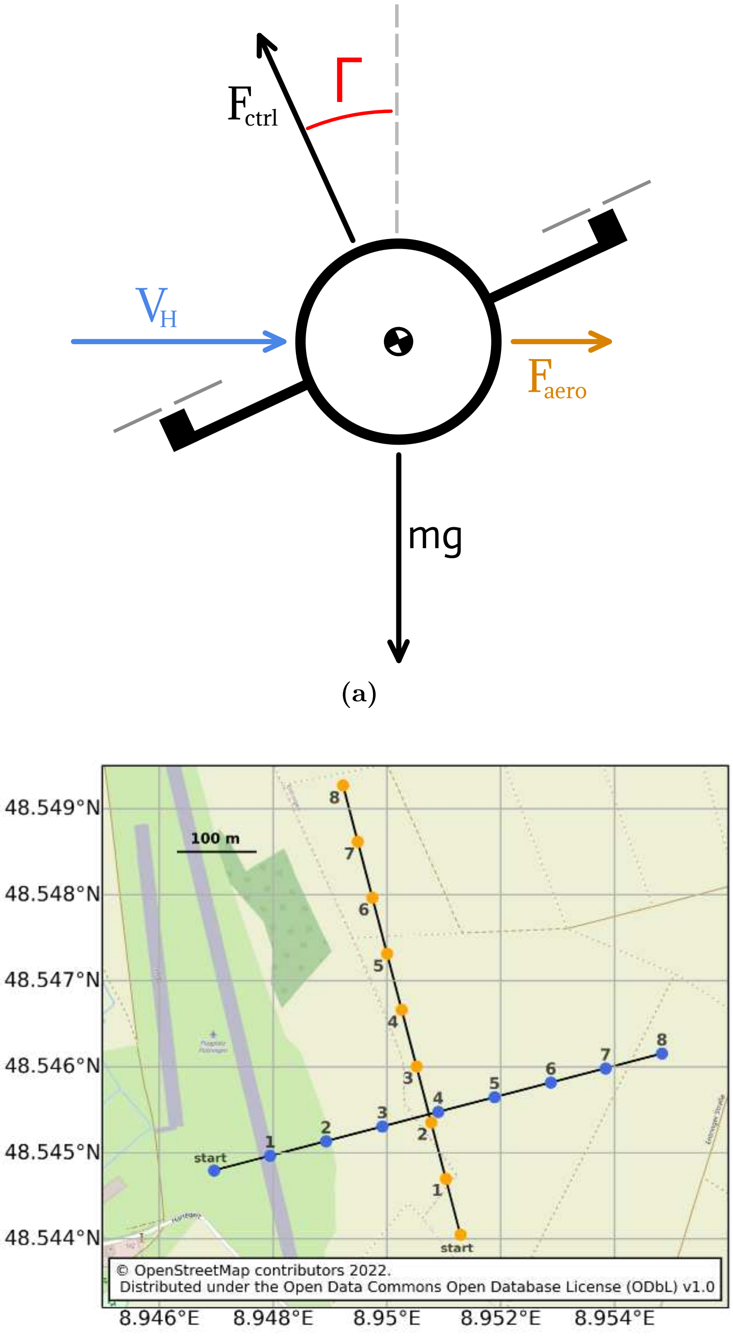

(a)

(b)

Figure 4.1: **a)** Representation of the forces acting on a multi-rotor while hovering. Γ is the tilt angle. **b)** Example of UAS mission (collection of waypoints), for the calibration flights. From BRAMATI et al. [14].

speeds.

The equation relating wind speed and tilt angle is readily obtained from the dynamics equations of the UAS and by modelling the drag force using the Reynolds equation[38]:

$$V = \sqrt{\frac{2mg\tan(\Gamma)}{\rho A_0 C_\mathrm{A}(\Gamma)}} \tag{4.1}$$

In this equation, m represents the mass of the multi-copter, g is the Earth's gravitational field, ρ denotes the density of air, and A_0 stands for a reference characteristic area specific to the UAS under examination. The term C_A is defined as:

$$C_\mathrm{A} = \frac{A(\Gamma)}{A_0} \cdot C_\mathrm{D}(\Gamma) \tag{4.2}$$

It encompasses UAS-related variables that are challenging to model accurately. Specifically, the cross-sectional area – representing the area exposed to wind – is inherently difficult to quantify, particularly as it varies with the inclination of the UAS. Similarly, the drag coefficient C_D follows the same pattern of variability.

After formalising the above-mentioned models and equations in detailed steps, Bramati et al. [14] deals with three different aspects of this method, described in the following sections.

4.1.1 Calibration strategy

To derive a calibration curve for equation 4.1 and thereby estimate wind speed from the multi-copter's tilt angle, it is essential to gather a dataset where both V and Γ are known. Typically, this involves conducting either wind tunnel tests[56] or in situ experiments near a sonic anemometer[17].

Wind tunnel testing presents some drawbacks such as high cost, spatial limitations that may not accommodate all UAS types, and potential biases introduced by wall effects. Conducting tests in real-world environments near sonic anemometers also poses challenges. Primarily, the inability to control wind speed is a significant drawback as the calibration is likely to be constrained to the wind speed range encountered during the day of the calibration flights.

To achieve a consistent mapping of tilt angle versus wind speed, our study introduces a strategy involving straight-line flights at different ground speeds conducted in low atmospheric wind conditions (see Figure 4.1b). In such a way, the stationary part of the straight flights can be representative of an hovering state, where the wind speed is essentially the ground speed. This approach is complemented by a post-processing algorithm capable of adjusting the calibration curve, even in the presence of wind during the flights. The methodology simply requires the capacity to fly in a sufficiently large open space, the size of which is determined by the maximum speed the user intends to calibrate. This method ensures minimal costs and a calibration curve tailored to the user's requirements, ensuring a uniform dataset across the entire flight envelope of the UAS.

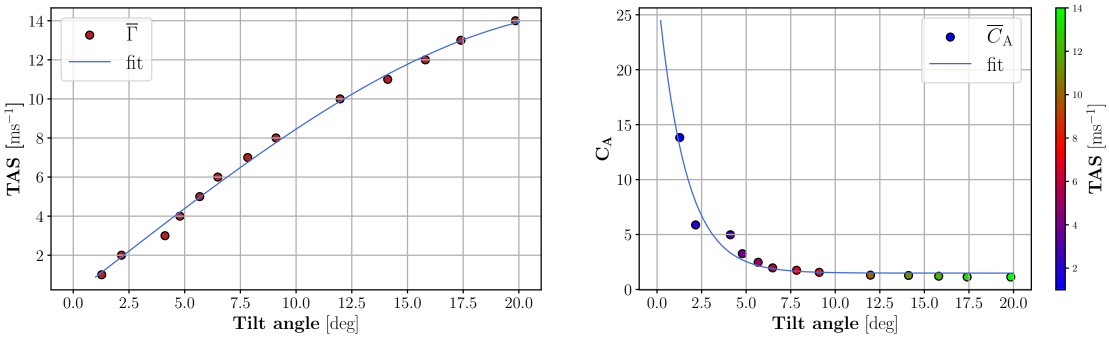

(a) (b)

Figure 4.2: The two different calibration models proposed in the publication. TAS stands for the true air speed of the copter during the calibration flights. This represents the atmospheric wind speed when the copter is hovering. From Bramati et al. [14].

4.1.2 Calibration model

When dealing with equation 4.1, there are two approaches upon obtaining a dataset of tilt angle versus V. The conventional method involves directly calibrating the relationship between these two variables, treating all factors to the right of the equation as unknown.

In contrast, the strategy proposed in this study suggests calibrating the term C_A, which is inherently linked to the specific UAS and remains the sole unknown component. This approach eliminates the dependency of the calibration curve on multi-copter mass and air density. Two distinct calibration curves were derived from the identical dataset of calibration flights (see Figure 4.2) for the modified DJI S900 UAS. Subsequent validation flights conducted near a sonic anemometer confirmed that both strategies yield comparable results in terms of precision and accuracy. Consequently, for ensuring an unbiased estimate, the preferred strategy is to use the C_A model. This approach accounts for potential variations in the UAS payload and the different environmental conditions the system may encounter throughout the year.

4.1.3 Directional independence and sensitivity enhancement

A notable modification to the conventional DJI S900 configuration employed in this study was the incorporation of a circular sphere around the frame of the UAS. This styrofoam sphere offered several benefits, including protection of the electronics and battery components against weathering and minor impacts.

However, the primary advantage provided by this addition was twofold in enhancing wind measurement acquisition. Firstly, a sphere inherently has isotropic properties, ensuring a consistent response to drag forces irrespective of the system's orientation relative to the wind direction. Consequently, there is no need for the *wind-vane* mode wherein the UAS must align itself with the wind direction before accurate measurements can be obtained.

Secondly, we demonstrated that the usage of this sphere increases the absolute value of the cross-sectional area, consequently augmenting the multi-copter's re-

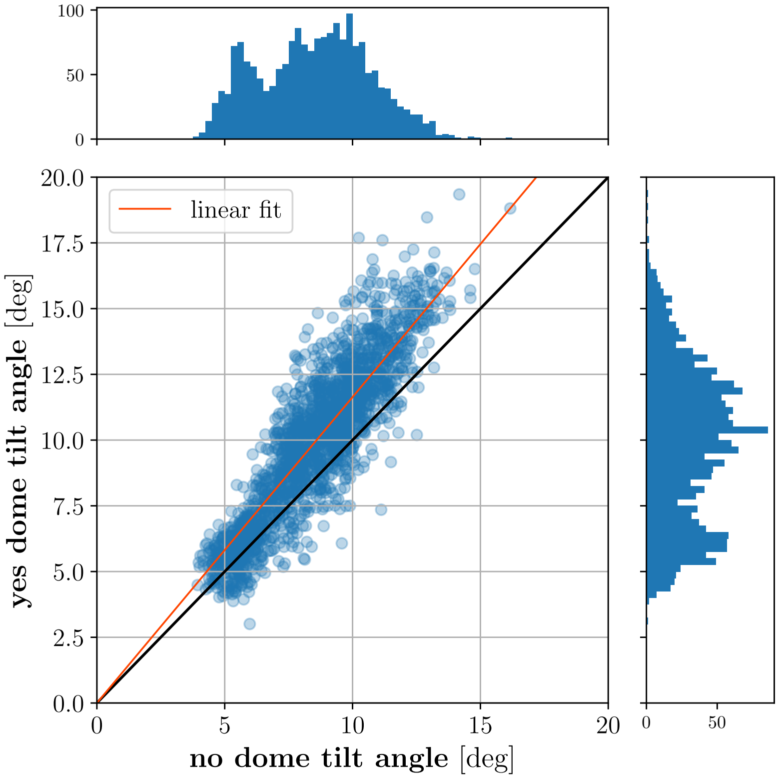

Figure 4.3: Comparison of tilt angle values obtained with two multi-copters of the same type flying simultaneously, one with the styrofoam sphere and one without. From Bramati et al. [14].

sponsiveness to atmospheric wind loads. Essentially, for identical atmospheric wind conditions, a system with a larger cross-sectional area necessitates a greater tilt angle. This translates to an enhanced sensitivity of the system, functioning as a sensor, to its inputs. In our study, we observed an approximate 16.5% increase in sensitivity with the incorporation of the sphere on the UAS frame.

4.2 Fixed-wing UASs for remote-sensing instruments validation

As part of the VALUAS project (Validation of remote sensing and numerical simulations of the deutsche wetterdienst (DWD) using UAS), three intensive observation periods (IOPs) were conducted at the boundary layer field site in Falkenberg site close to the MOL-RAO (Meteorological Observatory Lindenberg-Richard-Aßmann-Observatory). Several permanent instruments are installed in Falkenberg, including a 99 m height meteorological tower, providing a comprehensive dataset to study the so called *Lindenberg Column*[55]. These experimental campaigns took place over several consecutive weeks in different years (July 2020, June 2021, and November 2022) and involved the use of various types of weather-research UAS to collect data for comparison with more traditional measurement techniques as well as with newly installed DWL. In particular, the June 2021 campaign coincided with the FESSTVaL (Field Experiment on submesoscale spatio-temporal variability in Lindenberg) campaign, which saw multiple research teams collaborating to provide in situ measurements of the lower ABL.

4.2.1 Mean wind

In BOVENTER et al. [13], the dataset of the three IOPs of the VALUAS project were used to validate, under different operating conditions, the 10 minutes mean wind vector estimates of two DWLs (doppler wind lidar 143 and doppler wind lidar 177) installed and used by the deutsche wetterdienst. A detailed description of the LiDAR systems can be found in the aforementioned publication, here attached in the appendix.

The MASC-3, with its endurance of one and a half hours and ease in reaching altitudes around 2000 meters agl, ensured excellent efficiency in acquiring this type of data. Additionally, the typical issues related to the physical space required for take off and landing did not arise, as the measurement site is located in the countryside, surrounded by sufficiently large meadows. As a matter of facts, during these experimental campaigns, the MASC-3 UAS was successfully operated in more than 140 flights. This fixed-wing system operates a more complex data acquisition strategy compared to a multi-rotor UAS type. Since it must maintain a certain velocity relative to the surrounding air to generate the necessary lift for flying, a typical acquisition strategy involves flying straight segments of arbitrary ground length aligned with the wind direction (Figure 4.4). Each of these straight segments is usually referred to as a *leg*. To remain within the correct calibration range of the main wind measurement sensor (5HP mounted at the very front of the system), the MASC-3 is programmed to maintain a constant TAS of approximately 19.5 m s^{-1}. In this way a leg represents a snapshot of the wind conditions along the segment covered by the leg. The data collected with the weather-sensing UAS were used for several validation steps. The first step was to validate the UAS system itself against the cup anemometers and wind vanes installed on the meteorological tower at 98 m agl as a reference. For this type of validation, three different time averages were used: the average time of a single leg, 10 minutes, and 30 minutes.

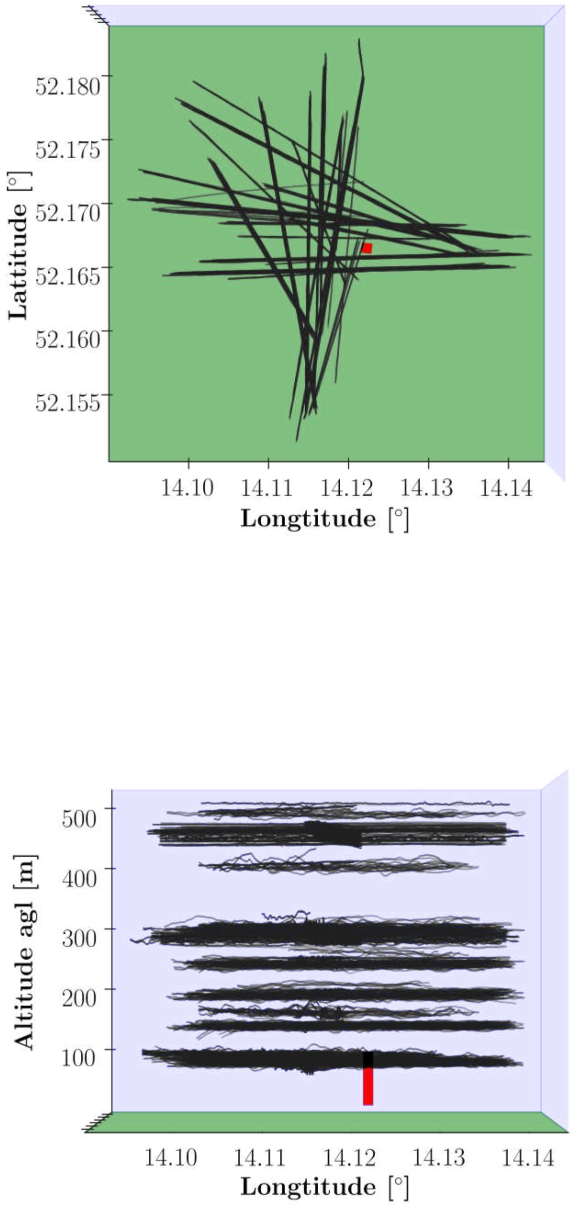

Figure 4.4: Representation of all the flight legs used for the mean wind vector analysis of the VALUAS project. The red column represents the Falkenberg meteorological tower. A consistent amount of legs are located around 99 m altitude which corresponds to the top of the tower itself. The height of the remaining legs has been chosen to match the scanning heights of the two DWLs systems. From BOVENTER et al. [13].

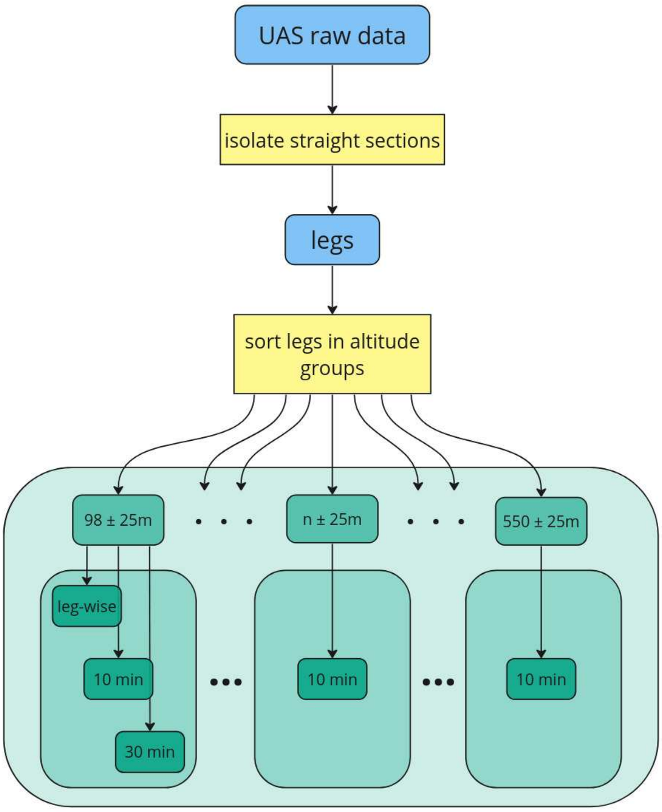

Figure 4.5: Flowchart of data processing. Only the legs at 98 m altitude have been grouped into three different time averages in order to study accuracy and precision of the MASC-3. For the UAS vs DWL comparison only 10-minutes averages have been used from all the available legs at different altitudes. From BOVENTER et al. [13].

Table 4.1: Statistical measures describing the quality of the MASC-3 UAS as horizontal wind vector sensor. RMSD represents the root mean squared deviation, MBD the mean bias deviation while R the Pearson correlation coefficient. The subscript v refers to the wind speed while ϕ to the wind direction. From Boventer et al. [13]

Wind speed

Averaging period	Number of data pairs n	RMSD_v	R_v	MBD_v
leg-wise	230	0.194	0.935	-0.018
10 minutes	54	0.137	0.971	-0.007
30 minutes	10	0.143	0.991	0.037

Wind Direction

Averaging period	Number of data pairs n	RMSD_ϕ	R_ϕ	MBD_ϕ
leg-wise	197	17.5°	0.982	4.7°
10 minutes	47	13.5°	0.987	3.3°
30 minutes	8	9.9°	0.989	2.7°

Once the accuracy and precision of the MASC-3 had been confirmed, the second part of the study involved validating the two DWLs by considering different operational parameters. For this purpose, data at all flight altitudes between 98 and 550 m agl were grouped into 10-minute averages to match the data format of the two DWLs. The breakdown of the data into different time averages is summarized in Figure 4.5.

An important parameter to consider when comparing two sensors, one stationary and one in motion as in our case, is what it was labeled as the *fetch angle.* It indicates how closely the trajectory of the UAS aligns with the direction of the atmospheric wind. Considering that the MASC-3 provides measurements of a spatially distributed dataset, the fetch angle indicates how much of that same air mass is effectively measured over time by the stationary sensor. The closer the fetch angle is to zero, the more these two sets of measurements will correspond to the same mass of air containing the same quantities. However, it's not always possible or easy to align the flight trajectory with the wind direction during flight. Therefore, in the initial phase of data filtering, a compromise was made between retaining a significant number of flight legs and discarding those legs with excessively high average fetch angles. The acceptance limit was set at 39.3° as legs with larger fetch angle values showed higher scatter in the wind speed magnitude when compared with the cup anemometers.

Once this filter was applied, the results of the validation of the weather-research UAS showed a progressive improvement in precision and accuracy in measuring the wind vector as the averaging time increased from leg-wise to 10 minutes. The results for the 30-minute average were considered unrepresentative due to being based on a sample of fewer than a dozen data points. The conclusion of this first part of the validation was to define the accuracy and precision of our UAS in terms of 10-minute wind retrieval as reported in Table 4.1. The next and most important part of this study shifts its focus to using the MASC-3 to validate the two DWLs systems. Initially, all available data were used to calculate any bias and/or scatter. Subsequently, the analysis was limited to conditions in which both DWLs were active simultaneously to obtain a comparison of the accuracy and precision of the two systems against each other.

In a further analysis, the flight legs were grouped into altitude ranges to check for any anomalous behavior exhibited by the two DWL at different altitudes. This analysis did not reveal any significant anomalies. On the contrary, as expected, the precision and accuracy of one of the DWLs improved where the laser beam was focused.

In the final part of the study, the analysis focused on the stability conditions of the ABL. The Bulk Richardson number was chosen to characterize different regimes. Fortunately, with data available from three different years and different seasons, the dataset covers a wide range of stability regimes. Due to the limited availability of data for the DWL143 system, the stability analysis was only performed for the DWL177 system. As expected, precision and accuracy improved as the stability of the system increased, and these metrics were even better than those of the MASC-3 system.

In conclusion, this study has demonstrated that the use of a fixed-wing UAS can effectively collect useful data in a variety of situations where traditional sensors struggle to achieve the same precision and accuracy. For average values of the wind vector, which tend to vary on a timescale greater than 10 minutes, it is sufficient to correct the data from the UAS based on the fetch angle parameter.

4.2.2 Turbulence

The same data set from the project VALUAS was employed in BRAMATI et al. [15] to investigate the feasibility of a comparative analysis between the weather-research UAS and a DWL in the context of turbulent quantities. Among the numerous sensors employed by the DWD during the three experimental campaigns there was a DWL capable of providing an estimate of the turbulent kinetic energy (TKE) with a temporal resolution of 30 minutes.

The MASC-3 data were processed and filtered in accordance with the methodology previously outlined in BOVENTER et al. [13], specifically by filtering the legs according to the so-called fetch angle using the same treshhold of 39.3°. The study of turbulent quantities poses additional challenges with regard to post-processing and comparison of data from two different sensors. Consequently, this study essentially corresponds to the first part of the previous study focused on mean wind. The objective at this initial stage was to quantify the accuracy and precision of the MASC-3 UAS in measuring TKE.

TKE is defined as the sum of the averages of the three fluctuating components of the wind speed squared and it can be obtained from the each and every UAS leg as:

$$k = \frac{1}{2} \cdot [\mathrm{Var}(u) + \mathrm{Var}(v) + \mathrm{Var}(w)] \tag{4.3}$$

The TKE measured by the MASC-3 was compared with a sonic anemometer mounted at 98 m agl on the Falkenberg meteorological tower which served as the reference instrument.

A challenge arises when comparing turbulent quantities, as these must be calculated for each individual leg, as this alone constitutes a coherent time series of

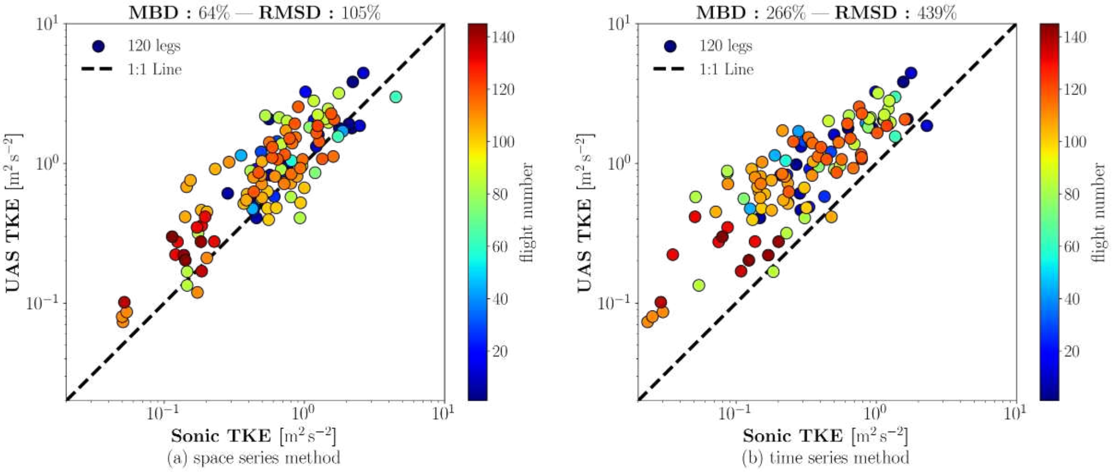

(a) space series method

(b) time series method

Figure 4.6: Comparison between TKE measured by the sonic anemometer and the MASC-3. Each of the scatter points corresponds to one leg. a) comparison performed with the correct amount of air for the sonic anemometer, b) comparison performed by simply considering the sonic and UAS time series cut with the start and end time of each leg. From Bramati et al. [15].

the state of the atmosphere. The combination of consecutive legs would result in the introduction of artificial frequency contributions, which would have a detrimental impact on the TKE calculation. From the perspective of UAS data, this is a relatively straightforward process, as the data format is limited to straight flight sections. However, we have opted to consider only those legs that are referred to as upwind, which are those where the MASC-3 flies against the wind. These legs are the longest in terms of time and, according to Lenschow, Mann, and Kristensen [49], guarantee a lower systematic statistical error.

In a second stage it is necessary to consider the type of comparison to be made with a static sensor. It is not possible to use as boundaries of the time series of the static sensor the beginning and end of each leg, since the UAS, moving an average of 1.8 km in its flight path, will sample a much larger amount of air than that recorded by the sonic anemometer. It is necessary to wait for the air mass measured by the UAS to be advected over the static sensor. This study delineates a methodology for identifying the optimal boundaries for the sonic anemometer time series. The identification of start and end of the sonic anemometer data is achieved by transforming the time series of both sensors into a space series and performing a cross-correlation between them. It is crucial to highlight that the efficacy of this procedure hinges on the fulfilment of two important assumptions: a zero fetch angle and the Taylor hypothesis of frozen turbulence. In the present case, both hypotheses are not strictly satisfied. The fetch angle hypothesis has been relaxed as it is practically impossible to perfectly align the MASC-3 trajectory with the wind direction, whereas the Taylor hypothesis has yet to be verified and represents one of the scientific questions addressed by the study. Nevertheless, the data displayed in figure 4.6 demonstrated that the utilisation of this algorithm markedly enhanced the comparisons between UAS and sonic, thereby effectively eliminating a large bias that was due to an erroneous amount of sampled air.

The persistence of a consistent bias and scatter in the comparison necessitated

Table 4.2: MBD and RMSD between UAS measurements and sonic anemometer measurements for the different wind directions. From Bramati et al. [15].

	E		**S**		**WNW**		**NNW**	
	MBD	RMSD	MBD	RMSD	MBD	RMSD	MBD	RMSD
TKE	59%	78%	21%	53%	68%	103%	97%	151%
Var(u)	37%	51%	43%	63%	55%	101%	97%	160%
Var(v)	92%	129%	-4%	59%	81%	147%	85%	142%
$\mathbf{TKE_H}$	59%	76%	13%	47%	62%	103%	87%	136%
Var(w)	62%	87%	51%	95%	92%	134%	122%	195%

further analysis. The division of the leg data with respect to the atmospheric wind direction demonstrated that the comparison statistics are significantly influenced by this latter variable. It was found that no other environmental or **wuas!** (**wuas!**) flight-dynamic parameter exerted a comparable influence to that of the atmospheric wind direction. An analysis of the UAS leg map in Figure 4.7 and the statistical breakdown for different incoming wind directions in Table 4.2 revealed that the best statistical outcomes occurred when the wind originated from the south. This region is characterized by cultivated fields and predominantly flat terrain, with altitudes slightly below the 73 m agl of the Falkenberg site. In contrast, the least favourable statistics were observed when the wind came from the west and north, areas with a high proportion of forest cover and at altitudes exceeding that of the Falkenberg site.

The initial conclusion of our study, which corroborates the findings of numerous previous publications[5],[11] and the results of the LITFASS[10] project, is that the terrain surrounding the Falkenberg test site is heterogeneous. The presence of a forest in the north-west inevitably results in a higher level of turbulence in the ABL. This additional contribution is present in the UAS data, particularly when the aircraft flies in proximity to the forest, yet is not recorded by the sonic anemometer on the meteorological tower. Therefore, it can be concluded that Taylor's frozen turbulence hypothesis is not satisfied. This implies that the precision and accuracy of the MASC-3 as a reference sensor for the DWL is not constant but is a function (at least in the first order) of the wind direction and, consequently, the direction of flight. It is thus not possible to definitively establish these two fundamental parameters for the MASC-3 in this context.

It is important to note that the observed result does not indicate any inherent limitations of the weather-sensing UAS system or its inability to accurately measure atmospheric turbulence. Conversely, the system has been validated in numerous studies with regard to the feasibility of measuring atmospheric eddies. The findings of this study indicate that it is not advisable to utilise a fixed-wing UAS for the validation of turbulence-related measurements of static sensors in heterogeneous terrain. This is due to the fact that such an approach may result in the measurement of a greater number of eddies than would be recorded by the aforementioned static sensor.

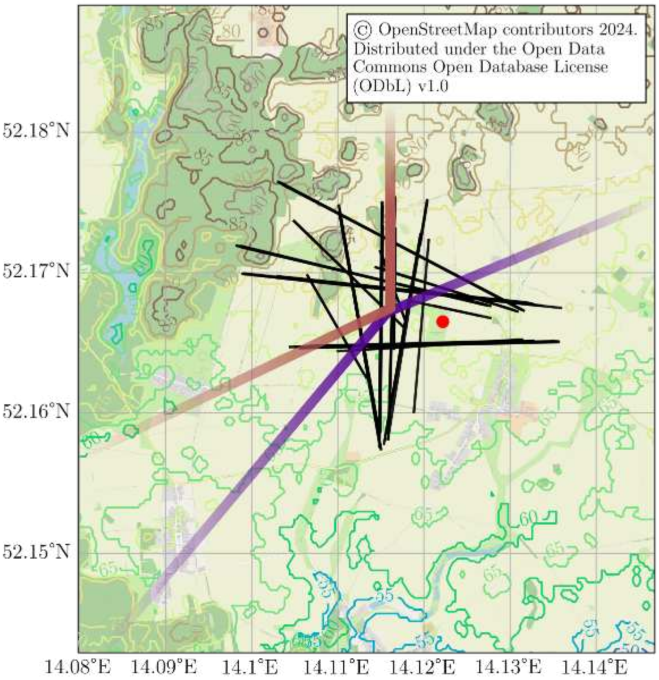

Figure 4.7: Map including all the legs and the two main wind direction sectors. The purple sector spans from 140° to 220° and includes the E (6 legs) and S (24 legs) wind direction groups: it is characterized by flat cultivated land and a lower elevation than the Falkenberg tower. The red sector spans from 240° to 360° and includes the WNW (47 legs) and the NNW (25 legs) groups: it is characterized by forest patches and a higher elevation than the Falkenberg tower. From Bramati et al. [15].

Chapter 5

Discussion

5.1 Validating remote sensing devices with fixed-wing UASs

The validation of sensors such as DWLs or other remote sensing instruments that profile thermodynamic variables in the lower ABL can be effectively conducted in situ using fixed-wing UAS systems. This approach, demonstrated in Boventer et al. [13], provides reliable results for time-averaged values the wind speed vector.

However, fixed-wing UASs are unique in the range of the meteorological instruments due to their horizontal movement at a velocity relative to the wind – the very quantity they aim to measure. This characteristic can be highly advantageous for mapping extensive areas both horizontally and vertically. Nonetheless, it also introduces significant challenges when these systems are compared with static sensors.

The main issue lies in the fact that a static sensor and a dynamic sensor, which moves relative to the wind, will only record the same values under two precise conditions: assuming the wind remains unchanged (i.e., stationary conditions) and assuming the UAS flight direction is perfectly aligned with the wind direction (fetch angle ≈ 0). While the first condition could be considered valid for short time intervals (no more than 10 minutes), realigning the flight direction with the wind direction during flight is extremely challenging for operators and sometimes entirely impossible due to flight area limitations. Additionally, at different altitudes, the wind direction tends to change constantly (Ekman spiral), further complicating the task of maintaining alignment with the flight track.

There is, therefore, no definitive method to avoid this problem either in situ or during post-processing. The only viable solution is to accept a margin of error and find a compromise between the number of flight legs to be discarded and the maximum fetch angle to be included in the *acceptable* data. This approach allows for a balance between retaining enough data for meaningful analysis and ensuring that the data included provides a reasonably accurate representation of the wind vector.

If this compromise works well for temporal averages of about 10 minutes, the problem becomes even more complicated when the subject of comparison is atmospheric turbulence. As explained in Bramati et al. [15], it is essential that quantities related to turbulent air motion are calculated on exactly the same air mass by both sensors. Ideally, this would require a null fetch angle and, in addition, the assumption that Taylor's frozen turbulence condition is met, meaning that turbulent statistics calculated over space and time variables yield identical results.

The method for identifying the correct air mass to be considered for the two types of sensors, as formalized in BRAMATI et al. [15], proves to be of considerable help but could be improved by more accurate planning of the flight mission. By fixing the beginning or end of each leg at the location of the static sensor, one would have a pivot point where the two time series are known to coincide. This approach eliminates the need to use the autocorrelation of the series provided by the two different systems each time. This strategy has already been used by RAUTENBERG et al. [67] and allowed for the comparison of the fixed-wing UAS MASC-3 with sensors mounted on a meteorological tower.

Moreover, since atmospheric turbulence is an extremely local phenomenon, the terrain in the flight area must be as homogeneous as possible. Obstacles like buildings or forests, as well as the different heat capacities of various types of soil, can easily generate local turbulent eddies that might be recorded by the UAS along its flight trajectory but, for one reason or another, are not advected towards the static sensor. In other words, the Taylor hypothesis never holds over heterogeneous terrain. The excellent results shown in RAUTENBERG et al. [67] were indeed obtained under highly stable atmospheric conditions over flat, homogeneous terrain (ice surface). If these conditions are not met, the UAS would, at best, measure the same turbulent statistics, but most likely it will overestimate them, as was the case for the experiments analyzed in BRAMATI et al. [15]. This does not necessarily mean that the MASC-3 provides incorrect data of turbulent quantities in the atmosphere, but simply that it is probably not the most suitable instrument for this specific type of validation under these environmental operating conditions.

5.2 Further insights on rotary-wings UASs wind measurements

5.2.1 Drag coefficient

The drag coefficient-based wind estimation model offers the significant advantage of being independent of parameters such as multi-copter mass and air density. This means that the system can be used consistently without the need for extensive post-processing corrections, regardless of the payload or variations in air density (such as altitude or seasonal changes). This represents a considerable improvement over the simpler tilt method proposed by NEUMANN and BARTHOLMAI [56].

Moreover, an interesting aspect worth exploring is whether similar multi-rotors exhibit comparable $C_{\mathrm{A}}(\Gamma)$ functions. Since both the X500 and S900 systems were constructed and adapted with the same design philosophy, it was possible to obtain a comparison by applying the same calibration procedure. The results, as shown in Figure 5.1, reveal that despite the significant size difference between the two systems, the $C_{\mathrm{A}}(\Gamma)$ functions have very similar values, particularly at tilt angles greater than 10 degrees. The largest discrepancies occur between 5° and 10°, likely

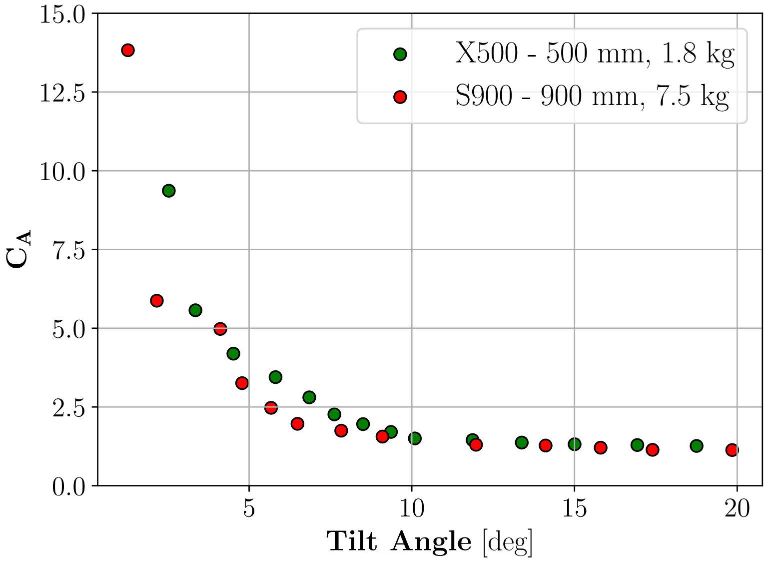

Figure 5.1: Comparison of the C_A coefficient obtained experimentally for the two copters of different size. The values of this parameter are particularly similar for both systems especially for tilt angles (and therefore wind speeds) exceeding 9-10°.

attributable to differences in the number of rotors and landing gear configurations between the two systems.

Thus, the incorporation of a spherical structure around the main body of the multi-copter not only enhances its sensitivity to atmospheric wind inputs but also defines a unique cross-sectional area value A_0, useful for normalizing the multi-copter's drag coefficient. This development paves the way for establishing a single $C_A(\Gamma)$ calibration curve applicable across systems of varying sizes and weights, thereby streamlining the deployment of a multi-purpose rotary-wings UAS fleet.

5.2.2 Turbulence

One pertinent question arises: how rapidly can wind be sampled using multi-copters? An initial insight is provided in Bramati et al. [14], where it is observed that the S900 wind estimate aligns with the power spectral density of the sonic anemometer up to approximately 10^{-1} Hz. Moreover, by conducting simultaneous flights alongside a sonic anemometer, the X500 and S900 systems were compared, revealing their respective power spectral densities, as depicted in Figure 5.2. Once again the S900 system deviates from the sonic anemometer's performance around 10^{-1} Hz, while the smaller and lighter X500 system seems to adhere to a similar trend, at least down to 1 Hz. These findings suggest an increase in valid sampling frequency as the mass of the multi-copter decreases. This observation is further supported by Wildmann and Wetz [95], where even lighter multi-copters exhibit similar resolution of turbulent eddies. However, it's important to note that the UASs utilized in this recent study have a flight endurance of only 15 minutes under optimal conditions. Therefore, with current technology, there exists a trade-off between the capability to resolve atmospheric turbulence and flight duration.

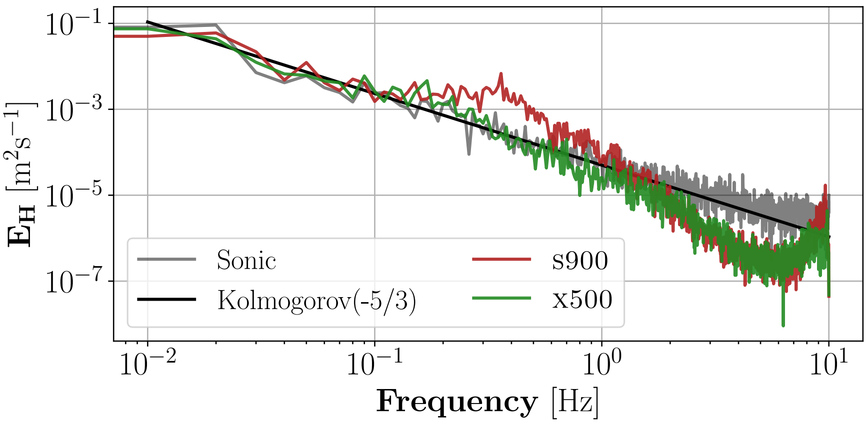

Figure 5.2: Comparison of the power spectral densities of the two copters of different size and weight, plotted together with a sonic anemometer spectrum and the Kolmogorov -5/3 decay law.

5.2.3 Case studies

This section presents several case applications where multi-rotor systems were used in diverse fields of research. The examples provided are not exhaustive of each research field but are intended to demonstrate how rotary-wing platforms serve as useful tools in numerous scientific disciplines.

Wind energy applications

The S900 system was used in a brief experimental campaign to map the horizontal plane of a wind turbine (WT)'s wake. The campaign focused on the Enercon E-82 E2 wind turbine, located at coordinates 48°24'14.8"N, 8°33'31.0"E, in the village of Schopfloch, Baden-Württemberg. This turbine, owned by Windkraftanlage Schopfloch/EnBW, has a rated power of 2 MW, a hub height of 138.4 meters agl, and a rotor diameter of 82 meters. Built in 2012, the turbine is depicted in Figure 5.3a.

The flight, conducted on 15 October 2021, involved 16 hovering points of 60 seconds each arranged in rows of four at varying distances behind the main rotor, starting ad half radius distance, all at the converter's hub height. One of these points was positioned outside the turbine's wake, while the other three in the same row were intended to capture the wake. As seen in Figure 5.3b, the multi-copter successfully captured the mean wind vector during this mission, highlighting typical characteristics of the near wake of a turbine. In the first row of points behind the turbine, the wind vector shows a lower modulus at the two points located at half of the radius distance from the center of the rotor, a typical phenomenon of the near wake where the velocity deficit forms a characteristic W-profile. Due to the imperfect alignment of the hovering points with the direction of the wake, it is difficult to determine how the wake has developed at the second rows of hovering points. However, it is likely that near-wake structures are still present because of the short distance behind the rotor (1D).

As already mentioned, the alignment of the mission with the turbine itself was

(a)

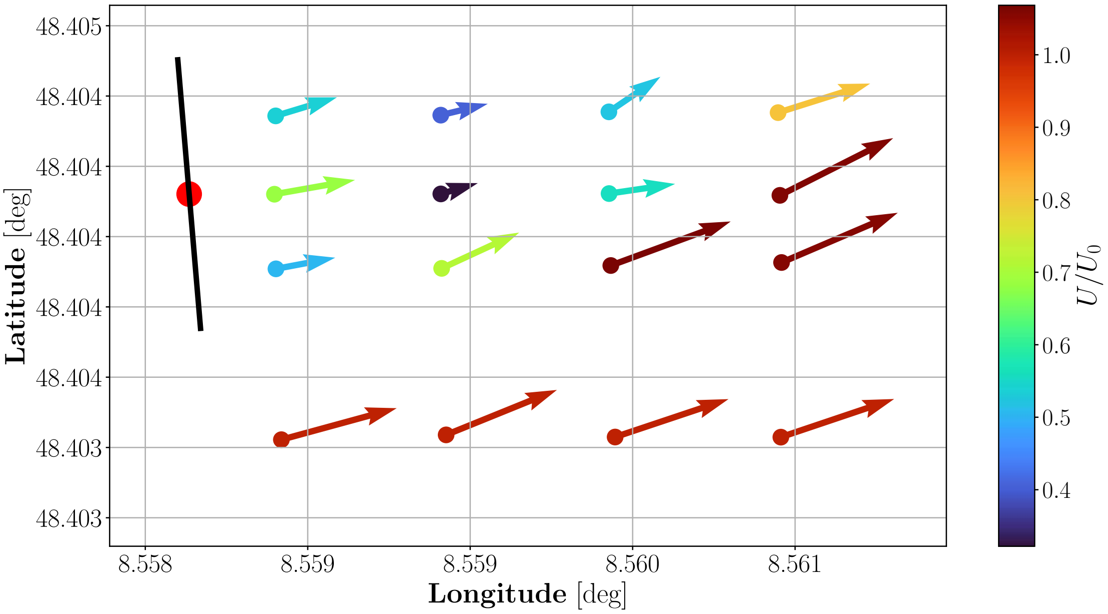

(b)

Figure 5.3: **a)** Wind turbine in Schopfloch, Baden Württemberg. **b)** Horizontal mapping of the Schopfloch wind turbine wake obtained during a S900 UAS mission.

Figure 5.4: The X500 UAS shortly after take off from the maintenance vessel inside the Rødsand II wind farm. For this specific missions the UAS has been equipped with floating bags inside the spherical dome and on the four arms, in order to grant buoyancy in case of landing on water.

not entirely successful, resulting in the multi-copter exiting the wake area in the last two rows. A slight increase in wind speed can still be observed near the boundaries of the wake.

As well as providing scientific insights, this mission also suggests that, given the unpredictable yawing of the turbine rotor, a cone-shaped mission should be adopted to map its wake, either to compensate for possible misalignment or simply to take into account the fact that the wake itself widens as the distance from the rotor increases. This experiment also confirms the safety and feasibility of flying and measuring very close to the wind turbine, maintaining a distance of just over 20 metres. Such proximity would be extremely dangerous to achieve using the MASC-3 system, especially considering the sudden change in TAS that the fixed-wing system would experience by entering the wake. Therefore, multi-rotors are more suitable for studying near-wake phenomena of wind turbines. These phenomena are of significant interest to researchers, who are constantly striving to create accurate analytical models. Real-world data from full-scale environments, as opposed to small-scale wind tunnel experiments, are increasingly needed for such research.

Another interesting case study involved a two-day experimental campaign on board a maintenance vessel used by RWE for turbine repair operations at the Rødsand II wind farm. This wind farm consists of 90 turbines, each with a capacity of 2.3 MW, a tower diameter of 90 meters, and a hub height of 69 meters. Using the X500 system, which was chosen due to limited space for take-off and landing, initial flights within the offshore wind farm (at turbine K07, 54°33'35.7"N, 11°31'19.0"E) were conducted the 22nd of September 2022 (Figure 5.4). The data acquisition strategy involved collecting vertical profiles with several hovering stations of approximately 40 seconds each, centrally with respect to the rotor, at two different distances behind the turbine. For safety reasons, the UAS was restricted from flying above 120 m agl. However, this limitation did not hinder the ability to map the entire vertical extent of the wind turbine rotor, as the turbines in this offshore wind farm are typically lower in height compared to onshore turbines. The two graphs in Figure 5.5 show the trend of the wind speed deficit measured by the multi-copter at distances of 0.6 and 0.9 rotor diameters behind the wind turbine. The velocity was normalized by recording the free-stream wind speed, outside the wake. For each distance, there are three different profiles taken at three different times of the

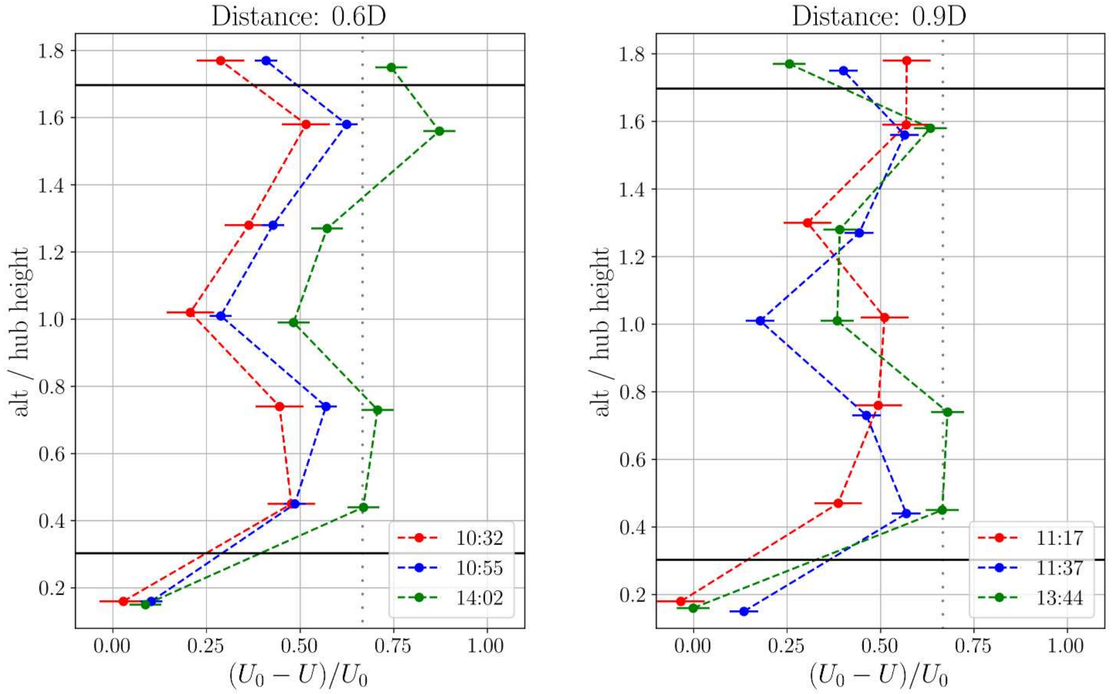

(a) 0.6 diameter behind the rotor. **(b)** 0.9 diameter behind the rotor.

Figure 5.5: Vertical profiles of the wind deficit behind the K07 turbine in the Rødsand II wind park.

day. The dashed grey line represents the theoretical limit for the velocity deficit as per Betz's theory.

At a distance of 0.6 rotor diameters, the velocity deficit exhibits a characteristic W-shaped pattern, which in this case is probably superimposed on a logarithmic increase of the mean wind profile in undisturbed conditions. Even at a distance of 0.9 diameters, this trend can still be observed, although the profile is beginning to lose its regularity compared to the graph on the left.

Additionally, it can be observed that even though the highest hovering point is formally outside the rotor area (represented in the figures by the two black lines), the velocity does not return to the undisturbed value. This indicates that the wake has already extended vertically to cover a greater area than just the rotor area.

This brief experimental campaign was very useful in ascertaining that the components used in the X500 system did not suffer from any particular problem in the challenging operational environment of an offshore maintenance vessel. No errors of the compass system were found related to the metal structures near the UAS, especially during take-off and landing. However, the initialization of the autopilot was slowed down by the oscillatory motion of the vessel, which did not allow for the correct initialization of the IMU. Since the landing target was a moving platform, this procedure was managed manually by the pilot. Occasionally, instability in the final approach was encountered due to turbulence generated by the structure of the boat itself.

Meteorology applications

In a recent experimental campaign the FW-XL10 system was deployed to validate a differential absorption lidar (DIAL). The primary goal of this campaign was to collect in situ data of the mixing ratio in the lower part of the ABL to address some discrepancies observed in the DIAL results. This instrument, operated by the DWD, in Lindenberg, Tauche, has two retrieval zones: a near range and a far range, which overlap at around 400-500 meters. This overlapping zone appears to contain artifacts that cannot be attributed to physical phenomena. Therefore, the most advanced and powerful rotary-wing UAS from the Umphy group was deployed for a brief experimental campaign: over two days, vertical profiles were conducted at a frequency of approximately two per hour, starting at 07:30 AM local time and continuing until 06:00 PM

A preliminary analysis of some of the most interesting profiles from the morning of May 9, 2024, is presented in Figure 5.6. The multi-copter was programmed to ascend to an altitude of 900 m agl at a speed of 5 m s^{-1} for both ascent and descent. Thanks to the high endurance of the FW-XL10 system, it was possible to complete up to three profiles per flight, approximately every 20-25 minutes. For space reasons, only the first profile of each flight is shown in Figure 5.6. The figure illustrates the development of the ABL throughout the morning, transitioning from the nocturnal SBL still evident at 07:23 AM (05:23 UTC) to a fully developed ABL by 09:57 AM (07:57 UTC).

The comparison of data between the weather-research UAS and DIAL is still being analysed. However, this campaign has demonstrated that multi-rotor systems are well-suited for continuous vertical profiling. Additionally, by incorporating further automation, such as automatic landing and recharging, these platforms can safely operate autonomously. This capability allows them to complement profiler and radiosonde measurements effectively.

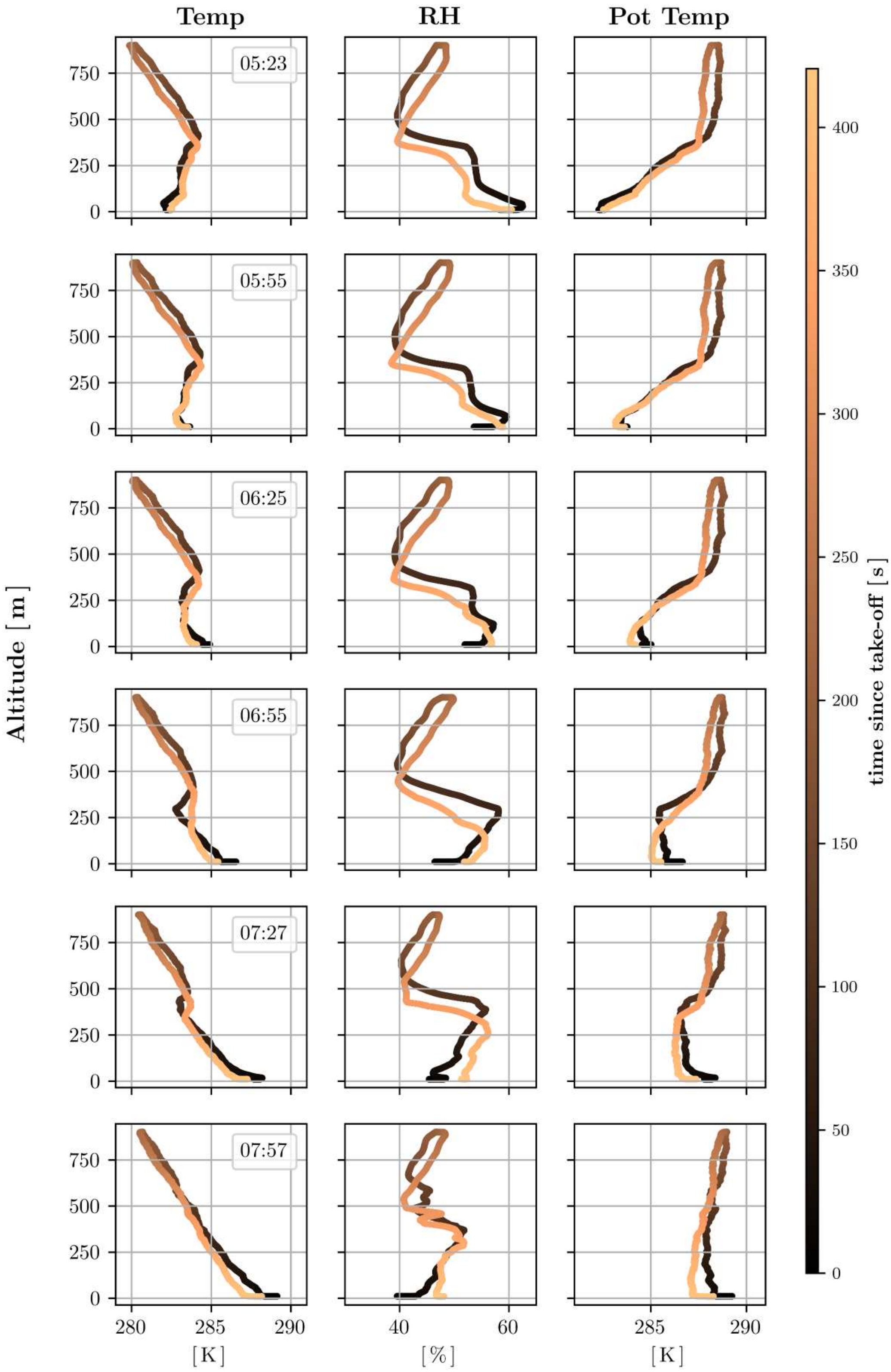

Figure 5.6: Quicklook of the thermodynamic variables collected the morning of May 9, 2024 by profiling the first 900 m of the lower ABL in Lindenberg, Tauche with the FW-XL10 UAS. Timestamp are in UTC.

Chapter 6

Outlook

Regarding the fixed-wing aircraft within the Umphy group's fleet, future developments will focus on integrating new sensors, either mounted on the wings via pods or within the sensorhood. Pods are particularly advantageous as they provide enough space to accommodate both the sensor and the entire acquisition system, facilitating easy interchangeability. Significant progress has already been made in this area with the development and introduction of OPC and charge pods.

The current advancements within the sensorhood system are focused on developing and integrating humidity sensors capable of achieving higher frequencies than those provided by the existing SHT sensors. These enhancements will enable the system to study latent heat fluxes more accurately. The integration of these advanced sensors will significantly augment the capabilities of the fixed-wing aircraft, allowing for more comprehensive and precise atmospheric measurements. This continuous evolution in sensor technology underscores the potential for fixed-wing platforms to contribute substantially to atmospheric research and environmental monitoring.

However, as emphasized throughout this text, the fixed-wing flight strategy lacks flexibility and requires straight-line paths to obtain valid time series of dynamic and thermodynamic quantities. For studies aimed at mapping atmospheric quantities on a horizontal and vertical plane or when covering long horizontal distances, this method reliably yields mean quantities, such as mean wind speed and direction. However, when it comes to acquiring data related to atmospheric turbulence, caution is needed. It is essential to assess whether the assumptions of uniform homogeneous turbulence are met and/or whether these assumptions are necessary for the specific case being studied.

A potential advancement for the MASC-3 platform is the transition to a vertical take-off and landing (VTOL) type aircraft. This development would address many of the issues associated with the large space required for take-off and landing in the current configuration. By adopting VTOL capabilities, the platform will become more versatile and easier to deploy in a wider range of environments, significantly enhancing its operational flexibility and efficiency.

Multicopter systems, on the other hand, can be operated in confined spaces and have the significant advantage of maintaining a fixed position during flight. This makes them particularly suitable for validating static sensors, flying close to fixed structures or buildings, and conducting vertical profile operations. However, even at the commercial level, it is challenging for these systems to achieve a flight time of more than 45 minutes.

The Umphy group's philosophy is to avoid mounting wind sensors on these systems in order to save weight and therefore flight time. Instead the multi-rotor's flight dynamics is used to estimate wind. This approach, explained and developed in this study, is left with some open questions. For instance, is it truly the case that the time resolution cannot exceed 1 Hz, as suggested by Wildmann and Wetz [95]? Is it possible to achieve a higher resolution without significantly impacting the system's endurance? These questions remain open and require further investigation to determine the optimal balance between wind measurement resolution and endurance for multi-rotor systems.

Another significant question is the feasibility of estimating the vertical velocity. This component of the wind vector is crucial for studying vertical fluxes in the atmosphere, such as momentum, heat, and latent heat fluxes. However, the magnitude of vertical velocity is typically an order of magnitude lower than that of horizontal wind. This makes it challenging to estimate vertical velocity using multi-rotor systems that rely on the tilt method. One possible approach is to analyse the RPM of the motors to determine if the system is experiencing positive or negative vertical wind. However, the equations governing the multi-copter's flight behavior are intrinsically interconnected. Thus, incorporating vertical wind estimation is likely to alter the method for obtaining horizontal wind, potentially complicating the overall process rather than simply adding to the theory discussed in Bramati et al. [14]. Further research is needed to develop a robust method for accurately estimating both vertical and horizontal wind components using multi-rotor systems.

Furthermore, both fixed-wing and multi-rotor systems face significant limitations due to adverse flight weather conditions. It is evident that beyond certain wind speeds, it becomes unsafe to take-off. Rainy conditions are also unsuitable for flight, primarily because the data acquisition electronics are overly exposed to moisture. To address this issue, a shielding system must be designed to protect the electronics from both solar radiation and atmospheric precipitation.

Another common challenge, particularly in continental Europe, is the risk of icing on the wings of fixed-wing aircraft and on the propellers of multi-rotor systems. Unfortunately, there is no way to completely prevent icing, which is inevitable when operating vertical profiles in certain atmospheric conditions. The only way to ensure safe flight under these circumstances is to develop a de-icing system that heats the leading and trailing edges of the airfoils at risk. This solution would allow for safe operation even in icing conditions, ensuring the reliability and safety of the data acquisition process.

Appendix A

First/corresponding author peer-reviewed publications

A Versatile Calibration Method for Rotary-Wing UAS as Wind Measurement Systems

MATTEO BRAMATI,[a] MARTIN SCHÖN,[a] DANIEL SCHULZ,[a] VASILEIOS SAVVAKIS,[a] YONGTAN WANG,[a] JENS BANGE,[a]
AND ANDREAS PLATIS[a]

[a] *Geo- und Umweltforschungszentrum, Eberhard Karls Universität Tübingen, Tübingen, Germany*

(Manuscript received 1 February 2023, in final form 2 October 2023, accepted 3 November 2023)

ABSTRACT: The use of small uncrewed aircraft systems (UAS) can effectively capture the wind profile in the lower atmospheric boundary layer. This study presents a calibration process to estimate the horizontal wind vector using a rotary-wing UAS in hovering conditions. This procedure does not require wind tunnels or meteorological masts, only the data from the flight control unit and a specific set of calibration flights. A model based on the UAS drag coefficient was proposed and compared to a traditional approach. Validation flights at the German Weather Service MOL-RAO observatory showed that the system can accurately predict wind speed and direction. A modified DJI S900 hexacopter with a Styrofoam sphere casing was used for the study and calibrated for wind speeds between 1 and 14 m s^{-1}. Power spectral density analysis showed the system's ability to resolve atmospheric eddies up to 0.1 Hz. The overall root-mean-square error was less than 0.7 m s^{-1} for wind speed and less than 8° for wind direction.

KEYWORDS: Wind; In situ atmospheric observations; Instrumentation/sensors; Measurements; Unpiloted aerial systems

1. Introduction

Wind field measurements in the lower atmospheric boundary layer are important for meteorological and industrial applications (Chioncel et al. 2011; Platis et al. 2020, 2021). Ultrasonic anemometers and cup anemometers, commonly used for weather forecasting, require mounting on a mast for single-point measurement. Lidar and sodar, on the other hand, offer remote sensing capabilities but have lower resolution and higher maintenance needs. All of these wind field measurement methods have limitations in terms of applicability, measurement accuracy, and cost.

Rotary-wing uncrewed aircraft systems (UAS), also known as multicopters, offer a cost-effective and flexible solution for measuring the horizontal wind vector (Barbieri et al. 2019). These systems can take off and land vertically, hover at a fixed point, and fly autonomously without prior knowledge of the wind field (Waslander and Wang 2009). In addition, several integrated sensors can be mounted on a multicopter to provide temperature, pressure, humidity, and CO$_2$ measurements (Segales et al. 2020; Bell et al. 2020; Varentsov et al. 2021). Previous studies have demonstrated the use of data gathered by frequent automated profiling to improve regional and mesoscale numerical weather prediction models (Chilson et al. 2019). Targeted observations can also be quickly scheduled to enhance the prediction of extreme weather events (Pinto et al. 2021). Despite limitations in flight endurance, automatic landing procedures and self-recharging stations can improve the operability of these systems.

Mounting onboard sensors, such as sonic anemometers (Shimura et al. 2018) and multihole pressure probes (Prudden et al. 2018), on small multicopters enables the measurement of atmospheric wind. However, the proper placement of these sensors is crucial to minimize the disturbance caused by the UAS rotors and maintain flight stability without compromising endurance.

The use of the effect of wind on a UAS's attitude to estimate the wind vector is a well-known method for horizontal wind estimation. Neumann and Bartholmai (2015) first introduced this approach and calibrated the UAS in a wind tunnel, achieving an estimation model with a root-mean-square error (RMSE) of 0.6 m s^{-1}. Palomaki et al. (2017) and Donnell et al. (2018) later compared an attitude-based wind estimation and the estimation from a sonic anemometer mounted on a multicopter to a ground based anemometer, obtaining similar statistics. Crowe et al. (2020) employed machine learning algorithms to model the relation between wind speed and multicopter attitude. Meier et al. (2022) investigated the performance of various methods based on the UAS's dynamic equations and aerodynamic parameters, aiming to measure horizontal and vertical wind during both hover and movement. Despite advancements in technology, the traditional approach proposed by Neumann and Bartholmai (2015) appears to remain the most accurate. Wetz et al. (2021) recently presented a wind measurement model that leverages the drag coefficient of a multicopter as a function of its attitude to calibrate the UAS. This approach assumes a linear relationship between the drag coefficient and the UAS's orientation when it is configured to face into the wind (i.e., in a wind-vane configuration). The authors then carried out UAS fleet flights to measure the vertical profile of the wind vector and compared the results with lidar data, finding excellent agreement and even higher temporal and spatial resolution. Wildmann and Wetz (2022) also recently demonstrated the capabilities of small, lightweight UASs for measuring the vertical wind component, paving the way for the use of this technology in turbulent flux calculations.

Denotes content that is immediately available upon publication as open access.

Corresponding author: Matteo Bramati, matteo.bramati@uni-tuebingen.de

Publisher's Note: This article was revised on 29 April 2024 to designate it as open access.

DOI: 10.1175/JTECH-D-23-0010.1

The traditional method for calibrating UAS systems involves the use of costly wind tunnels or masts equipped with anemometers (Abichandani et al. 2020). However, this approach is problematic as the test chamber must be large enough to avoid wall interferences (Ewald et al. 1998), and it is impossible to control the atmospheric wind. As a result, building a model that covers all possible wind speeds is a complex and time-consuming endeavor.

Brosy et al. (2017) introduced a calibration method that involves flying along a square racetrack path while maintaining a constant ground speed. This approach allows for in situ calibration in the natural atmospheric environment, providing a comprehensive mapping of the UAS attitude up to its maximum flight speed. Additionally, the procedure can be easily repeated for other multicopters under similar conditions. The author notes that these flights were conducted under weak atmospheric wind conditions (less than 1 m s^{-1}), but does not elaborate on how to handle the data in the presence of stronger winds.

This paper presents a comprehensive exploration of the latter approach, focusing on mapping the entire range of attitudes of a multirotor UAS. Emphasis is placed on the meticulous postprocessing of the data, specifically addressing the crucial task of filtering out the influence of atmospheric wind during calibration. The fundamental aspects of this filtering process are thoroughly elucidated. Despite the potential presence of atmospheric wind during calibration, our postprocessing algorithm allows for correction of the data to obtain a reliable calibration function.

In this work, we also analyze in detail the model involving the UAS drag coefficient. To improve the performance of the model, we modified the external shape of the multicopter by enclosing all electronic components in a Styrofoam sphere. This increased symmetry makes it possible to avoid the wind-vane mode, in which the copter would always try to face the incoming wind, and therefore would be slow for our system due to its size. Our model is explained in detail by analyzing the behavior of the drag coefficient versus the modified UAS attitude, and it is compared to the model introduced by Neumann and Bartholmai (2015) that maps the system attitude directly to the wind velocity. This text builds upon the premise previously explained by the authors in Bramati et al. (2022) by investigating, with a new set of flights, using two parallel multicopters, the effect of the Styrofoam sphere on the system as a wind speed sensor. The benefits of the new spherical-shaped configuration and the drag coefficient model are discussed throughout the text.

In section 2, the UAS used for the study is described, along with the theory of wind estimation. The process of linking the full rigid-body dynamics equations to the explicit relation between horizontal wind and multicopter attitude is outlined, with the assumptions made during this process highlighted. In section 3, the method for collecting calibration data is outlined. The postprocessing of the data is also discussed, as well as the introduction of the drag coefficient model and the Neumann and Bartholmai (2015) model. Section 4 presents the method used to evaluate the accuracy of the two models, including tests to determine the impact of mounting a Styrofoam sphere. We provide time series and spectral plots as evidence of our findings. A thorough analysis of the results, including the benefits of using a spherical dome and the impact of various parameters, is presented in section 5. In section 6, the conclusions of this study are presented and potential future developments are discussed.

TABLE 1. Relevant specifications of the UAS used in this study.

Characteristic	Description/value
Frame	DJI Spreading Wings S900
Flight control unit	PixHawk 2.1 Cube Orange
GNSS	Here3 GPS
Rotor–rotor distance	900 mm
Sphere diameter	500 mm
Multicopter weight	3.8 kg
Batteries weight	3.0 kg
Sphere weight	0.5 kg
Total weight	7.3 kg

2. Materials and methods

a. *Uncrewed aerial system*

The system used for this study is a rotary-wing UAS, specifically the DJI Spreading Wings S900 hexacopter (Table 1). Using open-source ArduCopter firmware (V4.0.5), the PixHawk 2.1 Cube Orange autopilot controls the system. The flight control unit utilizes a Here3 GPS antenna as a GNSS receiver. During each flight mission, the autopilot logs the flight parameters of the system, computed with its extended Kalman filter, at a frequency of 10 Hz. The only component retained from the original DJI electronics are the six built-in arms with electronic speed controllers (ESC). The servos responsible for retracting the landing gears have been removed to reduce weight.

The hexacopter's body is enclosed in a Styrofoam sphere (Fig. 1 and Fig. A1 in appendix A). The structure is composed of two parts with a thickness of 2 cm each. Using 3D printed acrylonitrile butadiene styrene (ABS) parts and two sets of Velcro straps for each arm, both halves are connected to the multicopter frame. The lower part of the sphere has been manually carved to accommodate the landing gears. As a result of this shape, symmetry is increased with respect to horizontal wind while a partial shelter is provided for electronics from external elements. Detailed discussion of this encasing will be included in section 5.

This system is powered by a pair of lithium polymer six cells batteries each rated at 12 Ah. The weight of the whole system is 7.3 kg, including the batteries: the maximum flight time is 24 min. In this configuration the hexacopter proved to fly up to a peak ground speed (GS) of 19 m s^{-1}.

Mission Planner is the software used on the ground station. This open-source program allows users to create missions with specific commands, simulate them, and then store them on the system. Several other parameters including the altitude, battery level, and orientation are monitored through the same interface during flight.

b. *Wind estimation theory*

1) REFERENCE FRAMES

To describe an airborne system's orientation, several reference frames can be used. In this study, only two of them are required:

FIG. 1. Modified DJI S900 hexacopter.

- Vehicle reference frame ($\mathbf{i}_1$, $\mathbf{i}_2$, $\mathbf{i}_3$): This reference frame has its origin in the center of gravity of the multicopter: $\mathbf{i}_1$ points toward north, $\mathbf{i}_2$ points toward east, and $\mathbf{i}_3 = \mathbf{i}_1 \times \mathbf{i}_2$ will consequently point toward the center of Earth.
- Body reference frame ($\mathbf{b}_1$, $\mathbf{b}_2$, $\mathbf{b}_3$): This reference frame shares the same origin with the previous. However, its axes move together with the vehicle: $\mathbf{b}_1$ points toward the front of the vehicle, $\mathbf{b}_2$ points toward the right of the vehicle, and $\mathbf{b}_3 = \mathbf{b}_1 \times \mathbf{b}_2$ will consequently be orthogonal to the plane defined by the first two.

Variables such as position or velocity can be expressed in relation to one frame or another by applying three planar rotations defined by Euler angles. The rotation sequence is roll(ϕ)–pitch(θ)–yaw(ψ) in order to switch from body to vehicle while vice versa to switch from vehicle to body. A rotation matrix is used to perform this operation mathematically:

$$\mathbf{R}_{V\to B} = \mathbf{R}_{\phi}(\phi)\mathbf{R}_{\theta}(\theta)\mathbf{R}_{\psi}(\psi) \tag{1}$$

$$= \begin{pmatrix} 1 & 0 & 0 \\ 0 & \cos(\phi) & \sin(\phi) \\ 0 & -\sin(\phi) & \cos(\phi) \end{pmatrix} \begin{pmatrix} \cos(\theta) & 0 & -\sin(\theta) \\ 0 & 1 & 0 \\ \sin(\theta) & 0 & \cos(\theta) \end{pmatrix} \begin{pmatrix} \cos(\psi) & \sin(\psi) & 0 \\ -\sin(\psi) & \cos(\psi) & 0 \\ 0 & 0 & 1 \end{pmatrix} \tag{2}$$

$$= \begin{pmatrix} c_\theta c_\psi & c_\theta s_\psi & -s_\theta \\ s_\phi s_\theta c_\psi - c_\phi s_\psi & s_\phi s_\theta s_\psi + c_\phi c_\psi & s_\phi c_\theta \\ c_\phi s_\theta c_\psi + s_\phi s_\psi & c_\phi s_\theta s_\psi - s_\phi c_\psi & c_\phi c_\theta \end{pmatrix}, \tag{3}$$

$$\mathbf{R}_{V\to B} = \mathbf{R}^T_{V\to B}, \tag{4}$$

with $c_\phi \triangleq \cos(\phi)$ and $s_\phi \triangleq \sin(\phi)$ and so on for the other Euler angles (from Beard and McLain 2012).

2) TILT ANGLE Γ

The tilt angle is defined as the angle between the vehicle reference frame vertical vector ($\mathbf{i}_3$) and the body reference frame vertical vector ($\mathbf{b}_3$) (Neumann and Bartholmai 2015; Palomaki et al. 2017). Figure 2 shows a simplified representation of the airborne system and tilt angle. Making use of the rotation matrix $\mathbf{R}_{B\to V}$ it is possible to obtain an expression for the tilt angle as a function of the pitch and roll angle only. Indeed, by expressing the $\mathbf{b}_3$ vector in the vehicle reference frame,

$$\mathbf{b}_3^V = \mathbf{R}_{B\to V} \cdot \mathbf{b}_3^B, \tag{5}$$

$$\mathbf{b}_3^V = \begin{bmatrix} c_\phi s_\theta c_\psi + s_\phi s_\psi \\ c_\phi s_\theta s_\psi - s_\phi c_\psi \\ c_\phi c_\theta \end{bmatrix}. \tag{6}$$

Thus, the tilt angle can be computed using the three components of the $\mathbf{b}_3^V$ vector:

$$\Gamma = \arctan\left[\frac{\sqrt{(c_\phi s_\theta c_\psi + s_\phi s_\psi)^2 + (c_\phi s_\theta s_\psi - s_\phi c_\psi)^2}}{c_\phi c_\theta}\right]. \tag{7}$$

By developing the calculation, it is possible to notice that the tilt angle does not depend on the yaw angle ψ:

$$\Gamma = \arctan\left[\frac{\sqrt{c_\phi^2 s_\theta^2 + s_\phi^2}}{c_\phi c_\theta}\right]. \tag{8}$$

However, the actual value of ψ cannot be ignored when determining the wind direction.

3) DYNAMICS EQUATIONS

In still air, rigid airborne systems are described by the following equations:

$$m\ddot{\mathbf{x}} = m\dot{\mathbf{x}} \times \boldsymbol{\omega} + \mathbf{F}_{\text{aero}}(\dot{\mathbf{x}}) + mg\mathbf{i}_3 - F_{\text{ctrl}}\mathbf{b}_3, \tag{9}$$

$$I\dot{\boldsymbol{\omega}} = I\boldsymbol{\omega} \times \boldsymbol{\omega} + \mathbf{M}_{\text{aero}}(\boldsymbol{\omega}, \dot{\mathbf{x}}) + \mathbf{M}_{\text{ctrl}}, \tag{10}$$

where m is the mass of the vehicle, $\mathbf{x}$ is its three-component position vector, $\boldsymbol{\omega}$ its three-component rotation rate vector, $\mathbf{F}_{\text{aero}}$ and $\mathbf{M}_{\text{aero}}$ are the aerodynamic forces and moments developing during flight while $F_{\text{ctrl}}\mathbf{b}_3$ and $\mathbf{M}_{\text{ctrl}}$ are the control forces and moments applied by the autopilot in order to achieve a specific mission (Gonzalez-Rocha et al. 2017). As a result of the assumption of still air conditions, the aerodynamic force $\mathbf{F}_{\text{aero}}$ is a function of only the UAS speed. Section 4 provides a detailed explanation of aerodynamic forces.

Considering steady ($\ddot{\mathbf{x}} = 0$ and $\dot{\boldsymbol{\omega}} = 0$) equilibrium conditions ($\dot{\mathbf{x}} = \dot{\mathbf{x}}_{\text{eq}}$ and $\boldsymbol{\omega} = 0$) the equations simplify and become independent of each other:

$$0 = \mathbf{F}_{\text{aero}}(\dot{\mathbf{x}}_{\text{eq}}) + mg\mathbf{i}_3 - F_{\text{ctrl}}\mathbf{b}_3, \tag{11}$$

$$0 = \mathbf{M}_{\text{aero}}(0, \dot{\mathbf{x}}_{\text{eq}}) + \mathbf{M}_{\text{ctrl}}. \tag{12}$$

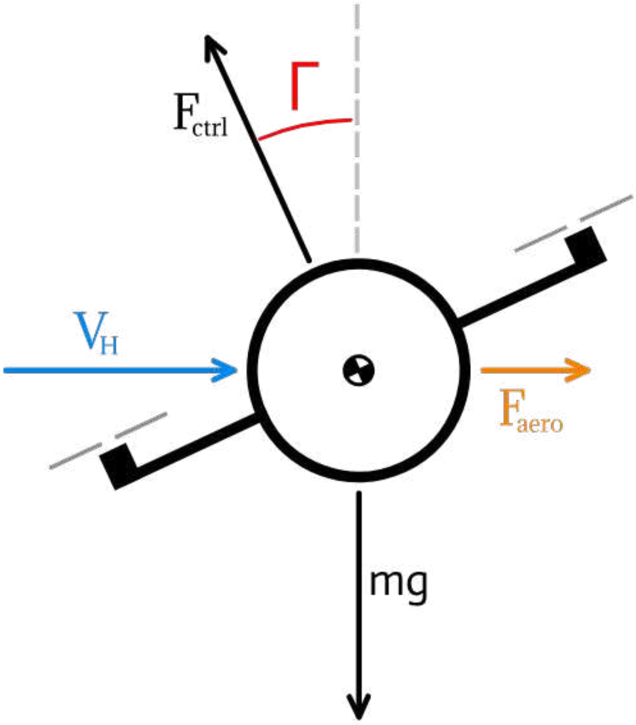

FIG. 2. Attitude of a multicopter while flying at constant speed or while hovering under the influence of horizontal atmospheric wind. The multicopter tilts (Γ) toward the wind direction so that it can balance the aerodynamic force ($\mathbf{F}_{aero}$).

Equation (11) has three components along the three directions of the vehicle reference frame. In the case of horizontal flight (with zero vertical wind speed) and no vertical aerodynamic forces developing in the previous condition, Eq. (11) can be written as follows:

$$F^x_{\mathrm{aero}}(\dot{x}_{\mathrm{eq}}) - F_{\mathrm{ctrl}}\,(c_\phi s_\theta c_\psi + s_\phi s_\psi) = 0, \tag{13}$$

$$F^y_{\mathrm{aero}}(\dot{y}_{\mathrm{eq}}) - F_{\mathrm{ctrl}}\,(c_\phi s_\theta s_\psi - s_\phi c_\psi) = 0, \tag{14}$$

$$mg - F_{\mathrm{ctrl}}\,c_\phi c_\theta = 0. \tag{15}$$

Accordingly, the vehicle will be subjected to the following total aerodynamic force:

$$F_{\mathrm{aero}} = \sqrt{(F^x_{\mathrm{aero}})^2 + (F^y_{\mathrm{aero}})^2} \tag{16}$$

$$= F_{\mathrm{ctrl}}\sqrt{(c_\phi s_\theta c_\psi + s_\phi s_\psi)^2 + (c_\phi s_\theta s_\psi - s_\phi c_\psi)^2} \tag{17}$$

$$= F_{\mathrm{ctrl}}\sqrt{c_\phi^2 s_\theta^2 + s_\phi^2}. \tag{18}$$

Computing the ratio between Eqs. (18) and (15),

$$\frac{F_{\mathrm{aero}}}{mg} = \frac{F_{\mathrm{ctrl}}\sqrt{c_\phi^2 s_\theta^2 + s_\phi^2}}{F_{\mathrm{ctrl}}\,c_\phi c_\theta} = \tan(\Gamma), \tag{19}$$

$$F_{\mathrm{aero}} = mg\tan(\Gamma). \tag{20}$$

Based on the assumptions made throughout the calculations, it is possible to obtain an equation for the aerodynamic forces as a function of the mass and orientation of the multicopter.

4) AERODYNAMIC FORCES

As a solid body moves relative to a surrounding fluid, a force distribution occurs at its surface. In general, this distribution is simplified by taking the equivalent components parallel and perpendicular to the direction of the relative velocity, as well as an equivalent moment based on a reference point (Anderson 2011). The parallel component is directed opposite to the relative velocity and is often called drag. Under the assumptions made in order to obtain Eq. (20), the drag is the only aerodynamic force acting on the system.

The absolute value of this force can be determined using the Rayleigh equation (Anderson 2011):

$$D = \frac{1}{2}\rho V^2 A C_D(\mathrm{Ma}, \mathrm{Re}) = F_{\mathrm{aero}}. \tag{21}$$

In this equation, ρ represents the fluid density, V is the relative velocity between the body and the fluid, A is the projection of the body shape exposed to the flow (cross-section area), and C_D is the drag coefficient, which is a function of the Mach number (Ma), Reynolds number (Re), and body geometry.

First of all, under the assumptions made in section 3—precisely the equilibrium hypothesis ($\dot{\mathbf{x}} = \dot{\mathbf{x}}_{\mathrm{eq}}$ and $\boldsymbol{\omega} = 0$) and the no vertical wind assumption—the velocity in Eq. (21) represents only the horizontal velocity. Furthermore, compared to fixed-wing aircraft and other common multicopters, our UAS offers a greater degree of axial symmetry in the horizontal plane. As a result, it is reasonable to assume that physical properties such as A and C_D are independent of direction of motion (Neumann and Bartholmai 2015; Wang et al. 2018; González-Rocha et al. 2019). It is also possible to neglect the effect of Mach number on the drag coefficient since the expected range of velocities is considerably lower than the speed of sound (up to 20 m s^{-1}).

5) WIND SPEED ESTIMATION

Combining Eqs. (20) and (21) leads to a nonlinear relation between V and the tilt angle:

$$\frac{\rho V^2 A C_D}{2mg} = \tan(\Gamma). \tag{22}$$

When the tilt (or velocity) varies, A and C_D may not be constant. As the drag coefficient depends on the Reynolds number, it cannot be considered constant a priori when flying at different speeds. The multicopter's physical components (rotors and landing gear) that change the cross-section area when tilting are included in the relation $A(\Gamma)$.

To simplify the mapping of $A(\Gamma)$, the following extended drag coefficient can be used:

$$C_A(\Gamma) = \frac{A(\Gamma)}{A_0}C_D(\Gamma). \tag{23}$$

To keep the coefficient dimensionless, A_0 is used as a reference area: in this case, the cross-section area of the Styrofoam sphere. As there is a unique relationship between Γ and V, C_D is now a function of tilt angle.

It is now possible to isolate V from Eq. (22):

$$V = \sqrt{\frac{2mg\tan(\Gamma)}{\rho A_0 C_A(\Gamma)}} = \sqrt{\frac{\tan(\Gamma)}{KC_A(\Gamma)}}, \tag{24}$$

with

$$K = \frac{\rho A_0}{2mg}. \tag{25}$$

So far, V has been defined as the horizontal velocity of the multicopter relative to the surrounding air; however, all equations from Eq. (13) on are also valid if the system hovers with a horizontal wind component, since this is also a steady and equilibrium state. The PosHold mode of ArduCopter's autopilot system can easily be used to achieve this state. As a result of the extended Kalman filter on board, the UAS is able to hold its location, heading, and altitude when in this specific flight mode.

A horizontal wind estimate can be obtained in two ways. The first involves directly characterizing the relation between tilt angle and velocity (Neumann and Bartholmai 2015), while the second involves characterizing the extended drag coefficient against the tilt angle and applying Eq. (24).

It is normally necessary to calibrate UAS in a wind tunnel or by using meteorological masts with higher accuracy reference sensors (Neumann and Bartholmai 2015; Palomaki et al. 2017). Wind tunnels, however, are often hard to find and can be extremely expensive per hour. Additionally, larger UAS would require larger test chambers to prevent wall-wake interference. An alternative approach involves calibrating the system by conducting hovering maneuvers in tandem with a sonic anemometer. However, this methodology is greatly influenced by meteorological conditions and may require several weeks to gather a sufficient amount of data encompassing the entire range of wind speeds suitable for utilizing the UAS as a wind sensor. The method described in this study is not dependent on the availability of elaborate equipment: it involves performing specific flights in the real environment to collect orientation data during constant speed segments.

An issue of this calibration procedure is that the multicopter can only be programmed to keep a specific ground speed while flying, but the velocity V that appears in Eqs. (21) and (24) is the true airspeed (TAS). GS and TAS are the same only when atmospheric wind is zero. In other words, the presence of any nonzero wind during the flights makes the GS different from the TAS. To correct the tilt angle taking atmospheric wind into account, calibration flights must be carefully planned and a systematic postprocessing procedure must be adopted. The choice of a calm day is therefore preferable not only for the former reason, but also to prevent unexpected gusts that could destabilize the flight controller.

6) WIND DIRECTION ESTIMATION

Calculating the wind direction (Λ) is straightforward. Given that the multicopter tilts in the same direction the wind blows, it is sufficient to calculate the projection of the $\mathbf{b}_3^B$ vector on the horizontal plane of the vehicle reference frame. Here, the yaw angle (ψ) must be taken into account:

$$\Lambda = \arctan\left[\frac{c_\phi s_\theta}{-s_\phi}\right] + \psi + 180°. \tag{26}$$

The last addition is necessary since there is a 180° difference, by definition, from the projected $\mathbf{b}_3^B$ and the meteorological wind direction. With Λ limited between 0° and 360°, Eq. (26) provides the horizontal wind direction from north, positive clockwise.

3. Calibration

The calibration flights were performed at the airfield located in Poltringen, Baden-Württemberg, Germany (UTC + 1 h), on 23 February 2021. Tübingen University's Umweltphysik group usually performs test flights at Poltringen airport because as a Landesbehörde, the university does not require special permission to fly UAVs with a mass less than 25 kg in line of sight. It was only necessary to get permission from the airport chief.

Calibration flights are designed to collect data to map multicopter behavior across different TAS. As a result of these data, it will be possible to obtain a direct relation between tilt angle and TAS as well as between C_A and tilt angle.

a. Flight description and meteorological conditions

For a broader understanding of the conditions in Poltringen on the measurement day, we use ERA5 (Hersbach et al. 2018) data from Baden-Württenberg. There was low wind speed, low cloud cover, and warm temperatures for 23 February, with maximum temperatures of 17°C toward the afternoon and lowest temperatures of 10°C toward the evening. A low surface wind speed around 1 m s^{-1} and an easterly wind direction were experienced during the first two flights (Table 2 and Fig. 3, 1400–1500 UTC).

The wind conditions changed between 1500 and 1600 UTC, and therefore between flight 2 and flight 3. The wind direction changed from east to southeast at 1600 and finally to south at 1700. At the same time, the surface wind speed increased to around 2 m s^{-1} at 1600 UTC and to 2–3 m s^{-1} at 1700 UTC (Fig. 3, 1600–1700 UTC).

During the mission, the UAS flew at an altitude of 50 m on a straight line in the direction of a waypoint and finally back to the starting point. This basic flight pattern was carried out for different GS from 1 to 14 m s^{-1} (safety limit). To gather more data for model calibration, the procedure was repeated for a direction perpendicular to the first flight. For each GS, the missions were planned so that equal numbers of data points would be collected, resulting in shorter distances for lower speeds and greater distances for higher speeds (Fig. 4).

Due to the battery endurance, the total number of flights has been divided into four missions. The mission sequence can be found in Table 2. An illustration of the GS behavior during the first mission is presented in Fig. 5. It is evident that the autopilot effectively maintains the desired GS for both the forward and backward segments. For higher GS values, the acceleration phase is extended, resulting in longer sections of the flight path

TABLE 2. Missions sequence. In Fig. 4, the E–W direction is represented by the blue dots and N–S by the orange dots. The surface wind speed (SWS) and direction (SWD) are obtained using ERA5.

No.	Flight	GS range (m s^{-1})	Start (UTC)	End (UTC)	SWS (m s^{-1})	SWD
1	E–W	$8 \rightarrow 1$	1403	1423	≤ 1	E
2	N–S	$8 \rightarrow 1$	1442	1502	≤ 1	E
3	E–W	$14 \rightarrow 10$	1533	1544	≈ 2	S–E
4	N–S	$14 \rightarrow 10$	1606	1619	≈ 2	S–E

being planned accordingly. The air density was determined by measuring atmospheric parameters at ground level.

The key to detecting any nonzero atmospheric wind is to fly forward and backward on a straight line. If a wind is present during these flights, it will interfere with the UAS with the same magnitude (assuming it is constant), but in the opposite direction. Therefore, this influence can be detected and corrected after recording, resulting in final calibration using the TAS rather than the GS. The next sections (sections 3b and 3c) deal with the data analysis and the data correction in order to tackle this issue.

b. Data analysis

First, the autopilot data have been filtered to be within ± 0.05 m s^{-1} around the desired GS. The band is uniform for all the tested velocities (orange segments in Fig. 5). Based on the Euler angles, the tilt angle and the extended drag coefficient have been computed by applying Eq. (8) and the inverse of Eq. (24):

$$C_A = \frac{\tan(\Gamma)}{KV^2}. \tag{27}$$

At this point the only way to solve Eq. (27) is to assume undisturbed wind conditions (TAS = GS) for the moment and use the multicopter V_{GS} instead of the TAS(V):

$$C_A = \frac{\tan(\Gamma)}{KV_{\mathrm{GS}}^2}. \tag{28}$$

Figure 6 shows the $\Gamma(V_{\mathrm{GS}})$ data and the $C_A|_{\mathrm{GS}}(\Gamma)$ data obtained for all the tested GSs for one flight direction.

During the first mission, which started at 1403 UTC, the data (mapping GSs from 8 to 1) show no discernible difference between the forward and backward part, and they are generally very well overlapped. In contrast, data gathered during the mission No. 3 mapping higher GSs, started at 1533 UTC reveal two very well-separated clouds of points: this is clear evidence of the presence of wind influencing the calibration process. Due to the wind, the multicopter has to tilt more when it is facing it (headwind); on its way back, it must tilt less since it is being pushed from behind (tailwind). There is also a similar pattern for the second flight direction: it shows that the wind velocity increased between the second and third mission. This can be seen as well in Fig. 6b where 8 lines are present for the velocities from 1 to 8 m s^{-1} while for the flights from 10 to 14 m s^{-1} we have two well-separated segments for each velocity, due to the presence of wind.

c. Data correction

Assume two unknown wind components u and v are present during calibration flights. Thus, the situation would be similar to that shown in Fig. 7. Due to the relatively short flight time, we can assume that the wind is constant for every GS along the same direction. At this point, Eq. (27) is used to model the UAS behavior in both forward (F) and backward (B) sections using the true airspeed (V). The tilt angles for the forward and backward calibration flights, Γ_F and Γ_B, are described by

$$\Gamma_F = \arctan[KC_{A,F}V_F^2], \tag{29}$$

$$\Gamma_B = \arctan[KC_{A,B}V_B^2]. \tag{30}$$

The TASs for the forward and backward part are modeled by simple trigonometric relations as in Fig. 7:

$$\Gamma_F = \arctan\{KC_{A,F}[(V_{\mathrm{GS}} - u)^2 + v^2]\}, \tag{31}$$

$$\Gamma_B = \arctan\{KC_{A,B}[(V_{\mathrm{GS}} + u)^2 + v^2]\}. \tag{32}$$

Note that $C_{A,F}$ and $C_{A,B}$ are not the same values shown in Fig. 6b since those values were calculated using Eq. (28). Using $C_{A,F}|_{\mathrm{GS}}$ and $C_{A,B}|_{\mathrm{GS}}$ to solve Eqs. (31) and (32) would result in the trivial solution $(u, v) = (0, 0)$ since those value were calculated under the hypothesis of zero wind disturbance.

Thus, the system [Eqs. (31) and (32)] has four unknowns ($C_{A,F}$, $C_{A,B}$, u, v) and therefore cannot be solved as it is since it theoretically has infinite solutions. Therefore, it becomes imperative to employ an approximation for two of the unknowns. Considering that the function C_A is defined as the arctangent of the tilt angle [Eq. (28)], and given that the tilt angle typically falls within a range of less than 25°, it is reasonable to adopt a linear approximation. For a particular V_{GS}, the two sets of data points representing $C_{A,F}$ and $C_{A,B}$ can be visualized as lying on a straight line that passes through the origin of the coordinate axes of Fig. 6. The slope of this line is determined by the V_{GS} value itself. An average between forward and backward data clouds is then used to calculate the corrected extended drag coefficient $C_A|_{\mathrm{GS}}$, shown in Fig. 8b, and solve the system. It is essential to note that the selection of this method is purely heuristic, and there might exist alternative solutions that could prove effective as well. For instance, one could consider a scenario where two different estimates for the two unknown drag coefficients align more closely with the actual values during forward and backward

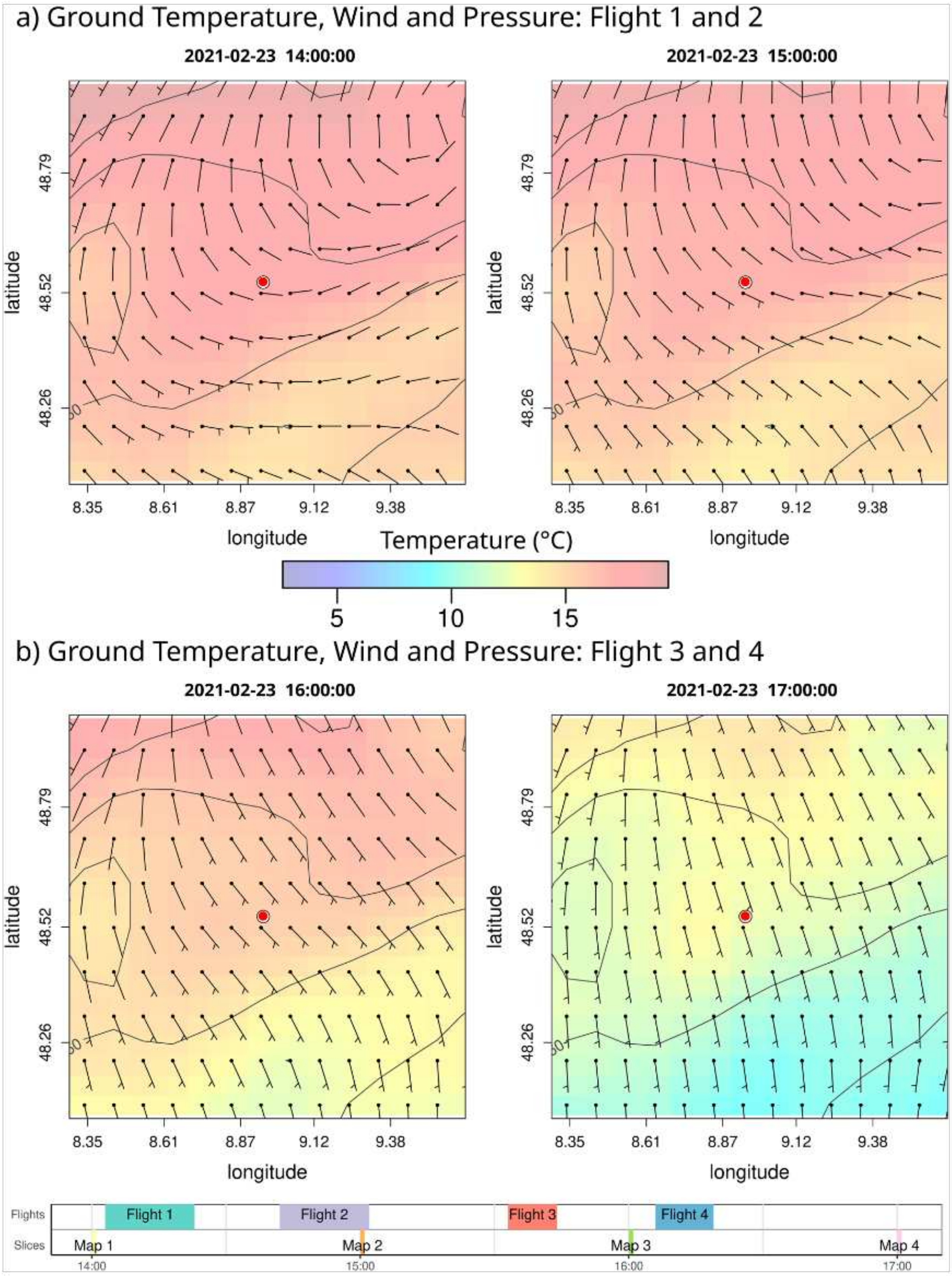

FIG. 3. Maps describing the atmospheric conditions (surface wind speed, direction, temperature, and pressure) at Poltringen airfield (48.545°N, 8.947°E; red dot) on the day of the calibration flights, 23 Feb 2021. The four plots describe the evolution of these parameters from (top left) 1400 UTC to (bottom right) 1700 UTC. The plots were generated using ERA5 with a 9 km grid resolution. Below the maps, a timeline shows when the four flights have been performed with respect to the four weather maps provided.

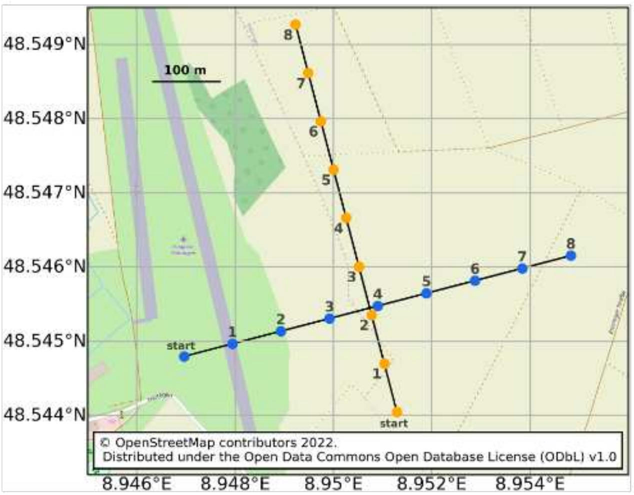

FIG. 4. Example of the calibration flight missions (8–1 m s^{-1}). Blue and orange points indicate the limits of each section at a specific ground speed. Since the multicopter reaches a steady condition faster at lower velocities, less distance needs to be covered.

flight. However, a deliberate decision was made to opt for the average as the chosen approach. By using these new extended drag coefficient values, updated tilt angle values ($\overline{\Gamma}$) are calculated by using Eq. (28):

$$\overline{C}_A = \text{mean}(C_{A,F}|_{\text{GS}}, C_{A,B}|_{\text{GS}})\,|_{\forall\,\text{GS}}, \tag{33}$$

$$\overline{\Gamma} = \arctan(K\overline{C}_A V_{\text{GS}}^2)\,|_{\forall\,\text{GS}}. \tag{34}$$

As a result, $\overline{C}_A$ values can be used to solve the system of Eqs. (31) and (32) by approximating $C_{A,F} = C_{A,B} = \overline{C}_A$. Despite the fact that equivalent values for the extended drag coefficient remain a heuristic approximation, u and v—the only unknowns—are consistent with ERA5 of the mean wind (Table 3 and Fig. 3).

d. *Calibration models*

After removing any atmospheric wind disturbance, it can be seen from Fig. 8 that the $\overline{\Gamma}$ and $\overline{C}_A$ values have a more regular trend. At this point, they can be fitted to define our wind estimation models.

For the first model, the corrected tilt angle and the tested GS are directly related for the estimation of the horizontal wind velocity. On the other hand, similar to the one used by Wetz et al. (2021), the second model describes the extended drag coefficient C_A as a function of tilt angle.

1) DIRECT MODEL

Researchers have already extensively studied this approach (Neumann and Bartholmai 2015) and found it to be effective.

A fitting is performed using the updated average tilt angles ($\overline{\Gamma}$) obtained from the two directions of flight (Fig. 8a). The fitting function is a third-order polynomial:

$$V(\Gamma) = c_3\Gamma^3 + c_2\Gamma^2 + c_1\Gamma + c_0, \tag{35}$$

with $c_3 = -5.56 \times 10^{-4}$, $c_2 = -1.75 \times 10^{-3}$, $c_1 = 0.88$, and $c_0 = 0$ (RMSE: 0.25 m s^{-1}). A null tilt angle would logically correspond to a zero wind speed, so the last coefficient is manually set to zero. The blue line in Fig. 8a shows the fitting function.

The Euler angles of the UAS are all that is required for this model. It is, however, a model that represents reality only when the same atmospheric conditions as the calibration flights exist. If temperature or pressure (thus air density) change, or if the multicopter mass changes, the horizontal wind estimates will be offset. Other than performing numerous calibration procedures with different payloads and atmospheric conditions, it is impossible to estimate the magnitude of the offset.

2) C_A MODEL

Here, the average points are fitted using an exponential decay function (Fig. 8b). The fitting is performed over the updated average value of the extended drag coefficient ($\overline{C}_A$):

$$C_A(\Gamma) = c_0 + c_1 e^{-\Gamma/c_2}, \tag{36}$$

with $c_0 = 1.487$, $c_1 = 26.123$, and $c_2 = 1.55$ (RMSE: 0.81).

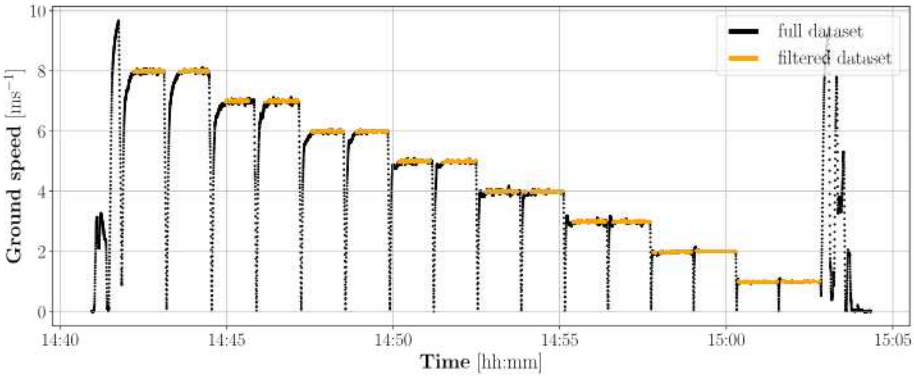

FIG. 5. An example of the ground speed data recorded during mission 2 (N–S direction; see Table 2). Data filtered for calibration are represented by the orange part. For each ground speed, two datasets were obtained from flying first toward the waypoint and then back.

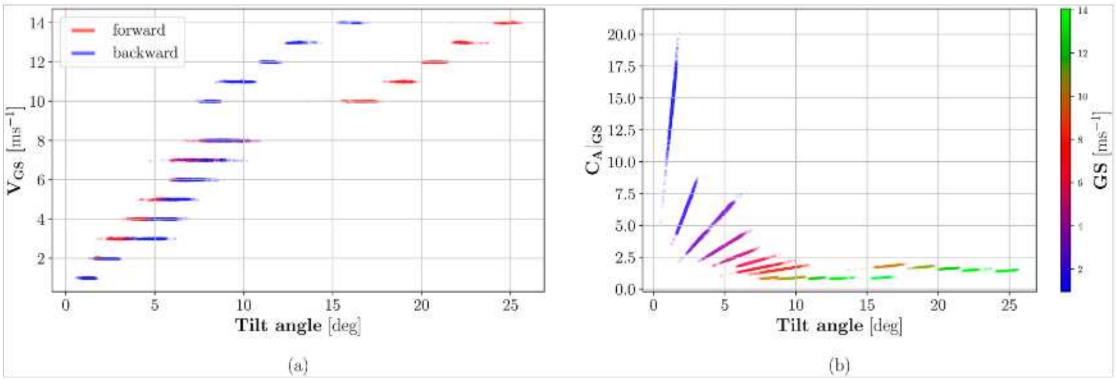

FIG. 6. (a) Tilt angles values recorded along the E–W direction (missions 1 and 3) for the ground speeds from 1 to 8 m s^{-1} and from 10 to 14 m s^{-1}, respectively. (b) Extended drag coefficient values obtained using Eq. (28) along the same direction plotted against the respective tilt angle values. The color represents the different ground speeds.

By using this function, it is possible to estimate the horizontal velocity described in Eq. (24). As additional inputs to the Euler angles, the air density and the mass of the multicopter must be provided [see Eq. (25)]. The air density is computed using pressure and temperature data, while the mass is measured using a scale before takeoff. In this way, the model can be applied to a variety of external conditions, making it more flexible. The mass of the system is present as a stand-alone parameter in Eq. (24); however, a different payload configuration will also affect the absolute values of the calibration function $C_A(\Gamma)$. Section 5 provides a more detailed analysis of this dependence.

4. Results from validation and parallel flights

a. Validation flights

In this section, the two models obtained from the calibration flight data are assessed for their quality. A Metek USA-1 ultrasonic anemometer mounted on a 99 m mast was used to compare the horizontal wind estimation. The comparison flights have been performed at the German Meteorological Service Boundary Layer Field Site of Falkenberg, Brandenburg, close to the MOL-RAO observatory site, in the framework of the VALUAS project, during the FESSTVaL field campaign in June 2021.

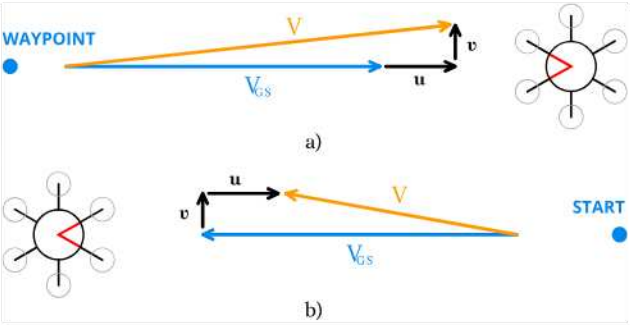

FIG. 7. Effect of a nonnegligible horizontal wind (u, v) during the calibration flights. (a) When the multicopter flies toward the waypoint, the wind disturbance increases the ground speed (V_{GS}), leading to a higher true airspeed (V). (b) As the multicopter returns to the starting position, the same wind disturbance causes a decrease in the true airspeed. The red lines on the multicopter represent its front part—as can be seen in Fig. 1—as well as the direction of motion.

Two sonic anemometers of the same type are mounted at 50 and 90 m altitude on the tower. These sensors provide a fast sampling of the three wind-vector components at 20 Hz, with a measurement range from 0 to 60 m s^{-1} and a declared accuracy of 0.01 m s^{-1} at 5 m s^{-1}. Due to their ability to resolve turbulence eddies at 10 Hz, these sensors are considered reliable references.

On 17 and 18 June 2021, several flights were conducted under variable atmospheric conditions, covering a range of 0.3–12.2 m s^{-1}. In these missions, the UAS hovered alongside the tower at the same altitude as the anemometers. A safety distance of approximately 10 m was maintained between the tower and the aircraft. During the wind validation, eight flights were conducted, with a total hovering time of more than 1.5 h (Table 4).

A 10 Hz resampling has been performed on the sonic anemometer data so that the multicopter data can be compared. To identify a potential time lag due to the safe distance between the UAS and tower, a cross correlation has been performed between the UAS and tower data. After synchronizing the two data series, the lag was removed.

1) NOISE LEVEL ANALYSIS

For understanding the minimum time scales of atmospheric eddies that the multicopter can resolve and where noise levels corrupt the measurements, the power spectral density (PSD) of horizontal wind can be useful. The average spectrum of all our flights (orange line in Fig. 9) was calculated using raw 10 Hz UAS data. Anemometer data are used to compute the blue spectrum. Kolmogorov (1941) −5/3 decay in quasi-isotropic turbulence is represented by the black line. In Fig. 9, there is a significant agreement between the multicopter and the reference up to 0.1 Hz (once every 10 s). No significant difference is present between the two different wind estimation models.

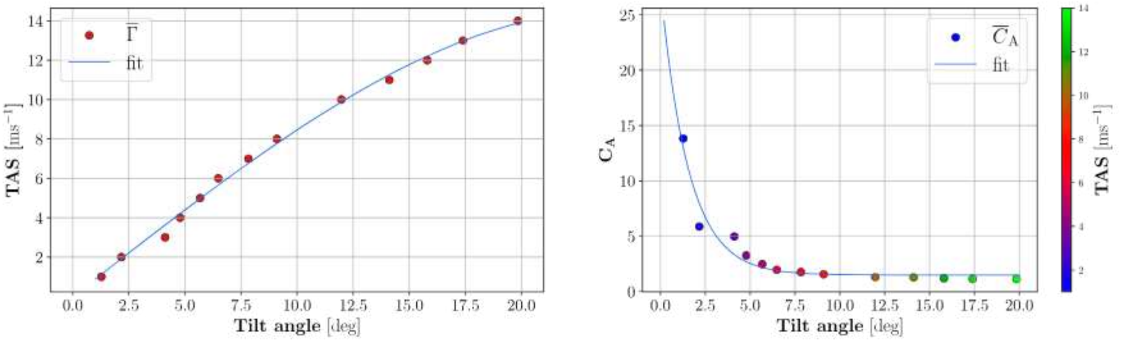

(a)

(b)

FIG. 8. (a) The red points mark the tilt angle data of Eq. (34) (after the postprocessing wind disturbance correction where GS = TAS). The blue line represents a third-order polynomial fit from (35) between the tilt angle and horizontal wind velocity. (b) The points mark the extended drag coefficient data of Eq. (33) (after the postprocessing wind disturbance correction where GS = TAS). The color map represents the true airspeed. The blue line represents the exponential decay of the C_A model in (36).

2) WIND SPEED AND DIRECTION RETRIEVAL ANALYSIS

For comparison of the time series, data have been resampled to 0.2 Hz (once every 5 s to prevent aliasing) based on the PSD plots: by doing so, unwanted oscillations are removed, and the analysis becomes more meaningful.

The plot of the flight No. 7 at 90 m is presented as an example in Fig. 10. During this mission the wind velocity varied between 5 and 11 m s^{-1}. The black line in Fig. 10a represents the ultrasonic anemometer (reference), while the green and red lines represent the result of the two wind estimation models together with their uncertainty bands. In Fig. 10b the wind direction estimation is plotted against the reference direction. Overall agreement is satisfactory. There is only a systematic discrepancy between UAS and sonics in the wind direction (usually around 15°). The complete time-series plot can be found in appendix B.

Figure 11 shows the comparison of the complete dataset collected during the 8 validation flights. It is possible to notice how low winds cause the accuracy of both models to decrease. In general, it was noticed a higher deviation of the two model with respect to the sonic when the wind speed was lower than 3 m s^{-1}. Since uniform band filtering of calibration data results in a higher percentage error at low speeds, both models are susceptible to errors in these conditions. For the C_A model, the drag coefficient uncertainty is higher at low calibration speeds. Last, Fig. 8 show that the average of velocity 3 m s^{-1} is not as close to the fit as the others, which indicates that the fitting could introduce errors depending on the wind speed.

TABLE 3. ERA5 surface wind speed and the wind speed obtained by solving Eqs. (31) and (32) (UAS WS: $\sqrt{u^2 + v^2}$) for the four calibration flights. The UAS WS is the average of the atmospheric wind speeds obtained for each GS during one mission.

No.	Start (UTC)	ERA5 WS (m s^{-1})	UAS WS (m s^{-1})
1	1403	≤1	0.47
2	1442	≤1	0.15
3	1533	≈2	1.60
4	1606	≈2	1.76

Figure 11 shows also a tendency of the C_A model to deviate from the linear behavior for the highest wind speeds recorded. This effect could be possibly corrected by either selecting a different fit function by extending the calibration GS range so that the final value of the extended drag coefficient could be better identified.

Table 5 presents the mean bias error (MBE) and RMSE for the two types of models. From the results, the accuracy of the two models is comparable and falls below 0.7 m s^{-1} after subtracting the MBE from both signals. Even though the DJI S900 multicopter modified for this study is several kilograms heavier than the other systems, the RMSE is close to previous studies.

MBE and the RMSE for the direction estimation are also reported in Table 5. The main issue in the direction estimation is the presence of a constant offset between the multicopter and the reference sensor of around 15° also reported by Wetz et al. (2021). The computation of the direction involved the yaw angle [Eq. (26)]: there is a possibility that the magnetometer has drifted from its original calibration or is simply slightly moved with respect to its original position, resulting in the constant offset. Wind direction variation is well captured by the multicopter, and the corrected RMSE is below 8°.

b. Parallel flights

To determine if the dome effectively increases the drag of the multicopter, two identical DJI S900s were used in parallel missions where one was equipped with the dome and the other was not. The frames of the multicopters were the same, and the flight controller parameters were also set to be identical for both vehicles. The S900 without the dome was given additional weight to simulate the weight of the dome. The two UAS were commanded to hover at 90 m with a 20 m distance between them, in a way that the wake of one would not affect the other. A total of 3 h of data were recorded between 16 and 22 November 2022 (Table 6) at the German Meteorological Service Boundary Layer Field Site of Falkenberg. During these days the copter with the dome recorded tilt angles ranging from 3° to 19.5°. This provided sufficient data for comparison across a large portion of the recorded tilt angles during the calibration flights. A cross correlation was performed on the raw time series of the two multicopters to correct

TABLE 4. Validation flights summary. The wind speed and direction range refers to the ultrasonic anemometer data.

No.	Date	Start (UTC)	End (UTC)	Wind speed range (m s^{-1})	Wind direction range
1	17 Jun 2021	0940	0957	2.0–10.0	90°–182°
2	17 Jun 2021	1106	1123	1.6–10.6	80°–193°
3	17 Jun 2021	1311	1328	0.3–8.2	94°–187°
4	18 Jun 2021	0815	0832	1.9–9.6	91°–219°
5	18 Jun 2021	0946	0954	2.6–10.1	103°–196°
6	18 Jun 2021	1054	1111	1.2–11.5	109°–219°
7	18 Jun 2021	1256	1301	3.3–12.2	109°–175°
8	18 Jun 2021	1319	1336	1.8–11.9	115°–200°

for any potential delays due to the different hovering positions. The data were then resampled to a frequency of 0.2 Hz.

Figure 12 illustrates the comparison of tilt angles between the two systems. It is evident that the multicopter with the Styrofoam sphere consistently measures higher values for the tilt angle. The linear fit (red line) indicates a 16% increase in tilt angle resulting from the larger cross-sectional area. This means that for the same input range (wind speed), the output (tilt angle) will be spread over a wider range, increasing the sensitivity of the copter as a wind sensor.

5. Discussion

a. Advantages of the multicopter shell

The spherical Styrofoam shell that encloses the multicopter offers several advantages. First, it protects the exposed electronics from precipitation and damage. Second, its symmetric shape ensures that the same cross-sectional area is always exposed to the wind, regardless of the wind direction. This is similar to the approach taken by Neumann and Bartholmai (2015), who used a quadcopter with a nearly symmetric, cylindrical fuselage for wind measurement and found that the radial orientation of the system to the wind direction was negligible. The same can be said for the spherical shell and hexacopter configuration used in this study, as it offers an even more symmetric shape than a quadcopter with four rotors.

The modified DJI S900 utilized in this study has a significantly larger fuselage cross section compared to the unmodified DJI S900, leading to an increase in air resistance but only a moderate increase in weight. This causes the multicopter to adopt a larger tilt angle in order to compensate for wind speed. Figure 13a shows the relationship between input (wind speed) and output (tilt angle) for both copter configurations. The line corresponding to the no dome configuration was obtained by lowering the direct model fit function by 16%. While the sensitivity is not constant due to the polynomial fit, the configuration with the dome always has a 16% higher local sensitivity than the no dome configuration (Fig. 13b).

b. Parameters' influence: Vertical velocity and mass

To a first approximation, the presence of a vertical wind velocity and the change in UAS mass have similar effects on the system despite their substantial differences.

So far, the vertical wind component has been ignored. However, its presence would create a drag force that would add or subtract weight to the system. Furthermore, a change in the UAS mass, such as one resulting from a different battery configuration or the addition of new sensors, affects the vertical force component as well.

Using constant flight speed/incoming wind speed as a calibration condition (denoted with subscript c), the following approximation [derived from Eq. (22)] holds for small tilt angle values:

$$\Gamma_c = \arctan\left(\frac{D}{2m_c g}\right) \approx \frac{D}{2m_c g}. \tag{37}$$

Then a variation in the vertical force component ΔF_z result in a modified tilt angle Γ_Δ:

$$\Gamma_\Delta \approx \frac{D}{2m_c g + \Delta F_z}. \tag{38}$$

This equation holds if the drag—the extended drag coefficient C_A—does not vary sensibly with the tilt: this happens, in our case, for wind speeds higher than 8 m s^{-1}.

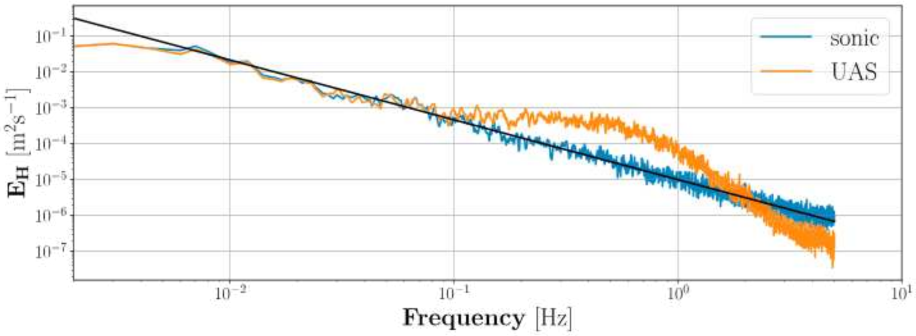

FIG. 9. Comparison between the power spectral density of the horizontal wind speed of the sonic anemometer (blue) and the UAS (orange). The black line is reported as a reference of the Kolmogorov −5/3 turbulence decay law.

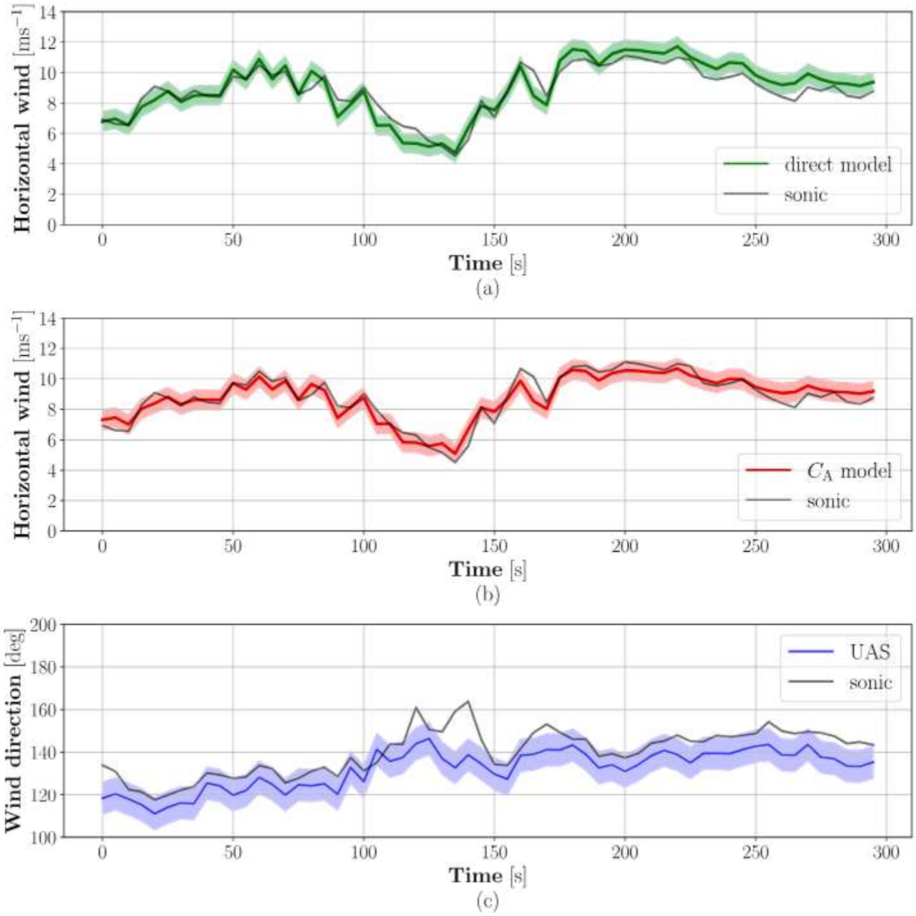

FIG. 10. Comparison between the horizontal wind vector detected by the ultrasonic anemometer (black) and by the multicopter. The plots show around 300 s of hovering at 90 m altitude for flight 7. All the time series have been resampled to 0.2 Hz for the comparison. (a),(b) Wind magnitude obtained with the two models using the UAS tilt angle (green and red). (c) Horizontal wind direction.

1) VERTICAL WIND SPEED

For vertical wind disturbances, the magnitude of the disturbance force,

$$\Delta F_z = f(t), \tag{39}$$

is typically a function of time and can vary in complexity, ranging from being a constant term in the case of complex terrain (zum Berge et al. 2021), to being time dependent when encountering a rising column of warm air (thermal). This variation in the vertical wind component can introduce bias in the estimation of horizontal wind, potentially making it difficult to identify and maintain consistency during a single flight. Since the calibration flights were conducted over flat terrain, it is unlikely that the calibration data will be offset in a constant manner. Furthermore, the amount of data gathered for each flight velocity is sufficient to filter out any possible vertical gusts.

In a first approximation the ratio between the tilt angle at calibration conditions and the distorted tilt angle will be

$$\frac{\Gamma_c}{\Gamma_\Delta} = \frac{m_c g + \Delta F_z}{m_c g}. \tag{40}$$

Then the undesired tilt angle will be

$$\Gamma_\Delta = \frac{m_c g}{m_c g + \Delta F_z}\Gamma_c. \tag{41}$$

To have a 10% variation in the tilt angle when the weight force of the multicopter is 70°N (see Table 1) and assuming the same $C_A(\Gamma)$ relation for the vertical extended drag coefficient, a w component of 5–6 m s^{-1} would be necessary. In reality, such values are infrequent for vertical atmospheric winds; however, if the multicopter was lighter, this influence would be stronger.

2) MASS

With different payload configurations, ΔF_z will be constant with respect to time (for electrical propulsion):

$$\Delta F_z = \Delta m g. \tag{42}$$

Similar to the previous case, the distorted tilt angle will become

$$\Gamma_\Delta = \frac{m_c g}{m_c g + \Delta m g}\Gamma_c. \tag{43}$$

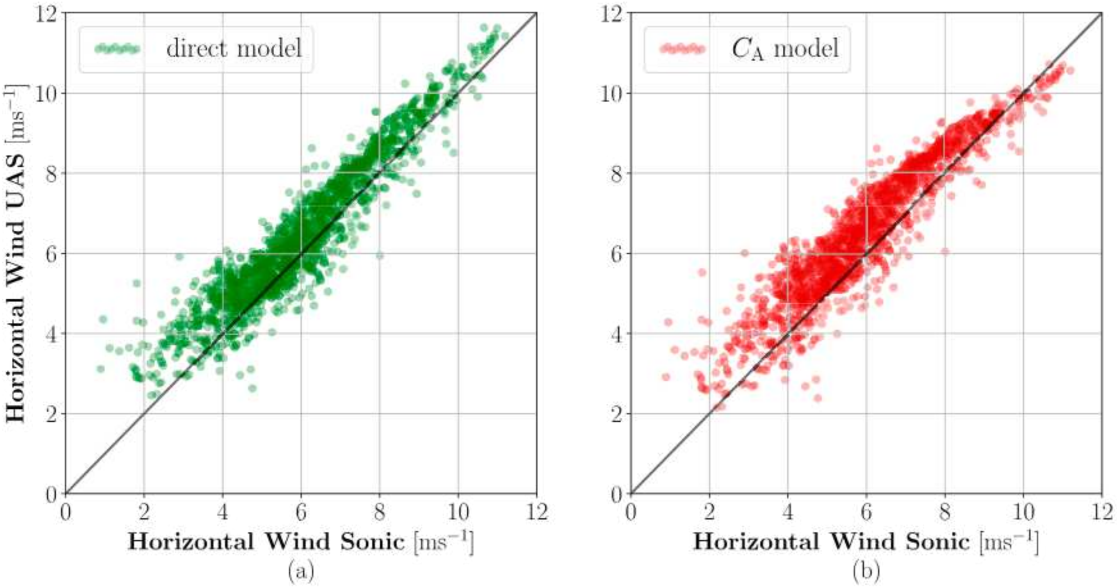

FIG. 11. Comparison between the horizontal wind vector detected by the ultrasonic anemometer and by the multicopter throughout all the eight validation flights. (a) Wind magnitude obtained with the direct model. (b) Wind magnitude obtained with the C_A model.

In this situation, however, 700 g are enough to achieve a 10% variation of the tilt angle. For our specific case, mass variations of 1 kg are completely reasonable (a single 12.000 mAh battery weighs 1.5 kg).

As the mass is unchanged during calibration flights, a variation in the multicopter mass introduces a constant bias into the direct model (section 1). As the $C_A(\Gamma)$ function becomes approximately constant at high wind speeds, an increase in mass should not affect the extended drag coefficient model. With a constant extended drag coefficient, according to Eq. (24), the parameters defining the wind speed (air density, multicopter mass, tilt angle, and C_A itself) are all independent. It is sufficient to weigh the system and insert the correct mass value in the equation. However, at low wind speeds also the C_A model depends on the multicopter mass since the extended drag coefficient is not constant anymore. In this specific range the C_A is still a function sensible to any change of tilt angle and therefore sensible changes of mass. Due to the nonlinearity of Eq. (38), it is difficult to estimate the influence since changing the denominator will also change the drag force sensibly.

c. Parameters' influence: Air density

Variations in air density modify the horizontal component of the force system by altering drag. Because C_A also varies with tilt angle, estimating the effect of this variation is not straightforward:

$$\Gamma_c = \arctan\left[\frac{\rho_c V^2 C_A(\Gamma)}{2mg}\right] \approx \frac{\rho_c V^2 C_A(\Gamma)}{2mg}. \tag{44}$$

If a density variation is present, then

$$\frac{\Gamma_c}{\Gamma_\Delta} = \frac{\rho_c C_A(\Gamma_c)}{\rho_\Delta C_A(\Gamma_\Delta)}. \tag{45}$$

Under the conditions in which the ratio between the two drag coefficient is almost 1, so for wind speeds above 8 m s^{-1} the distorted tilt angle will be

$$\Gamma_\Delta = \frac{\rho_\Delta}{\rho_c}\Gamma_c. \tag{46}$$

The calibration took place at $\rho_c = 1.181$ kg m^{-3}. If the system is used under different atmospheric conditions, the direct model will always have a constant offset in the wind estimation. For instance, in an environment with $\rho_\Delta = 0.95$ kg m^{-3}, the tilt angle is approximately reduced by 20%. The C_A model avoids this offset by taking air density into account. The UAS must be equipped with additional sensors in order to obtain this information, since the autopilot alone cannot do it.

TABLE 5. Statistics of the wind-vector estimation. The RMSE is computed after removing the MBE between the multicopter and ultrasonic anemometer signals.

	MBE	RMSE	Unit
Direct model	0.32	0.64	m s^{-1}
C_A model	0.57	0.66	m s^{-1}
Direction	−14.7	7.6	°

TABLE 6. Parallel flights summary.

No.	Date	Start (UTC)	End (UTC)	Tilt angle range
1	16 Nov 2022	1110	1134	7.9°–17.7°
2	16 Nov 2022	1352	1416	6.2°–11.7°
3	17 Nov 2022	0940	1002	7.3°–19.4°
4	17 Nov 2022	1055	1119	6.1°–15.7°
5	17 Nov 2022	1238	1304	7.4°–18.8°
6	18 Nov 2022	0938	0958	6.0°–15.7°
7	18 Nov 2022	1104	1127	6.9°–14.9°
8	22 Nov 2022	0854	0915	3.0°–8.9°
9	22 Nov 2022	1054	1115	4.3°–8.3°

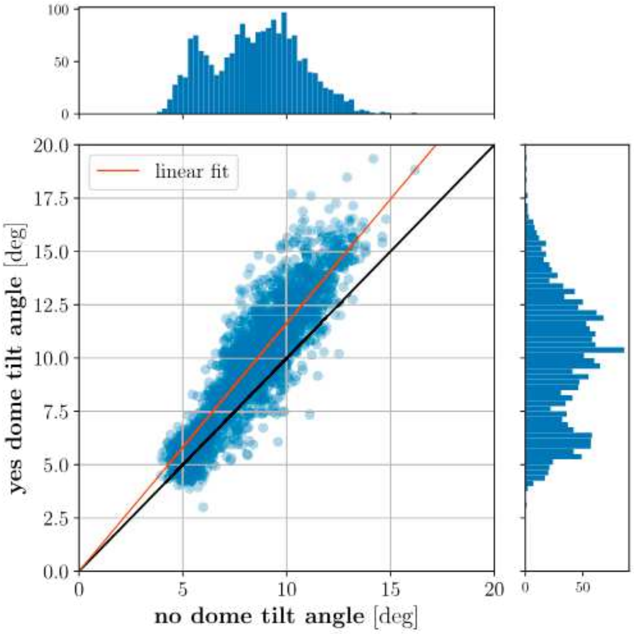

FIG. 12. Comparison of the tilt angle of two DJI S900, one with the sphere and the other one without. In total, 3 h of hovering are plotted with the tilt angle of the UAS with the dome ranging from 3° to 19.5°. The red line represent the linear fit of the cloud of points.

d. Uncertainties and limitations

Calibration should be performed in near-zero wind conditions as explained throughout the text. It is still possible to proceed even in suboptimal conditions with the help of a data correction algorithm. Based on the maximum GS and maximum flight speed of the system, a theoretical limit on atmospheric wind magnitude can be determined:

$$V_{\text{wind}} \leq V_{\text{UAS}}^{\max} - V_{\text{calib}}^{\max}. \qquad (47)$$

The maximum airspeed of the UAS, denoted as $V_{\text{UAS}}^{\max}$, is typically provided by the UAS manufacturer or determined through field tests by commanding full forward input. In our study, the value of $V_{\text{UAS}}^{\max}$ (19 m s^{-1}) was obtained using the latter method. On the other hand, $V_{\text{calib}}^{\max}$ is entirely at the discretion of the user. In most cases, one would aim to map a wide range of values. However, due to the necessity of incorporating excessively long straight sections into the flight path, a compromise needs to be reached when considering the highest values. Consequently, in this study, we selected a value of 14 m s^{-1} as the maximum calibrated airspeed. This choice was made specifically to avoid the need for beyond visual line of sight (BVLOS) operations when mapping higher speeds.

The system can only maintain a constant GS under the conditions of Eq. (47). Nevertheless, we do not take into account gusts when calculating this simple equation. It is precisely gusts that destabilize the system during flight. In light of the autopilot's ability to stabilize the vehicle without creating a hazardous situation, the maximum atmospheric wind speed will have to be reevaluated.

Using steady equilibrium as a basis, the differential equations describing the motion of the UAS can be simplified advantageously in this study. As a result, it is possible to derive the key equation of the model, Eq. (24) in a matter of steps. However, it is assumed that the copter tilt angle represents the actual wind speed at any given time. This hypothesis ignores any transients that may occur during a flight. It is necessary to build more complex models that also incorporate the dynamics of the system in order to explain this phenomenon. Nevertheless, this would require accurate analysis of the

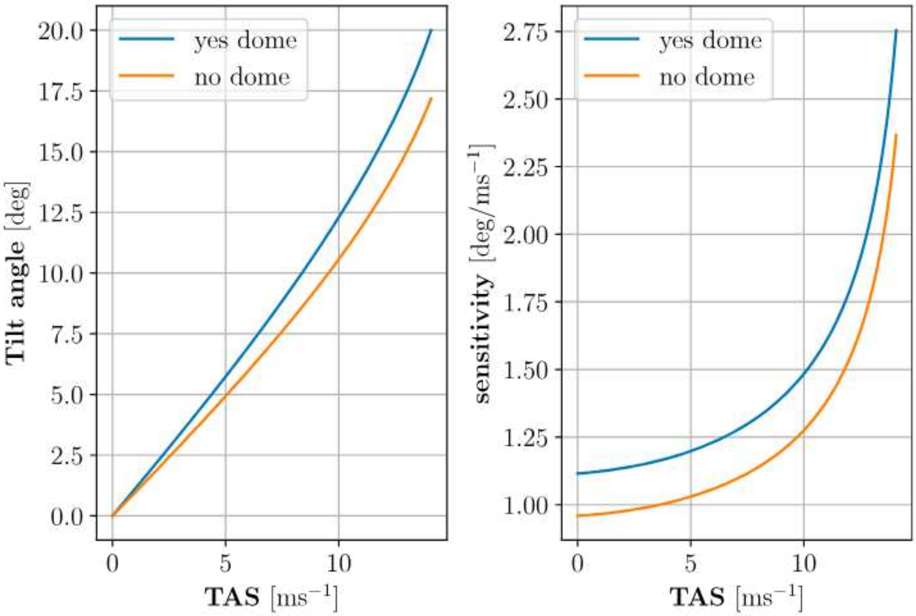

(a) (b)

FIG. 13. (a) Dome and no dome calibration curves comparison. (b) Dome and no dome sensitivity comparison.

aircraft's geometric and aerodynamic characteristics (e.g., moments of inertia around the three axes of rotation).

6. Conclusions and outlook

To develop models for estimating horizontal wind, we performed a series of perpendicular flights at constant ground speed using a multicopter. This method allows us to gather valuable data without the need for wind tunnels or meteorological masts. It is important to conduct the calibration flights under specific weather conditions, such as no wind, to ensure high data quality. However, even if wind is present, a heuristic postprocessing method can be used to filter out the wind disturbance components and still calibrate the models. A pseudocode of the whole calibration and postprocessing procedure can be found in appendix C.

To improve the symmetry of the system, we enclosed the multicopter body and electronics in a Styrofoam dome. This design allows only the roll and pitch angles to be used to calculate the tilt angle. Additionally, the sphere shape allows aerodynamic forces to be uniformly generated in response to wind coming from any direction, resulting in more regular tilting with respect to the wind. Furthermore, by increasing the cross-sectional area of the UAS, we were able to increase the sensitivity of the system to wind speed.

Using UAS tilt angle data, two different models have been developed to estimate horizontal wind:

- A direct approach where the data from the calibration flights have been used in order to generate a relation between the tilt angle and the horizontal wind speed.
- An indirect approach where the same data have been used to generate a relation between the tilt angle and the extended drag coefficient C_A.

An ultrasonic anemometer reference sensor was used to compare and test both models. The multicopter's ability to resolve wind speed to a frequency of 10^{-1} Hz was confirmed by following the $-5/3$ turbulence decay. The models had RMSEs lower than 0.7 m s^{-1} for velocities ranging from 0.3 to 12 m s^{-1}.

The direct model always applies a constant offset if parameters such as the multicopter's mass or air density change. In contrast, the C_A model uses those parameters as inputs, so it is not affected by errors caused by changes in air density and is less affected by variations in payload.

The wind direction is also calculated through a direct relationship between all three Euler angles. Once the offset is identified, the RMSE drops below 8°.

Using a dual GPS module configuration could improve future developments. This would allow for calculation of the vehicle's heading without relying on a compass, which is the primary source of uncertainty.

The C_A model could be further improved by conducting additional calibration flights with increasing payloads. This would allow the extended drag coefficient to become a function of two parameters (tilt angle and mass), eliminating the bias at lower speeds.

For lighter copters, higher sampling frequencies and correlation of the power delivered by the motors with the tilt angle could be used to study the vertical wind component w, due to their lower inertia.

Acknowledgments. We thank Frank Beyrich and the German Meteorological Service (DWD) for providing the infrastructure at the MOL-RAO and the ultrasonic anemometer data. The measurements in Falkenberg, which provided the data for the validation, were performed as a supplement to a lidar validation flight project funded by the DWD under the funding code 4819EMF01 (VALUAS).

Data availability statement. The data are available from the author upon request.

APPENDIX A

S900 Configuration

Figure A1 presents the details of the DJI S900 UAS system.

FIG. A1. Exploded view of the DJI S900 frame together with the custom built Styrofoam dome.

APPENDIX B

Full Time Series

Figures B1 and B2 present comparisons between the horizontal wind vector detected by the ultrasonic anemometer (black) and by the multicopter at 50 and 90 m, respectively.

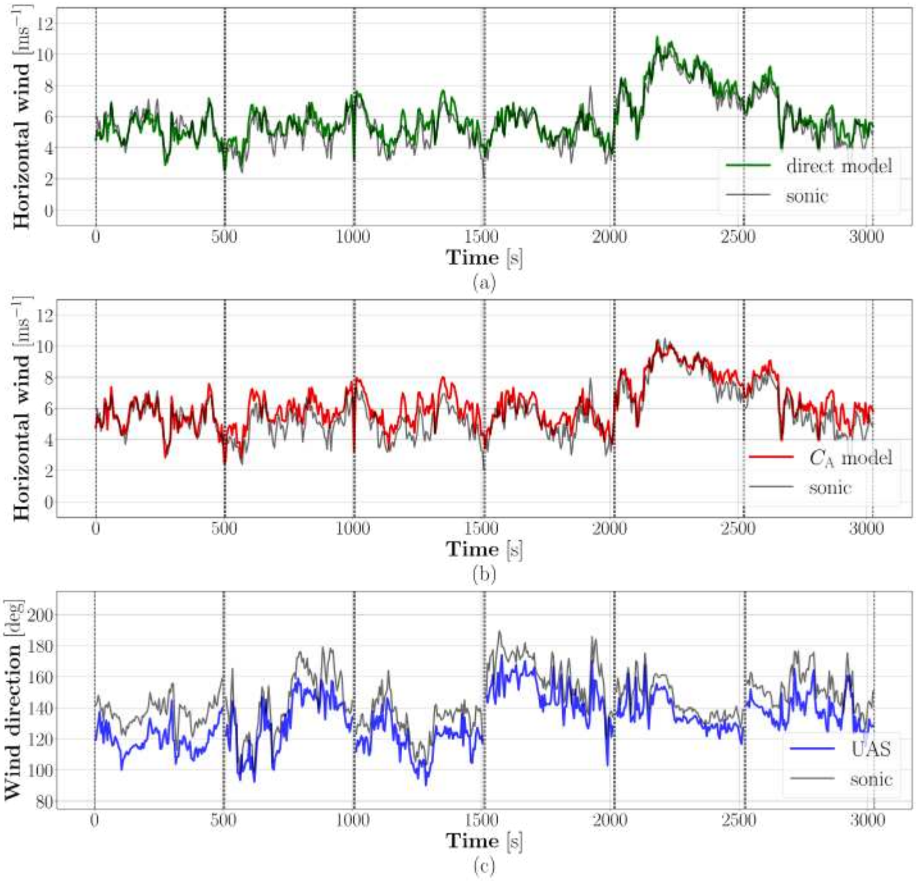

FIG. B1. Comparison between the horizontal wind vector detected by the ultrasonic anemometer (black) and by the multicopter. The plots show all the available hovering data at 50 m altitude. All the time series have been resampled to 0.2 Hz for the comparison. (a),(b) Wind magnitude obtained with the two models using the UAS tilt angle (green and red). (c) Horizontal wind direction.

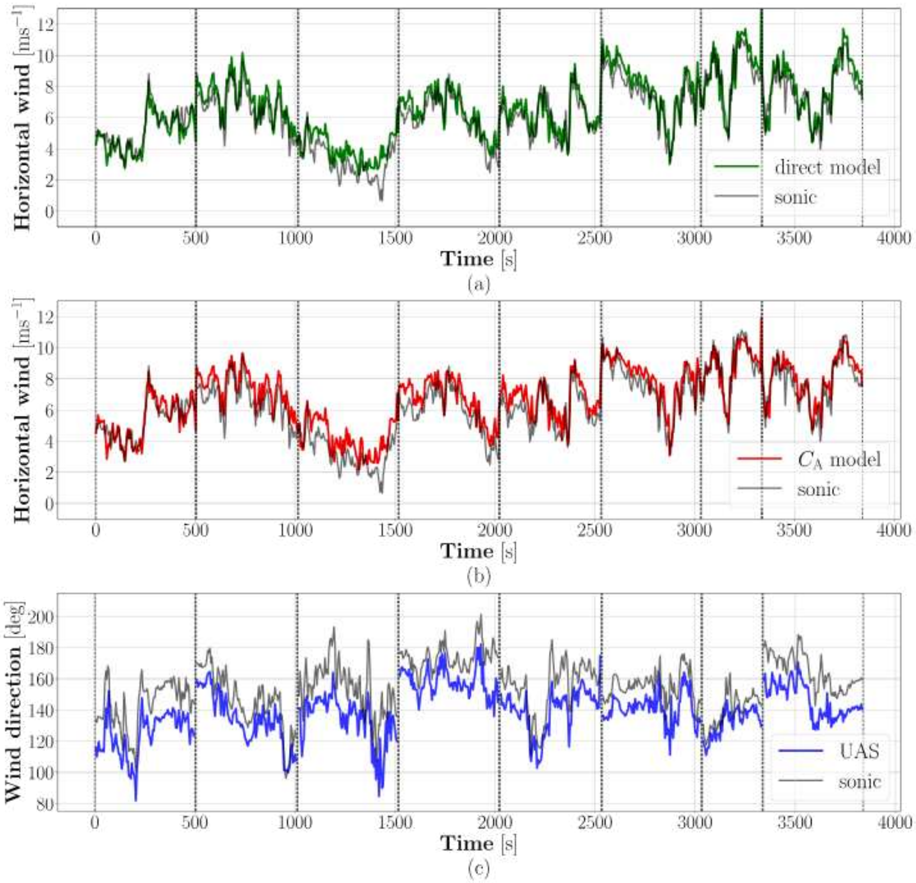

FIG. B2. Comparison between the horizontal wind vector detected by the ultrasonic anemometer (black) and by the multicopter. The plots show all the available hovering data at 90 m altitude. All the time series have been resampled to 0.2 Hz for the comparison. (a),(b) Wind magnitude obtained with the two models using the UAS tilt angle (green and red). (c) Horizontal wind direction.

APPENDIX C

Pseudocode for UAS Calibration

```
PSEUDOCODE

HYPOTHESES
Steady ($\ddot{\mathbf{x}} = 0$ and $\dot{\boldsymbol{\omega}} = 0$) equilibrium conditions
  ($\dot{\mathbf{x}} = \dot{\mathbf{x}}_{eq}$ and $\boldsymbol{\omega} = 0$)
Horizontal flight (with zero vertical wind speed)

FLIGHTS
In a day of low wind ($<1$ m s$^{-1}$)
for every GS in GS range do
    Perform UAS forward and backward flights
end for

DATA
for each flight do
    for each GS do
        Filter data around the desired GS
        Separate forward and backward sections
        Use Euler angle to compute the tilt angles [Eq. (8)] → $\Gamma_F$, $\Gamma_B$
        Compute drag coefficients [Eq. (28)] → $C_{A,F}$, $C_{A,B}$
        Apply heuristic data correction [Eqs. (33) and (34)] → $\overline{C}_A$, $\overline{\Gamma}$
    end for
end for
Average data of all flights performed
Perform fit in order to obtain the calibration curves
```

REFERENCES

Abichandani, P., D. Lobo, G. Ford, D. Bucci, and M. Kam, 2020: Wind measurement and simulation techniques in multi-rotor small unmanned aerial vehicles. *IEEE Access*, **8**, 54 910–54 927, https://doi.org/10.1109/ACCESS.2020.2977693.

Anderson, J. D., 2011: *Fundamentals of Aerodynamics*. 5th ed. McGraw-Hill, 1106.

Barbieri, L., and Coauthors, 2019: Intercomparison of small unmanned aircraft system (sUAS) measurements for atmospheric science during the LAPSE-RATE campaign. *Sensors*, **19**, 2179, https://doi.org/10.3390/s19092179.

Beard, R. W., and T. W. McLain, 2012: *Small Unmanned Aircraft: Theory and Practice*. Princeton University Press, 320 pp.

Bell, T. M., B. R. Greene, P. M. Klein, M. Carney, and P. B. Chilson, 2020: Confronting the boundary layer data gap: Evaluating new and existing methodologies of probing the lower atmosphere. *Atmos. Meas. Tech.*, **13**, 3855–3872, https://doi.org/10.5194/amt-13-3855-2020.

Bramati, M., M. Schön, D. Schulz, V. Savvakis, J. Bange, and A. Platis, 2022: A stand-alone calibration approach for attitude-based multi-copter wind measurement systems. *Atmos. Meas. Tech.*, https://doi.org/10.5194/amt-2022-113.

Brosy, C., K. Krampf, M. Zeeman, B. Wolf, W. Junkermann, K. Schäfer, S. Emeis, and H. Kunstmann, 2017: Simultaneous multicopter-based air sampling and sensing of meteorological variables. *Atmos. Meas. Tech.*, **10**, 2773–2784, https://doi.org/10.5194/amt-10-2773-2017.

Chilson, P. B., and Coauthors, 2019: Moving towards a network of autonomous UAS atmospheric profiling stations for observations in the Earth's lower atmosphere: The 3D mesonet concept. *Sensors*, **19**, 2720, https://doi.org/10.3390/s19122720.

Chioncel, C., C. Petru, and N. Gillich, 2011: Overview of classic and modern wind measurement techniques, basis of wind project development. *An. Univ. Eftimie Murgu*, **18**, 73–80.

Crowe, D., R. Pamula, H. Y. Cheung, and S. F. De Wekker, 2020: Two supervised machine learning approaches for wind velocity estimation using multi-rotor copter attitude measurements. *Sensors*, **20**, 5638, https://doi.org/10.3390/s20195638.

Donnell, G. W., J. A. Feight, N. Lannan, and J. D. Jacob, 2018: Wind characterization using sUAS. *2018 Atmospheric Flight Mechanics Conf.*, Atlanta, GA, AIAA, AIAA 2018-2986, https://doi.org/10.2514/6.2018-2986.

Ewald, B., and Coauthors, 1998: Wind tunnel wall correction. NATO AGARD Rep. AGARD-AG-336, 560 pp.

Gonzalez-Rocha, J., C. A. Woolsey, C. Sultan, N. Rose, and S. F. De Wekker, 2017: Measuring atmospheric winds from quadrotor motion. *AIAA Atmospheric Flight Mechanics Conf.*, Grapevine, TX, AIAA, AIAA 2017-1189, https://doi.org/10.2514/6.2017-1189.

——, ——, ——, and S. F. De Wekker, 2019: Sensing wind from quadrotor motion. *J. Guid. Control Dyn.*, **42**, 836–852, https://doi.org/10.2514/1.G003542.

Hersbach, H., and Coauthors, 2018: ERA5 hourly data on single levels from 1979 to present. C3S CDS, accessed 17 January 2022, https://doi.org/10.24381/cds.adbb2d47.

Kolmogorov, A., 1941: The local structure of turbulence in incompressible viscous fluid for very large Reynolds' numbers. *Akad. Nauk SSSR Dokl.*, **30**, 301–305.

Meier, K., R. Hann, J. Skaloud, and A. Garreau, 2022: Wind estimation with multirotor UAVs. *Atmosphere*, **13**, 551, https://doi.org/10.3390/atmos13040551.

Neumann, P. P., and M. Bartholmai, 2015: Real-time wind estimation on a micro unmanned aerial vehicle using its inertial measurement unit. *Sens. Actuators*, **235A**, 300–310, https://doi.org/10.1016/j.sna.2015.09.036.

Palomaki, R. T., N. T. Rose, M. van den Bossche, T. J. Sherman, and S. F. De Wekker, 2017: Wind estimation in the lower atmosphere using multirotor aircraft. *J. Atmos. Oceanic Technol.*, **34**, 1183–1191, https://doi.org/10.1175/JTECH-D-16-0177.1.

Pinto, J. O., and Coauthors, 2021: The status and future of small uncrewed aircraft systems (UAS) in operational meteorology. *Bull. Amer. Meteor. Soc.*, **102**, E2121–E2136, https://doi.org/10.1175/BAMS-D-20-0138.1.

Platis, A., and Coauthors, 2020: Long-range modifications of the wind field by offshore wind parks—Results of the Project WIPAFF. *Meteor. Z.*, **29**, 355–376, https://doi.org/10.1127/metz/2020/1023.

——, and Coauthors, 2021: Evaluation of a simple analytical model for offshore wind farm wake recovery by in situ data and Weather Research and Forecasting simulations. *Wind Energy*, **24**, 212–228, https://doi.org/10.1002/we.2568.

Prudden, S., A. Fisher, M. Marino, A. Mohamed, S. Watkins, and G. Wild, 2018: Measuring wind with small unmanned aircraft systems. *J. Wind Eng. Ind. Aerodyn.*, **176**, 197–210, https://doi.org/10.1016/j.jweia.2018.03.029.

Segales, A. R., B. R. Greene, T. M. Bell, W. Doyle, J. J. Martin, E. A. Pillar-Little, and P. B. Chilson, 2020: The CopterSonde: An insight into the development of a smart unmanned aircraft system for atmospheric boundary layer research. *Atmos.*

Meas. Tech., **13**, 2833–2848, https://doi.org/10.5194/amt-13-2833-2020.

Shimura, T., M. Inoue, H. Tsujimoto, K. Sasaki, and M. Iguchi, 2018: Estimation of wind vector profile using a hexarotor unmanned aerial vehicle and its application to meteorological observation up to 1000 m above surface. *J. Atmos. Oceanic Technol.*, **35**, 1621–1631, https://doi.org/10.1175/JTECH-D-17-0186.1.

Varentsov, M., and Coauthors, 2021: Balloons and quadcopters: Intercomparison of two low-cost wind profiling methods. *Atmosphere*, **12**, 380, https://doi.org/10.3390/atmos12030380.

Wang, J.-Y., B. Luo, M. Zeng, and Q.-H. Meng, 2018: A wind estimation method with an unmanned rotorcraft for environmental monitoring tasks. *Sensors*, **18**, 4504, https://doi.org/10.3390/s18124504.

Waslander, S. L., and C. Wang, 2009: Wind disturbance estimation and rejection for quadrotor position control. *AIAA Infotech@Aerospace Conf.*, Seattle, WA, AIAA, I@A-47, https://doi.org/10.2514/6.2009-1983.

Wetz, T., N. Wildmann, and F. Beyrich, 2021: Distributed wind measurements with multiple quadrotor unmanned aerial vehicles in the atmospheric boundary layer. *Atmos. Meas. Tech.*, **14**, 3795–3814, https://doi.org/10.5194/amt-14-3795-2021.

Wildmann, N., and T. Wetz, 2022: Towards vertical wind and turbulent flux estimation with multicopter uncrewed aircraft systems. *Atmos. Meas. Tech.*, **15**, 5465–5477, https://doi.org/10.5194/amt-15-5465-2022.

zum Berge, K., and Coauthors, 2021: A two-day case study: Comparison of turbulence data from an unmanned aircraft system with a model chain for complex terrain. *Bound.-Layer Meteor.*, **180**, 53–78, https://doi.org/10.1007/s10546-021-00608-2.

Validation of Doppler Wind Lidar Measurements with an Uncrewed Aircraft System (UAS) in the Daytime Atmospheric Boundary Layer

JAKOB BOVENTER,[a] MATTEO BRAMATI,[a] VASILEIOS SAVVAKIS,[a] FRANK BEYRICH,[b] MARKUS KAYSER,[b]
ANDREAS PLATIS,[a] AND JENS BANGE[a]

[a] *Eberhard Karls Universität Tübingen, Geo- und Umweltforschungszentrum, Tübingen, Germany*
[b] *Meteorological Observatory Lindenberg–Richard-Aßmann-Observatory, German Meteorological Service (DWD)*

(Manuscript received 21 September 2023, in final form 4 April 2024, accepted 7 May 2024)

ABSTRACT: One of the most widely used systems for wind speed and direction observations at meteorological sites is based on Doppler wind lidar (DWL) technology. The wind vector derivation strategies of these instruments rely on the assumption of stationary and homogeneous horizontal wind, which is often not the case over heterogeneous terrain. This study focuses on the validation of two DWL systems, operated by the German Weather Service [Deutscher Wetterdienst (DWD)] and installed at the boundary layer field site Falkenberg (Lindenberg, Germany), with respect to measurements from a small, fixed-wing uncrewed aircraft system (UAS) of the type Multi-Purpose Airborne Sensor Carrier (MASC-3). A wind vector intercomparison at an altitude range from 100 to 500 m between DWL and UAS is performed, after a quality control of the aircraft's data accuracy against a cup anemometer and wind vane mounted on a meteorological mast also operating at the location. Both DWL systems exhibit an overall root-mean-square difference in the wind vector retrieval of less than 22% for wind speed and lower than 18° for wind direction. The enhancement or deterioration of these statistics is analyzed with respect to scanning height and atmospheric stability. The limitations of this type of validation approach are highlighted and accounted for in the analysis.

KEYWORDS: Wind; Instrumentation/sensors; Lidars/Lidar observations; Measurements; Remote sensing; Unpiloted aerial systems

1. Introduction

Doppler wind lidar (DWL) systems are used in a broad spectrum of applications like quasi-operational measurements of the wind vector at meteorological observation sites (Päschke et al. 2015), wind profiling from satellites (Chanin et al. 1992; Witschas et al. 2020), detection of gravity waves in the strato- and mesosphere (Baumgarten et al. 2015), monitoring wind shear for flight safety (Nechaj et al. 2019), or wind energy applications (Käsler et al. 2010; Liu et al. 2019; Wildmann et al. 2019). Numerical weather prediction (NWP) models need vertical profiles of state and process variables in the atmospheric boundary layer (ABL) to improve the prescription of initial conditions for the simulations (Knist et al. 2018).

Common measuring strategies for deriving the horizontal wind vector from DWL measurements are the Doppler beam swinging (DBS) and the velocity–azimuth display (VAD) method (Reitebuch and Hardesty 2021). Both scanning strategies rely on the assumption of homogeneity and stationarity of the horizontal wind vector in the analyzed air volume during the scan. However, these conditions are usually not fulfilled in reality, especially over heterogeneous terrain. Hence, a detailed quantification of the statistical uncertainty and systematic errors of DWL data is required for the different scan strategies and atmospheric conditions (Rahlves et al. 2022). Since calibration and validation of remote sensing instruments in a laboratory are impossible due to their range, resolution, and volume-sensing approach (Reitebuch and Hardesty 2021), there is a need for other validation methods.

There are various approaches to validate DWL data both with numerical simulation and in a real-world scenario. Large-eddy simulations (LES) have been extensively employed to identify DWL errors and uncertainties for different applications and specific flow conditions by implementing virtual lidar models in the simulation domain (Lundquist et al. 2015; Gasch et al. 2020). Rahlves et al. (2022) used LES and showed that the statistical uncertainty of DWL data decreases with increasing averaging time. Moreover, an analysis taking into account the wind field variability highlighted a statistical error in the $O(1)$ m s^{-1} for 10-min averaged wind speed in a moderately convective ABL, while exceeding 2 m s^{-1} in strongly convective conditions. Cohn and Goodrich (2002) compared radar wind profiler (RWP) and DWL data showing a standard deviation of 0.88 m s^{-1} between both systems for the horizontal wind estimation. However, this result is based on a single 2.3-h sample and did not account for variations caused by atmospheric conditions. Päschke et al. (2015) compared a 1-yr dataset of 30-min averages of DWL data with data from an operational 482-MHz RWP and revealed a good agreement between the two systems, with root-mean-square differences ranging between 0.5 and 0.7 m s^{-1} for wind speed and between 5° and 10° for wind direction. Due to the lower altitude limit of the RWP, no comparisons were available for altitudes below 500 m above ground level (AGL) and shorter temporal averages.

Another possible validation method is through the usage of radio soundings. In a 2-day experiment, Ishii et al. (2005)

Denotes content that is immediately available upon publication as open access.

Corresponding author: Matteo Bramati, matteo.bramati@uni-tuebingen.de

DOI: 10.1175/JTECH-D-23-0127.1

showed a good agreement between DWL and radiosonde data, with a mean bias of 0.2 m s^{-1} and 1.4° and a standard deviation of 1.4 m s^{-1} and 3.5°. Mariani et al. (2020) compared in a 19-month campaign, two DWL scanning methods with radiosonde data at three locations in the Arctic region. In their study, both scanning methods utilized 70° elevation angle: the VAD method (eight 45° spaced beams) exhibited a smaller mean bias (-0.27 m s^{-1}) than the DBS method (-0.46 m s^{-1}), both compared to the radiosonde. In the Lidar Measurement Campaign Sola (LIMECS), Kumer et al. (2014) found a strong correlation of horizontal wind between altitudes of 500 and 1325 m, but a weak correlation (correlation coefficient $R = 0.6$) below 500 m. Mariani et al. (2020) and Kumer et al. (2014) observed that the comparability of horizontal wind measurements below 500 m is challenging due to the radiosonde's pendulum motion. Moreover, the vertical resolution is coarse; there is no temporal averaging; and the radiosonde's drift increases the horizontal displacement, collectively contributing to biases. Comparison studies using cup anemometers are limited to the ground (Lawrence et al. 1972), or to the maximum height of a meteorological tower such as 100 m in Smith et al. (2006), or 116 m in Gottschall et al. (2012), Courtney et al. (2008).

Ultimately, there is a gap in data availability at an altitude range between 100 m (towers) and 500 m (due to the unavailability of RWP data and coarse, biased radiosonde data). This gap includes the influence of atmospheric stability on DWL systems, which, according to virtual lidar models employed in LES simulations, is not negligible (Robey and Lundquist 2022) but has not been verified with experimental data (Klaas-Witt and Emeis 2022; Gasch et al. 2020). An accurate validation within this altitude gap and across different ABL stability conditions can be achieved using high-resolution in situ airborne wind measurements by uncrewed aircraft systems (UASs). As pointed out in Bange et al. (2021), a small research UAS delivers as accurate thermodynamic and turbulence data as a large crewed research aircraft although carrying a smaller scientific payload and endurance but at much lower operational costs and logistic efforts. Furthermore, a small research UAS is capable of measuring the three-dimensional turbulent wind vector with very high temporal and spatial resolutions without the disturbing effect of a large fuselage, wings, and propellers (Platis et al. 2016; Rautenberg et al. 2019; zum Berge et al. 2021; Schön et al. 2022). Small UASs were already applied in the past for remote sensing validation (Martin et al. 2011). An overview of meteorological UAS and research aircraft, in general, can be found in Bange et al. (2013, 2021).

In this study, in situ turbulent wind vector measurements were obtained using a UAS of type Multi-Purpose Airborne Sensor Carrier-3 (MASC-3) (Rautenberg et al. 2019). These measurements were carried out by the Environmental Physics Team of the University of Tübingen, Germany, during three intensive observation periods (IOPs) in July 2020, June 2021, and November 2022, in the frame of the Validation of numerical simulations and remote sensing using UAS (VALUAS) project. The goal was to use data provided by the UAS as a reference for assessing the wind speed and direction accuracy between 100 and 500 m AGL of two DWLs operated by the German Weather Service [Deutscher Wetterdienst (DWD)].

FIG. 1. The position of the measurement site, GM Falkenberg, about 60 km southeast of Berlin, Germany.

The experiments' motive was for the following questions to be addressed:

- How much does the spatial separation of the DWL beam and the UAS flight path limit the comparability?
- Is there an altitude dependence of the intercomparison results between the DWL and UAS wind measurements?
- Does atmospheric stability influence the intercomparison results?

The manuscript is structured as follows: in section 2, the instruments (UAS, meteorological tower, and DWL including scan strategy), the site, and the data analysis methods are presented. Section 3 shows and discusses the results of the VALUAS IOPs including a quality control of the UAS wind measurements using the meteorological tower instruments at Falkenberg. The overall performance of two DWLs is analyzed and compared to UAS in situ data taking into account several variables such as the UAS fetch angle, flight altitude, and atmospheric stability. In section 4, the conclusions and recommendations for future studies are given.

2. Materials and methods

a. *Measurement site and experimental setup*

All meteorological measurements described in this study were conducted at the boundary layer field site Falkenberg (in German: Grenzschichtmessfeld, GM Falkenberg) of the DWD, about 60 km southeast of Berlin, Germany (Fig. 1). Flat farmland with few forest patches and small villages in between dominates the landscape around the measurement site (Mengelkamp et al. 2006). The DWD operates this site to investigate the ABL in the rural landscape around Lindenberg to complete the so-called "Lindenberg Column" reference profile measurements of the whole troposphere (Neisser et al. 2002). Three IOPs at the GM Falkenberg were conducted in the framework of the project VALUAS. The first campaign

FIG. 2. Top of the meteorological mast at the MOL-Richard-Aßmann Observatory (RAO) site at GM Falkenberg, close to Lindenberg, with the installed cup anemometers and wind vane at 98 m above the ground. Picture was taken with a DJI mavic the morning of 25 Nov 2022.

(IOP-1) took place from 7 to 29 July 2020, the second (IOP-2) from 7 June until 2 July 2021, and the third (IOP-3) from 17 to 29 November 2022 (list of flights available in appendix A). During these IOPs, two DWLs of type Halo Photonics Streamline were deployed next to the 99-m meteorological tower (Fig. 2). The free space area of the site was also used for the UAS of type MASC-3 takeoff and landing procedures to conduct the necessary measurement flights for comparison.

b. Meteorological tower

The GM Falkenberg hosts a 99-m high meteorological tower at 52°10′N, 14°07′E, 73 m above mean sea level (Fig. 2). The tower provides horizontal wind measurements with cup anemometers (Thies 4.3303.22.000) at 10, 20, 40, 60, 80, and 98 m and wind vanes (Thies 4.3121.32.000) at 40 and 98 m. Water vapor and air temperature are measured using Vaisala HUMICAP humidity and temperature probes of type HMP45 in combination with R. M. Young model 43408 aspirated radiation shields at 10, 20, 40, 60, 80, and 98 m. Surface pressure at the tower (1 m above ground level) is measured by a Vaisala PTB220A barometer. Data of wind speed and wind direction were available as 1- and 10-min averages, while 10-min averages were used for the other atmospheric variables.

c. Doppler wind lidars

For this study, DWD provided data from two Halo Photonics DWL systems: a regular Streamline unit (S/N 177) owned by DWD and a Streamline XR unit (S/N 143) as a contribution from the Technical University of Berlin to the Field Experiment on Submesoscale Spatio-Temporal Variability in Lindenberg (FESSTVaL) campaign. Therefore, WL143 was present for the 2021 campaign only, while WL177 was operated during all three IOPs.

To derive the mean wind using DWLs, the Meteorological Observatory Lindenberg (MOL) uses a best practice VAD variant, which has proven to be particularly efficient over years of testing. The variant used in Lindenberg is described in Päschke et al. (2015) and Teschke and Lehmann (2017). This method allows for a simple calculation of uncertainties as well as efficient quality control via common fit parameters, namely, the coefficient of determination (R2) and the condition number of the algebraic least squares regression (CN). In addition, this VAD utilizes the minimum number of directions available for the calculation as a consistency criterion. For example, with 24 viewing directions and the minimum number of directions set to 12, there are practically no outliers in the wind retrieval.

WL143 uses DWD's VAD variant with 75° elevation and 24 different scan directions, which takes around 120 s to complete a full azimuth circle, while WL177 applies a continuous scanning mode (CSM) at 62° elevation designed for measuring wind gusts, which completes a full azimuth circle in just 3.4 s. Due to their different pulse durations, system type, and scan mode, both lidar products differ in their height resolution and maximum height. Additionally, the lowest gate in each lidar makes up the blind zone. Hence, usable data start at 70 and 40 m for WL143 and WL177, respectively (see Table 1). It is important to note that due to their different configurations, a single line-of-sight (LOS) measurement of WL143 averages 30 000 individual pulses, while WL177's rapid scanning uses only 3000 pulses. This has influence on the measurement quality and requires a different filter method prior to the wind retrieval because filtering data with the common signal-to-noise ratio (SNR) approach would result in a marked loss of data availability. Therefore, the retrieval for both lidars was conducted with the consensus filter method. This filter is based on the random sample consensus (Fischler and Bolles 1981), and it is used operationally in DWD's radar wind profiler network. The wind processing was conducted with DWD's Doppler lidar processing toolbox1[1] using a time window of 10 min. The toolbox incorporates the consensus filter and can process conical scans like VAD and CSM.

d. UAS platform

For obtaining the in situ horizontal wind velocity, the fixed-wing UAS platform MASC-3 (Wildmann et al. 2017; Rautenberg et al. 2019; zum Berge et al. 2021; Schön et al. 2022; zum Berge et al. 2023) was employed (Fig. 3). The scientific payload consists of a five-hole probe (5HP), an inertial measurement unit (IMU), and a fast thin-wire resistance thermometer operated together to get high-resolution wind measurements (van den Kroonenberg et al. 2008; Wildmann et al. 2014a,b). MASC-3 uses a sampling frequency of 100 Hz to measure the three-dimensional wind vector and air temperature. The three-dimensional wind vector in Earth's coordinate system is calculated using raw data from the 5HP, IMU, and GPS data, along the three-dimensional flight path of the UAS. Rautenberg et al. (2019) presented a detailed

---

[1] The Doppler lidar toolbox, developed within DWD's ground-based remote sensing department, is an open source tool to help operators of Doppler lidars, both Streamline and WindCube systems, to process conical lidar measurement in a standardized approach. It takes the native data formats as input, takes care of the prior filtering steps, performs the wind calculation, and outputs the results as netCDF data. The toolbox together with additional information is available at https://github.com/mkay-atm/dl_toolbox.

TABLE 1. Measurement properties of the DWL instruments WL177 and WL143 deployed at GM Falkenberg (WL177 during all IOPs, WL143 during IOP-2 only).

Manufacturer/type	WL177 Halo photonics/streamline	WL143 Halo photonics/streamline XR
S/N	177	143
Laser wavelength	1.5 μm	1.5 μm
Pulse duration τ_p	187 ns	340 ns
Pulse repetition frequency (PRF)	10 kHz	10 kHz
Detector sampling rate	50 MHz	50 MHz
Scan/No. of directions/elevation/filter	CSM/—/62°/consensus	VAD/24/75°/consensus
Time window	10 min	10 min
Time to complete azimuth circle T	3.4 s	120 s
Focus setting	500 m	∞
Vertical range	13–2 636 m	23–11 568 m
Vertical resolution (nominal)	27 m	46 m
Line-of-sight resolution (measured)	30 m	48 m
Blindzone	Lowest gate, until 40 m	Lowest gate, until 70 m
Pulses per ray	3000	30 000
Instrument software version	Streamline 14–8	Streamline 14–8
Retrieval software	DWD DL-Toolbox v. 1.0	DWD DL-Toolbox v. 1.0

description of the complete MASC-3, its sensor system, and the raw data postprocessing procedures.

FLIGHT STRATEGY

Measurement flights were carried out by repeatedly flying along straight and level ground tracks (legs) at various altitudes between 89 and 550 m above the ground (Fig. 4), with a constant indicated airspeed of 18.5 m s^{-1}. Each flight leg has a duration of at least 1 min. To compare flight leg data to the averages provided by the cup anemometers at the tower and to the DWLs, several consecutive flight legs at the same altitude were combined to cover a measurement time of at least 10 min.

e. UAS data processing

All flight legs were initially sorted into different altitude groups. Since this study aimed to validate DWLs with UAS measurements, the groups' vertical extent was set to be as close as possible to a multiple of the height resolution of the WL177 (the one with the most extensive dataset). The extent was set accordingly to approximately 50 m.

FIG. 3. The UAS platform MASC-3 in flight (2-m length, 4-m wingspan, 8-kg takeoff mass, and 18.5 m s^{-1} constant true airspeed). The standard turbulence instrumentation is mounted at the very front of the aircraft. The pusher–engine configuration with two rotor blades is visible at the tail of the UAS. Courtesy of Ines Schäfer.

The flight legs within a specific altitude group were then divided into suitable time intervals. The length of these intervals varies based on the desired averaging time. Executing this process was complex as legs at the same altitude tended to have varying duration times. This occurred because the UAS maintained a constant indicated airspeed, causing the ground speed and, consequently, the duration of each leg to differ depending on factors like wind direction, flight direction, and wind speed.

Finally, for every time interval and altitude group, the median of wind speed and wind direction was calculated from the UAS dataset. The results of the calculation were then compared with tower and DWL data for the same altitude range and time.

1) AVERAGING TIMES

As explained in the previous section, each and every flight leg has a different duration due to the flight conditions. The procedure to get the leg bins varies, depending on the averaging time.

Legwise average: Considering the highest resolution of cup anemometer data (1 min), a leg is considered valid if it lasts at least 60 s, ensuring a unique identification for comparison with the anemometer dataset. However, it is even possible for single legs to exceed 300 s in duration due to encountering strong headwinds. In such cases, the decision was made to avoid dividing the legs into multiple subsections. This choice is completely arbitrary. One can also decide to divide the legs into units of 60 s, but then other problems arise, such as if a leg is not an exact multiple of a minute, which part of the leg should be discarded? Instead, an easier and more convenient approach involved averaging the cup anemometer data

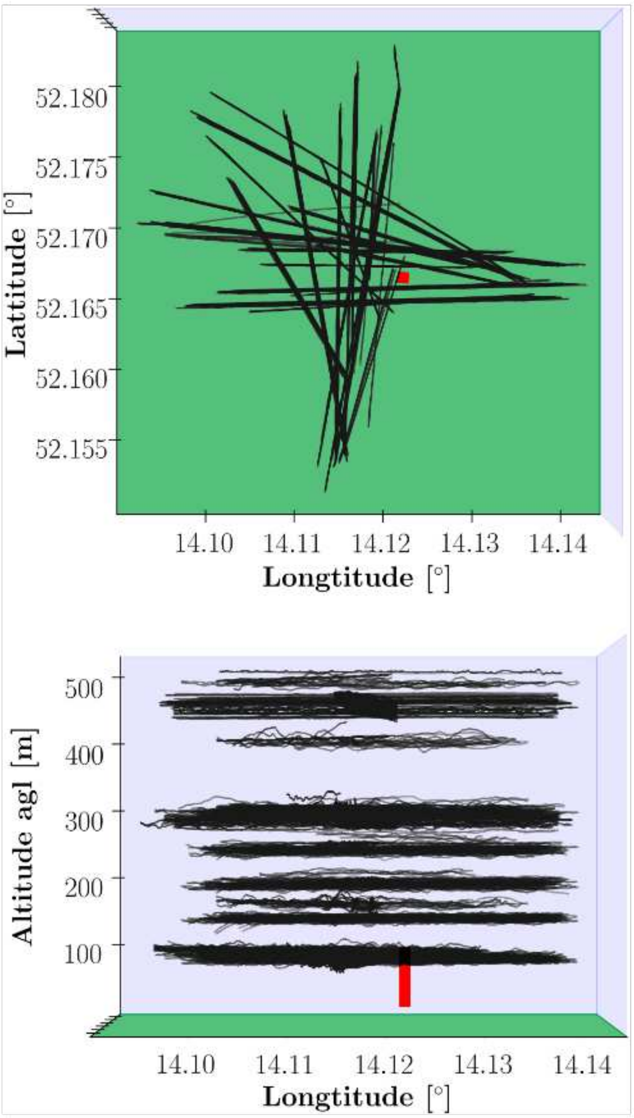

FIG. 4. The three-dimensional extent of all the UAS legs used for this study. The red column represents the meteorological 99-m tower.

collected throughout the entire leg. The distribution and mean value of the legwise average at 98 m AGL for UAS quality assurance are presented in Fig. 5a.

The 10- and 30-min averages: Given that there are no individual legs that last exactly 10 or 30 min, our approach involves considering consecutive legs and creating a representative interval of either 10 or 30 min. To accomplish this, we opted to group together the number of legs that, when combined, come closest to the desired average duration. This strategy may sometimes result in a group duration that is lower or higher than the required average, but it would still be closer to the 10- or 30-min average compared to adding or removing another leg to the group. Figures 5b and 5c display histograms depicting the distribution and mean value of leg groups for the UAS quality assurance at 98 m AGL with 10- and 30-min averages. These histograms demonstrate that while shorter leg groups are present, the overall average duration aligns with the respective requested time average.

For the quality assurance of the UAS measurements (comparison with tower data), all three different averaging periods were used: legwise, 10 min, and 30 min. For the DWL validation, the investigation of the crosswind, altitude, and atmospheric stability effects, 10-min data averages from UAS and DWL were used. Table 2 gives an overview of the different systems and the availability of data products for the three averaging periods, while appendix B shows a schematic flowchart of the UAS data processing procedure.

From the UAS leg groups, the first timestamp of the first leg in the group and the last timestamp of the last leg in the group were used as the start and end time. Then, depending on the time average, the data from the other systems were either picked up as a single value (DWLs and 10-min tower data) or averaged if more values were present between the start and end time (1-min tower data).

2) SPATIAL SEPARATION EFFECT (FETCH ANGLE)

When comparing stationary measurements of a cup anemometer or DWL with data from a moving platform like a UAS, the effect of spatial separation has to be considered. The stationary sensor probes the air transported by the mean wind vector across its position (advection). On the contrary, the UAS is moving through the air quickly enough so that the gathered data might be interpreted as a snapshot of the air mass. It depends on wind direction, speed, and the relative position of the UAS flight path with respect to the stationary instrument, whether the probed air masses are identical or not.

The flight paths for this study were designed in a way that the UAS was always flying toward or away from the location of the stationary measurements (tower or DWL) on repetitive flight legs, ideally aligning the ground trajectory with the mean wind direction. Aircraft controlled by an autopilot system can follow a preprogrammed ground track with high accuracy, independently of the current wind direction in the atmosphere. Hence, despite a careful mission planning, there could be an angle α (fetch angle) between the flight direction (track) of the UAS and the wind direction ϕ.

This angle α can range from 0° (headwind or tailwind) to 90° (crosswind) on repetitive legs. Headwind is coming from the opposite direction the aircraft is flying, parallel to its flight direction. Tailwind is going in the same direction as the aircraft, parallel to its flight direction. Pure crosswind crosses the aircraft track perpendicularly without any headwind or tailwind components.

The aircraft moves through the air, while the air itself moves in Earth's coordinate system due to the mean wind vector. In the case of $\alpha \approx 0$ (head or tailwind), the aircraft is probing exactly the same air mass that is advected over the stationary measurement sensor. Part of the air moves perpendicular to the aircraft's ground track at higher crosswind angles. Then, the aircraft probes different air masses on several repetitive legs compared to the one advected over the stationary measurement sensor.

Besides that, the probed air continuously exchanges energy and momentum with the surrounding air (depending on the

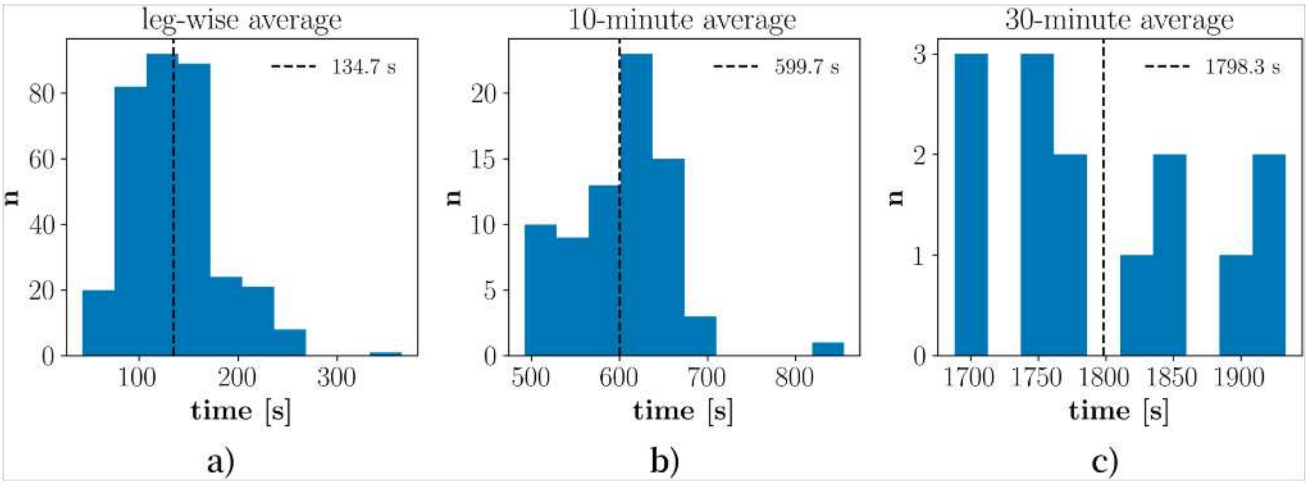

FIG. 5. Distribution (blue histogram) and mean value (vertical black dashed line) of the leg bin duration for the three different time averages at 98 m AGL.

local turbulent mixing) and the heterogeneous surface. The degree of similarity of influence onto the measured airborne data and the stationary instruments differs with the fetch angle α. For $\alpha \approx 90°$, the surface to the left or right of the ground track influences the measurements about as strong as the surface along the ground track.

Comparing aircraft measurements with sensors that are stationary at the ground (e.g., towers or DWL) requires considering that for small fetch angles α, the air is advected along the aircraft track toward the stationary sensor, in case the aircraft is moving toward or away from the tower or DWL. More prominent fetch angles mean that the air advected toward the stationary sensor only crosses the aircraft's track at one location. This raises the question of whether the agreement of the UAS and tower or DWL data depends on the fetch angle α between the wind direction and flight direction.

Therefore, before any comparison with any stationary sensor, an analysis of the influence of the fetch angle was performed.

f. Statistical measures

To compare datasets from the tower, UAS, and DWL measurements on a statistical basis, suitable statistical quantities (measures) are defined in the following, both for horizontal wind speed v and direction ϕ.

1) WIND SPEED

The meteorological wind vector is defined by $\mathbf{u} = (u, v, w)$ with u being positive eastward, v being positive northward, and w being positive upward. However, since the vertical wind component is not the subject of the present study, mainly the horizontal wind vector is analyzed and referred to in polar coordinates using the wind speed variable $v = |(u, v)|$ and direction ϕ (with $\phi = 0$ for wind coming from the north).

TABLE 2. Averaging times and their usage in this study for each system.

Measurement system	Legwise	10 min	30 min
UAS	×	×	×
Tower cup anemometer and vane	×	×	×
WL143		×	
WL177		×	

For a pair of wind speed measurements, one is obtained from UAS A and the other is from a second system S (i.e., cup anemometer mounted on the tower, WL143, or WL177, respectively) from the identical time and altitude group, averaged over the same period (e.g., leg duration, 10 min, 30 min), we define a normalized, relative, dimensionless wind difference [Eq. (1)]. As the scope of the analysis is to validate DWL measurements on the basis of UAS data, the latter is considered the reference and used for the normalization in the equation:

$$Y_i = \frac{\overline{v}_{A,i} - \overline{v}_{S,i}}{\overline{v}_{A,i}}. \tag{1}$$

The relative deviation has the advantage over the absolute deviation that it is not sensitive to the absolute value of the wind speed. To compare all dataset pairs $i = 1, \ldots, n$, we use the mean bias and the root-mean-square difference (RMSD) and the Pearson correlation coefficient:

$$B_Y = \frac{1}{n}\sum_{i=1}^{n} Y_i, \tag{2}$$

$$\sigma_Y = \sqrt{\frac{1}{n}\sum_{i=1}^{n} Y_i^2}, \tag{3}$$

$$R_v = \frac{\sum_{i=1}^{n}(\overline{v}_{A,i} - \langle v_A\rangle)(\overline{v}_{S,i} - \langle v_S\rangle)}{\sqrt{\sum_{i=1}^{n}(\overline{v}_{A,i} - \langle v_A\rangle)^2}\sqrt{\sum_{i=1}^{n}(\overline{v}_{S,i} - \langle v_S\rangle)^2}}, \tag{4}$$

where $\langle v_A\rangle$ and $\langle v_S\rangle$ are the mean horizontal wind velocities averaged over the entire dataset:

TABLE 3. Statistical measures evaluating the fetch angle α effect for the UAS quality assessment. The α limits are chosen in such a way to split as evenly as possible the data pairs n between the different groups.

Wind speed						Wind direction					
Group	α	Data pairs n	σ_Y	R_v	B_Y	Group	α	Data pairs n	σ_ϕ	R_ϕ	B_ϕ
		Legwise average						Legwise average			
1	0°–23.6°	123	0.148	0.937	−0.012	1	0°–23.6°	114	15.1	0.985	1.7
2	23.6°–39.3°	103	0.229	0.913	−0.029	2	23.6°–39.3°	82	20.3	0.980	6.5
3	39.3°–90°	122	0.323	0.837	−0.011	3	39.3°–90°	100	20.8	0.979	3.1
		10-min average						10-min average			
1	0°–23.6°	29	0.109	0.962	0.001	1	0°–23.6°	27	10.6	0.989	0.3
2	23.6°–39.3°	25	0.164	0.976	−0.016	2	23.6°–39.3°	20	16.7	0.986	7.4
3	39.3°–90°	23	0.286	0.884	−0.041	3	39.3°–90°	17	18.9	0.977	−1.9

$$\langle v_A \rangle = \frac{1}{n}\sum_{i=1}^{n}\overline{v}_{A,i}. \tag{5}$$

2) WIND DIRECTION

The same statistical measures are used for the wind direction. However, in contrast to the wind speed, the differences in wind direction measurements between UAS (index A) and tower or DWL (index S) are not normalized:

$$\Delta\overline{\phi}_i = \overline{\phi}_{A,i} - \overline{\phi}_{S,i}. \tag{6}$$

Additionally, only data pairs with wind speeds exceeding 2 m s^{-1} are considered when comparing wind directions. This filtering process is necessary because low wind speeds tend to exhibit significant fluctuations in wind direction (Davies and Thomson 1999), rendering meaningful comparisons impractical.

g. *Atmospheric stability measures*

The lapse rate γ and the bulk Richardson number Ri_b are used to investigate the influence of atmospheric stability on the DWL measurements. The first measures static stability due to temperature gradients over a specific height difference (thermal stratification). In contrast, the second one also considers the horizontal wind speed gradient (shear) in the vertical direction (dynamic stratification).

The lapse rate γ is calculated with the difference $\Delta\Theta_v$ of potential virtual temperature between two heights Δz according to

$$\gamma = \frac{d\Theta_v}{dz} \approx \frac{\Delta\Theta_v}{\Delta z}. \tag{7}$$

In the case of a statically stable atmosphere, $\gamma > 0$; in the case of a statically unstable atmosphere, $\gamma < 0$. For the case of a neutral atmosphere, $\gamma = 0$.

According to Stull (2016), Ri_b is calculated by

$$\mathrm{Ri}_b = \frac{g\Delta\Theta_v\Delta z}{\overline{T}_v[(\Delta u)^2 + (\Delta v)^2]}, \tag{8}$$

with $g = 9.81$ m s^{-2}, $\Delta\Theta_v$ as the difference of potential virtual temperature between two heights, and $\overline{T}_v$ as the arithmetical mean of the virtual temperatures between the two heights. The values $(\Delta u)^2$ and $(\Delta v)^2$ are the difference in the two horizontal wind components.

In this study, Ri_b is calculated using variables measured at $z_1 = 1$ m and $z_2 = 98$ m while γ for $z_1 = 1$ m and $z_2 = 10$ m, since this lower part of the atmosphere primarily influences the difference in the virtual potential temperature. As the wind speed on the ground is zero, the approximation $u_{1\mathrm{m}} \approx 0$ is considered and Eq. (8) then becomes

$$\mathrm{Ri}_b = \frac{g\Delta\Theta_v\Delta z}{\overline{T}_v(u^2 + v^2)}. \tag{9}$$

At Eq. (9), u and v are now the two horizontal wind components at the upper end of the vertical column, i.e., at 98-m altitude. Since the atmospheric pressure is only measured at a level of 1 m, the barometric equation [Eq. (10)] solved for pressure at the higher altitude (p_{z2}, i.e., $p_{98\mathrm{m}}$ and $p_{10\mathrm{m}}$) is used to obtain a value for the atmospheric pressure at different height levels

$$p_{z2} = p_{1\mathrm{m}}\exp\left(\frac{-g\Delta z}{R_d\overline{T}_v}\right). \tag{10}$$

3. Results and discussion

a. *Quality assurance of UAS data*

Before UAS data are used to validate DWL data, the UAS measurements were compared to tower data for quality assurance.

Quality control was performed by comparing the horizontal wind speed and direction measured by UAS with the tower measurement at 98 m AGL. Time-averaged cup anemometer data were compared to the corresponding flight legs at 98 m during the same time. The averaging periods were defined as the duration of one flight leg (legwise, see above), 10, and 30 min.

1) FETCH ANGLE ANALYSIS

At first, an analysis of the spatial separation effect was performed on the legwise and 10-min average data (the 30-min average was not used due to the small size of this dataset). Results are reported in Table 3. This analysis shows that the

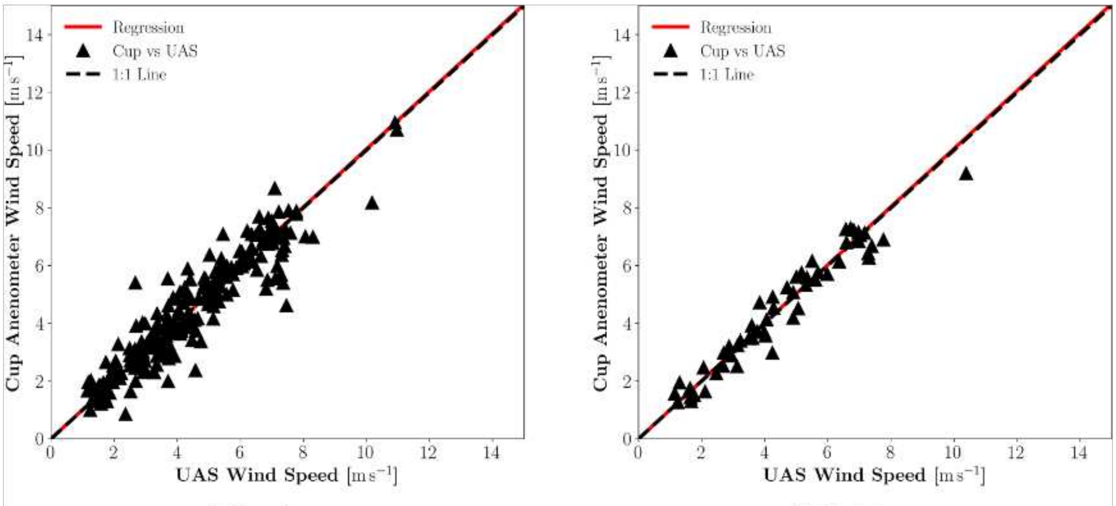

(a) leg-wise average

(b) 10-minute average

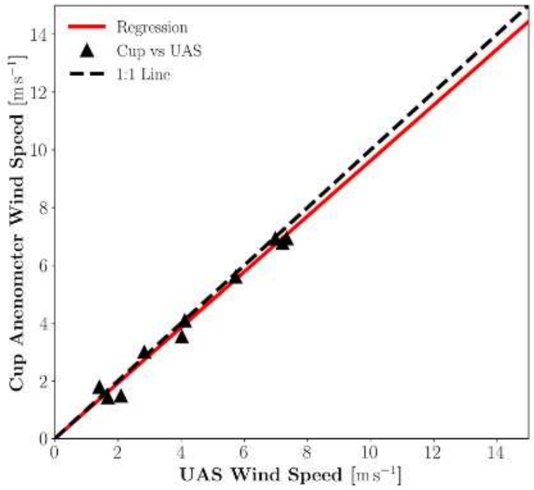

(c) 30-minute average

FIG. 6. Comparison of UAS wind speed data with cup anemometer data at 98 m AGL. (a)–(c) Different averaging intervals explained in section 2e(1). The red lines are the result of linear regressions (same in the following diagrams).

RMSD for both wind speed and direction increases with the fetch angle. The agreement of the wind speed measurements is more affected than the wind direction measurements.

To have a good compromise between the data quality and the dataset's size, it was chosen to use only the data with a fetch angle α lower than 39.3° for the further analysis.

2) FINAL QUALITY ASSESSMENT

Figures 6 and 7 show the result of the comparison for both wind speed and wind direction for the filtered dataset (fetch angle α lower than 39.3°): each data point in the diagrams represents one pair of UAS and tower measurements. Table 4 presents the corresponding statistical measures.

The normalized mean bias B_Y for wind speed is always less than 4%. With a mean wind speed of 6 m s^{-1}, this equals to an error of 0.24 m s^{-1}. Such a small value indicates that any systematic difference between UAS and tower measurements regarding wind speed is negligible. The normalized RMSD σ_Y is about 20% for the legwise average. This high initial value is probably caused by atmospheric turbulence. The correlation between the tower-mounted cup anemometer and the UAS-based 5HP measurements is always more than 0.9. When increasing the averaging period to 10 and 30 min, the correlation coefficient R_v grows and σ_Y drops: the statistical agreement between both systems increases strongly, mainly due to the low-pass filtering of turbulent motion. The fact that the 30-min case has the highest correlation, despite the low number of data points, implies that a lower correlation in the shorter averaging times is mainly due to the random turbulence error in the convective boundary layer, which affects measurements due to spatial separation.

The wind direction also shows a high degree of agreement between tower and flight data, as long as data points with wind speeds below 2 m s^{-1} (black triangles in Fig. 7) are removed when calculating the statistics. Low wind speeds naturally have a high variation in the wind direction, thus making comparability unfeasible. For the wind direction, the correlation

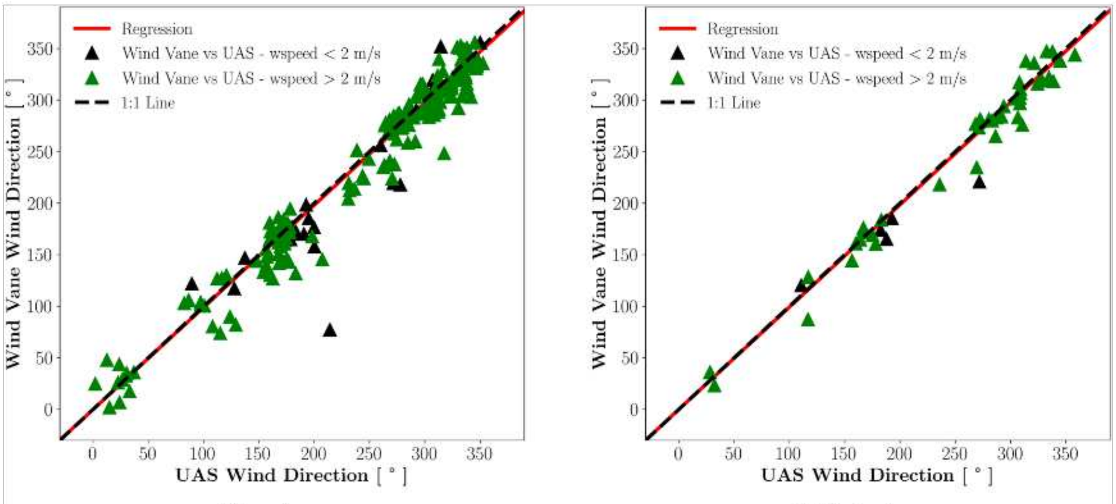

(a) leg-wise average

(b) 10-minute average

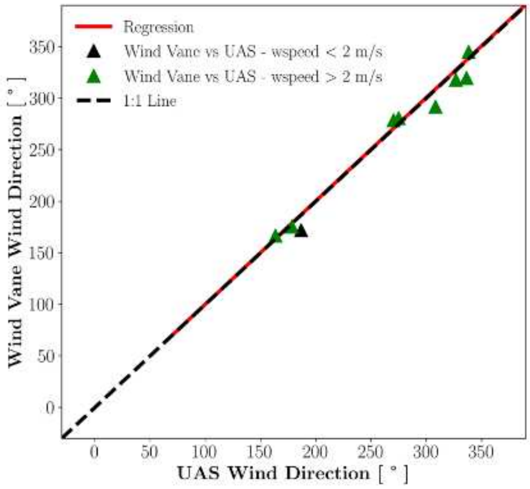

(c) 30-minute average

FIG. 7. Comparison of UAS wind direction data with vane data at 98 m AGL. (a)–(c) Different averaging intervals explained in section 2e(1).

reaches already 0.98 using legwise averaging. The root-mean-square difference σ_ϕ is about 17.5° due to turbulent fluctuations, dropping to 9.9° for a 30-min averaging. The mean bias B_ϕ drops from 4.7° for the legwise averages down to 2.7° for a 30-min averaging, indicating that there is very low significant systematic difference between tower and UAS-measured wind directions.

The quality assurance of the UAS measurements using the tower data for comparison highlights that despite the different measurement principles, the UAS is a well-suited tool for DWL validation.

Considering that the next comparison involves 10-min average data, our reference system can be characterized by negligible B_Y with $\sigma_Y = 13.7\%$ and $B_\phi = 3.3°$ with $\sigma_\phi = 13.5°$.

b. Doppler wind lidar validation

As described in section 2e(1), consecutive UAS flight legs at a constant altitude were grouped to calculate the 10-min

TABLE 4. Statistical measures describing the quality of the UAS as a horizontal wind vector sensor. For the wind direction, only data where the wind speed is higher than 2 m s^{-1} are considered.

Wind speed					Wind direction				
Averaging period	Number of data pairs n	σ_Y	R_υ	B_Y	Averaging period	Number of data pairs n	σ_ϕ	R_ϕ	B_ϕ
Legwise	230	0.194	0.935	−0.018	Legwise	197	17.5°	0.982	4.7°
10 min	54	0.137	0.971	−0.007	10 min	47	13.5°	0.987	3.3°
30 min	10	0.143	0.991	0.037	30 min	8	9.9°	0.989	2.7°

TABLE 5. Statistical measures evaluating the fetch angle α effect on the wind speed and direction data for the UAS vs WL177 comparison. The α limits are chosen in such a way to split as evenly as possible the data pairs n between the different groups.

Wind speed						Wind direction					
Group	α	Data pairs n	σ_Y	R_v	B_Y	Group	α	Data pairs n	σ_ϕ	R_ϕ	B_ϕ
1	0°–14.1°	68	0.107	0.974	0.049	1	0°–14.1°	46	14.0°	0.986	2.3°
2	14.1°–23.6°	69	0.117	0.980	0.062	2	14.1°–23.6°	56	16.7°	0.984	−0.7°
3	23.6°–39.3°	68	0.184	0.955	0.061	3	23.6°–39.3°	42	22.4°	0.980	−5.9°
4	39.3°–90°	70	0.195	0.838	0.014	4	39.3°–90°	38	21.3°	0.970	0.5°

averaged data for the DWL validation, as the operational DWL dataset provided by the DWD consists of 10-min averages. This procedure leads to a database consisting of averaged data pairs (UAS, DWL) of wind speed and direction for both types of DWL measurements.

In the first step, all available altitudes from the whole dataset are compared. 53 (UAS, WL143) and 275 (UAS, WL177) data pairs are available for the wind speed comparison. This difference is because WL143 was not operated during the IOP-1 and IOP-3 in 2020 and 2022.

In the case of wind direction, for WL177, only data from 2021 to 2022 are shown and analyzed since, in 2020, technical issues with wind-direction derivation for this device occurred. This technical problem, combined with the criterion of taking pairs where the wind speed is above 2 m s^{-1}, reduced the number of wind direction data pairs (UAS, WL177) to 182 and (UAS, WL143) to 41.

To refer to the DWL systematic measurement error to the tower measurement, in the following analysis, the variable B will be computed as

$$B_{\mathrm{dwl,tow}} = B_{\mathrm{uas,tow}} - B_{\mathrm{uas,dwl}}, \tag{11}$$

where the values for the $B_{\mathrm{uas,tow}}$ were defined for the 10-min average at the end of section 3a(2).

1) FETCH ANGLE ANALYSIS

To evaluate the effect of spatial separation, the database consisting of data pairs of UAS and DWL measurements averaged over 10 min was split into four parts, similarly to section 3a(1). Since the data availability of the WL143 is not as good as the one of the WL177, only the WL177 system is taken into account here. The effect of the spatial separation due to the fetch angle α is expected to be similar for both DWL systems since they are situated next to each other at the measurement site.

Table 5 lists the result and statistical measures for the WL177. The statistical measures R, B, σ show an increase of σ_Y and σ_ϕ with the rising fetch angle. The correlation coefficient R_v for the wind speed decreases, down to 0.83 for fetch angles from ≈40° to 90°, while B_Y does not show a clear tendency. In contrast to this, the correlation coefficient of the wind direction shows a slight decrease only for the fourth group (≈40° to 90°), which contains the most significant fetch angles α, i.e., strong crosswind flights. The bias of the wind direction between WL177 and UAS also does not show a clear tendency.

Summing up, the measures R, B, σ that describe statistical and systematic differences between the UAS and the DWL data are affected by the fetch angle α (or crosswind flights), but as long as $\alpha < 39.3°$, the influence is considered acceptable. This condition reduces the usable wind speed datasets from 275 to 205 (UAS, WL177) and from 53 to 46 (UAS, WL143), while for wind direction, it is from 182 to 144 (UAS, WL177) and from 41 to 38 (UAS, WL143).

2) OVERALL VALIDATION

Figure 8 shows scatter diagrams for wind speed and direction for both DWL instruments compared with UAS measurements. Table 6 lists the corresponding statistical measures.

For both DWL, the correlation with the UAS data is high: more than 0.94 for the wind speed and more than 0.98 for the wind direction and comparable with the agreement between tower and UAS data.

The WL143 statistical scatter for wind speed σ_Y is more significant than the WL177. In contrast, the scatter for wind direction (σ_ϕ) is smaller. The reason might be the different scanning strategy (see section 2c) or the different turbulent conditions since the two datasets do not cover identical meteorological situations.

The systematic differences between UAS and DWL in wind speed are almost one order of magnitude larger than the UAS–tower agreement, especially for the 10-min average. According to Eq. (1), the WL143 shows a 5.1% tendency to overestimate the horizontal wind velocity. At the same time, the WL177 tends to underestimate it by 5.7%. The 5.1% underestimation in WL177 can be attributed to a noise-induced bias that becomes increasingly noticeable in the case of weak signals (Päschke and Detring 2023, manuscript submitted to *Atmos. Meas. Tech. Discuss.*). For WL134, the amount of data pairs for the comparison is only a fifth of the number of the data pairs available for WL177. Additionally, no wind speed was much greater than 10 m s^{-1}. Therefore, the point cloud is more compact and the linear regression is not as stable as for the comparison with WL177 and hence, the results are less reliable. This hints that for a reliable comparison, the data points should cover a considerable range of velocities. The systematic differences between the reference platform and the DWL wind direction are almost negligible, even though the WL177 seems to be the more accurate.

3) SIMULTANEOUS VALIDATION

The dataset was cut-filtered to investigate how both systems compare with the same atmospheric conditions by considering

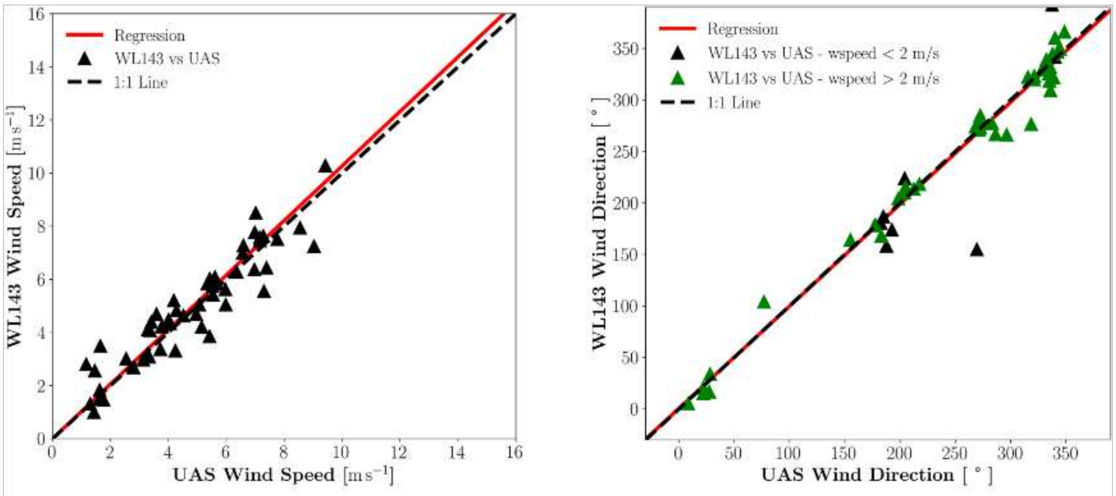

(a) UAS vs WL143: wind speed

(b) UAS vs WL143: wind direction

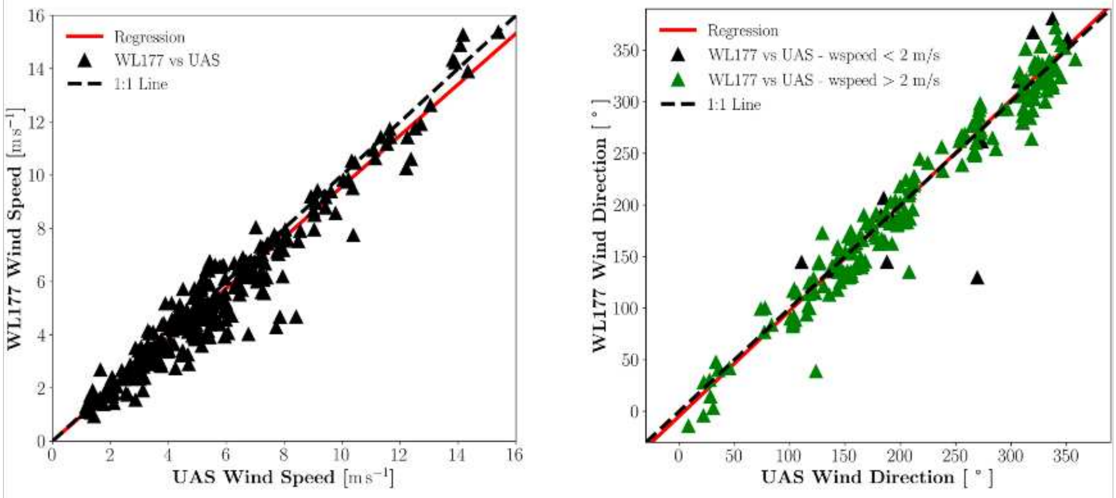

(c) UAS vs WL177: wind speed

(d) UAS vs WL177: wind direction

FIG. 8. UAS wind speed and direction data compared to WL143 and WL177 data, respectively, for 10-min averaging intervals. See Table 6 for the corresponding statistical measures.

only situations where the two lidars operated simultaneously (viz., only during IOP-2 in 2021). This filtering does not reduce the size of the (UAS, WL143) dataset but discards most of the data pairs (UAS, WL177). The final number of entries is 45 for the wind speed and 38 for the wind direction.

The statistical measures of the simultaneous comparison are shown in Table 7. The statistics are consistent with Table 6 and confirm the conclusions drawn in section 3b(2).

It should be noted that WL143 operates with a smaller zenith angle: this implies that the projection of the radial winds on the horizontal wind vector is smaller and thus probably more uncertain, especially in the convective ABL. Moreover, a 10-min average for WL143 just contains five scan cycles against more than 170 for the WL177.

c. *Effect of the altitude*

In this section, the 10-min averaged data pairs are used to investigate whether a dependency of the overall data quality on the scanning altitude is present. The data pairs were subdivided into altitude groups and compared to the closest DWL range

TABLE 6. The statistical measures of the overall comparison of UAS with both DWL systems. These measures statistically describe the scatter diagrams of Fig. 8.

Wind speed					Wind direction				
DWL	Data pairs n	σ_Y	R_v	B_Y	DWL	Data pairs n	σ_ϕ	R_ϕ	B_ϕ
WL143	46	0.211	0.941	-0.051	WL143	38	13.6°	0.992	2.4°
WL177	205	0.140	0.978	0.057	WL177	144	17.7°	0.983	-1.2°

TABLE 7. The statistical measures of the simultaneous comparison of UAS with both DWL systems.

Wind speed					Wind direction				
DWL	Data pairs n	σ_Y	R_v	B_Y	DWL	Data pairs n	σ_ϕ	R_ϕ	B_ϕ
WL143	45	0.213	0.938	−0.049	WL143	38	13.6°	0.992	2.4°
WL177	45	0.163	0.959	0.044	WL177	38	17.8°	0.987	1.0°

gate. Table 8 and Fig. 9 show the quality measures for the altitude analysis.

Due to the limited quantity of available data pairs for WL143, a comprehensive analysis was only feasible for two different altitudes. The upper gate exhibits a statistical scatter σ_Y that is more than twice as high compared to the lower gate, despite having a similar correlation R_v. Additionally, the systematic difference ($B_Y \approx 9\%$) is significantly larger at higher altitudes. The scatter for wind direction σ_ϕ behaves similarly to wind speed, as well as the systematic difference. However, the σ_ϕ values are very close to the 10-min UAS versus tower uncertainty, making it challenging to draw a definitive conclusion.

The larger size of the WL177 dataset allowed a subdivision into more altitude groups: 4 for the wind speed while only 3 for the wind direction due to the additional filtering discarding low wind speed conditions. In the case of wind speed determined by WL177, the statistical scatter σ_Y is comparable for the first three altitudes but shows a clear improvement for the last range: this range is indeed where the WL177 has its focus set to and therefore provides the best SNR. However, this improvement is still much smaller than the scatter between UAS and tower measurements, rendering any further analysis inconclusive. The correlation of wind speed generally increases with altitude, except for a drop to 0.918 in the second altitude range. For the same range gate group, B_Y reaches a maximum of 9.2% but decreases with increasing altitude. Concerning WL177 wind direction, there is no discernible trend in the quality statistics, although the second altitude group appears to be less accurate.

SIMULTANEOUS ANALYSIS OF ALTITUDE EFFECT

Similar to the analysis performed in section 3b(3), again the overall dataset was filtered to compare conditions in which both lidars were operating at the same time. In such a way, a valid comparison of the two systems under the same atmospheric conditions can be exploited and the results are reported in Table 9.

The two DWLs have similar wind speed measurement quality for the lower altitude group, and there is a tendency toward larger scatter by increasing the scanning altitude. This increase of the statistical scatter seems to be more pronounced for the WL143. For the systematic error, the tendency is opposite for the two systems: WL143 is very accurate in the first altitude, while drifting in the second and vice versa for the WL177.

For the wind direction, measurements of the WL143 have less scatter than the other systems on both altitudes, yet the tendency of increased scatter with altitude is always followed. Regarding the systematic error, the tendency is analogous to the wind speed measurement.

d. Effect of the atmospheric stability

In the last step, our study analyzes whether atmospheric stability has an effect on the lidar wind estimation. To thoroughly examine the impact on the measurements, it was crucial to acquire an ample amount of data under both stable and unstable conditions. However, the WL143 data solely cover IOP-2, restricting the availability of sufficient pairs for stable conditions. Consequently, the investigation of the influence of atmospheric stability was limited to the WL177 system.

1) RICHARDSON NUMBER

First, Ri_b was used as a stability criterion calculated as explained in section 2g. Figure 10 shows the calculated Ri_b for all the 10-min data pairs. Since the biggest share of flights has been conducted during daytime and in two campaigns in

TABLE 8. Statistical measures evaluating the altitude dependency of the wind speed and direction measurement for the two DWLs.

Wind speed						Wind direction					
Data pairs n	UAS altitude	Range gates	σ_Y	R_v	B_Y	Data pairs n	UAS altitude	Range gates	σ_ϕ	R_ϕ	B_ϕ
		WL143						WL143			
24	86–103 m	70–116 m	0.133	0.948	−0.011	18	86–103 m	70–116 m	9.7°	0.992	1.9°
16	297–303 m	301 m	0.304	0.940	−0.091	14	297–303 m	301 m	16.3°	0.985	3.6°
		WL177						WL177			
51	81–103 m	93 m	0.158	0.948	0.067	40	81–103 m	93–172 m	14.2°	0.987	3.3°
43	142–249 m	146–252 m	0.167	0.918	0.092	63	238–317 m	225–305 m	20.9°	0.979	−3.9°
69	273–317 m	278–305 m	0.141	0.983	0.050	41	393–488 m	384–490 m	15.5°	0.980	−1.6°
42	393–493 m	384–490 m	0.065	0.990	0.025						

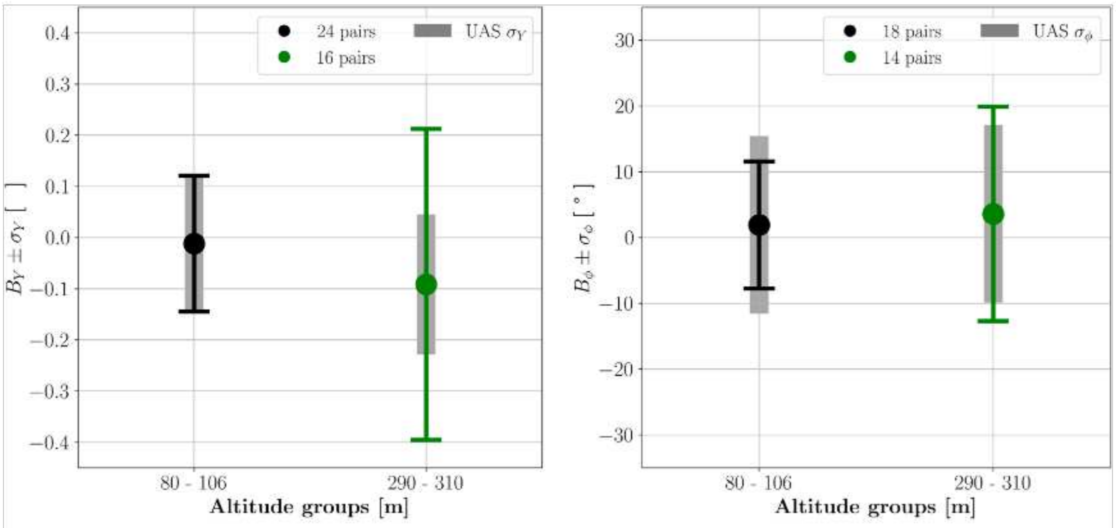

(a) WL143 wind speed (b) WL143 wind direction

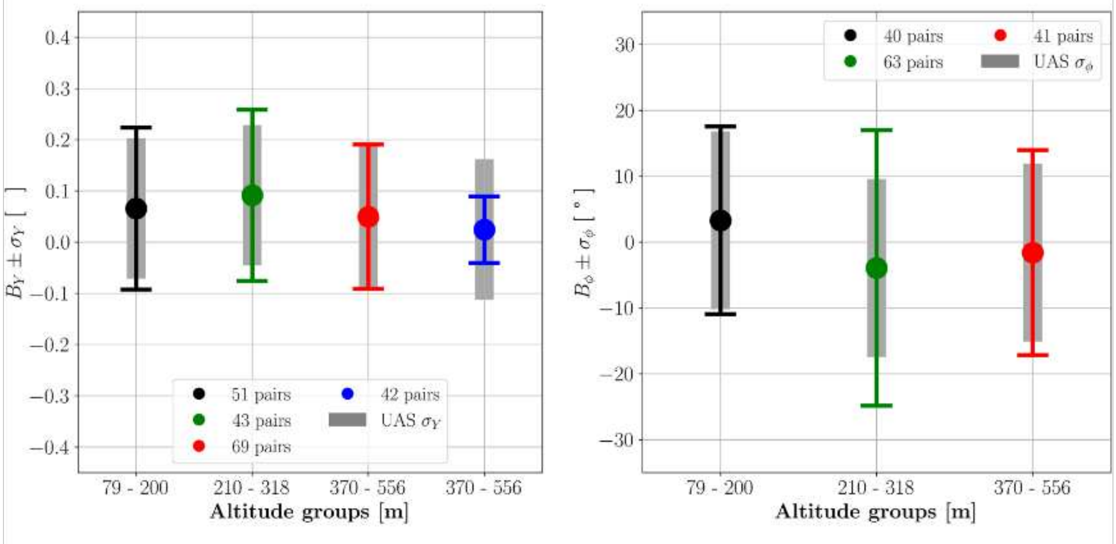

(c) WL177 wind speed (d) WL177 wind direction

FIG. 9. Statistical measures evaluating the altitude dependency of the wind speed and direction measurement for the two DWLs.

summertime (IOP-1 and IOP-2), more data pairs are for the unstable case than for stable.

The 10-min data were here divided into four groups. The grouping of the positive Ri_b values represents thermal and dynamic stable conditions ($\mathrm{Ri}_b > 0.25$) or only thermal stable conditions ($0 < \mathrm{Ri}_b < 0.25$) (Stull 2016). The subdivision of the negative values was performed by mirroring the boundaries of the positive values simply in order to

TABLE 9. Statistical measures evaluating the altitude dependency for DWLs under the same atmospheric conditions (analogous to the simultaneous comparison).

Wind speed						Wind direction					
Data pairs n	UAS altitude	Range gates	σ_Y	R_v	B_Y	Data pairs n	UAS altitude	Range gates	σ_ϕ	R_ϕ	B_ϕ
		WL143						WL143			
23	86–103 m	70–116 m	0.133	0.943	−0.006	18	86–103 m	70–116 m	9.7°	0.992	1.9°
16	297–303 m	301 m	0.304	0.940	−0.091	14	297–303 m	301 m	16.3°	0.985	3.6°
		WL177						WL177			
23	86–103 m	93 m	0.151	0.950	0.07	18	86–103 m	93 m	15.5°	0.979	3.9°
16	297–303 m	305 m	0.187	0.980	0.03	14	297–303 m	305 m	21.9°	0.976	−0.9°

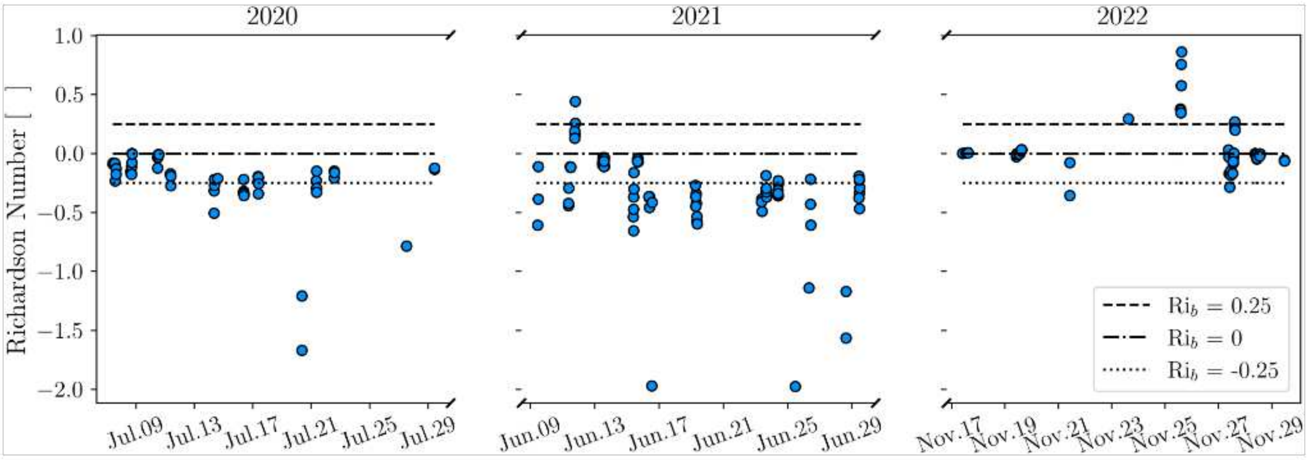

FIG. 10. Times series of Ri_b for all the 10-min data pairs available. Values below the critical value of 0.25 denote dynamically unstable conditions, while values higher than 0.25 suggest a stable ABL.

split the dataset into two groups with significant amount of entries.

2) LAPSE RATE

In addition to evaluating atmospheric stability from the Richardson number, the same was done with the lapse rate, calculated according to section 2g by using data between 1- and 10-m height above the ground level. By taking the lapse rate as a stability criterion, more data pairs are classified into the stable atmospheric conditions doubling in the end the amount of data in this group. Figure 11 shows the time series of the lapse rate for all the 10-min data pairs. The tendency is similar to Fig. 10; however, more points are above the boundary at zero.

3) STABILITY DEPENDENCY

By analyzing the statistical measures shown in Fig. 12 and reported in Tables 10 and 11, it is possible to clearly identify an improvement in the DWL wind speed measurement with increasing atmospheric stability. It seems that both values for the bias and the statistical scatter decrease significantly when the atmosphere is stable. This behavior was somehow expected as it is well known that under these specific conditions, the ABL is less active and tends to suppress turbulent motions, resulting in a reduction of the inhomogeneity and nonstationarity of the wind field being measured. However, the scatter is very close to the uncertainty of the UAS itself already in unstable conditions, while for a stable atmosphere, it is way lower. Due to this fact, it is not possible to prove the actual value for the scatter in stable conditions; however, it is plausible that even the uncertainty of the UAS would decrease if calculated only under stable atmospheric conditions. Therefore, the general behavior of these statistical measures is still considered valid.

The wind-direction measurements also show a similar tendency for the statistical scatter. Regardless of the specific value difference between the bulk Richardson number and lapse rate, with stable conditions, the scatter is lower. The tendency is reversed when it comes to the bias where a slightly larger systematic difference is encountered in stable atmospheric conditions.

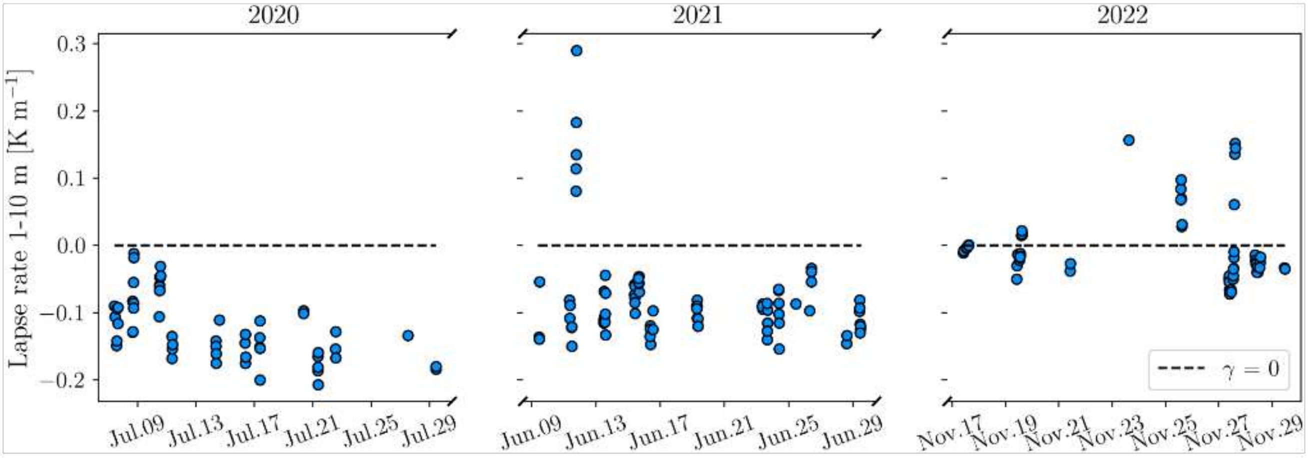

FIG. 11. Time series of the lapse rate for all the 10-min data pairs available. Values below 0 denote unstable conditions dominated by convection, while values higher than 0 suggest a stable ABL.

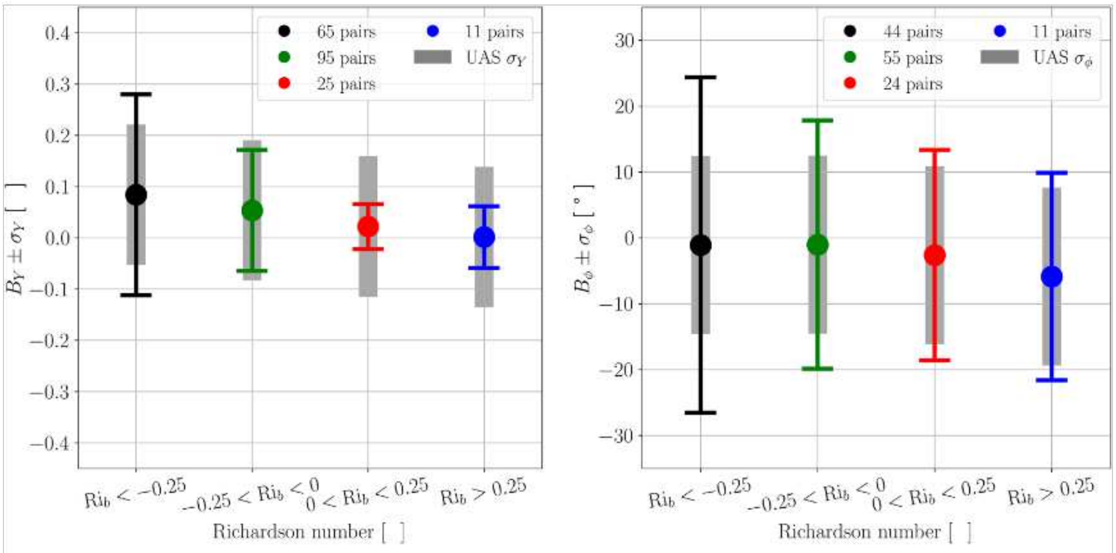

(a) WL177 wind speed (b) WL177 wind direction

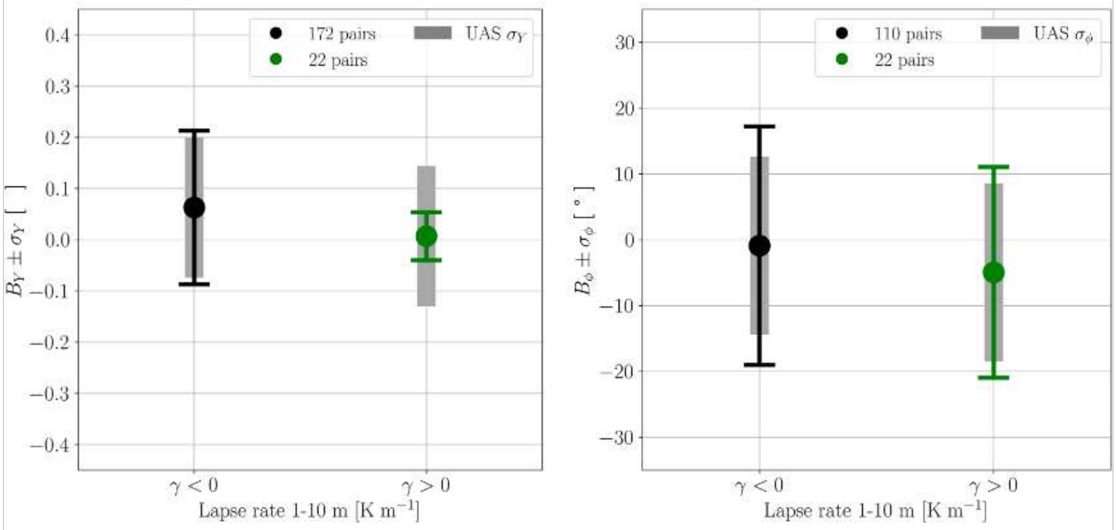

(c) WL177 wind speed (d) WL177 wind direction

FIG. 12. Visual representation of the statistical measures of the atmospheric stability effect on wind speed and direction measurement for WL177.

In conclusion, analyzing the atmospheric stability based on both bulk Richardson number and lapse rate shows that with increasing stability, the WL177 wind vector quality is increasing.

4. Conclusions and outlook

In the framework of the VALUAS project, three field campaigns (IOPs 1–3) during July 2020, June 2021, and November 2022 were carried out at the boundary layer field site Falkenberg, about 60 km southeast of Berlin, in flat but heterogeneous terrain.

The goal of the campaigns and the ongoing data analysis was the validation of Doppler wind lidar (DWL) systems using small uncrewed aircraft systems (UASs) with a special focus on the height range 100–500 m. The latter were operated by the University of Tübingen, while two DWLs running in different modes (WL143 and WL177) were operated by the German Weather Service [Deutscher Wetterdienst (DWD)]. In total, 146 research flights were performed with a typical duration of 1.5 h each. For this study, data from 73 flights were used.

The statistical analysis applied mainly consists of determining systematic differences (bias) B, scatter σ expressed by the root-mean-square difference, correlation coefficients R, and linear regressions in the scatter diagrams.

For both UAS–tower and UAS–DWL validation, the airborne-measured in situ data were subdivided and grouped in a way that data pairs (UAS vs DWL) were as much representative of the same air volume as possible. But of course, instruments like cup anemometers or DWL probe the atmosphere vertically from a fixed location, while aircraft operating on straight and

TABLE 10. Wind speed and direction differences UAS vs WL177. The four different Ri_b groups indicate unstable conditions (groups 1 and 2), statically stable but dynamically unstable conditions (group 3), and stable conditions (group 4).

Wind speed						Wind direction					
Group	Ri_b	Data pairs n	σ_Y	R_v	B_Y	Group	Ri_b	Data pairs n	σ_ϕ	R_ϕ	B_ϕ
1	$\mathrm{Ri}_b < -0.25$	65	0.196	0.854	0.084	1	$\mathrm{Ri}_b < -0.25$	44	25.5°	0.976	−1.1°
2	$-0.25 < \mathrm{Ri}_b < 0$	95	0.118	0.965	0.054	2	$-0.25 < \mathrm{Ri}_b < 0$	55	18.9°	0.990	−1.0°
3	$0 < \mathrm{Ri}_b < 0.25$	25	0.044	0.991	0.022	3	$0 < \mathrm{Ri}_b < 0.25$	24	16.0°	0.985	−2.6°
4	$\mathrm{Ri}_b > 0.25$	11	0.060	0.957	0.002	4	$\mathrm{Ri}_b > 0.25$	11	15.7°	0.980	−5.9°

level flight sections (legs) gives horizontal datasets at fixed altitudes. Thus, the two systems do not necessarily probe the same air mass. This factor was considered in the present study by a fetch angle α. For small to medium α (which represents more or less the crosswind share of the airborne measured in situ data), no significant effect on the statistics of both UAS versus tower and UAS versus DWL was found. For $\alpha > 40°$, the fetch angle effect became noticeable and degraded the statistical agreement.

The first part of the presented analysis validates the UAS data versus tower measurements (cup anemometer and vane) at 98 m AGL. As already shown in the past, see, e.g., Martin et al. (2011), a small research UAS is able to measure—among other quantities—the horizontal wind vector with high accuracy. In the present study, the systematic bias between tower-based cup anemometer and vane data versus the airborne wind vector is about 0.7% (wind speed) and below 4° (direction) for 10-min averaged data. The correlation coefficient between tower and UAS data is better than 0.95 for both wind speed and direction using 10-min averages.

The general comparison of both DWL (WL143 and WL177) versus UAS using the entire database shows that both approaches for measuring the mean horizontal wind velocity v and direction ϕ yield data in good agreement: correlation coefficients are higher than 0.94 for wind speed and above 0.98 for wind direction. Systematic differences between DWL- and UAS-derived wind direction are both lower than 2.5°. However, systematic overestimation (WL143) of 5.1% and underestimation (WL177) of 5.7% were found regarding the horizontal wind speed.

The grouping of the dataset in altitude ranges (up to 550 m AGL) revealed a dependency of the intercomparison results on height. The WL177 system shows an improvement in the wind speed retrieval quality over altitude, while the wind direction retrieval quality does not show a clear tendency: WL177 is operated with a focus setting at 500 m; this typically implies the best SNR values around this height range. It also seems that the lower range gates contribute more in the underestimation of the wind speed. It should be remembered that the UAS crosses a mixed landscape with some patches of forest in the vicinity of GM Falkenberg. This may have some influence on the wind measurements, especially at the lowest levels. In contrast, the WL143 system shows a decrease in the quality of the wind speed and direction retrieval with increasing altitude, with wind speed being the most affected. Here, on the other hand, it is the higher-range gate that overestimates the wind velocity. Furthermore, up to heights of 500 m, no significant adverse impact of the wider scan cone (resulting from a larger zenith angle) of WL177 is observed in comparison to WL143. This observation holds true despite the fact that the majority of our data was collected within the unstable convective boundary layer.

Atmospheric stability was examined on the basis of the temperature lapse rate γ (i.e., indication of statically stable or unstable conditions) and the bulk Richardson number Ri_b (i.e., indication of dynamically stable or unstable conditions). Temperature differences at the lower level of the surface layer from 1 to 10 m indicated mostly statically unstable conditions during the first two IOPs in the summers of 2020 and 2021 ($\gamma < 0$), while mainly stable conditions were present during the last IOP during autumn of 2022 ($\gamma > 0$), as indicated in Figs. 10 and 11. In both cases of wind speed and direction, a general tendency toward a better agreement between the UAS and WL177 is observed through the correlation coefficient, bias, and standard deviation during more stable conditions. Such conditions dampen vertical air exchange and create a more homogeneous, undisturbed wind field, which is closer to the inherent assumption of wind homogeneity that lidar systems often undertake, when they are in operation. This justifies how the overall statistics between the UAS and WL177 improve the more stable conditions, as shown in Tables 10 and 11.

Several postprocessing algorithms have been developed and are presently employed for processing data from DWLs operated by the German Weather Service. A forthcoming study aims to investigate the distinctions among these algorithms, utilizing the existing reference UAS data within the altitude range of 100–500 m.

TABLE 11. Wind speed and direction differences UAS vs WL177 for thermally stable (2) and unstable cases (1).

Wind speed						Wind direction					
Group	γ	Data pairs n	σ_Y	R_v	B_Y	Group	γ	Data pairs n	σ_ϕ	R_ϕ	B_ϕ
1	$\gamma < 0$	172	0.150	0.977	0.063	1	$\gamma < 0$	110	18.1°	0.984	−0.9°
2	$\gamma > 0$	22	0.047	0.991	0.007	2	$\gamma > 0$	22	16.0°	0.985	−4.9°

Furthermore, the available database comprises of airborne in situ measurements of turbulence data for the 3D wind vector and air temperature. A subsequent phase of research will be dedicated to the validation of the turbulence variables obtained from DWLs by comparing them against the UAS dataset.

Acknowledgments. The authors thank the German Weather Service [Deutscher Wetterdienst (DWD)] for funding and supporting this research, specifically the Federal Ministry for Education and Research for Project Funding (NABF), under grant agreement with a reference: 4819EMF01. The authors declare no conflicts of interest. Jakob Boventer performed all the flights included in the study, did the initial analysis and drafted a first version of the manuscript. Matteo Bramati and Vasileios Savvakis were part of the flight operations, data acquisition, continued and expanded the analysis/discussion, and concluded the writing of the manuscript. Frank Beyrich contributed with guidance on the analysis procedure, discussion and scientific aims of the manuscript. Markus Keyser was involved in writing the description of the lidar systems and assisted in data retrieval from the instruments. Andreas Platis and Jens Bange supervised the flight operations, analysis and discussion, and contributed to the writing of the manuscript.

Data availability statement. The data used in this work can become available from the corresponding author upon reasonable request.

APPENDIX A

Flight Overview

The complete list of flights performed during the three VALUAS IOPs is reported in Table A1.

TABLE A1. List of all MASC-3 measurement times and their contribution to the validation with different timeframes during the IOP-1, IOP-2, and IOP-3 in the years 2020, 2021, and 2022 at the MOL-RAO.

Flight No.	Date	Measurement time (UTC)	Flight No.	Date	Measurement time (UTC)
1	7 Jul 2020	0950–1051	94	16 Jun 2021	0846–0958
2	7 Jul 2020	1314–1357	95	16 Jun 2021	1217–1336
3	7 Jul 2020	1516–1541	101	19 Jun 2021	0624–0735
5	8 Jul 2020	1506–1610	102	19 Jun 2021	0826–0911
6	8 Jul 2020	1654–1800	103	21 Jun 2021	1254–1412
8	9 Jul 2020	0941–1100	104	23 Jun 2021	0827–0944
9	10 Jul 2020	0924–1046	105	23 Jun 2021	1537–1649
10	10 Jul 2020	1119–1214	106	24 Jun 2021	0857–1007
11	10 Jul 2020	1312–1408	107	25 Jun 2021	0836–0918
12	11 Jul 2020	0820–0910	108	25 Jun 2021	1019–1148
18	12 Jul 2020	1225–1336	109	25 Jun 2021	1419–1536
21	13 Jul 2020	1326–1439	110	26 Jun 2021	0635–0800
22	14 Jul 2020	0818–0859	111	26 Jun 2021	0915–1030
25	16 Jul 2020	0840–0958	113	28 Jun 2021	1453–1609
28	17 Jul 2020	0830–0938	115	29 Jun 2021	1007–1151
29	17 Jul 2020	1138–1246	118	2 Jul 2021	1316–1349
31	18 Jul 2020	0843–0931	119	2 Jul 2021	1654–1817
34	20 Jul 2020	0835–0952	121	17 Nov 2022	0955–1027
35	20 Jul 2020	1110–1218	122	17 Nov 2022	1254–1342
37	21 Jul 2020	0808–0923	123	17 Nov 2022	1431–1507
42	22 Jul 2020	1325–1436	126	19 Nov 2022	1007–1109
44	23 Jul 2020	1029–1131	127	19 Nov 2022	1225–1327
48	24 Jul 2020	1231–1329	128	19 Nov 2022	1418–1518
52	25 Jul 2020	1031–1108	131	21 Nov 2022	0923–1034
56	27 Jul 2020	1158–1229	134	23 Nov 2022	1419–1508
62	29 Jul 2020	0959–1033	135	25 Nov 2022	1345–1458
73	7 Jun 2021	1325–1419	136	27 Nov 2022	0902–100
74	8 Jun 2021	0929–1051	137	27 Nov 2022	1051–1124
75	8 Jun 2021	1231–1348	138	27 Nov 2022	1253–1412
76	9 Jun 2021	1051–1148	139	27 Nov 2022	1432–1508
82	11 Jun 2021	0829–0956	140	28 Nov 2022	0849–0951
83	11 Jun 2021	1109–1209	141	28 Nov 2022	1015–1128
84	11 Jun 2021	1755–1913	142	28 Nov 2022	1250–1403
85	13 Jun 2021	1132–1238	144	29 Nov 2022	0846–1001
86	13 Jun 2021	1330–1436	145	29 Nov 2022	1035–1149
92	15 Jun 2021	0928–1031	146	29 Nov 2022	1249–1356
93	15 Jun 2021	1534–1655			

APPENDIX B

UAS Data Processing Flowchart

Figure B1 displays in a schematic way the steps of the UAS data processing.

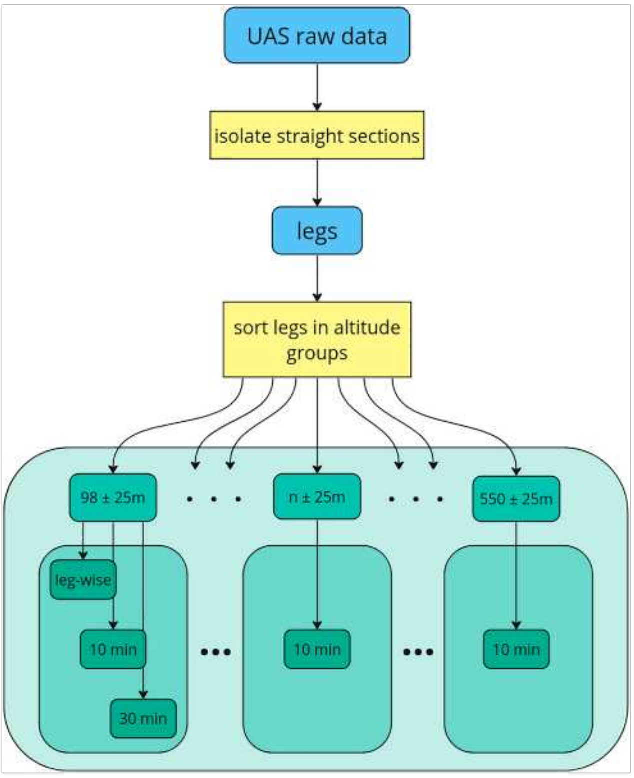

FIG. B1. Schematic representation of the UAS raw data processing procedure. Only the data at the cup anemometer altitude (98 m) are split into three different averaging times. For all the other altitude groups, only 10-min averages are computed and used for WL validation.

REFERENCES

Bange, J., and Coauthors, 2013: Measurement of aircraft state and thermodynamic and dynamic variables. *Airborne Measurements for Environmental Research: Method and Instruments*, A. Kokhanovsky, M. Wendisch, and J.-L. Brenguier, Eds., John Wiley and Sons, 7–75, https://doi.org/10.1002/9783527653218.ch2.

——, J. Reuder, and A. Platis, 2021: Unmanned aircraft systems. *Springer Handbook of Atmospheric Measurements*, T. Foken, Ed., Springer, 1331–1349, https://doi.org/10.1007/978-3-030-52171-4_49.

Baumgarten, G., J. Fiedler, J. Hildebrand, and F.-J. Lübken, 2015: Inertia gravity wave in the stratosphere and mesosphere observed by Doppler wind and temperature lidar. *Geophys. Res. Lett.*, **42**, 10 929–10 936, https://doi.org/10.1002/2015GL066991.

Chanin, M. L., A. Garnier, A. Hauchecorne, and J. Porteneuve, 1992: Description of a Doppler Rayleigh lidar for measuring winds in the middle atmosphere. *Appl. Phys.*, **55B**, 35–40, https://doi.org/10.1007/BF00348610.

Cohn, S. A., and R. K. Goodrich, 2002: Radar wind profiler radial velocity: A comparison with Doppler lidar. *J. Appl. Meteor.*, **41**, 1277–1282, https://doi.org/10.1175/1520-0450(2002)041<1277:RWPRVA>2.0.CO;2.

Courtney, M., R. Wagner, and P. Lindelöw, 2008: Testing and comparison of lidars for profile and turbulence measurements in wind energy. *IOP Conf. Ser.: Earth Environ. Sci.*, **1**, 012021, https://doi.org/10.1088/1755-1315/1/1/012021.

Davies, B. M., and D. J. Thomson, 1999: Comparisons of some parametrizations of wind direction variability with observations. *Atmos. Environ.*, **33**, 4909–4917, https://doi.org/10.1016/S1352-2310(99)00287-3.

Fischler, M. A., and R. C. Bolles, 1981: Random sample consensus: A paradigm for model fitting with applications to image analysis and automated cartography. *Commun. ACM*, **24**, 381–395, https://doi.org/10.1145/358669.358692.

Gasch, P., A. Wieser, J. K. Lundquist, and N. Kalthoff, 2020: An LES-based airborne Doppler lidar simulator and its application to wind profiling in inhomogeneous flow conditions. *Atmos. Meas. Tech.*, **13**, 1609–1631, https://doi.org/10.5194/amt-13-1609-2020.

Gottschall, J., M. S. Courtney, R. Wagner, H. E. Jørgensen, and I. Antoniou, 2012: Lidar profilers in the context of wind energy–A verification procedure for traceable measurements. *Wind Energy*, **15**, 147–159, https://doi.org/10.1002/we.518.

Ishii, S., K. Mizutani, T. Aoki, M. Sasano, Y. Murayama, T. Itabe, and K. Asai, 2005: Wind profiling with an eye-safe coherent Doppler lidar system: Comparison with radiosondes and VHF radar. *J. Meteor. Soc. Japan*, **83**, 1041–1056, https://doi.org/10.2151/jmsj.83.1041.

Käsler, Y., S. Rahm, R. Simmet, and M. Kühn, 2010: Wake measurements of a multi-MW wind turbine with coherent long-range pulsed Doppler wind lidar. *J. Atmos. Oceanic Technol.*, **27**, 1529–1532, https://doi.org/10.1175/2010JTECHA1483.1.

Klaas-Witt, T., and S. Emeis, 2022: The five main influencing factors for lidar errors in complex terrain. *Wind Energy Sci.*, **7**, 413–431, https://doi.org/10.5194/wes-7-413-2022.

Knist, C., V. Lehmann, and M. Kayser, 2018: Das Vorhaben "Pilotstation bodengebundene Fernerkundung". MOL-RAO Aktuell, 2 pp., https://www.dwd.de/DE/forschung/atmosphaerenbeob/lindenbergersaeule/rao_download/aktuell_2018_02.pdf;jsessionid=895B74A1FF037CAC36DB9BF61BB7A2A7.live11054?__blob=publicationFile&v=1.

Kumer, V.-M., J. Reuder, and B. R. Furevik, 2014: A comparison of lidar and radiosonde wind measurements. *Energy Procedia*, **53**, 214–220, https://doi.org/10.1016/j.egypro.2014.07.230.

Lawrence, T. R., D. J. Wilson, C. E. Craven, I. P. Jones, R. M. Huffaker, and J. A. L. Thomson, 1972: A laser velocimeter for remote wind sensing. *Rev. Sci. Instrum.*, **43**, 512–518, https://doi.org/10.1063/1.1685674.

Liu, Z., J. F. Barlow, P.-W. Chan, J. C. H. Fung, Y. Li, C. Ren, H. W. L. Mak, and E. Ng, 2019: A review of progress and applications of pulsed Doppler wind lidars. *Remote Sens.*, **11**, 2522, https://doi.org/10.3390/rs11212522.

Lundquist, J. K., M. J. Churchfield, S. Lee, and A. Clifton, 2015: Quantifying error of lidar and sodar Doppler beam swinging measurements of wind turbine wakes using computational fluid dynamics. *Atmos. Meas. Tech.*, **8**, 907–920, https://doi.org/10.5194/amt-8-907-2015.

Mariani, Z., R. Crawford, B. Casati, and F. Lemay, 2020: A multi-year evaluation of Doppler lidar wind-profile observations in the Arctic. *Remote Sens.*, **12**, 323, https://doi.org/10.3390/rs12020323.

Martin, S., J. Bange, and F. Beyrich, 2011: Meteorological profiling of the lower troposphere using the research UAV "M^2AV Carolo". *Atmos. Meas. Tech.*, **4**, 705–716, https://doi.org/10.5194/amt-4-705-2011.

Mengelkamp, H.-T., and Coauthors, 2006: Evaporation over a heterogeneous land surface. *Bull. Amer. Meteor. Soc.*, **87**, 775–786, https://doi.org/10.1175/BAMS-87-6-775.

Nechaj, P., L. Gaál, J. Bartok, O. Vorobyeva, M. Gera, M. Kelemen, and V. Polishchuk, 2019: Monitoring of low-level wind shear by ground-based 3D lidar for increased flight safety, protection of human lives and health. *Int. J. Environ. Res. Public Health*, **16**, 4584, https://doi.org/10.3390/ijerph16224584.

Neisser, J., W. Adam, F. Beyrich, U. Leiterer, and H. Steinhagen, 2002: Atmospheric boundary layer monitoring at the meteorological observatory Lindenberg as a part of the "Lindenberg Column": Facilities and selected results. *Meteor. Z.*, **11**, 241–253, https://doi.org/10.1127/0941-2948/2002/0011-0241.

Päschke, E., R. Leinweber, and V. Lehmann, 2015: An assessment of the performance of a 1.5 μm Doppler lidar for operational vertical wind profiling based on a 1-year trial. *Atmos. Meas. Tech.*, **8**, 2251–2266, https://doi.org/10.5194/amt-8-2251-2015.

Platis, A., B. Altstädter, B. Wehner, N. Wildmann, A. Lampert, M. Hermann, W. Birmili, and J. Bange, 2016: An observational case study on the influence of atmospheric boundary-layer dynamics on new particle formation. *Bound.-Layer Meteor.*, **158**, 67–92, https://doi.org/10.1007/s10546-015-0084-y.

Rahlves, C., F. Beyrich, and S. Raasch, 2022: Scan strategies for wind profiling with Doppler lidar–An Large-Eddy Simulation (LES)-based evaluation. *Atmos. Meas. Tech.*, **15**, 2839–2856, https://doi.org/10.5194/amt-15-2839-2022.

Rautenberg, A., and Coauthors, 2019: The multi-purpose airborne sensor carrier MASC-3 for wind and turbulence measurements in the atmospheric boundary layer. *Sensors*, **19**, 2292, https://doi.org/10.3390/s19102292.

Reitebuch, O., and R. M. Hardesty, 2021: Doppler wind lidar. *Springer Handbook of Atmospheric Measurements*, T. Foken, Ed., Springer, 759–797, https://doi.org/10.1007/978-3-030-52171-4_27.

Robey, R., and J. K. Lundquist, 2022: Behavior and mechanisms of Doppler wind lidar error in varying stability regimes. *Atmos. Meas. Tech.*, **15**, 4585–4622, https://doi.org/10.5194/amt-15-4585-2022.

Schön, M., and Coauthors, 2022: Case studies of the wind field around Ny-Ålesund, Svalbard, using unmanned aircraft. *Polar Res.*, **41**, 1–15, https://doi.org/10.33265/polar.v41.7884.

Smith, D. A., M. Harris, A. S. Coffey, T. Mikkelsen, H. E. Jørgensen, J. Mann, and R. Danielian, 2006: Wind lidar evaluation at the Danish wind test site in Høvsøre. *Wind Energy*, **9**, 87–93, https://doi.org/10.1002/we.193.

Stull, R., 2016: *Practical Meteorology: An Algebra-Based Survey of Atmospheric Science*. BC Open Textbook Collection, AVP International, University of British Columbia, 926 pp., https://books.google.de/books?id=xP2sDAEACAAJ.

Teschke, G., and V. Lehmann, 2017: Mean wind vector estimation using the velocity–azimuth display (VAD) method: An explicit algebraic solution. *Atmos. Meas. Tech.*, **10**, 3265–3271, https://doi.org/10.5194/amt-10-3265-2017.

van den Kroonenberg, A., T. Martin, M. Buschmann, J. Bange, and P. Vörsmann, 2008: Measuring the wind vector using the autonomous mini aerial vehicle M^2AV. *J. Atmos. Oceanic Technol.*, **25**, 1969–1982, https://doi.org/10.1175/2008JTECHA1114.1.

Wildmann, N., M. Hofsäß, F. Weimer, A. Joos, and J. Bange, 2014a: MASC–a small Remotely Piloted Aircraft (RPA) for wind energy research. *Adv. Sci. Res.*, **11**, 55–61, https://doi.org/10.5194/asr-11-55-2014.

——, S. Ravi, and J. Bange, 2014b: Towards higher accuracy and better frequency response with standard multi-hole probes in turbulence measurement with remotely piloted aircraft (RPA). *Atmos. Meas. Tech.*, **7**, 1027–1041, https://doi.org/10.5194/amt-7-1027-2014.

——, S. Bernard, and J. Bange, 2017: Measuring the local wind field at an escarpment using small remotely-piloted aircraft. *Renewable Energy*, **103**, 613–619, https://doi.org/10.1016/j.renene.2016.10.073.

——, N. Bodini, J. K. Lundquist, L. Bariteau, and J. Wagner, 2019: Estimation of turbulence dissipation rate from Doppler wind lidars and in situ instrumentation for the Perdigão 2017 campaign. *Atmos. Meas. Tech.*, **12**, 6401–6423, https://doi.org/10.5194/amt-12-6401-2019.

Witschas, B., C. Lemmerz, A. Geiß, O. Lux, U. Marksteiner, S. Rahm, O. Reitebuch, and F. Weiler, 2020: First validation of Aeolus wind observations by airborne Doppler wind lidar measurements. *Atmos. Meas. Tech.*, **13**, 2381–2396, https://doi.org/10.5194/amt-13-2381-2020.

zum Berge, K., and Coauthors, 2021: A two-day case study: Comparison of turbulence data from an unmanned aircraft system with a model chain for complex terrain. *Bound.-Layer Meteor.*, **180**, 53–78, https://doi.org/10.1007/s10546-021-00608-2.

——, A. Gaiser, H. Knaus, A. Platis, and J. Bange, 2023: Seasonal changes in boundary-layer flow over a forested escarpment measured by an uncrewed aircraft system. *Bound.-Layer Meteor.*, **186**, 69–91, https://doi.org/10.1007/s10546-022-00743-4.

In Situ Uncrewed Aircraft Measurements of Turbulent Kinetic Energy over Heterogeneous Terrain

MATTEO BRAMATI,[a] VASILEIOS SAVVAKIS,[a] FRANK BEYRICH,[b] JENS BANGE,[a] AND ANDREAS PLATIS[a]

[a] *Eberhard Karls Universität Tübingen, Geo- und Umweltforschungszentrum, Tübingen, Germany*
[b] *Meteorological Observatory Lindenberg - Richard-Aßmann-Observatory, German Meteorological Service (DWD), Offenbach, Germany*

(Manuscript received 22 February 2024, in final form 18 October 2024, accepted 9 January 2025)

ABSTRACT: Turbulent kinetic energy (TKE) is a key variable in understanding the energy dynamics within the atmospheric boundary layer. Accurate characterization of TKE is crucial for several applications, especially in regions characterized by complexity and heterogeneity. This study investigates the comparison between a moving sensor, an uncrewed aircraft system (UAS), and a stationary sensor, a sonic anemometer, in the heterogeneous terrain of the boundary layer field site Falkenberg (Lindenberg, Germany) operated by the German Weather Service (DWD). The UAS, a multipurpose airborne sensor carrier (MASC-3), was operated during three measurement campaigns in July 2020, June 2021, and November 2022, respectively. The comparison pairs UAS measurements with data collected by a sonic anemometer positioned at a height of 90 m on a meteorological tower. The analysis focuses on careful data processing and precise synchronization of the time series from both sensors, so that the same air mass is taken into account when calculating turbulence statistics. The study examines several parameters that can affect the quality of the comparison. The analysis showed that the bias and scatter between the two sensors are a function of the wind direction: the best agreement was recorded when the wind came from the south, a region of flat terrain (bias of 21%, scatter of 53%). Conversely, less favorable statistics were obtained when the wind blew from a sector between west to north, regions that are predominantly characterized by forest cover (bias of 68%, scatter of 103%). This result illustrates the difficulties of comparing UAS measurements along a 1.5–2.0-km long path with stationary point measurements above a heterogeneous land surface.

KEYWORDS: Complex terrain; Turbulence; Wind; Measurements

1. Introduction

One of the most crucial quantities to consider when studying phenomena such as convection and wind shear in the atmospheric boundary layer (ABL) is turbulent kinetic energy (TKE). It is defined as the mean kinetic energy that stems from the variances of the three wind velocity components; it is physically related to the kinetic energy of the turbulent eddies and directly connected to the transport of momentum, heat, and moisture (Stull 1988). Over the decades, several studies have focused on characterizing and modeling its budget equation (Wyngaard and Coté 1971; Lenschow 1974; Caughey and Wyngaard 1979). This attention arises from the fact that certain components of the TKE budget are directly related to commonly used atmospheric stability parameters. The objective of these studies has been to identify similarities or scaling parameters under specific atmospheric conditions, with the ultimate goal of facilitating the development of simplified analytical models (Wyngaard 1992).

The exponential growth in computing capabilities over recent decades has led to the widespread use of large-eddy simulation (LES) models and high-resolution numerical weather forecast models (Andren et al. 1994; Stoll et al. 2020). TKE is a key parameter in various turbulence models used in LES, as it provides a quantitative measure of the turbulence intensity and dynamics, particularly at scales that are not directly resolved in the simulations. These tools, created by various research groups, often yield similar outcomes (Hodgson et al. 2023), but, as for any numerical simulation, validation through experimental results is still crucial (El Bahlouli et al. 2020; Platis et al. 2021; zum Berge et al. 2021). Moreover, obtaining input parameters closely aligned with realistic conditions becomes essential for enhancing the model's ability to accurately simulate real-world turbulent flows and, therefore, to provide reliable forecasting results (Bielli and Roux 1999; Xu et al. 2009; Wang et al. 2010; Auerswald et al. 2012; Brilouet et al. 2020).

For these reasons, there is a significant demand for in situ measurements of turbulent quantities (Wilczak et al. 2019), particularly in areas where simulations deal with distinctive topography, heterogeneous terrain, or natural obstacles; essentially, regions where the characteristics deviate from the conventional flat and homogeneous terrain (Risanto et al. 2023). This is because over such terrains, simplified models such as similarity constants cannot be used reliably (Foken 2006), given that different terrain surfaces facilitate the development and interaction of boundary layers with profoundly different characteristics (Kalthoff et al. 1998; Kossmann et al. 1998; Bou-Zeid et al. 2020).

In the atmosphere, TKE can be determined with high-resolution measurements of the three-dimensional wind vector

---

Denotes content that is immediately available upon publication as open access.

Corresponding author: Matteo Bramati, matteo.bramati@uni-tuebingen.de

DOI: 10.1175/JTECH-D-24-0026.1

(Foken and Bange 2021). For ground-based meteorological stations or towers, sonic anemometers provide such detailed measurements. However, these sensors provide fixed-point measurements that are generally limited to altitudes close to the ground or up to heights of 300 m at a very few instrumented tall towers. Measurements at higher levels or based on more flexible measurement strategies can only be obtained by using crewed (Lenschow 1970, 1974; Pennell and LeMone 1974; Nicholls and Readings 1979; Tjernström and Smedman 1993; Lohou et al. 1998; Brooks et al. 2003; Saïd et al. 2010; Cook and Renfrew 2015; Brilouet et al. 2020; Siedersleben et al. 2020; Syed et al. 2022; Platis et al. 2022, 2023) or uncrewed aircrafts systems (UASs) (Reuder et al. 2012; Platis et al. 2016; Alaoui-Sosse et al. 2019; Lampert et al. 2020; zum Berge et al. 2021; Chechin et al. 2021; Wildmann and Wetz 2022; zum Berge et al. 2022; Shelekhov et al. 2022).

As mentioned by Bange et al. (2021), smaller research UAS can provide accurate data on temperature, humidity, and wind, comparable to larger crewed aircraft and can fly at lower altitudes. Even though these UAS have smaller payloads and less endurance, they come with cost and logistical advantages that make them suitable tools for capturing detailed small-scale patterns of atmospheric wind, temperature, and moisture fields (Platis et al. 2016; Rautenberg et al. 2019b; zum Berge et al. 2021; Schön et al. 2022; de Boer et al. 2024). Moreover, the application of small UAS for remote sensing validation has been established in previous studies (Martin et al. 2011). For a comprehensive overview of meteorological UAS and research aircraft in general, readers are directed to Bange et al. (2013).

In our study, fixed-wing UASs of type multipurpose airborne sensor carrier (MASC-3) (Rautenberg et al. 2019b) were employed by the Environmental Physics Group of the University of Tübingen, Germany, to collect in situ turbulent wind-vector measurements during three intensive observation periods (IOPs) in 2020, 2021, and 2022, in the frame of the validation of numerical simulations and remote sensing using UAS (VALUAS) project. One of the objectives of the project was to utilize UAS-derived data as a reference for evaluating the accuracy and precision of TKE retrievals between 100 m and 500 m above ground level (AGL) obtained by Doppler wind lidars (DWLs) operated by the German Weather Service [Deutscher Wetterdienst (DWD)].

However, turbulence-related in situ measurements and remote sensing devices validation using fixed-wing UAS have rarely been practiced, and a few existing studies note the importance of terrain homogeneity on the results (Beyrich et al. 2012; Sun et al. 2023). As highlighted by Rautenberg et al. (2019b), the ability to accurately compare data obtained from a flying fixed-wing UAS with a stationary sensor depends on the validity of the Taylor hypothesis of frozen turbulence. Therefore, it becomes crucial to examine carefully whether this hypothesis holds true and if terrain heterogeneity plays a role in its validity.

The primary objective of this initial phase of the study is to evaluate the accuracy and precision of the UAS system itself in measuring TKE. This is achieved by comparing its measurements with those obtained from an ultrasonic anemometer mounted on a meteorological tower. A similar investigation was previously conducted, wherein the MASC-3 system flew over a flat, homogeneous ice surface under strong stable conditions in Finland. The results, presented by Rautenberg et al. (2019b), showcased a high level of agreement between the flying system and a sonic anemometer installed on a meteorological tower and demonstrated the capabilities of the MASC-3 to measure statistical moments up to second order. However, for the region where the VALUAS IOPs took place, previous studies (Bange et al. 2002; Beyrich et al. 2006; Platis et al. 2017a,b) on low-altitude flights for momentum and sensible heat fluxes indicated that the results were highly dependent on the roughness of the surface below, and flights over a forested area resulted in larger fluxes. These results were also in alignment with direct measurements from ground stations at the same location. Furthermore, the effect of land use and vegetation type on resulting turbulent flux calculations has been shown to be significant between classes of different surface characteristics such as water, or a forest (Beyrich et al. 2002a,b, 2006). Building on these premises, this study addresses the following questions:

- How can data from a UAS be compared accurately with that from a stationary sensor?
- Is it feasible to compare turbulence measurements obtained by a stationary sensor and a UAS over heterogeneous terrain, such as that encountered during the VALUAS IOPs? Does the Taylor hypothesis of frozen turbulence remain valid?
- How is the quality of the comparison, and are there any flight-specific factors influencing it?

The manuscript is structured as follows: section 2 introduces the measurement site, outlines the three field campaigns, and discusses the two systems considered for the comparison. Special attention is given to data handling, as there is currently no established method for processing and comparing datasets from stationary and moving sensors, requiring careful consideration and clarification. The turbulent quantity under analysis (TKE) is defined, along with the quality metrics employed to assess the precision and accuracy of one sensor compared to the other. In section 3, the results of the three IOPs are presented in an overall plot, proving the advantages of the data-handling algorithm. Subsequently, the influence of different parameters on the quality of the comparison is studied in detail. Finally, section 4 summarizes the key findings of the study and provides an assessment of the feasibility of the potential next validation of the DWLs by using the UAS dataset.

2. Materials and methods

a. *Measurement site and campaigns*

The boundary layer field site Falkenberg [in German, Grenzschicht-Messfeld (GM) Falkenberg] of the DWD, about 60 km southeast of Berlin, Germany, hosted all the measurement campaigns for this study.

The DWD operates this site to study the ABL in the area around the Meteorological Observatory Lindenberg–Richard Aßmann Observatory (MOL-RAO), aiming to provide comprehensive measurements of the entire tropospheric reference profile known as the "Lindenberg column" (Neisser et al. 2002). The field site is situated upon a low grass meadow and surrounded closely by agricultural fields on which mostly rye, triticale, rape, maize, and sunflowers are grown as typical vegetation. The small village of Falkenberg is located approximately 600 m to the southeast, while forest patches grow in the western and northwestern areas approximately 1.5 km distant. The results of the Lindenberg Inhomogeneous Terrain—Fluxes between Atmosphere and Surface: A Long-Term Study project (LITFASS) (Beyrich et al. 2002a) demonstrate within an area of 20 × 20 km^2 surrounding the GM Falkenberg, how the turbulent fluxes, and in particular vertical momentum and heat fluxes, are extremely dependent on the local surface properties (Bange et al. 2002; Beyrich et al. 2006; Platis et al. 2017a,b). Moreover, it was also noted how even above the same surface (forest, meadow, or agricultural field), there can be very high variability of the turbulent quantities and fluxes mostly due to inhomogeneities in the soil moisture content (Mengelkamp et al. 2006). Therefore, the terrain surrounding the measurement site is considered heterogeneous.

In the framework of the VALUAS project, three IOPs were conducted at the GM Falkenberg. Details about the three measurement campaigns are reported in Table 1, while more in-depth details of the flights are presented in appendix A.

b. *MASC-3 uncrewed aircraft system*

The well-established UAS platform MASC-3 was utilized to collect in situ measurements of atmospheric quantities during the three IOPs (Fig. 1). MASC-3 has demonstrated its reliability across a diverse range of studies, establishing itself as a dependable platform for sampling the lower atmospheric boundary layer (Wildmann et al. 2017; zum Berge et al. 2021; Schön et al. 2022; zum Berge et al. 2022). High-resolution measurements of the three-dimensional wind vector are achieved by outfitting the system with a five-hole probe (5HP), an inertial measurement unit (IMU), and a fast thin-wire resistance thermometer (van den Kroonenberg et al. 2008; Wildmann et al. 2014a,b).

A comprehensive description of the UAS system, including the scientific payload and data postprocessing algorithms, is provided in Rautenberg et al. (2019b). Operating at a constant airspeed (AS) of 19.5 m s^{-1}, the UAS gathers valuable data along so-called "legs," which denote straight and leveled flight sections. Due to challenges in accurately postprocessing the wind vector during turns, only the legs are considered in the subsequent analysis. Mission planning ensured that the aircraft traveled both forward and backward along the same path, with adjustments made to align with the prevailing wind direction as closely as possible. Table 2 outlines the characteristics of the MASC-3 measurement outputs.

TABLE 1. Details of the three measurement campaigns carried out at GM Falkenberg by the Eberhard Karls Universität Tübingen Umweltphysik group in the framework of the VALUAS project including the number of flights and the number of legs (see section 2b) considered for this study.

	Start date	End date	N_{flights}	N_{legs}
IOP-1	7 Jul 2020	29 Jul 2020	13	30
IOP-2	7 Jun 2021	2 Jul 2021	17	84
IOP-3	17 Nov 2022	29 Nov 2022	8	15

FIG. 1. The UAS platform MASC-3 and launching catapult before takeoff. The standard turbulence instrumentation is mounted at the very front of the aircraft. Additional (electrical charge and particle—not topic of this study) sensors are mounted on the wings. The pusher engine with two rotor blades is at the tail of the UAS.

c. *Sonic anemometer*

Two Metek USA-1 ultrasonic anemometers are mounted on the DWD's meteorological tower at heights of 50 and 90 m AGL (see Table 2). These anemometers operate continuously, providing three-dimensional wind vector measurements at a sampling frequency of 20 Hz.

Situated on horizontal booms extending southward from the main tower structure, these anemometers encounter limitations in specific wind directions due to interference from the tower itself. For this study, we focused on the ultrasonic anemometer mounted at 90 m AGL (Fig. 2).

d. *Data processing*

1) DATA FILTERING

As mentioned in section 2c, the highest ultrasonic anemometer installed at Falkenberg is positioned at a height of 90 m AGL. Consequently, among all the UAS flight legs, only those with an average altitude below 105 m and above 80 m AGL were selected.

Additionally, the permanent sensor has limitations in certain wind directions, as its data should not be used for comparison due to the tower's structure standing on the one side of the ultrasonic anemometer. This creates artificial disturbances when the wind blows from between 0° and 50°. A second filter is then applied to the entire set of legs to remove cases where this condition is met. Approximately 6% of the flight legs fall into this category and were consequently excluded from further analysis.

The analysis outlined in Boventer et al. (2024) underscores the significance of maintaining a low angle between the ground trajectory of the aircraft and the mean atmospheric wind direction. This is crucial to ensure that the tower-

TABLE 2. Basic measurement characteristics of the MASC-3 (Rautenberg et al. 2019a,b) and the Metek USA-1 sonic anemometer mounted at 90-m height on the meteorological tower.

	MASC-3	Metek USA-1 sonic anemometer
Sampling rate	100 Hz	20 Hz
Atmospheric wind range	0–30 m s^{-1}	0–60 m s^{-1}
Wind speed accuracy	≈0.2 m s^{-1} @ 9 m s^{-1}	2%
Wind direction accuracy	≈0.4° @ 9 m s^{-1}	2° @ 5 m s^{-1}
Resolution	0.001 m s^{-1}, 0.001°	0.01 m s^{-1}, 0.1°

mounted sensor and the airborne platform measure the same air mass. Further details about this parameter, referred to as the fetch angle, can be found in the aforementioned study.

Thus, in a third and final filtering step, the flight legs were precisely assessed for the fetch angle. Similar to Boventer et al. (2024), only legs with a fetch angle smaller than 40° were considered for further comparison. This additional criterion resulted in the removal of another 35% of the remaining legs.

2) UPWIND AND DOWNWIND LEGS

As detailed in Rautenberg et al. (2019b) and emphasized in section 2b, the MASC-3 flight controller is programmed to maintain a constant AS during flight, irrespective of the atmospheric wind, by using propulsion and pitch in order to regulate the speed. The flight strategy involves flying continuously straight legs between two waypoints, resulting in legs of equal length in space but changing duration in time in case the atmospheric wind is not zero. In the presence of nonzero wind and given the low fetch angle values resulting from the filtering, the UAS flies against the wind on one leg (headwind) and with the wind on the other leg (tailwind). These two conditions are commonly referred to as upwind and downwind legs. It is straightforward that during upwind legs, the ground speed of the aircraft is lower, while it is higher for downwind legs. With legs of equal length, this effect results in time series of different durations, where the time difference between upwind and downwind sections is merely a function of the magnitude of the meteorological horizontal wind speed. Figure 3 illustrates a clear example of the difference between upwind and downwind legs during flight number 118. In accordance with Lenschow et al. (1994), a single, longer data series provides a lower systematic statistical error over turbulent quantity measurements compared to averaging multiple shorter series. Therefore, only the upwind legs are considered for the comparison with the ultrasonic anemometer.

FIG. 2. View on the upper part of the 99-m tower at GM Falkenberg toward WSW, the sonic is mounted on the boom pointing to the left (S) at a height of 90 m. From Boventer et al. (2024).

3) TIME SERIES VERSUS SPACE SERIES

The histogram in Fig. 4 shows the distribution of the spatial length of the 120 legs that passed the aforementioned filters.

Although a direct comparison between the UAS leg data and the ultrasonic anemometer data from the beginning to the end of the leg may appear to be a straightforward approach, a closer examination reveals that it is, in fact, flawed and would inevitably yield misleading results. This discrepancy can be attributed to the fundamentally different measurement methods employed by the two sensors. The anemometer, which is mounted on a tower, samples the air mass that is advected through it, whereas the UAS maintains a fixed AS as it flies through the air. Provided that the wind speed does not exceed the target AS maintained by the autopilot, it will consistently sample a greater volume of air than a stationary sensor in the same period of time. To overcome this difference when comparing high-resolution UAS and ground-based sonic data, both time series must be converted into space series, thus ensuring that the same air masses are being compared.

This assumption is valid only if we consider no crosswind along the flight leg and if the Taylor hypothesis of frozen turbulence holds.

The leg-space series is obtained by integrating the instantaneous true AS (TAS) measured by the sensor payload over the logging time of the leg. The same procedure is applied to the sonic anemometer, using the horizontal wind speed and considering a wider start and end time, given that it always takes longer for the sonic anemometer to sample the same air mass as the UAS. The challenge arises in determining the correct position for the smaller UAS-space series within the wider sonic-space series. In other words, the objective is to identify the identical air mass for both sensors. This procedure is not straightforward, as the overlap of the two data series depends on the relative position in space of the beginning and end of the legs with respect to the tower and the direction of the mean wind.

A mathematical method for obtaining this information is to perform a cross correlation of the two series and identify the maximum value in the cross-correlation coefficient, which indicates the point of greatest similarity between the two series. This procedure facilitates the identification of the spatial lag between MASC-3 and the ultrasonic anemometer data. The aforementioned correction has been applied to the upwind leg of Fig. 3, as depicted in Fig. 5. This information enables

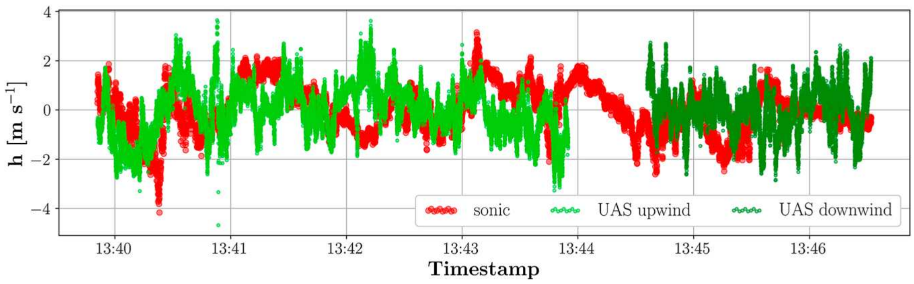

FIG. 3. Example of time difference between upwind (light green) and downwind (dark green) legs. The variable h represents the fluctuating part of the horizontal wind speed. Time series from flight 118 (2 Jul 2021): the mean horizontal wind speed is 7.0 m s^{-1}, the upwind leg duration is around 244 s, while the downwind leg lasts only 116 s.

the determination of the start and end timestamps for the sonic data, thus ensuring their complete representativeness of the air mass sampled by the UAS during each leg.

Figure 6 displays the distribution of the UAS time series duration (Fig. 6a) together with the distribution of the respective duration of the sonic anemometer time series (Fig. 6b) and the horizontal length of the air volume sampled by the two sensors (Fig. 6c): it can be noted, as previously explained, that the sonic anemometer takes longer than the UAS to sample the same length of the air volume. Only after applying this filtering and these corrections, the two datasets, which differ in duration but sample an equal amount of air, can be used for calculating turbulent quantities that can be meaningfully compared.

It is important to remember that this algorithm is based on two assumptions that are linked to each other. These are the Taylor hypothesis of frozen turbulence and the assumption that the trajectory of the UAS during its mission is perfectly aligned with the wind direction. In the case of our dataset, it is not possible to verify both hypotheses, so it would be unwise to expect to have eliminated all uncertainties simply by this procedure. Taylor's hypothesis is the subject of one scientific question of the present study. Therefore, it is not yet possible to consider it valid. Moreover, in order to maintain a significant number of legs in our analysis, it is necessary to relax the condition on the crosswind. However, as will be shown in the following sections, the application of this method to the present dataset provides a significant improvement in the process of comparison between the UAS and the sonic anemometer.

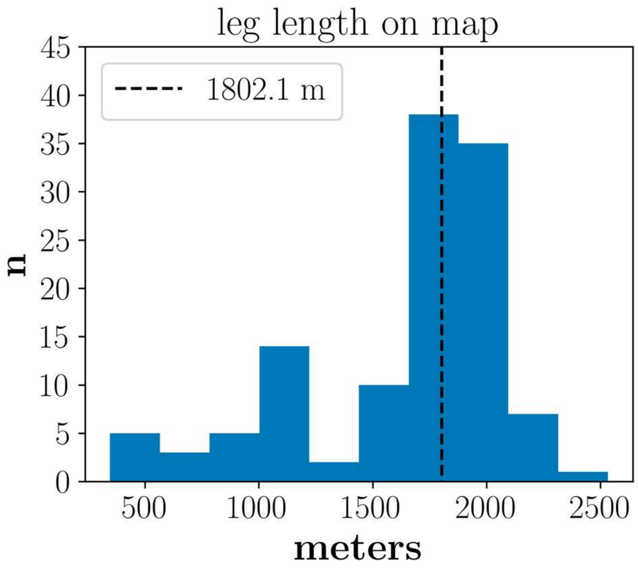

FIG. 4. Distribution of leg length for the data used in the analysis. The black line represents the median value.

e. *Turbulent quantities*

Making use of the common Reynolds decomposition, the wind vector can be written as

$$\mathbf{U} = \overline{\mathbf{U}} + \mathbf{u}, \tag{1}$$

with $\overline{\mathbf{U}}$ being the vector of the mean values of the wind speed while $\mathbf{u} = [u, v, w]$ being the vector of the fluctuating component. Given this definition, it is possible to define the following variables which are of interest for the rest of the analysis.

TKE

The turbulent kinetic energy per unit mass k is defined as the sum of the averages of the three fluctuating components of the wind speed squared (Pope 2001):

$$k = \frac{1}{2}(\overline{u^2} + \overline{v^2} + \overline{w^2}). \tag{2}$$

For discrete random variables such as the three components of the fluctuating velocity, the TKE can be easily computed by summing the variances of the three components:

$$k = \frac{1}{2}[\mathrm{Var}(u) + \mathrm{Var}(v) + \mathrm{Var}(w)]. \tag{3}$$

The calculation of TKE in this study is performed over each of the UAS legs and over the corresponding sonic anemometer corrected time series and employs the formulation of Eq. (3) also implemented in Büchau et al. (2024) after linearly detrending both time series.

f. *Quality metrics*

To compare the two datasets, one coming from the meteorological tower and the other one from the UAS, we define the following statistical quantities:

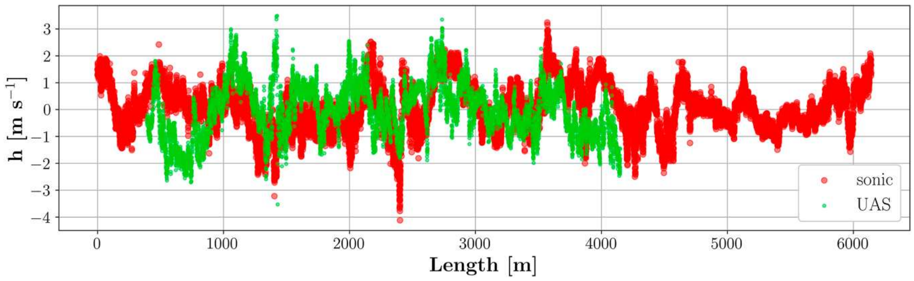

FIG. 5. Example of space-series conversion and synchronization. Here, the two space series are overlapped to obtain the maximum of the cross correlation between them as explained in section 2d(3). The variable h represents the fluctuating part of the horizontal wind speed. Space series from flight 118 (2 Jul 2021): the mean horizontal wind speed is 7.0 m s^{-1}. The leg shown here corresponds to the upwind leg of Fig. 3.

1) BIAS DIFFERENCE AND MEAN BIAS DIFFERENCE

For each UAS leg, we have corresponding TKE measurements obtained from the MASC-3 and the sonic anemometer. The bias difference (BD) is defined as the normalized error between the two measurements:

$$\mathrm{BD}_i = \frac{k_i^{\mathrm{UAS}} - k_i^{\mathrm{sonic}}}{k_i^{\mathrm{sonic}}}. \tag{4}$$

Here, i represents any specific measurement within our dataset. We chose to normalize with the measurement from the sonic anemometer, as this instrument serves as our reference in the initial phase of this study.

Consequently, the mean BD (MBD) will be simply the average over the total number of elements N (number of legs) in the dataset of the BDs:

$$\mathrm{MBD} = \frac{1}{N}\sum_{i=1}^{N} \mathrm{BD}_i. \tag{5}$$

This quantity serves to unveil the presence of any systematic measurement error between the two sensors. In the context of this study, where we aim to conduct a form of calibration for one system (the UAS) using a reference (the sonic anemometer), the BD statistical measure defines the accuracy of the instrument under the calibration procedure. It effectively quantifies the extent to which the UAS measurements align with the reference sonic anemometer, providing crucial insights into the calibration process.

2) RMSD

The root-mean-square difference (RMSD) is defined as the square root of the average of the squared BDs:

$$\mathrm{RMSD} = \sqrt{\frac{1}{N}\sum_{i=1}^{N} \mathrm{BD}_i^2}. \tag{6}$$

This metric serves as a representative measure of the scatter of the data around the reference value. In other words, it allows us to assess the uncertainty of our instrument when measuring TKE.

3. Results and discussion

a. TKE comparison

Figure 7 presents a direct comparison of the TKE measurements acquired using the sonic anemometer and the UAS. Figure 7a illustrates the outcome of our data postprocessing, following the method detailed in section 2d(3). In contrast,

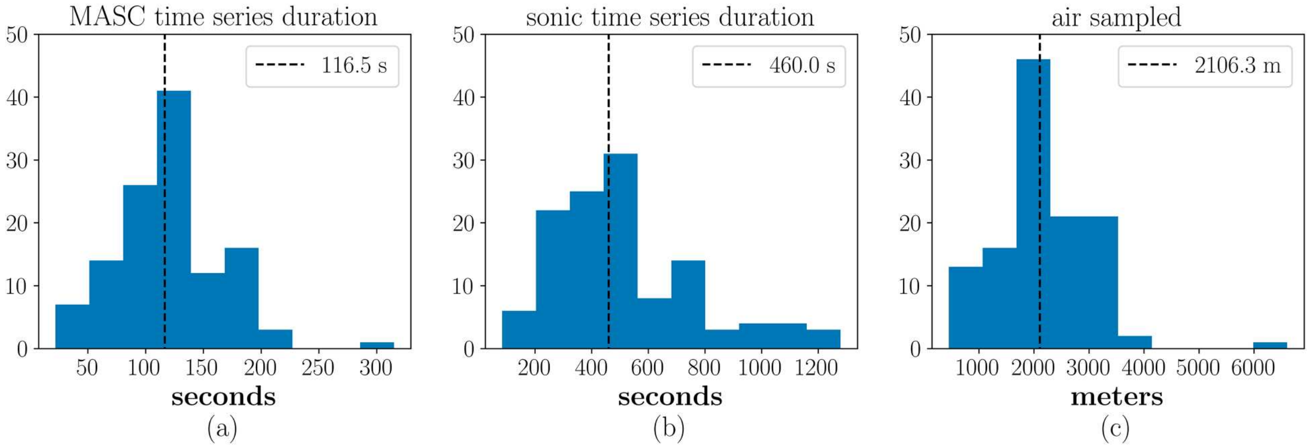

FIG. 6. Distribution of (a) MASC-3 time series duration, namely, the length in time of each UAS leg; (b) sonic anemometer time series duration after the space-series conversion synchronization with the UAS signal; and (c) horizontal length of the air volume sampled by the two sensors.

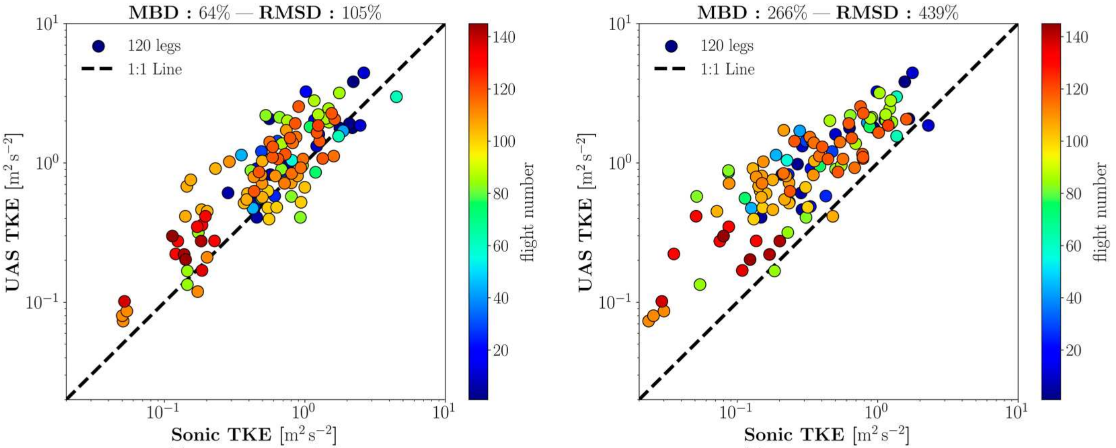

(a) space series method (b) time series method

FIG. 7. Comparison between TKE measured by the sonic anemometer on the meteorological tower and the UAS system. Each of the scatter points corresponds to one UAS leg. (a) Comparison performed over shifted space series; (b) comparison performed by simply considering the sonic and UAS time series cut with the start and end time of each leg.

Fig. 7b displays same values obtained using the same UAS data series, but the sonic data series are simply confined within the start and end of each leg.

These two graphs prove that the comparison performed in this last way is inherently flawed. The comparison of two equally long time series results in a different amount of air sampled by the two systems, with the sonic sensor consistently sampling less air. It is evident that, although the validity of the frozen turbulence hypothesis remains so far unverified and despite a permitted crosswind angle of up to 40°, the simple act of comparing an equivalent amount of air reduces the overestimation of TKE by a factor of 3 or more.

Nevertheless, even when the appropriate postprocessing method is employed, the MBD between the UAS and the reference is still 64%, indicating a systematic overestimation in measurements obtained from the uncrewed aircraft in comparison to the tower reference. Furthermore, the RMSD stands at 105%. This overestimation and scatter appear to be consistent for all the three components of the TKE (appendix B), suggesting that there is no systematic measurement error along any particular direction. This discrepancy demands further investigation to ascertain whether factors pertaining to the UAS or atmospheric conditions exert a substantial influence or whether the two hypotheses that are not entirely fulfilled are the sources of this residual bias.

b. *Spatial influence*

Given the comparatively poorer statistical performance compared to the mean wind analysis conducted in Boventer et al. (2024) (MBD: 1.8%, RMSD: 19.4% for leg-cup anemometer comparison), initial interest was placed on whether further filtering of the results by using the relative distance to the reference sensor would improve the statistics. As elucidated in section 2d, the two measurement devices operate on inherently different principles and methodologies. Despite the meticulous postprocessing corrections described in section 2d(3), statistical disparities may persist owing to the fundamental difference that the two sensors do not measure at the same location. As a result, the UAS legs underwent a progressive filtering process, taking into account circular regions around the meteorological tower. The minimum radius around the tower was established at 300 m, while the maximum radius (where all data are encompassed) was set at 1800 m. An additional criterion was implemented, stating that any new leg entering the subsequent circular region must sample at least 100 m of air. Figure 8a visually illustrates the various circular regions around the meteorological tower.

As we gradually expand the area around the meteorological tower, two distinct factors can influence the TKE comparison statistics. First, in the smallest area (only 300 m around the tower), approximately 50% of the legs fall within this range; as we increase the radius, more legs are encompassed in the analysis, with all legs included once the 800-m radius circle around the tower is reached. Second, as the area considered expands, a larger fraction of each leg is included in the analysis. Consequently, the length of the space series used to calculate TKE progressively increases.

In an attempt to discern between these two effects, two distinct analyses were conducted. The first, depicted in Fig. 8b, involved calculating TKE quality metrics for each leg solely at the moment it entered the analysis area, without updating the values at subsequent iterations. This approach involved generally shorter space series than the ones available from each leg; however, it allowed visualizing the influence of the increasing number of legs within our statistical sample. Initially, just over 50% of the legs (66) are included in the calculation of MBD and RMSD, with 100% of the legs being reached at a radius of 800 m. It can be observed that both MBD and RMSD do not vary significantly as the sample population increases: MBD starts at 82% and stabilizes at 73% when all legs are considered, while RMSD fluctuates but consistently remains around 135%.

On the other hand, Fig. 8c illustrates an analysis where only the 66 legs within the circle of radius 300 m were utilized for calculating quality metrics, ignoring any leg that would enter

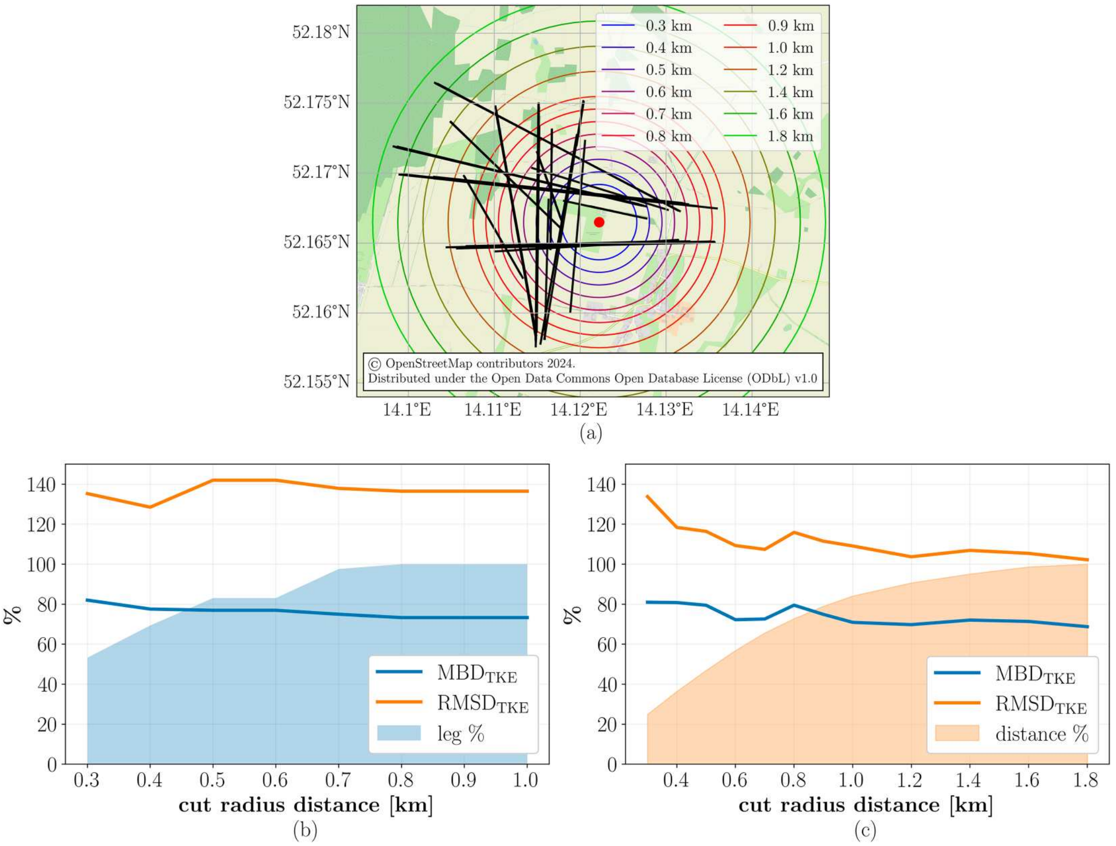

FIG. 8. (a) Map of all the legs used for the analysis with the corresponding increasing cut circles around the meteorological tower. (b) Behavior of the TKE statistics (MBD and RMSD expressed in percentage) with increasing cut radius, increasing the number of legs but not their space extent. (c) Behavior of the TKE statistics (MBD and RMSD expressed in percentage) with increasing cut radius, increasing the leg's space extent but not their number.

the area of interest in further iterations. As the area considered around the meteorological tower expands, the length of each leg increases, consequently increasing the space series length and the amount of air utilized for TKE statistics computation. Initially, only about 25% of the total air is utilized to compute MBD and RMSD, with 100% being utilized only in the area with a radius greater than 1800 m.

Once again, MBD initiates at 82% and decreases to approximately the value depicted in Fig. 7c (around 64%), confirming the adequacy of our statistical sample while also indicating the bias's independence of the leg length. Conversely, RMSD decreases from an initial value of 135%–105%, meaning that considering the legs in their completeness leads to an uncertainty reduction of the measurement although it means flying further from the tower.

c. *Influence of environmental and UAS-related variables*

Our UAS was primarily programmed to execute flight paths aligned either in the north–south (NS) or east–west (EW) directions based on the prevailing wind direction each day. Due to the terrain characteristics, it appears of interest to investigate whether one direction yields better outcomes when comparing the TKE measurements of the two sensors. The parameter indicating the precise direction toward which the UAS is flying is denoted as ground course ψ, typically ranging from 0° to 360° (starting from north in a clockwise direction). However, at this point, it is irrelevant toward where exactly the UAS is flying: what matters is just the orientation of the leg on the map; therefore, wrapping the ground course between 0° and 180° makes the analysis and the plotting of the results simpler and easier. A ground course of 0° or 180° signifies a perfect NS leg, whereas 90° represents a perfect EW orientation.

As depicted in Fig. 9, the flights at approximately 90 m exhibit a distinct grouping into two primary ground course directions. However, in order to accurately classify the legs as either NS or EW, it is essential to allow for some margin around 90° as well as around 0° or 180°. We chose to keep a margin of ±30° around the exact NS and EW directions, in a way described in Table 3.

Figure 10 presents a scatterplot comparison of the TKE for the two distinct ground course groups. The number of legs is almost evenly divided between the NS and EW groups. However, the statistics do not appear to be dependent on the specific ground course: the MBD remains just above 60%, while the RMSD is 114% for the NS direction and 100% for the EW direction.

However, even within these two ground course groups, there is a substantial difference due to the wind direction, which determines the direction of the upwind legs used for

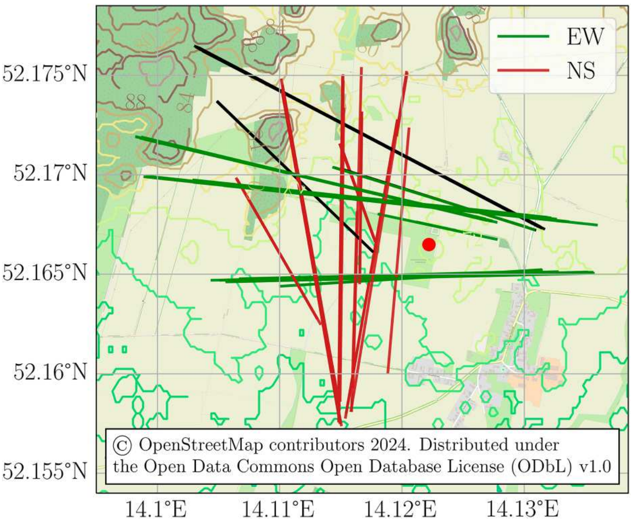

FIG. 9. Map including all the legs considered for the TKE analysis. The red dot represents the meteorological tower at the GM Falkenberg. The legs plotted in red belong to the NS ground course group, while the ones in green belong to the EW ground course group. The black lines do not belong to either of the two groups and were excluded from further analysis.

the analysis. Thus, we decided to further split the two ground course groups based on the main wind direction. The EW group was divided into two subgroups representing winds coming from the east (E) and west-northwest (WNW), while the NS group was split into winds coming from the south (S) and north-northwest (NNW). The details of the splitting are summarized in Table 4.

The four subgroups encompass all legs where the wind originated from the regions visualized in Fig. 11: S and E correspond to the purple sector, while WNW and NNW correspond to the red sector. In the S and E group, the wind blows from an area predominantly characterized by flatland and cultivated ground, whereas in the other two groups, the wind comes from an area where forest patches of different sizes are present.

TABLE 3. NS and EW leg group splitting according to the ground course ψ.

ψ group	ψ boundaries	N_{legs}
NS	$0° \leq \psi \leq 30°$ $150° \leq \psi \leq 180°$	49
EW	$60° \leq \psi \leq 120°$	60

The TKE comparison for the four subgroups is depicted in Fig. 12, while the MBD and RMSD for all the TKE components are reported in Table 5. Unfortunately, the E group comprises only six legs which makes the statistics more uncertain than for the other groups. This analysis reveals that during the NS ground course legs with wind coming from a southern direction (S, flat land), the MBD is 3 times smaller than in cases where the wind blows from WNW (forest): around 21% against 68%. Additionally, the data scatter is 2 times less for the S group. Moreover, it can be noticed in Table 5 that when flying north–south legs with wind coming from the south, the variance of the main wind component, in this case v, agrees almost perfectly (only 4% difference) with what is recorded by the sonic anemometer. A similar behavior can be seen for the E subgroup, where the lowest MBD and scatter are recorded for the variance of the u component; however, as already mentioned, this group is probably not big enough to be taken as a valid reference. The same tendency also appears when comparing S with NNW with even higher MBD (97%) and RMSD (151%). This suggests that even for NS ground course legs, when the wind blows from the forest region, the statistics considerably worsen.

The reasons for this poorer comparison observed for the two wind directions WNW and NNW (hereafter abbreviated as NW) are difficult to pinpoint, as the variables involved are numerous and can act in opposite directions, masking the effects of each other. In the following sections, the data available in terms of TKE have been analyzed by separating the two wind directions mentioned above and trying to find a correlation in the TKE BD as a function of some important

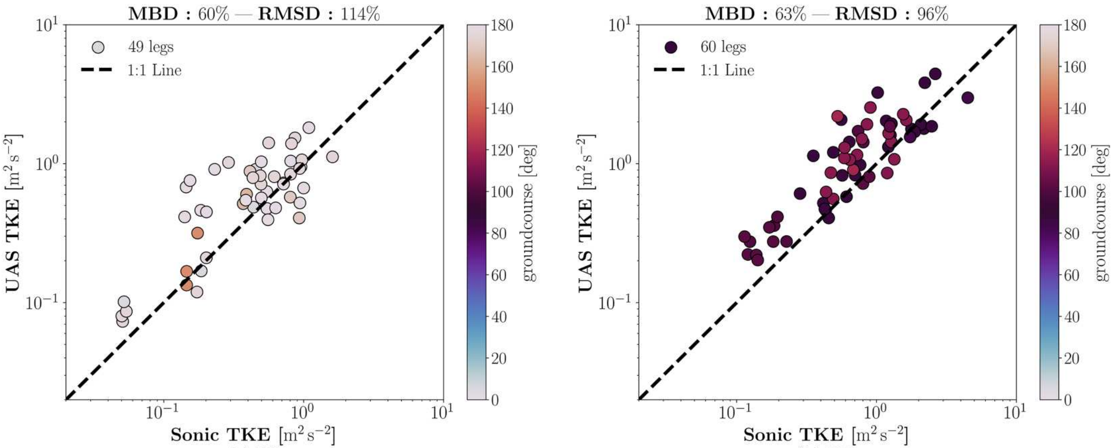

(a) NS

(b) EW

FIG. 10. Comparison between TKE measured by the sonic anemometer and the UAS system. (a) NS ground course and (b) EW ground course.

TABLE 4. Subgroup division of the ground course NS and EW groups. The different subgroups are generated according to the mean wind direction.

ψ group	WD group	WD$_{\text{min}}$	WD$_{\text{max}}$	N_{legs}
NS	S	140°	220°	24
	NNW	300°	360°	25
EW	E	60°	120°	6
	WNW	240°	330°	47

variables related to both the environmental conditions and the UAS itself.

d. *Average altitude*

As depicted in Fig. 13a, the average altitude of each leg can exhibit variations of up to 15 m around the target altitude of 90 m. This is due to the fact that some of the legs were not programmed to be flown exactly at 90 m, and also because of the many thermals that the UAS can encounter on its way, especially during the summer flights. The Pearson correlation coefficient (Benesty et al. 2009) of the BD with the flight altitude is remarkably weak for the NW direction, revealing that this specific parameter has no discernible influence on the quality of the comparison between the two sensors when the wind blows from this specific direction. On the other hand, it is interesting to see that when analyzing the legs with south wind direction (the dark purple ones), there is a slight tendency to improve the BD, with the smallest values being around 90 m as expected. The correlation is still quite low, but a dependency is definitely discernible when compared to the other wind direction.

e. *Fetch angle*

As elucidated in section 2d(1) and in Boventer et al. (2024), the fetch angle holds substantial significance in this analysis, and a threshold of 40° was previously implemented to enhance the quality of comparisons. Hence, it is essential to reevaluate whether there persists a discernible dependency of the bias difference on this variable.

Figure 13b indicates a weak, if not entirely nonexistent, correlation. Therefore, it appears that this variable does not exert significant influence at this point on the quality of comparison between the sonic anemometer and a mobile UAS platform.

f. *Bulk Richardson number*

The bulk Richardson number (Ri$_b$) serves as an indicator of the stability of the lower ABL. Stull (2016) defines Ri$_b$ as

$$\mathrm{Ri}_b = \frac{g\Delta\Theta_v \Delta z}{\overline{T}_v[(\Delta u)^2 + (\Delta v)^2]}, \qquad (7)$$

with $g = 9.81$ m s^{-2}, $\Delta\Theta_v$ being the difference of potential virtual temperature between two heights, and $\overline{T}_v$ being the arithmetical mean of the virtual temperatures between the two heights. The $(\Delta u)^2$ and $(\Delta v)^2$ are the differences in the two horizontal wind components.

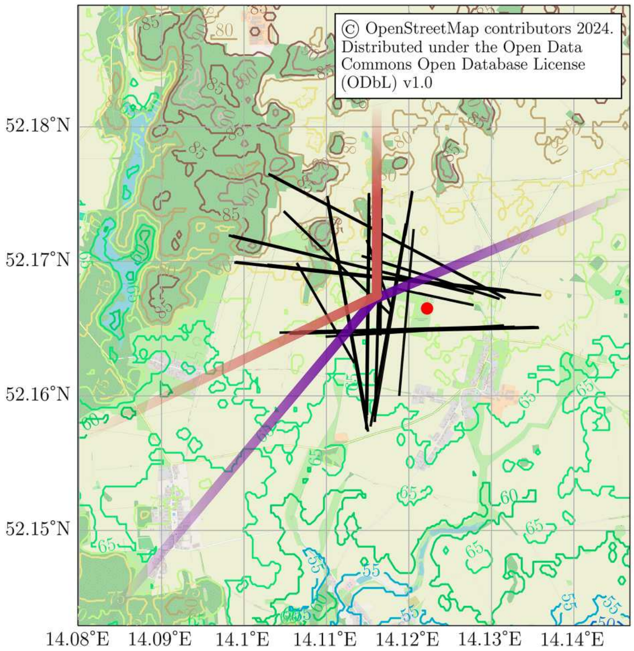

FIG. 11. Map including all the legs and the two main wind direction sectors considered for the analysis. The purple sector spans from 140° to 220° (flat land), while the red sector spans from 240° to 360° (forest).

In this study, Ri$_b$ is computed using variables sampled at $z_1 = 1$ m and $z_2 = 98$ m by the instrumentation of the GM Falkenberg at the meteorological tower location. The wind speed at 1-m height was approximated as $u_{1\text{m}} \approx 0$, $v_{1\text{m}} \approx 0$, and Eq. (7) then becomes

$$\mathrm{Ri}_b = \frac{g\Delta\Theta_v \Delta z}{\overline{T}_v(u^2 + v^2)}, \qquad (8)$$

with u and v being now the two horizontal wind components at the upper end of the vertical column, i.e., at 98-m altitude.

The Ri$_b$ values above 0.25 signify thermally and dynamically stable conditions, $0 < \mathrm{Ri}_b < 0.25$ indicates solely thermally stable conditions, and $\mathrm{Ri}_b < 0$ suggests a thermally unstable lower ABL. Figure 13c illustrates the relationship between the BD and Ri$_b$ for all legs. Again, the correlation coefficient is exceptionally weak for the NW wind direction, suggesting that atmospheric stability does not significantly affect the quality of the comparison between the UAS and sonic anemometers. For the south wind direction group, the correlation coefficient is slightly higher, but it is difficult to find a clear dependency, at least for $\mathrm{Ri}_b > 0$, and there is only one point with stable atmospheric conditions, so it is difficult to draw any conclusions.

g. *TKE*

Exploring whether the discrepancy between the two measurements of TKE correlates with the TKE value itself is an intriguing aspect to investigate. As depicted in Fig. 13d, the correlation between bias and TKE appears relatively weak for both wind directions. However, in both cases, it is negative, and it is noteworthy that the largest bias tends to occur for relatively low TKE values.

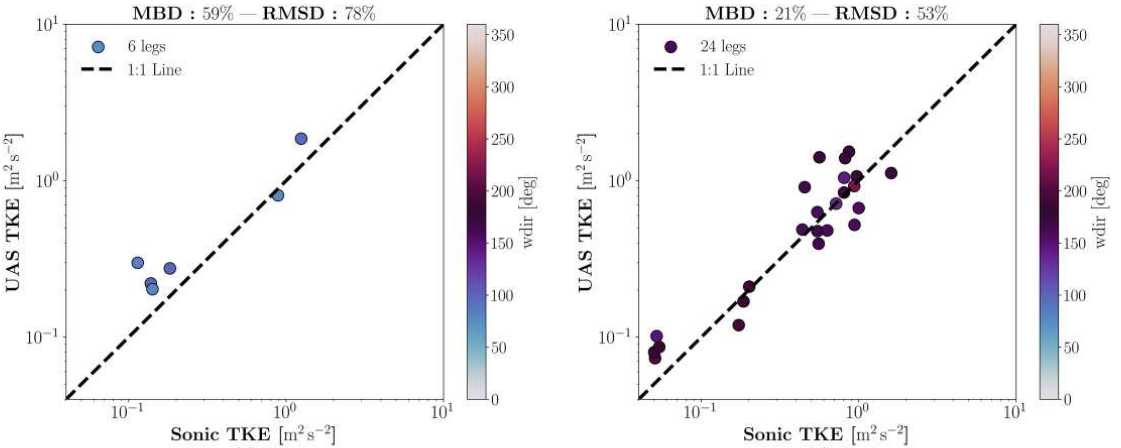

(a) E (b) S

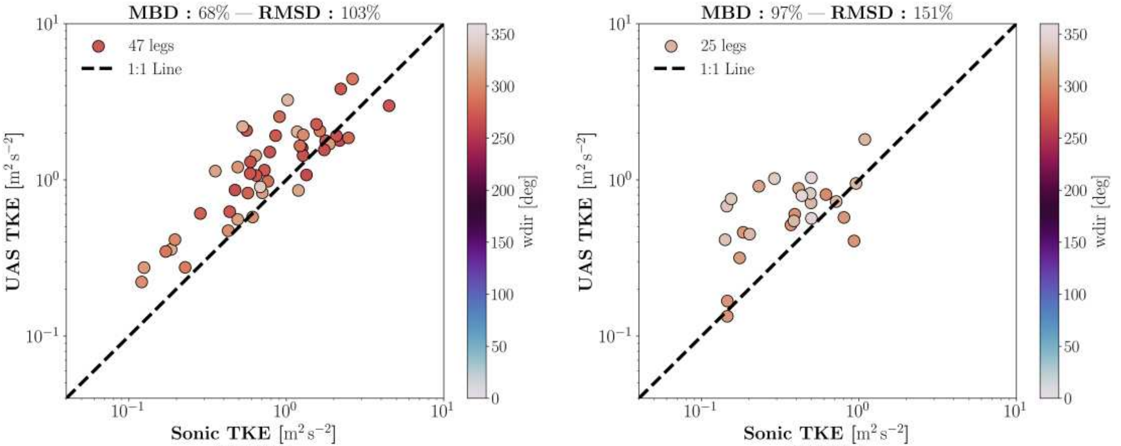

(c) WNW (d) NNW

FIG. 12. Comparison between TKE measured by the sonic anemometer and the UAS system. (a) Subgroup of the EW ground course legs, wind blows from E; (b) subgroup of the NS ground course legs, wind blows from south; (c) subgroup of the EW ground course legs, wind blows from WNW; (d) subgroup of the NS ground course legs, wind blows from NNW.

This can be due to the inherent uncertainty in the measurements with both systems but also to the fact that under conditions where the turbulence level is relatively low (e.g., lower than 1 m^2 s^{-2}), local effects—such as the terrain footprint—might still be present but not dissipating rapidly enough. Consequently, these effects could potentially corrupt the measurement over a span of several hundred meters, contributing to the observed discrepancies and underlining the influence of surface heterogeneity on the observations. Although this is only speculation, it may be a reasonable explanation for this weak dependence.

h. TAS standard deviation

As described in section 2b, the UAS is programmed to maintain a constant TAS. Clearly, this is possible on average, but instantaneously, the system will be subject to acceleration

TABLE 5. MBD and RMSD between UAS measurements and sonic anemometer measurements for the different ground course subgroups.

	E		S		WNW		NNW	
	MBD (%)	RMSD (%)	MBD (%)	RMSD (%)	MBD (%)	RMSD (%)	MBD (%)	RMSD (%)
TKE	59	78	21	53	68	103	97	151
Var(u)	37	51	43	63	55	101	97	160
Var(v)	92	129	−4	59	81	147	85	142
TKE$_H$	59	76	13	47	62	103	87	136
Var(w)	62	87	51	95	92	134	122	195

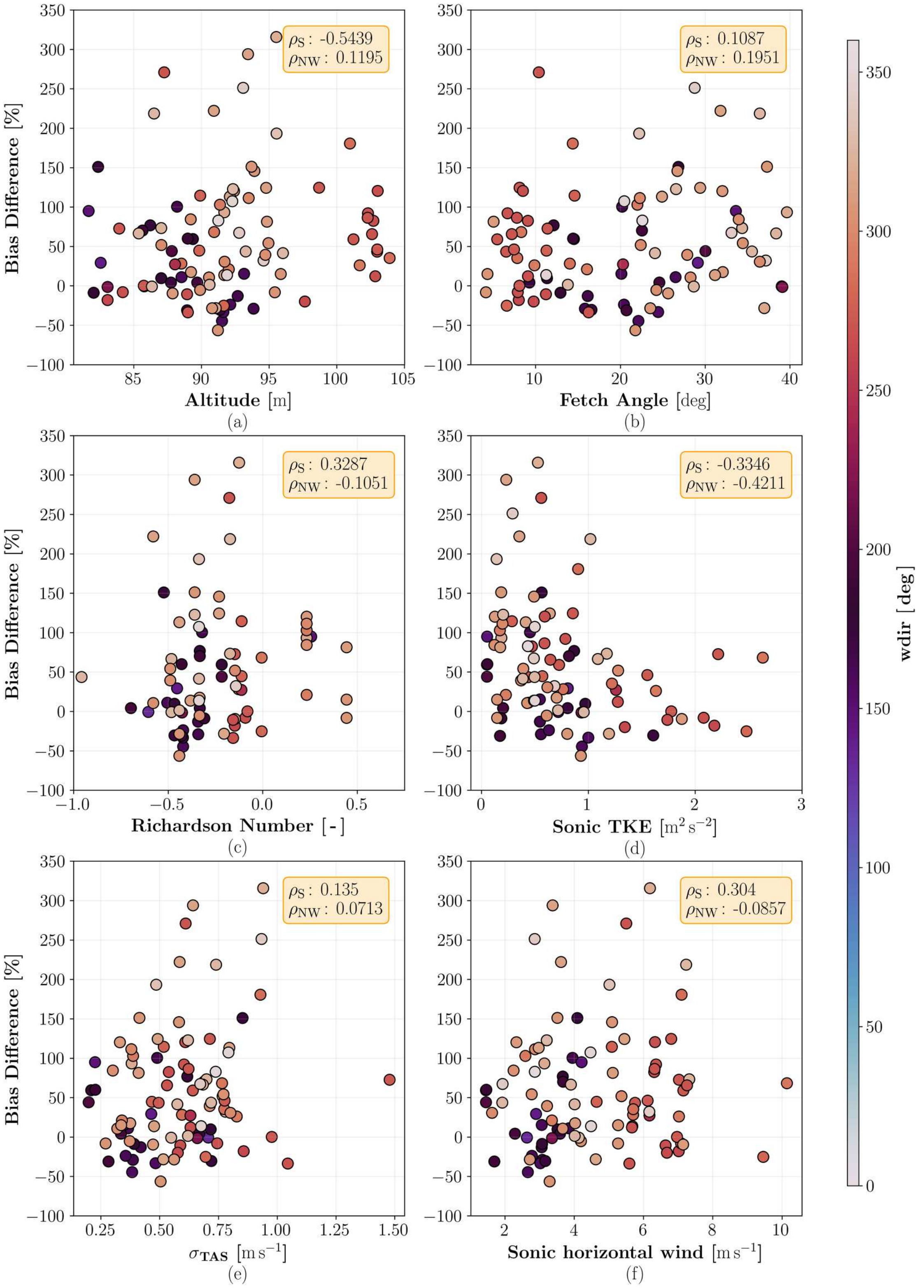

FIG. 13. Influence of six different variables on the BD between UAS and sonic anemometer. (a) Average leg altitude, (b) fetch angle, (c) bulk Richardson number, (d) TKE recorded by the sonic anemometer, (e) UAS TAS standard deviation, and (f) mean horizontal wind recorded by the sonic anemometer. Each point in the plot represents one flight leg, while ρ represents the Pearson correlation coefficient (Benesty et al. 2009).

and deceleration caused by various factors including vertical wind, turbulent eddies, and thermal currents. No matter how robust the flight control system is, it will take some time for it to adapt to the new flight conditions. To try to describe, and take into account this phenomenon, the parameter considered here is the standard deviation of the TAS. Figure 13e shows the BD of the TKE as a function of this flight system parameter. Clearly, higher values of the standard deviation represent legs where the UAS had more difficulty in keeping the TAS value constant. In any case, no clearly defined BD dependence can be observed for this parameter either for the wind direction coming from flat terrain or for the wind direction sector coming from the forest.

i. Mean horizontal wind speed

The last variable analyzed here is the mean horizontal wind measured by our reference sensor, the sonic anemometer. Again, the BD shows no dependence on increasing wind speed, and the correlation coefficient for both wind direction groups only confirms what is clear from a visual inspection of Fig. 13f.

j. Terrain characteristics

The only conclusion that can be drawn from the analysis of all these variables is that there must be something else influencing the distribution of BDs between the UAS and the sonic anemometer, especially for the NW wind direction. As indicated by numerous preceding studies (Bange et al. 2002; Platis et al. 2017b), the terrain heterogeneity surrounding GM Falkenberg bears significant importance. It is well known that turbulent fluxes are generally higher over forested regions. The presence of trees increases the roughness length, and a shear layer forms in the downwind region: both factors increase the mechanical turbulence (Bange et al. 2002; Mengelkamp et al. 2006; zum Berge et al. 2022). Although we cannot provide incontrovertible evidence for the following statements, we suspect that the reasons for the poorer comparison observed in the NW directions are due to the flight path crossing areas of forest and a wind blowing from the direction of forest. In addition, looking at the elevation contours in Fig. 11, it can be seen that the northwest area also has a slightly higher elevation than the south area. The forest area is at an elevation of around 85–90 m AGL, while the tower site is at 73 m AGL. This difference, although small, must be added to the height of the trees, and since the MASC flies by maintaining the same altitude with respect to the starting point, this means that the distance between the UAS and the top of the trees is even smaller. It is the authors' opinion that these two effects together result in a high inhomogeneity of atmospheric turbulence. Of course, these factors are not the only ones that cause such high TKE scatter between their systems, but they seem to be the ones that have the largest influence, somewhat overriding other variables to which TKE seems to be less sensitive (e.g., exact flight altitude). The even higher MBD (97%) and RMSD (151%) of the NNW subgroup might also be a consequence of the disturbance of the tower structure on the sonic signal, still present despite filtering wind directions between 0° and 50°.

4. Conclusions and outlook

As part of the VALUAS project, three intensive observation periods were conducted near GM Falkenberg, over a heterogeneous rural landscape southeast of Berlin. The UAS of type MASC-3, operated by the University of Tübingen, was deployed to collect more than 43 h of flight data at various altitudes. This dataset were intended for use in validating new DWL systems employed by the German Weather Service (DWD). In a prior study by Boventer et al. (2024), the validity of utilizing UASs to provide a reference for these systems was demonstrated, specifically focusing on mean wind speed and direction.

In the initial phase of this study, the analysis of flight data is expanded to encompass atmospheric wind fluctuation components through turbulent kinetic energy (TKE). The specific focus on this variable arises from the fact that the DWL systems slated for validation provide an estimate of TKE over a 30-min time average.

The primary objective of this analysis is to evaluate the capabilities of a fixed-wing UAS system in delivering accurate TKE measurements above a distinctly heterogeneous terrain and to assess whether Taylor's hypothesis of frozen turbulence holds true under these conditions.

The current study builds upon concepts explained in Boventer et al. (2024), such as the fetch angle, and establishes a detailed and systematic method for filtering and synchronizing measurements obtained from the UAS and a sonic anemometer operated as a reference sensor on a meteorological tower at 90 m above ground level. This data processing step is crucial due to the intrinsic differences in measurement methods between the two compared sensors: one captures measurements along a straight line traversing the lower atmospheric boundary layer, while the other functions as a static sensor.

In the text, the correctness of the postprocessing algorithm is demonstrated, which reduces the bias and scatter between UAS and sonic anemometer measurements by 3/4. Additionally, the influence of the total number of legs and their length on the quality metrics is examined. It is found that increasing the leg length significantly reduces the scatter but only slightly affects the bias between the two systems. However, considering all flight legs under analysis together, there remains a noticeable bias between the two systems of 64% and a scatter of 105%.

A subsequent analysis indicates improved agreement between the UAS and the sonic anemometer (MBD: 21%, RMSD: 53%) when the flight path is directed from north to south and the wind originates from the south, encompassing predominantly flat and cultivated land. In contrast, when the wind blows from the west-northwest, characterized by forest-covered land, the quality metrics more than double (MBD: 68%, RMSD: 103%).

In light of these results, it is evident that the frozen turbulence hypothesis is not verified. It is the authors' opinion that in this specific case, the terrain heterogeneity plays a predominant role when comparing a stationary and a moving sensor as it has been shown that other variables have little or even no influence on the UAS–sonic anemometer comparison.

These findings present new challenges in validating lidars using the MASC-3 dataset within the VALUAS project. While it is reasonable to restrict the dataset to wind directions from the south, this results in a significant reduction in the available legs. Furthermore, at higher altitudes, the effect of the terrain may be less pronounced than at the 90 m AGL of the data considered in this analysis. In light of the current situation, where the comparison results are already predominantly dependent on the wind direction, the additional dependence on flight altitude introduces a further variable that cannot be compared with any reference sensor.

Given the particular test site and flight strategy in question, it is not possible to ascertain the accuracy of the UAS TKE estimate with sufficient confidence. It is important to note that this issue is not inherently related to the accuracy of the UAS data acquisition capabilities, which have been previously validated in other studies. Rather, it is a consequence of the fact that one sensor is stationary while the other is moving in space.

The optimal methodology for conducting comparative experiments at the Falkenberg site with regard to turbulent quantities would be the utilization of rotary-wing UAS, which are capable of maintaining a fixed spatial position while measuring atmospheric flow conditions.

Acknowledgments. The authors thank the German Weather Service (DWD) for funding and supporting this research under Grant Agreement with a reference: 4819EMF01. The authors declare no conflict of interest.

Data availability statement. The data of the 2021 IOP are publicly available at Jung et al. (2023). The rest of the data can become available from the corresponding author upon reasonable request.

APPENDIX A

Flights Overview

The flights used in this study (Table A1) are approximately the same as those used in Boventer et al. (2024) where the UAS is validated against the tower and subsequently the two DWLs are validated against the UAS in terms of mean wind speed. For this purpose, the missions were designed to fly at different altitudes for at least 10 min. This strategy provides an average of two legs per altitude, and therefore, we only have two legs around 90 m, after which the UAS would climb to the next predefined altitude. For the next part of this work, the comparison between the UAS and DWL in terms of TKE, the MASC-3 had to fly for at least 30 min at each altitude, as the DWL TKE estimates are given with a frequency of one every 30 min. As a result, some of the flights (e.g., 110, 111, 115, 119, 131) have several legs around 90 m.

TABLE A1. List of all MASC-3 measurement legs used in this analysis of IOP-1, IOP-2, and IOP-3 in the years 2020, 2021, and 2022 at the MOL-RAO.

Leg No.	Flight No.	Start	Δt (s)	WS (m s^{-1})	WD (°)	Leg No.	Flight No.	Start	Δt (s)	WS (m s^{-1})	WD (°)
1	1	1010:43 UTC 7 Jul 2020	154	7.0	271	36	82	0835:39 UTC 11 Jun 2021	36	2.7	308
2	1	1017:03 UTC 7 Jul 2020	147	7.0	262	37	82	0839:10 UTC 11 Jun 2021	37	2.7	305
3	2	1316:47 UTC 7 Jul 2020	145	7.0	267	38	82	0842:42 UTC 11 Jun 2021	36	4.6	327
4	2	1322:54 UTC 7 Jul 2020	135	7.0	271	39	83	1109:11 UTC 11 Jun 2021	84	4.0	334
5	3	1518:49 UTC 7 Jul 2020	126	5.7	285	40	83	1114:05 UTC 11 Jun 2021	84	6.2	340
6	3	1524:36 UTC 7 Jul 2020	127	5.5	269	41	83	1119:01 UTC 11 Jun 2021	84	6.2	320
7	5	1509:27 UTC 8 Jul 2020	97	4.0	230	42	84	1901:55 UTC 11 Jun 2021	90	6.2	311
8	5	1515:09 UTC 8 Jul 2020	98	4.0	237	43	84	1906:38 UTC 11 Jun 2021	90	5.1	306
9	5	1520:57 UTC 8 Jul 2020	103	4.1	237	44	84	1911:20 UTC 11 Jun 2021	90	5.3	307
10	6	1654:52 UTC 8 Jul 2020	117	4.6	278	45	85	1205:47 UTC 13 Jun 2021	183	8.6	327
11	6	1700:36 UTC 8 Jul 2020	109	5.1	276	46	85	1212:48 UTC 13 Jun 2021	181	8.1	332
12	10	1122:06 UTC 10 Jul 2020	108	6.1	231	47	85	1219:52 UTC 13 Jun 2021	62	6.6	326
13	10	1127:43 UTC 10 Jul 2020	119	6.2	245	48	85	1227:19 UTC 13 Jun 2021	199	7.5	327
14	11	1314:02 UTC 10 Jul 2020	197	9.4	280	49	85	1234:36 UTC 13 Jun 2021	182	7.5	323
15	11	1321:11 UTC 10 Jul 2020	106	10.1	289	50	86	1401:55 UTC 13 Jun 2021	161	6.7	340
16	18	1227:49 UTC 12 Jul 2020	121	7.2	327	51	86	1408:43 UTC 13 Jun 2021	195	8.2	332
17	18	1233:45 UTC 12 Jul 2020	131	7.3	324	52	86	1416:08 UTC 13 Jun 2021	183	7.9	338
18	22	0820:42 UTC 14 Jul 2020	100	3.8	159	53	86	1423:16 UTC 13 Jun 2021	169	7.5	339
19	22	0826:15 UTC 14 Jul 2020	106	3.9	264	54	86	1430:21 UTC 13 Jun 2021	172	7.3	337
20	25	0842:30 UTC 16 Jul 2020	105	4.2	302	55	101	0704:28 UTC 19 Jun 2021	123	3.1	165
21	25	0848:15 UTC 16 Jul 2020	107	4.0	310	56	101	0711:06 UTC 19 Jun 2021	123	3.1	159
22	28	0833:29 UTC 17 Jul 2020	116	5.4	313	57	101	0717:42 UTC 19 Jun 2021	123	3.1	164
23	28	0839:14 UTC 17 Jul 2020	111	5.1	307	58	101	0724:20 UTC 19 Jun 2021	124	2.8	159
24	42	1328:04 UTC 22 Jul 2020	125	7.1	309	59	101	0730:59 UTC 19 Jun 2021	119	2.7	158
25	42	1333:35 UTC 22 Jul 2020	117	5.4	300	60	102	0908:39 UTC 19 Jun 2021	127	3.0	155
26	44	1032:12 UTC 23 Jul 2020	91	3.6	314	61	104	0936:16 UTC 23 Jun 2021	56	2.8	304
27	44	1037:26 UTC 23 Jul 2020	95	3.7	303	62	104	0940:50 UTC 23 Jun 2021	57	3.2	303
28	56	1204:39 UTC 27 Jul 2020	80	2.9	140	63	105	1636:32 UTC 23 Jun 2021	56	3.5	307
29	62	0959:43 UTC 29 Jul 2020	91	5.6	269	64	105	1641:02 UTC 23 Jun 2021	56	3.4	315
30	62	1004:33 UTC 29 Jul 2020	107	6.6	266	65	105	1645:30 UTC 23 Jun 2021	58	3.2	328
31	74	0938:06 UTC 8 Jun 2021	47	4.6	316	66	106	0935:09 UTC 24 Jun 2021	67	4.0	327
32	74	0942:28 UTC 8 Jun 2021	26	5.7	313	67	106	0940:13 UTC 24 Jun 2021	71	5.0	333
33	76	1143:41 UTC 9 Jun 2021	89	3.9	325	68	106	0945:22 UTC 24 Jun 2021	70	5.0	336
34	76	1146:35 UTC 9 Jun 2021	73	4.1	326	69	106	0950:28 UTC 24 Jun 2021	72	5.1	337
35	82	0832:10 UTC 11 Jun 2021	33	3.0	315	70	106	0955:35 UTC 24 Jun 2021	71	4.5	347
71	106	1000:40 UTC 24 Jun 2021	66	4.5	347	96	119	1701:27 UTC 2 Jul 2021	181	6.7	263
72	108	1100:02 UTC 25 Jun 2021	119	1.8	121	97	119	1708:16 UTC 2 Jul 2021	172	6.7	271
73	108	1107:46 UTC 25 Jun 2021	117	1.8	75	98	119	1714:53 UTC 2 Jul 2021	189	7.2	271
74	108	1123:09 UTC 25 Jun 2021	113	1.9	201	99	119	1721:44 UTC 2 Jul 2021	169	7.3	269
75	108	1142:18 UTC 25 Jun 2021	117	1.9	209	100	119	1728:20 UTC 2 Jul 2021	157	6.3	266
76	110	0721:31 UTC 26 Jun 2021	114	1.9	326	101	119	1734:40 UTC 2 Jul 2021	153	5.8	272
77	110	0729:08 UTC 26 Jun 2021	112	1.6	301	102	119	1740:59 UTC 2 Jul 2021	151	5.7	267

TABLE A1. (*Continued*)

Leg No.	Flight No.	Start	Δt (s)	WS (m s^{-1})	WD (°)	Leg No.	Flight No.	Start	Δt (s)	WS (m s^{-1})	WD (°)
78	110	0736:44 UTC 26 Jun 2021	113	1.9	339	103	119	1747:17 UTC 2 Jul 2021	160	5.7	285
79	110	0744:16 UTC 26 Jun 2021	119	2.9	340	104	119	1754:11 UTC 2 Jul 2021	189	6.1	272
80	110	0751:52 UTC 26 Jun 2021	121	2.9	353	105	119	1801:05 UTC 2 Jul 2021	186	6.4	269
81	111	0954:28 UTC 26 Jun 2021	111	1.5	200	106	119	1807:52 UTC 2 Jul 2021	171	6.3	270
82	111	1001:51 UTC 26 Jun 2021	110	1.5	183	107	119	1814:26 UTC 2 Jul 2021	167	6.3	267
83	111	1009:13 UTC 26 Jun 2021	111	1.5	187	108	122	1336:10 UTC 17 Nov 2022	315	11.1	97
84	111	1016:37 UTC 26 Jun 2021	110	1.7	191	109	131	1010:36 UTC 21 Nov 2022	110	3.1	318
85	111	1024:00 UTC 26 Jun 2021	110	2.3	194	110	131	1014:04 UTC 21 Nov 2022	86	2.2	303
86	113	1607:08 UTC 28 Jun 2021	99	2.6	132	111	131	1017:05 UTC 21 Nov 2022	92	2.3	309
87	115	1100:18 UTC 29 Jun 2021	119	3.2	172	112	131	1020:34 UTC 21 Nov 2022	86	2.6	290
88	115	1107:42 UTC 29 Jun 2021	134	3.5	178	113	131	1023:34 UTC 21 Nov 2022	122	2.9	299
89	115	1115:25 UTC 29 Jun 2021	132	3.6	172	114	131	1030:10 UTC 21 Nov 2022	119	3.4	292
90	115	1123:08 UTC 29 Jun 2021	129	3.6	176	115	136	1018:53 UTC 27 Nov 2022	22	3.1	182
91	115	1130:49 UTC 29 Jun 2021	119	3.7	190	116	138	1402:58 UTC 27 Nov 2022	120	4.2	147
92	115	1138:21 UTC 29 Jun 2021	108	3.4	221	117	142	1353:51 UTC 28 Nov 2022	160	7.2	97
93	115	1145:46 UTC 29 Jun 2021	110	4.1	175	118	142	1400:53 UTC 28 Nov 2022	90	7.1	100
94	118	1339:51 UTC 2 Jul 2021	194	7.0	291	119	144	0958:06 UTC 29 Nov 2022	157	4.1	80
95	118	1347:13 UTC 2 Jul 2021	200	7.1	284	120	145	1145:45 UTC 29 Nov 2022	147	3.9	82

APPENDIX B

TKE Components

In this appendix, the comparison of the individual components of the TKE variable is plotted together with the TKE of the horizontal wind (Fig. B1). They consist of the variance of the three components of the wind vector. The data shown in these plots consist of the same legs of Fig. 7 before the application of any filtering on the ground course or wind direction.

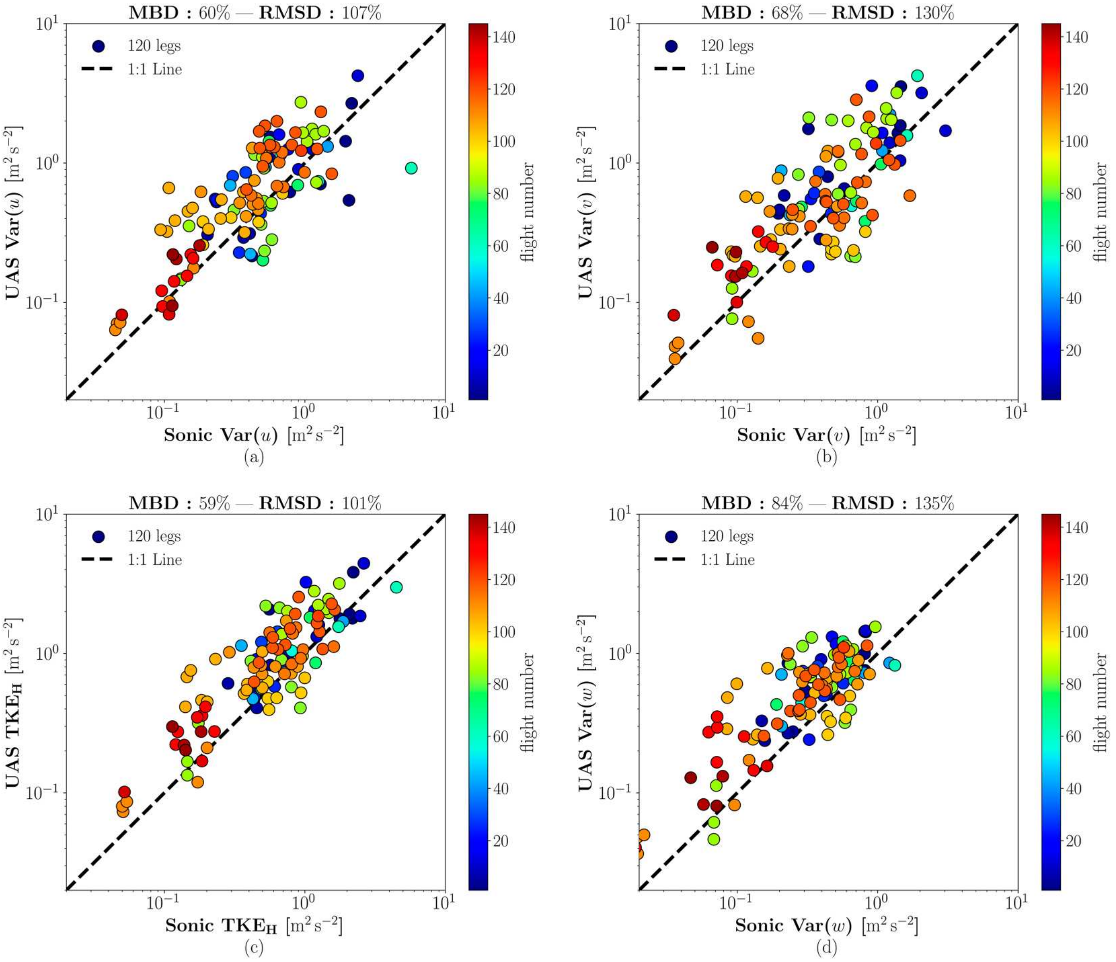

FIG. B1. Comparison between variables measured by the sonic anemometer on the meteorological tower and the UAS system. Each of the scatter points corresponds to one UAS leg. (a) Var(u), (b) Var(v), (c) TKE$_H$, and (d) Var(w).

REFERENCES

Alaoui-Sosse, S., P. Durand, P. Medina, P. Pastor, M. Lothon, and I. Cernov, 2019: OVLI-TA: An unmanned aerial system for measuring profiles and turbulence in the atmospheric boundary layer. *Sensors*, **19**, 581, https://doi.org/10.3390/s19030581.

Andren, A., A. R. Brown, P. J. Mason, J. Graf, U. Schumann, C.-H. Moeng, and F. T. M. Nieuwstadt, 1994: Large-eddy simulation of a neutrally stratified boundary layer: A comparison of four computer codes. *Quart. J. Roy. Meteor. Soc.*, **120**, 1457–1484, https://doi.org/10.1002/qj.49712052003.

Auerswald, T., J. Bange, T. Knopp, K. Weinman, and R. Radespiel, 2012: Large-eddy simulations of realistic atmospheric turbulence with the DLR-TAU-code initialized by in situ airborne measurements. *Comput. Fluids*, **66**, 121–129, https://doi.org/10.1016/j.compfluid.2012.06.013.

Bange, J., F. Beyrich, and D. A. M. Engelbart, 2002: Airborne measurements of turbulent fluxes during LITFASS-98: Comparison with ground measurements and remote sensing in a case study. *Theor. Appl. Climatol.*, **73**, 35–51, https://doi.org/10.1007/s00704-002-0692-6.

——, and Coauthors, 2013: Measurement of aircraft state and thermodynamic and dynamic variables. *Airborne Measurements for Environmental Research*, John Wiley and Sons, 7–75, https://doi.org/10.1002/9783527653218.ch2.

——, J. Reuder, and A. Platis, 2021: Unmanned aircraft systems. *Springer Handbook of Atmospheric Measurements*, T. Foken, Ed., Springer International Publishing, 1331–1349, https://doi.org/10.1007/978-3-030-52171-4_49.

Benesty, J., J. Chen, Y. Huang, and I. Cohen, 2009: Pearson correlation coefficient. *Noise Reduction in Speech Processing*, Springer Topics in Signal Processing, Vol. 2, Springer, 1–4, https://doi.org/10.1007/978-3-642-00296-0_5.

Beyrich, F., H.-J. Herzog, and J. Neisser, 2002a: The LITFASS project of DWD and the LITFASS-98 experiment: The project strategy and the experimental setup. *Theor. Appl. Climatol.*, **73**, 3–18, https://doi.org/10.1007/s00704-002-0690-8.

——, and Coauthors, 2002b: Experimental determination of turbulent fluxes over the heterogeneous LITFASS area: Selected results from the LITFASS-98 experiment. *Theor. Appl. Climatol.*, **73**, 19–34, https://doi.org/10.1007/s00704-002-0691-7.

——, and Coauthors, 2006: Area-averaged surface fluxes over the litfass region based on eddy-covariance measurements. *Bound.-Layer Meteor.*, **121**, 33–65, https://doi.org/10.1007/s10546-006-9052-x.

——, and Coauthors, 2012: Towards a validation of scintillometer measurements: The LITFASS-2009 experiment. *Bound.-Layer Meteor.*, **144**, 83–112, https://doi.org/10.1007/s10546-012-9715-8.

Bielli, S., and F. Roux, 1999: Initialization of a cloud-resolving model with airborne Doppler radar observations of an oceanic tropical convective system. *Mon. Wea. Rev.*, **127**, 1038–1055, https://doi.org/10.1175/1520-0493(1999)127<1038:IOACRM>2.0.CO;2.

Bou-Zeid, E., W. Anderson, G. G. Katul, and L. Mahrt, 2020: The persistent challenge of surface heterogeneity in boundary-layer meteorology: A review. *Bound.-Layer Meteor.*, **177**, 227–245, https://doi.org/10.1007/s10546-020-00551-8.

Boventer, J., M. Bramati, V. Savvakis, F. Beyrich, M. Kayser, A. Platis, and J. Bange, 2024: Validation of Doppler Wind Lidar measurements with an Uncrewed Aircraft System (UAS) in the daytime atmospheric boundary layer. *J. Atmos. Oceanic Technol.*, **41**, 705–723, https://doi.org/10.1175/JTECH-D-23-0127.1.

Brilouet, P.-E., P. Durand, G. Canut, and N. Fourrié, 2020: Organized turbulence in a cold-air outbreak: Evaluating a large-eddy simulation with respect to airborne measurements. *Bound.-Layer Meteor.*, **175**, 57–91, https://doi.org/10.1007/s10546-019-00499-4.

Brooks, I. M., S. Söderberg, and M. Tjernström, 2003: The turbulence structure of the stable atmospheric boundary layer around a coastal headland: Aircraft observations and modelling results. *Bound.-Layer Meteor.*, **107**, 531–559, https://doi.org/10.1023/A:1022822306571.

Büchau, Y. G., and Coauthors, 2024: Parmesan: Meteorological timeseries and turbulence analysis backed by symbolic mathematics. *J. Open Source Software*, **9**, 6127, https://doi.org/10.21105/joss.06127.

Caughey, S. J., and J. C. Wyngaard, 1979: The turbulence kinetic energy budget in convective conditions. *Quart. J. Roy. Meteor. Soc.*, **105**, 231–239, https://doi.org/10.1002/qj.49710544315.

Chechin, D. G., A. Y. Artamonov, N. Y. Bodunkov, M. Y. Kalyagin, A. M. Shevchenko, and D. N. Zhivoglotov, 2021: Development of an unmanned aerial vehicle to study atmospheric boundary-layer turbulent structure. *J. Phys.: Conf. Series*, **1925**, 012068, https://doi.org/10.1088/1742-6596/1925/1/012068.

Cook, P. A., and I. A. Renfrew, 2015: Aircraft-based observations of air–sea turbulent fluxes around the British Isles. *Quart. J. Roy. Meteor. Soc.*, **141**, 139–152, https://doi.org/10.1002/qj.2345.

de Boer, G., and Coauthors, 2024: Evaluation and intercomparison of small uncrewed aircraft systems used for atmospheric research. *J. Atmos. Oceanic Technol.*, **41**, 127–145, https://doi.org/10.1175/JTECH-D-23-0067.1.

El Bahlouli, A., D. Leukauf, A. Platis, K. zum Berge, J. Bange, and H. Knaus, 2020: Validating CFD predictions of flow over an escarpment using ground-based and airborne measurement devices. *Energies*, **13**, 4688, https://doi.org/10.3390/en13184688.

Foken, T., 2006: 50 years of the Monin–Obukhov similarity theory. *Bound.-Layer Meteor.*, **119**, 431–447, https://doi.org/10.1007/s10546-006-9048-6.

——, and J. Bange, 2021: Wind sensors. *Springer Handbook of Atmospheric Measurements*, Springer Handbooks, Springer International Publishing, 243–272, https://doi.org/10.1007/978-3-030-52171-4_9.

Hodgson, E. L., M. Souaiby, N. Troldborg, F. Porté-Agel, and S. J. Andersen, 2023: Cross-code verification of non-neutral ABL and single wind turbine wake modelling in LES. *J. Phys.: Conf. Series*, **2505**, 012009, https://doi.org/10.1088/1742-6596/2505/1/012009.

Jung, S., J. Boventer, A. Platis, and J. Bange, 2023: Fixed-wing UAS wind and turbulence measurements at GM Falkenberg during FESSTVAL 2020 and 2021. German Meteorological Service (DWD), https://doi.org/10.25592/uhhfdm.11229.

Kalthoff, N., H.-J. Binder, M. Kossmann, R. VÖgtlin, U. Corsmeier, F. Fiedler, and H. Schlager, 1998: Temporal evolution and spatial variation of the boundary layer over complex terrain. *Atmos. Environ.*, **32**, 1179–1194, https://doi.org/10.1016/S1352-2310(97)00193-3.

Kossmann, M., R. Vögtlin, U. Corsmeier, B. Vogel, F. Fiedler, H.-J. Binder, N. Kalthoff, and F. Beyrich, 1998: Aspects of the convective boundary layer structure over complex terrain.

Atmos. Environ., **32**, 1323–1348, https://doi.org/10.1016/S1352-2310(97)00271-9.

Lampert, A., and Coauthors, 2020: Unmanned aerial systems for investigating the polar atmospheric boundary layer—Technical challenges and examples of applications. *Atmosphere*, **11**, 416, https://doi.org/10.3390/atmos11040416.

Lenschow, D. H., 1970: Airplane measurements of planetary boundary layer structure. *J. Appl. Meteor.*, **9**, 874–884, https://doi.org/10.1175/1520-0450(1970)009<0874:AMOPBL>2.0.CO;2.

——, 1974: Model of the height variation of the turbulence kinetic energy budget in the unstable planetary boundary layer. *J. Atmos. Sci.*, **31**, 465–474, https://doi.org/10.1175/1520-0469(1974)031<0465:MOTHVO>2.0.CO;2.

——, J. Mann, and L. Kristensen, 1994: How long is long enough when measuring fluxes and other turbulence statistics? *J. Atmos. Oceanic Technol.*, **11**, 661–673, https://doi.org/10.1175/1520-0426(1994)011%3C0661:HLILEW%3E2.0.CO;2.

Lohou, F., B. Campistron, A. Druilhet, P. Foster, and J. P. Pages, 1998: Turbulence and coherent organizations in the atmospheric boundary layer: A radar-aircraft experimental approach. *Bound.-Layer Meteor.*, **86**, 147–179, https://doi.org/10.1023/A:1000613232592.

Martin, S., J. Bange, and F. Beyrich, 2011: Meteorological profiling of the lower troposphere using the research UAV "M^{2}AV Carolo". *Atmos. Meas. Tech.*, **4**, 705–716, https://doi.org/10.5194/amt-4-705-2011.

Mengelkamp, H.-T., and Coauthors, 2006: Evaporation over a heterogeneous land surface. *Bull. Amer. Meteor. Soc.*, **87**, 775–786, https://doi.org/10.1175/BAMS-87-6-775.

Neisser, J., W. Adam, F. Beyrich, U. Leiterer, and H. Steinhagen, 2002: Atmospheric boundary layer monitoring at the meteorological observatory Lindenberg as a part of the "Lindenberg Column": Facilities and selected results. *Meteor. Z.*, **11**, 241–253, https://doi.org/10.1127/0941-2948/2002/0011-0241.

Nicholls, S., and C. J. Readings, 1979: Aircraft observations of the structure of the lower boundary layer over the sea. *Quart. J. Roy. Meteor. Soc.*, **105**, 785–802, https://doi.org/10.1002/qj.49710544604.

Pennell, W. T., and M. A. LeMone, 1974: An experimental study of turbulence structure in the fair-weather trade wind boundary layer. *J. Atmos. Sci.*, **31**, 1308–1323, https://doi.org/10.1175/1520-0469(1974)031<1308:AESOTS>2.0.CO;2.

Platis, A., B. Altstädter, B. Wehner, N. Wildmann, A. Lampert, M. Hermann, W. Birmili, and J. Bange, 2016: An observational case study on the influence of atmospheric boundary-layer dynamics on new particle formation. *Bound.-Layer Meteor.*, **158**, 67–92, https://doi.org/10.1007/s10546-015-0084-y.

——, D. Martinez-Villagrasa, F. Beyrich, and J. Bange, 2017a: Analysis of the influence of a lake on the lower convective boundary layer from airborne observations. *Meteor. Z.*, **26**, 161–180, https://doi.org/10.1127/metz/2016/0802.

——, A. F. Moene, D. M. Villagrasa, F. Beyrich, D. Tupman, and J. Bange, 2017b: Observations of the temperature and humidity structure parameter over heterogeneous terrain by airborne measurements during the LITFASS-2003 campaign. *Bound.-Layer Meteor.*, **165**, 447–473, https://doi.org/10.1007/s10546-017-0290-x.

——, and Coauthors, 2021: Evaluation of a simple analytical model for offshore wind farm wake recovery by in situ data and Weather Research and Forecasting simulations. *Wind Energy*, **24**, 212–228, https://doi.org/10.1002/we.2568.

——, M. Hundhausen, A. Lampert, S. Emeis, and J. Bange, 2022: The role of atmospheric stability and turbulence in offshore wind-farm wakes in the German Bight. *Bound.-Layer Meteor.*, **182**, 441–469, https://doi.org/10.1007/s10546-021-00668-4.

——, Y. Büchau, S. Zuluaga, and J. Bange, 2023: The impact of offshore wind farms on the latent heat flux. *Meteor. Z.*, **32**, 261–277, https://doi.org/10.1127/metz/2023/1171.

Pope, S. B., 2001: Turbulent flows. *Meas. Sci. Technol.*, **12**, 2020, https://doi.org/10.1088/0957-0233/12/11/705.

Rautenberg, A., J. Allgeier, S. Jung, and J. Bange, 2019a: Calibration procedure and accuracy of wind and turbulence measurements with five-hole probes on fixed-wing unmanned aircraft in the atmospheric boundary layer and wind turbine wakes. *Atmosphere*, **10**, 124, https://doi.org/10.3390/atmos10030124.

——, and Coauthors, 2019b: The multi-purpose airborne sensor carrier MASC-3 for wind and turbulence measurements in the atmospheric boundary layer. *Sensors*, **19**, 2292, https://doi.org/10.3390/s19102292.

Reuder, J., M. O. Jonassen, and H. Ólafsson, 2012: The small unmanned meteorological observer SUMO: Recent developments and applications of a micro-UAS for atmospheric boundary layer research. *Acta Geophys.*, **60**, 1454–1473, https://doi.org/10.2478/s11600-012-0042-8.

Risanto, C. B., J. M. Moker Jr., A. F. Arellano Jr., C. L. Castro, Y. L. Serra, T. M. Luong, and D. K. Adams, 2023: On the collective importance of model physics and data assimilation on mesoscale convective system and precipitation forecasts over complex terrain. *Mon. Wea. Rev.*, **151**, 1993–2008, https://doi.org/10.1175/MWR-D-22-0221.1.

Saïd, F., G. Canut, P. Durand, F. Lohou, and M. Lothon, 2010: Seasonal evolution of boundary-layer turbulence measured by aircraft during the AMMA 2006 special observation period. *Quart. J. Roy. Meteor. Soc.*, **136**, 47–65, https://doi.org/10.1002/qj.475.

Schön, M., and Coauthors, 2022: Case studies of the wind field around Ny-Ålesund, Svalbard, using unmanned aircraft. *Polar Res.*, **41**, 1–15, https://doi.org/10.33265/polar.v41.7884.

Shelekhov, A., A. Afanasiev, E. Shelekhova, A. Kobzev, A. Tel'minov, A. Molchunov, and O. Poplevina, 2022: Low-altitude sensing of urban atmospheric turbulence with UAV. *Drones*, **6**, 61, https://doi.org/10.3390/drones6030061.

Siedersleben, S. K., and Coauthors, 2020: Turbulent kinetic energy over large offshore wind farms observed and simulated by the mesoscale model WRF (3.8.1). *Geosci. Model Dev.*, **13**, 249–268, https://doi.org/10.5194/gmd-13-249-2020.

Stoll, R., J. A. Gibbs, S. T. Salesky, W. Anderson, and M. Calaf, 2020: Large-eddy simulation of the atmospheric boundary layer. *Bound.-Layer Meteor.*, **177**, 541–581, https://doi.org/10.1007/s10546-020-00556-3.

Stull, R., 2016: *Practical Meteorology: An Algebra-based Survey of Atmospheric Science*. BC Open Textbook Collection, AVP International, University of British Columbia, 942 pp., https://books.google.de/books?id=xP2sDAEACAAJ.

Stull, R. B., 1988: *An Introduction to Boundary Layer Meteorology*. Kluwer Academic, 666 pp.

Sun, Y., and Coauthors, 2023: Quality evaluation for measurements of wind field and turbulent fluxes from a UAV-based eddy covariance system. *Atmos. Meas. Tech.*, **16**, 5659–5679, https://doi.org/10.5194/amt-16-5659-2023.

Syed, A. H., J. Mann, A. Platis, and J. Bange, 2022: Turbulence above offshore wind farms measured by aircraft. *J. Phys.:*

Conf. Series, **2265**, 022065, https://doi.org/10.1088/1742-6596/2265/2/022065.

Tjernström, M., and A.-S. Smedman, 1993: The vertical turbulence structure of the coastal marine atmospheric boundary layer. *J. Geophys. Res.*, **98**, 4809–4826, https://doi.org/10.1029/92JC02610.

van den Kroonenberg, A., T. Martin, M. Buschmann, J. Bange, and P. Vörsmann, 2008: Measuring the wind vector using the autonomous mini aerial vehicle M^2AV. *J. Atmos. Oceanic Technol.*, **25**, 1969–1982, https://doi.org/10.1175/2008JTECHA1114.1.

Wang, Y., C. Williamson, G. Huynh, D. Emmitt, and S. Greco, 2010: Diagnostic wind model initialization over complex terrain using the airborne Doppler wind lidar data. *Open Remote Sens. J.*, **3**, 17–27, https://doi.org/10.2174/1875413901003010017.

Wilczak, J. M., and Coauthors, 2019: Data assimilation impact of in situ and remote sensing meteorological observations on wind power forecasts during the first Wind Forecast Improvement Project (WFIP). *Wind Energy*, **22**, 932–944, https://doi.org/10.1002/we.2332.

Wildmann, N., and T. Wetz, 2022: Towards vertical wind and turbulent flux estimation with multicopter uncrewed aircraft systems. *Atmos. Meas. Tech.*, **15**, 5465–5477, https://doi.org/10.5194/amt-15-5465-2022.

——, M. Hofsäß, F. Weimer, A. Joos, and J. Bange, 2014a: MASC—A small Remotely Piloted Aircraft (RPA) for wind energy research. *Adv. Sci. Res.*, **11**, 55–61, https://doi.org/10.5194/asr-11-55-2014.

——, S. Ravi, and J. Bange, 2014b: Towards higher accuracy and better frequency response with standard multi-hole probes in turbulence measurement with remotely piloted aircraft (RPA). *Atmos. Meas. Tech.*, **7**, 1027–1041, https://doi.org/10.5194/amt-7-1027-2014.

——, S. Bernard, and J. Bange, 2017: Measuring the local wind field at an escarpment using small remotely-piloted aircraft. *Renewable Energy*, **103**, 613–619, https://doi.org/10.1016/j.renene.2016.10.073.

Wyngaard, J. C., 1992: Atmospheric turbulence. *Annu. Rev. Fluid Mech.*, **24**, 205–234, https://doi.org/10.1146/annurev.fl.24.010192.001225.

——, and O. R. Coté, 1971: The budgets of turbulent kinetic energy and temperature variance in the atmospheric surface layer. *J. Atmos. Sci.*, **28**, 190–201, https://doi.org/10.1175/1520-0469(1971)028<0190:TBOTKE>2.0.CO;2.

Xu, J., S. Rugg, L. Byerle, and Z. Liu, 2009: Weather forecasts by the WRF-ARW model with the GSI data assimilation system in the complex terrain areas of southwest Asia. *Wea. Forecasting*, **24**, 987–1008, https://doi.org/10.1175/2009WAF2222229.1.

zum Berge, K., and Coauthors, 2021: A Two-day case study: Comparison of turbulence data from an unmanned aircraft system with a model chain for complex terrain. *Bound.-Layer Meteor.*, **180**, 53–78, https://doi.org/10.1007/s10546-021-00608-2.

——, A. Gaiser, H. Knaus, A. Platis, and J. Bange, 2022: Seasonal changes in boundary-layer flow over a forested escarpment measured by an uncrewed aircraft system. *Bound.-Layer Meteor.*, **186**, 69–91, https://doi.org/10.1007/s10546-022-00743-4.

Bibliography

[1] Pramod ABICHANDANI et al. 'Wind Measurement and Simulation Techniques in Multi-Rotor Small Unmanned Aerial Vehicles'. In: *IEEE Access* 8 (2020), pp. 54910–54927. DOI: `10.1109/ACCESS.2020.2977693`.

[2] Naveed AKHTAR, Beate GEYER, and Corinna SCHRUM. 'Larger wind turbines as a solution to reduce environmental impacts'. In: *Scientific Reports* 14.1 (2024), pp. 1–12. DOI: `10.1038/s41598-024-56731-w`.

[3] John D. ANDERSON. *Fundamentals of aerodynamics*. 5th. McGraw-Hill, Feb. 2011. ISBN: 9780073398105.

[4] Takashi ASAEDA, Vu Thanh CA, and Akio WAKE. 'Heat storage of pavement and its effect on the lower atmosphere'. In: *Atmospheric Environment* 30.3 (1996). Conference on the Urban Thermal Environment Studies in Tohwa, pp. 413–427. DOI: `https://doi.org/10.1016/1352-2310(94)00140-5`.

[5] Jens BANGE, Frank BEYRICH, and Dirk ENGELBART. 'Airborne measurements of turbulent fluxes during LITFASS-98: Comparison with ground measurements and remote sensing in a case study'. In: *Theoretical and Applied Climatology* 73 (Dec. 2002), pp. 35–51. DOI: `10.1007/s00704-002-0692-6`.

[6] Edward J. BANNISTER, Angus R. MACKENZIE, and Xiaoming CAI. 'Realistic Forests and the Modeling of Forest-Atmosphere Exchange'. In: *Reviews of Geophysics* 60.1 (2022), e2021RG000746. DOI: `https://doi.org/10.1029/2021RG000746`.

[7] Mohammad BAROONI et al. 'Floating Offshore Wind Turbines: Current Status and Future Prospects'. In: *Energies* 16.1 (2023). DOI: `10.3390/en16010002`.

[8] Jamal A. BAROUDI, Venkata DINAVAHI, and Andrew M. KNIGHT. 'A review of power converter topologies for wind generators'. In: *Renewable Energy* 32.14 (2007), pp. 2369–2385. DOI: `https://doi.org/10.1016/j.renene.2006.12.002`.

[9] Frank BEYRICH. 'Mixing height estimation from sodar data — A critical discussion'. In: *Atmospheric Environment* 31.23 (1997), pp. 3941–3953. ISSN: 1352-2310. DOI: `https://doi.org/10.1016/S1352-2310(97)00231-8`.

[10] Frank BEYRICH, H. J. HERZOG, and J. NEISSER. 'The LITFASS project of DWD and the LITFASS-98 experiment: The project strategy and the experimental setup'. In: *Theoretical and Applied Climatology* 73.1-2 (2002), pp. 3–18. DOI: `10.1007/s00704-002-0690-8`.

[11] Frank Beyrich et al. ‘Experimental determination of turbulent fluxes over the heterogeneous LITFASS area: Selected results from the LITFASS-98 experiment’. In: *Theoretical and Applied Climatology* 73.1-2 (2002), pp. 19–34. doi: `10.1007/s00704-002-0691-7`.

[12] Michael Börngen and Thomas Foken. ‘150 Years: The Leipzig Meteorological Conference, 1872, a Milestone in International Meteorological Cooperation’. In: *Meteorologische Zeitschrift* 31.5 (Dec. 2022), pp. 415–427. doi: `10.1127/metz/2022/1134`.

[13] Jakob Boventer et al. ‘Validation of Doppler Wind Lidar Measurements with an Uncrewed Aircraft System (UAS) in the Daytime Atmospheric Boundary Layer’. In: *Journal of Atmospheric and Oceanic Technology* 41.7 (2024), pp. 705–723. doi: `10.1175/JTECH-D-23-0127.1`.

[14] Matteo Bramati et al. ‘A Versatile Calibration Method for Rotary-Wing UAS as Wind Measurement Systems’. In: *Journal of Atmospheric and Oceanic Technology* 41.1 (2024), pp. 25–43. doi: `10.1175/JTECH-D-23-0010.1`.

[15] Matteo Bramati et al. ‘In Situ Uncrewed Aircraft Measurements of Turbulent Kinetic Energy over Heterogeneous Terrain’. In: *Journal of Atmospheric and Oceanic Technology* 42.3 (2025), pp. 319–338. doi: `10.1175/JTECH-D-24-0026.1`.

[16] Carlo Cintolesi et al. ‘Characterisation of flow dynamics within and around an isolated forest, through measurements and numerical simulations’. In: *Agricultural and Forest Meteorology* 339 (2023), p. 109557. doi: `https://doi.org/10.1016/j.agrformet.2023.109557`.

[17] David Crowe et al. ‘Two supervised machine learning approaches for wind velocity estimation using multi-rotor copter attitude measurements’. In: *Sensors (Switzerland)* 20.19 (2020), pp. 1–13. doi: `10.3390/s20195638`.

[18] Gennaro D’Amato et al. ‘The effects of climate change on respiratory allergy and asthma induced by pollen and mold allergens’. In: *Allergy* 75.9 (2020), pp. 2219–2228. doi: `https://doi.org/10.1111/all.14476`.

[19] Peter Davidson. *Turbulence: An Introduction for Scientists and Engineers.* Oxford University Press, June 2015. isbn: 9780198722588. doi: `10.1093/acprof:oso/9780198722588.001.0001`.

[20] Luigi Di Puglia Pugliese, Francesca Guerriero, and Giusy Macrina. ‘Using drones for parcels delivery process’. In: *Procedia Manufacturing* 42 (2020), pp. 488–497. doi: `https://doi.org/10.1016/j.promfg.2020.02.043`.

[21] Hugo Díaz and Carlos Guedes Soares. ‘Review of the current status, technology and future trends of offshore wind farms’. In: *Ocean Engineering* 209 (2020), p. 107381. issn: 0029-8018. doi: `https://doi.org/10.1016/j.oceaneng.2020.107381`.

[22] Jamil Ramsi Farkat Diógenes et al. ‘Barriers to onshore wind energy implementation: A systematic review’. In: *Energy Research & Social Science* 60 (2020), p. 101337. doi: `https://doi.org/10.1016/j.erss.2019.101337`.

[23] Asmae EL BAHLOULI et al. 'Comparison of CFD Simulation to UAS Measurements for Wind Flows in Complex Terrain: Application to the WINSENT Test Site'. In: *Energies* 12 (May 2019), p. 1992. DOI: `10.3390/en12101992`.

[24] Stefan EMEIS. 'Vertical Profiles Over Flat Terrain'. In: *Wind Energy Meteorology: Atmospheric Physics for Wind Power Generation*. Cham: Springer International Publishing, 2018, pp. 31–90. ISBN: 978-3-319-72859-9. DOI: `10.1007/978-3-319-72859-9_2`.

[25] Stefan EMEIS. 'Wind Regimes'. In: *Wind Energy Meteorology: Atmospheric Physics for Wind Power Generation*. Cham: Springer International Publishing, 2018, pp. 11–30. ISBN: 978-3-319-72859-9. DOI: `10.1007/978-3-319-72859-9_2`.

[26] Stefan EMEIS. 'Winds in Complex Terrain'. In: *Wind Energy Meteorology: Atmospheric Physics for Wind Power Generation*. Cham: Springer International Publishing, 2018, pp. 91–112. ISBN: 978-3-319-72859-9. DOI: `10.1007/978-3-319-72859-9_2`.

[27] Alexander A. FLEM et al. 'Experimental Characterization of Propeller-Induced Flow (PIF) below a Multi-Rotor UAV'. In: *Atmosphere* 15.3 (2024). ISSN: 2073-4433. DOI: `10.3390/atmos15030242`.

[28] Steven J. FLETCHER. 'Chapter 14 - Observations'. In: *Data Assimilation for the Geosciences (Second Edition)*. Ed. by Steven J. FLETCHER. Second Edition. Elsevier, 2023, pp. 601–629. ISBN: 978-0-323-91720-9. DOI: `https://doi.org/10.1016/B978-0-32-391720-9.00018-8`.

[29] Federico FLORES et al. 'The Life Cycle of a Radiosonde'. In: *Bulletin of the American Meteorological Society"* 94.2 (2013), pp. 187–198. DOI: `10.1175/BAMS-D-11-00163.1`.

[30] Thomas FOKEN, Frank BEYRICH, and Volker WULFMEYER. 'Introduction to Atmospheric Measurements'. In: *Springer Handbook of Atmospheric Measurements*. Ed. by Thomas FOKEN. Cham: Springer International Publishing, 2021, pp. 3–31. ISBN: 978-3-030-52171-4. DOI: `10.1007/978-3-030-52171-4_1`.

[31] H. Howard FRISINGER. 'Aristotle's Meteorologica'. In: *The History of Meteorology: to 1800*. Boston, MA: American Meteorological Society, 1983, pp. 14–23. ISBN: 978-1-940033-91-4. DOI: `10.1007/978-1-940033-91-4_2`.

[32] H. Howard FRISINGER. 'The Beginning'. In: *The History of Meteorology: to 1800*. Boston, MA: American Meteorological Society, 1983, pp. 1–13. ISBN: 978-1-940033-91-4. DOI: `10.1007/978-1-940033-91-4_1`.

[33] Ibon GALPARSORO et al. 'Reviewing the ecological impacts of offshore wind farms'. In: *npj Ocean Sustainability* 1.1 (2022), pp. 1–8. DOI: `10.1038/s44183-022-00003-5`.

[34] John R. GARRATT. *The Atmospheric Boundary Layer*. Cambridge Atmospheric and Space Science Series. Cambridge University Press, 1994. ISBN: 9780521467452.

[35] Mauro Ghirardelli et al. ‘Flow Structure around a Multicopter Drone: A Computational Fluid Dynamics Analysis for Sensor Placement Considerations’. In: *Drones* 7.7 (2023). doi: `10.3390/drones7070467`.

[36] Paul Gipe and Erik Möllerström. ‘An overview of the history of wind turbine development: Part I—The early wind turbines until the 1960s’. In: *Wind Engineering* 46 (Aug. 2022), p. 0309524X2211178. doi: `10.1177/0309524X221117825`.

[37] Paul Gipe and Erik Möllerström. ‘An overview of the history of wind turbine development: Part II–The 1970s onward’. In: *Wind Engineering* 47 (Sept. 2022), p. 0309524X2211225. doi: `10.1177/0309524X221122594`.

[38] Javier González-Rocha et al. ‘Sensing wind from quadrotor motion’. In: *Journal of Guidance, Control, and Dynamics* 42.4 (2019), pp. 836–852. issn: 15333884. doi: `10.2514/1.G003542`.

[39] Mostafa Hassanalian and Abdessattar Abdelkefi. ‘Classifications, applications, and design challenges of drones: A review’. In: *Progress in Aerospace Sciences* 91 (2017), pp. 99–131. doi: `https://doi.org/10.1016/j.paerosci.2017.04.003`.

[40] John L. Heilbron. *The Oxford Companion to the History of Modern Science*. Oxford University Press, 2003. isbn: 9780199891153. doi: `10.1093/acref/9780195112290.001.0001`.

[41] James R. Holton and Gregory J. Hakim. ‘Chapter 1 - Introduction’. In: *An Introduction to Dynamic Meteorology (Fifth Edition)*. Ed. by James R. Holton and Gregory J. Hakim. Fifth Edition. Boston: Academic Press, 2013, pp. 1–29. isbn: 978-0-12-384866-6. doi: `https://doi.org/10.1016/B978-0-12-384866-6.00001-5`.

[42] Pietro Iob et al. ‘Avalanche Rescue with Autonomous Drones’. In: *2020 IEEE 7th International Workshop on Metrology for AeroSpace (MetroAeroSpace)*. 2020, pp. 319–324. doi: `10.1109/MetroAeroSpace48742.2020.9160116`.

[43] John Kaldellis and Dimitrios Zafirakis. ‘The wind energy (r)evolution: A short review of a long history’. In: *Renewable Energy* 36 (July 2011), pp. 1887–1901. doi: `10.1016/j.renene.2011.01.002`.

[44] Olaf Kolle et al. ‘Ground-Based Platforms’. In: *Springer Handbook of Atmospheric Measurements*. Ed. by Thomas Foken. Cham: Springer International Publishing, 2021, pp. 155–182. isbn: 978-3-030-52171-4. doi: `10.1007/978-3-030-52171-4_6`.

[45] T. G. Konrad et al. ‘A Small, Radio-Controlled Aircraft As A Platform for Meteorlogical Sensors’. In: *Johns Hopkins APL Technical Digest* December (1970), pp. 11–19.

[46] Simone Kotthaus et al. ‘Atmospheric boundary layer height from ground-based remote sensing: a review of capabilities and limitations’. In: *Atmospheric Measurement Techniques* 16.2 (2023), pp. 433–479. doi: `10.5194/amt-16-433-2023`.

[47] Branislava LALIC et al. ‘Wind profile within the forest canopy and in the transition layer above it’. In: *Environmental Modelling & Software* 18.10 (2003). Integrating Environmental Modelling and GI-Technology, pp. 943–950. DOI: `https://doi.org/10.1016/S1364-8152(03)00068-9`.

[48] Volker LEHMANN and William BROWN. ‘Radar Wind Profiler’. In: *Springer Handbook of Atmospheric Measurements.* Ed. by Thomas FOKEN. Cham: Springer International Publishing, 2021, pp. 901–933. ISBN: 978-3-030-52171-4. DOI: `10.1007/978-3-030-52171-4_31`.

[49] Donald LENSCHOW, J. MANN, and Leif KRISTENSEN. ‘How Long Is Long Enough When Measuring Fluxes and Other Turbulence Statistics?’ In: *jaot* 11 (June 1994), pp. 661–673. DOI: `10.1175/1520-0426(1994)011<0661:HLILEW>2.0.CO;2`.

[50] Daniel LEUENBERGER et al. ‘Improving High-Impact Numerical Weather Prediction with Lidar and Drone Observations’. In: *Bulletin of the American Meteorological Society* 101.7 (2020), E1036–E1051. DOI: `https://doi.org/10.1175/BAMS-D-19-0119.1`.

[51] Andrew C. LORENC. ‘Analysis methods for numerical weather prediction’. In: *Quarterly Journal of the Royal Meteorological Society* 112.474 (1986), pp. 1177–1194. DOI: `https://doi.org/10.1002/qj.49711247414`.

[52] Moritz MAUZ et al. ‘First identification and quantification of detached-tip vortices behind a wind energy converter using fixed-wing unmanned aircraft system’. In: *Wind Energy Science* 4 (Aug. 2019), pp. 451–463. DOI: `10.5194/wes-4-451-2019`.

[53] Moritz MAUZ et al. ‘Miniature high-frequency chilled-mirror hygrometer for atmospheric measurements aboard fixed wing UAS’. In: *Meteorologische Zeitschrift* 29 (Nov. 2020). DOI: `10.1127/metz/2020/1026`.

[54] Sven MAYER, Lars LISCHKE, and Pawel W. WOŹNIAK. ‘Drones for Search and Rescue’. In: *1st International Workshop on Human-Drone Interaction.* Ecole Nationale de l’Aviation Civile [ENAC]. Glasgow, United Kingdom, May 2019.

[55] Joachim NEISSER et al. ‘"Atmospheric boundary layer monitoring at the Meteorological Observatory Lindenberg as a part of the "Lindenberg Column": Facilities and selected results"’. In: *Meteorologische Zeitschrift* 11.4 (Oct. 2002), pp. 241–253. DOI: `10.1127/0941-2948/2002/0011-0241`.

[56] Patrick P. NEUMANN and Matthias BARTHOLMAI. ‘Real-time wind estimation on a micro unmanned aerial vehicle using its inertial measurement unit’. In: *Sensors and Actuators A: Physical* 235 (2015), pp. 300–310.

[57] Francesco. NEX et al. ‘UAV in the advent of the twenties: Where we stand and what is next’. In: *ISPRS Journal of Photogrammetry and Remote Sensing* 184.October 2021 (2022), pp. 215–242. DOI: `10.1016/j.isprsjprs.2021.12.006`.

[58] Albert OUDE NIJHUIS et al. ‘Wind Hazard and Turbulence Monitoring at Airports with Lidar, Radar, and Mode-S Downlinks: The UFO Project’. In: *Bulletin of the American Meteorological Society* 99 (May 2018). DOI: `10.1175/BAMS-D-15-00295.1`.

[59] Eileen PÄSCHKE, Ronny LEINWEBER, and Volker LEHMANN. ‘An assessment of the performance of a 1.5 μm Doppler LiDAR for operational vertical wind profiling based on a 1-year trial’. In: *Atmospheric Measurement Techniques* 8.6 (2015), pp. 2251–2266. DOI: `10.5194/amt-8-2251-2015`.

[60] James O. PINTO et al. ‘The status and future of small uncrewed aircraft systems (UAS) in operational meteorology’. In: *Bulletin of the American Meteorological Society* 102.11 (2021), E2121–E2136. DOI: `10.1175/BAMS-D-20-0138.1`.

[61] William M. PITTS. ‘Wind effects on fires’. In: *Progress in Energy and Combustion Science* 17.2 (1991), pp. 83–134. ISSN: 0360-1285. DOI: `https://doi.org/10.1016/0360-1285(91)90017-H`.

[62] Stephen B. POPE. *Turbulent Flows*. Cambridge University Press, 2000.

[63] Fernando PORTÉ-AGEL, Majid BASTANKHAH, and Sina SHAMSODDIN. ‘Wind-Turbine and Wind-Farm Flows: A Review’. In: *Boundary-Layer Meteorology* 174.1 (2020), pp. 1–59. DOI: `10.1007/s10546-019-00473-0`.

[64] Samuel PRUDDEN et al. ‘Measuring wind with Small Unmanned Aircraft Systems’. In: *Journal of Wind Engineering and Industrial Aerodynamics* 176.March (2018), pp. 197–210. ISSN: 01676105. DOI: `10.1016/j.jweia.2018.03.029`.

[65] Alexander RAUTENBERG et al. ‘Calibration Procedure and Accuracy of Wind and Turbulence Measurements with Five-Hole Probes on Fixed-Wing Unmanned Aircraft in the Atmospheric Boundary Layer and Wind Turbine Wakes’. In: *Atmosphere* 10 (Mar. 2019), p. 124. DOI: `10.3390/atmos10030124`.

[66] Alexander RAUTENBERG et al. ‘Reviewing Wind Measurement Approaches for Fixed-Wing Unmanned Aircraft’. In: *Atmosphere* 9.11 (2018). ISSN: 2073-4433. DOI: `10.3390/atmos9110422`.

[67] Alexander RAUTENBERG et al. ‘The Multi-Purpose Airborne Sensor Carrier MASC-3 for Wind and Turbulence Measurements in the Atmospheric Boundary Layer’. In: *Sensors* 19.10 (2019). DOI: `10.3390/s19102292`.

[68] Oliver REITEBUCH and R. Michael HARDESTY. ‘Doppler Wind Lidar’. In: *Springer Handbook of Atmospheric Measurements*. Ed. by Thomas FOKEN. Cham: Springer International Publishing, 2021, pp. 759–797. ISBN: 978-3-030-52171-4. DOI: `10.1007/978-3-030-52171-4_27`.

[69] Abderahman REJEB et al. ‘Drones in agriculture: A review and bibliometric analysis’. In: *Computers and Electronics in Agriculture* 198 (2022), p. 107017. DOI: `https://doi.org/10.1016/j.compag.2022.107017`.

[70] Nathan B. ROBERTS et al. ‘Current summary of the evidence in drone-based emergency medical services care’. In: *Resuscitation Plus* 13 (2023), p. 100347. DOI: `https://doi.org/10.1016/j.resplu.2022.100347`.

[71] Tiago Guedes Russomanno et al. 'Drone-Based Position Detection in Sports—Validation and Applications'. In: *Frontiers in Physiology* 13 (2022). DOI: `10.3389/fphys.2022.850512`.

[72] Martin Schön et al. 'Case studies of the wind field around Ny-Ålesund, Svalbard, using unmanned aircraft'. In: *Polar Research* 41 (Nov. 2022). DOI: `10.33265/polar.v41.7884`.

[73] Martin Schön et al. 'Fair Weather Atmospheric Charge Measurements with a Small UAS'. In: *Journal of Atmospheric and Oceanic Technology* 39 (Aug. 2022). DOI: `10.1175/JTECH-D-22-0025.1`.

[74] Martin Schön et al. 'OPC-Pod: A New Sensor Payload to Measure Aerosol Particles for Small Uncrewed Aircraft Systems'. In: *Journal of Atmospheric and Oceanic Technology* (May 2024). DOI: `10.1175/JTECH-D-23-0078.1`.

[75] Frederick G. Shuman. 'History of Numerical Weather Prediction at the National Meteorological Center'. In: *Weather and Forecasting* 4.3 (1989), pp. 286–296. DOI: `10.1175/1520-0434(1989)004<0286:HONWPA>2.0.CO;2`.

[76] Julia Slingo and Tim Palmer. 'Uncertainty in Weather and Climate Prediction'. In: *Philosophical transactions. Series A, Mathematical, physical, and engineering sciences* 369 (Dec. 2011), pp. 4751–67. DOI: `10.1098/rsta.2011.0161`.

[77] Tyler Stehly, Patrick Duffy, and Daniel Mulas Hernando. *2022 Cost of Wind Energy Review.* 2023. DOI: `10.2172/2278805`.

[78] Roland B. Stull. 'Application of the Governing Equations to Turbulent Flow'. In: *An Introduction to Boundary Layer Meteorology.* Ed. by Roland B. Stull. Dordrecht: Springer Netherlands, 1988, pp. 76–114. ISBN: 978-94-009-3027-8. DOI: `10.1007/978-94-009-3027-8_1`.

[79] Roland B. Stull. 'Atmospheric Boundary Layer'. In: *Practical Meteorology: An Algebra-based Survey of Atmospheric Science.* BC Open Textbook Collection. AVP International, University of British Columbia, 2016, pp. 687–722. ISBN: 9780888651761.

[80] Roland B. Stull. 'Atmospheric Forces & Wind'. In: *Practical Meteorology: An Algebra-based Survey of Atmospheric Science.* BC Open Textbook Collection. AVP International, University of British Columbia, 2016, pp. 289–329. ISBN: 9780888651761.

[81] Roland B. Stull. 'Convective Mixed Layer'. In: *An Introduction to Boundary Layer Meteorology.* Ed. by Roland B. Stull. Dordrecht: Springer Netherlands, 1988, pp. 441–498. ISBN: 978-94-009-3027-8. DOI: `10.1007/978-94-009-3027-8_1`.

[82] Roland B. Stull. 'General Circulation'. In: *Practical Meteorology: An Algebra-based Survey of Atmospheric Science.* BC Open Textbook Collection. AVP International, University of British Columbia, 2016, pp. 329–389. ISBN: 9780888651761.

[83] Roland B. Stull. 'Mean Boundary Layer Characteristics'. In: *An Introduction to Boundary Layer Meteorology.* Ed. by Roland B. Stull. Dordrecht: Springer Netherlands, 1988, pp. 1–20. isbn: 978-94-009-3027-8. doi: `10.1007/978-94-009-3027-8_1`.

[84] Roland B. Stull. 'Similarity Theory'. In: *An Introduction to Boundary Layer Meteorology.* Ed. by Roland B. Stull. Dordrecht: Springer Netherlands, 1988, pp. 347–404. isbn: 978-94-009-3027-8. doi: `10.1007/978-94-009-3027-8_1`.

[85] Roland B. Stull. 'Some Mathematical and Conceptual Tools: Part 1. Statistics'. In: *An Introduction to Boundary Layer Meteorology.* Ed. by Roland B. Stull. Dordrecht: Springer Netherlands, 1988, pp. 29–75. isbn: 978-94-009-3027-8. doi: `10.1007/978-94-009-3027-8_1`.

[86] Roland B. Stull. 'Stable Boundary Layer'. In: *An Introduction to Boundary Layer Meteorology.* Ed. by Roland B. Stull. Dordrecht: Springer Netherlands, 1988, pp. 499–544. isbn: 978-94-009-3027-8. doi: `10.1007/978-94-009-3027-8_1`.

[87] Roland B. Stull. 'Turbulence Kinetic Energy, Stability, and Scaling'. In: *An Introduction to Boundary Layer Meteorology.* Ed. by Roland B. Stull. Dordrecht: Springer Netherlands, 1988, pp. 151–196. isbn: 978-94-009-3027-8. doi: `10.1007/978-94-009-3027-8_1`.

[88] Irene Suomi and Timo Vihma. 'Wind Gust Measurement Techniques—From Traditional Anemometry to New Possibilities'. In: *Sensors* 18.4 (2018). issn: 1424-8220. doi: `10.3390/s18041300`.

[89] Mateusz Taszarek, Sebastian Kendzierski, and Natalia Pilguj. 'Hazardous weather affecting European airports: Climatological estimates of situations with limited visibility, thunderstorm, low-level wind shear and snowfall from ERA5'. In: *Weather and Climate Extremes* 28 (2020), p. 100243. issn: 2212-0947. doi: `https://doi.org/10.1016/j.wace.2020.100243`.

[90] William Thielicke et al. 'Towards accurate and practical drone-based wind measurements with an ultrasonic anemometer'. In: *Atmospheric Measurement Techniques* 14.2 (2021), pp. 1303–1318. doi: `10.5194/amt-14-1303-2021`.

[91] Ioannis Tsiropoulos et al. 'Towards net-zero emissions in the EU energy system by 2050'. In: KJ-NA-29981-EN-N (2020). doi: `10.2760/081488`.

[92] Thomas Tomkins Warner. 'Model initialization'. In: *Numerical Weather and Climate Prediction.* Cambridge University Press, 2010, pp. 198–251.

[93] Tamino Wetz, Norman Wildmann, and Frank Beyrich. 'Distributed wind measurements with multiple quadrotor unmanned aerial vehicles in the atmospheric boundary layer'. In: *Atmospheric Measurement Techniques* 14.5 (May 2021), pp. 3795–3814. doi: `10.5194/amt-14-3795-2021`.

[94] Norman Wildmann, Nikola Vasiljevic, and Thomas Gerz. 'Wind turbine wake measurements with automatically adjusting scanning trajectories in a multi-Doppler lidar setup'. In: *Atmospheric Measurement Techniques* 11.6 (2018), pp. 3801–3814. doi: `10.5194/amt-11-3801-2018`.

[95] Norman Wildmann and Tamino Wetz. ‘Towards vertical wind and turbulent flux estimation with multicopter uncrewed aircraft systems’. In: *Atmospheric Measurement Techniques* 15.18 (2022), pp. 5465–5477. doi: `10.5194/amt-15-5465-2022`.

[96] Kjell Zum Berge et al. ‘A Two-Day Case Study: Comparison of Turbulence Data from an Unmanned Aircraft System with a Model Chain for Complex Terrain’. In: *Boundary-Layer Meteorology* 180 (July 2021). doi: `10.1007/s10546-021-00608-2`.

[97] Kjell Zum Berge et al. ‘Seasonal Changes in Boundary-Layer Flow Over a Forested Escarpment Measured by an Uncrewed Aircraft System’. In: *Boundary-Layer Meteorology* 186 (Sept. 2022). doi: `10.1007/s10546-022-00743-4`.